Climate of the next million years : which scenarios for the future?

Gaëlle Leloup

université PARIS-SACLAY

Le climat du prochain million d'années : quels scénarios pour le futur ?

Climate of the next million years : which scenarios for the future ?

Thèse de doctorat de l'université Paris-Saclay

École doctorale n° 129, Sciences de l'Environnement d'Ile-de-France SEIF
Spécialité de doctorat: Instrumentation, télédétection, observation et techniques spatiales pour l'océan, l'atmosphère et le climat
Graduate School : Géosciences, climat, environnement et planètes.
Référent : Université de Versailles Saint-Quentin-en-Yvelines

Thèse préparée au **LSCE** (Université Paris-Saclay, CNRS, CEA, UVSQ), sous la direction de **Didier PAILLARD**, directeur de recherche, la co-direction de **Didier ROCHE**, directeur de recherche, le co-encadrement de **Christophe DUMAS**, ingénieur chercheur, **Aurélien QUIQUET**, chargé de recherche

Thèse soutenue à Paris-Saclay, le 3 Février 2023, par

Gaëlle LELOUP

Composition du jury

Membres du jury avec voix délibérative

Amaëlle Landais Directrice de Recherche CNRS, LSCE	Présidente
Michel CRUCIFIX Professeur, UC Louvain	Rapporteur et examinateur
Roderik van de Wal Professeur, Utrecht University	Rapporteur et examinateur
Catherine Ritz Directrice de Recherche CNRS émérite, IGE	Examinatrice

THESE DE DOCTORAT
NNT : 2023UPASJ001

université PARIS-SACLAY

ÉCOLE DOCTORALE
Sciences de l'Environnement d'Île-de-France (SEIF)

Titre: Le climat du prochain million d'années : quels scénarios pour le futur ?
Mots clés: climat, calotte de glace, cycle du carbone

Résumé: Tandis que de nombreuses études s'intéressent à l'impact des émissions anthropiques de gaz à effet de serre sur le climat du prochain siècle, très peu s'intéressent aux impacts à plus grande échelle de temps, de plusieurs dizaines de milliers d'années jusqu'à un million d'années. Cependant, dû au long temps de résidence du CO_2 dans les enveloppes superficielles de la Terre, les émissions anthropiques actuelles vont impacter le climat bien au-delà du prochain siècle. L'objectif de cette thèse est d'élargir le cadre des études actuelles sur le climat du prochain million d'années, en revisitant certaines des hypothèses classiquement faites. Les études existantes considèrent rarement une fonte partielle ou totale de la calotte Antarctique et supposent que les concentrations atmosphériques de CO_2 reviennent à la valeur pré-industrielle au bout de centaines de milliers d'années, grâce à la rétroaction des silicates. Dans cette étude, nous considérons les évolutions possibles de la calotte Antarctique. Plus précisément, j'ai étudié l'équilibre de la calotte Antarctique pour différents niveaux de CO_2 atmosphérique, en utilisant le modèle système terre de complexité intermédiaire iLOVECLIM, couplé au modèle de calotte Antarctique GRISLI. Pour cela, j'ai d'abord appliqué des niveaux de CO_2 croissants, jusqu'à ce que la calotte Antarctique fonde entièrement, puis j'ai appliqué des niveaux de CO_2 décroissants, jusqu'à ce que la calotte re-grossisse. Nos résultats montrent qu'il y a un fort effet d'hystérésis. Notre configuration permet de prendre en compte la rétroaction de l'albédo sur la fonte, et produit des transitions entre des états de l'Antarctique englacés ou désenglacés plus brutales que dans des études ne prenant pas en compte cette rétroaction. La limite en CO_2 conduisant à une glaciation ou déglaciation de l'Antarctique dépend de la configuration orbitale. En parallèle, j'ai développé un modèle conceptuel pour le cycle du carbone géologique, qui comporte des équilibres multiples, ayant pour objectif de reproduire des cycles de plusieurs millions d'années dans le $\delta^{13}C$, en cohérence avec les données. Ces éventuels équilibres multiples dans le cycle du carbone pourraient donner lieu à une évolution du CO_2 atmosphérique à long terme très différente de celle modélisée dans de précédentes études. Enfin, nous discutons des implications de nos résultats sur une possible sortie du Quaternaire, avec non seulement une fin des glaciations de l'hémisphère Nord mais aussi une fonte totale de la calotte Antarctique.

université PARIS-SACLAY

ÉCOLE DOCTORALE
Sciences de l'Environnement d'Île-de-France (SEIF)

Title: Climate of the next million year : which scenarios for the future ?
Keywords: climate, ice sheet, carbon cycle

Abstract: While many studies focus on the impacts of anthropogenic greenhouse gas on climate on the timescale of the next century, very few have investigated the impacts on a longer timescale, from tens of millennia to a million years. However, due to the long lifetime of CO_2 in Earth's surface reservoirs, current anthropogenic emissions are expected to impact the climate on a much longer timescale than the coming century. The objective of this thesis is to broaden the scope of existing studies on the climate of the next million years, by revisiting some of their classical hypotheses. Existing studies rarely consider a partial or total melt of the Antarctic ice sheet, and assume that atmospheric CO_2 concentrations come back to pre-industrial levels after hundreds of thousands years, due to silicate weathering. In this study, we explore potential evolutions of the Antarctic ice sheet. More precisely, I have investigated the long term equilibrium of the Antarctic ice sheet under different CO_2 levels, using the Earth System model of intermediate complexity iLOVECLIM, coupled to the GRISLI Antarctic ice sheet model, by first applying increasing CO_2 levels until the Antarctic ice sheet retreats entirely, and then applying decreasing CO_2 levels until the ice sheet regrows. Our results show that the ice sheet exhibits a strong hysteresis behavior. Due to the inclusion of the albedo-melt feedback in our setup, the transition between a glaciated Antarctic ice sheet and an ice-free Antarctic and conversely is more brutal than in previous studies not including this feedback. The CO_2 threshold for both Antarctic glaciation and deglaciation varies with the orbital configuration. Additionally, I have developed a conceptual model for the geological carbon cycle that includes multiple equilibria in order to reproduce multi million year cycles in the $\delta^{13}C$ that are coherent with the data. These potential multiple equilibria in the carbon cycle could lead to a widely different atmospheric CO_2 concentration evolution on long timescales, compared to existing studies. Finally, we discuss the implications of our results on a potential end of the Quaternary in the future, with a disappearance of Northern Hemisphere glaciations, but also a disappearance of the Antarctic ice sheet.

Remerciements

Pour me motiver pendant l'écriture du manuscrit, je me suis plusieurs fois visualisée arrivée à cette étape finale, l'écriture des remerciements. Maintenant que la soutenance est passée et que les dernières corrections du manuscrit ont été faites, je procrastine, car il n'est finalement pas si simple de trouver les bons mots pour exprimer ma gratitude envers toutes les personnes qui m'ont accompagnée au cours de cette thèse!

Pour commencer, un immense merci à Didier P., sans qui, il va sans dire, cette thèse aurait été bien différente. Lors de mon stage de master, je n'étais pas encore sûre de vouloir continuer en thèse, mais tes explications sur les paléoclimats et l'originalité du sujet m'ont convaincue ! Merci pour ta grande pédagogie, ta disponibilité et ta confiance tout au long de la thèse. Un immense merci également à Didier R., Christophe et Aurélien pour votre encadrement, vos conseils, idées, et aide sur les modèles iLOVECLIM et GRISLI.

J'ai eu la chance de réaliser cette thèse dans l'équipe CLIM, une équipe bienveillante dans laquelle j'ai pu trouver du soutien à la fois scientifiquement et humainement. Grâce à vous, je me suis très rapidement sentie intégrée au LSCE.

Dès mes premiers jours de stage, j'ai été particulièrement bien accueillie par Fanny, Julia et Marie dans le bureau Arc-En-Ciel. Merci pour vos conseils toujours avisés et votre soutien. Ça a été très rassurant de vous voir passer toutes les "étapes" de la thèse un an avant moi. Notre entraide à la fois sur le plan professionnel et personnel et qui a perduré après votre départ du labo, m'a été très précieuse. Mon seul regret est que le covid ne nous ait pas permis d'être toutes les quatre dans le bureau aussi souvent que je l'aurais souhaité ! Merci à Diane, Delphine, et Si Qing d'avoir accompli avec brio la lourde tâche de les remplacer au sein du bureau Arc-En-Ciel.

Au-delà du bureau Arc-En-Ciel, j'ai également toujours pu compter sur notre "groupe de fille" : Alizée C., Alizée D., Audrey, Sophie, Stella, merci infiniment pour votre écoute, votre soutien et tous les bons moments passés ensemble au labo et en dehors. Merci également à Dieu, Lucille, Maureen, Ségolène, Yann pour les nombreux repas, cafés et verres partagés. Thomas, Elias, merci pour cette amitié qui aura continué bien au delà de votre présence au labo, pour tous ces bons moments, les WE de rando, les spectacles d'impro, les conférences, les "grandes marches" dans Paris, et les incontournables soupes de pois cassés.

Merci à tous les membres de l'Association Avenir Climatique, une association grâce à laquelle j'ai beaucoup appris et ai rencontré beaucoup de personnes très inspirantes. Un merci tout particulier à Marie-Laure et Marine, pour tous ces moments partagés à ÉduClimat et pour cette belle amitié qui perdure depuis.

Un immense merci à ma famille, et mes parents qui m'ont toujours soutenue et aidée au cours de mes études et de la thèse. Mon Boudin (ceci est un surnom affectueux et validé par l'intéressée) que j'aime et que j'admire, merci pour ton soutien sans faille depuis maintenant 26 ans.

Et enfin, Clément, merci pour le bonheur immense que tu m'apportes au quotidien, merci pour ton soutien pendant la thèse, et particulièrement pendant les dernières semaines (les derniers mois...?) où je n'ai pas toujours été facile à vivre... J'espère réussir à faire aussi bien pour toi !

Contents

Introduction

What will be the impact of current's human societies on climate, at a geological timescale ? Do the current release of carbon to the atmosphere due to human activities has the power to interfere with the natural climatic evolution ? Does this perturbation correspond to a change of geological era ?

The question of the long-term "irreversibility" of the climate changes we are producing arises. This question also has very practical implications in the case of high-level radioactive waste, that remain dangerous for hundred of thousand years. Currently envisaged solutions for high-level radioactive waste management include disposal in deep geological formations, for hundreds of thousand years. The possible long term impacts of climatic changes on the safety of radioactive waste repositories in these deep formations thus needs to be assessed.

In the field of climate modelling, many studies focus on the impact of anthropogenic greenhouse gas emissions on the future evolution of the different components of the climate system : atmosphere, ocean, vegetation, cryosphere. The rise in atmospheric carbon dioxide (CO_2) concentration due to human activities increases the Earth's radiative forcing. This leads to an increase in global atmospheric temperature, changes in the atmospheric and oceanic circulation, and the cryosphere.

Created in 1988 in order to provide policymakers with regular scientific assessments on climate change, its implications and potential future risks, the Intergovernmental Panel on Climate Change (IPCC) reviews the state of knowledge on climate change. In its latest report, the IPCC stated that "Observed increases in well-mixed greenhouse gas (GHG) concentrations since around 1750 are unequivocally caused by human activities." and "It is unequivocal that human influence has warmed the atmosphere, ocean and land. Widespread and rapid changes in the atmosphere, ocean, cryosphere and biosphere have occurred" [IPCC, 2021]. As future global warming will depend on the amount of anthropogenic emissions, with higher levels of greenhouse gas emissions associated with higher greenhouse gas concentration and warming [IPCC, 2021], several emission scenarios have been developed in order to compare model projections for different amounts of anthropogenic emissions [Meinshausen et al., 2011, 2020]. These scenarios were called Representative Concentration Pathways (RCP) in previous IPCC reports and are called Shared Socio-economic Pathways (SSP) in the latest report, AR 6. The SSP scenarios range from a low emission scenario, SSP1-1.9 that reflects most closely a 1.5°C target under the Paris agreement, to a high fossil fuel development throughout the 21st century scenario, SSP5-8.5, which approximately corresponds to the RCP4.5 "business as usual" scenario used in previous reports [Meinshausen et al., 2020]. At the horizon of 2100, the global mean surface temperature increase compared to the pre-industrial period is projected to be of 2.1°C to 3.5°C (with a

best estimate of 2.7°C), under the "middle of the road" greenhouse gas emission scenario, SSP2-4.5, and 3.3°C to 5.7°C (with a best estimate of 4.4°C) under the very high greenhouse gas emission scenario (SSP5-8.5) [IPCC, 2021]. Looking at the horizon 2300, the global mean temperature increase compared to pre-industrial is projected to be 2.3°C- 4.6°C under SSP2-4.5, and 6.6°C–14.1°C under SSP5-8.5 [Lee et al., 2021].

Comparison with past climates is insightful to put these temperature increases into context [Burke et al., 2018b, Tierney et al., 2020a]. The Cenozoic climate (66 Myr BP to present) is characterized by four different climatic states : the Hothouse, Warmhouse, Coolhouse and Icehouse states [Westerhold et al., 2020]. During the Warmhouse, and Hothouse global mean temperatures were respectively more than 5°C and more than 10°C than at pre-industrial. The Warmhouse and Hothouse state prevailed from the start of the Cenozoic, to the Eocene-Oligocene Transition. During the Hothouse, in the early Eocene, CO_2 levels were estimated to be ∼1500 ppm [Rae et al., 2021], and ∼1000 ppm in the Warmhouse phase of the middle to late Eocene. Around ∼34 Myr BP, at the Eocene-Oligocene transition the Warmhouse transitioned into the Coolhouse state, marked by a strong temperature drop and increase in continental ice volume, due to the development of the Antarctic ice sheet. The CO_2 levels are estimated to have fallen to $\sim$ 800 ppm at the Eocene-Oligocene Transition. The Coolhouse state, that spans $\sim$ 34 Ma to 3.3 Ma BP, covers the Oligocene and Miocene. The Icehouse state, started 3.3 Myr BP, is driven by the waning and waxing of ice sheets in the Northern Hemisphere, known as the glacial-interglacial cycles. Global mean temperature expected at the end of the 23rd century, under SSP2-4.5 (2.3°C–4.6°C higher than at pre-industrial) has not been experienced since the Mid Pliocene, about three million years ago. Under SSP5-8.5, global mean temperature expected at the end of the 23rd century (6.6°C–14.1°C higher than over the period 1850–1900) overlaps with the range estimated for the Miocene Climatic Optimum (5°C–10°C higher) and Early Eocene Climatic Optimum (10°C–18°C higher), about 15 and 50 million years ago, respectively. Under high emission scenarios, the CO_2 level is expected to peak around 2200 ppm; a level that has not been seen in the course of the Cenozoic [Rae et al., 2021].

The majority of studies in the field of future climate, and the one reviewed by the IPCC only focus on the timescale of the end of the century or a few centuries (up to 2300). Very few studies exist on multi-millenial timescale, and even less at the million year timescale. However, it is certain that impacts of current anthropogenic greenhouse gas emissions will continue after 2100. The timescale associated with a return to pre-industrial CO_2 levels is currently estimated to be several hundred thousands years [Archer et al., 1997, 1998, Archer, 2005, Lord et al., 2016], which allows reactions with slower components of the Earth systems, such as ice sheets [Winkelmann et al., 2015].

This raises the question of the impact of the anthropogenic perturbation in

terms of geological era. Will the Earth enter a new state ? Leave the Quaternary Icehouse marked by an alternance of glacial-interglacial cycles in the Northern Hemisphere ? Is a partial or complete retreat of Antarctica possible ? Will these changes be transient or permanent ?

In this thesis, we focus on two key elements of the Earth system on long timescales : ice sheets and the carbon cycle. Despite their scarcity, some studies on the long term fate of atmospheric CO_2 and ice sheets after the anthropogenic perturbation do exist.

Some studies focus on the evolution of atmospheric CO_2 levels following emission on the timescale of hundreds of millenia to a million years [Archer et al., 1997, 1998, Archer, 2005, Lord et al., 2016]. For instance, Lord et al. [2016] used an Earth System Model (cGENIE), to determine the time needed to return to pre-industrial CO_2 levels after a given fossil fuel release. In cGENIE, the additional atmospheric carbon dioxide is progressively removed by different inorganic processes having different timescales : chemical equilibrium with the ocean and export of carbon at depth due to the oceanic circulation, on a timescale from year to millenia, carbonate dissolution on a timescale of 1 kyr to 10 kyr, and ultimately via silicate weathering, on a timescale of 200 -300 kyr. The cGENIE model was forced with different emission scenarios, allowing to obtain a "response function" : a function that describes the CO_2 concentration evolution over time, depending on the cumulative CO_2 emissions. Lord et al. [2016] have found that independently of the emission scenarios, 7% of emissions are ultimately removed by silicate weathering. In the case of a pulse emission of 5 000 GtC (which corresponds approximately to the sum of already achieved emissions and emissions of the scenario SSP5-8.5 until year 2250), $\sim$35%, 12%, and 7% of the carbon emitted remains in the atmosphere after respectively 1 000 years, 10 000 years and 100 000 years, leading to atmospheric CO_2 concentration of respectively $\sim$ 1100 ppm, 560 ppm, and 440 ppm. However, the authors have stressed that their study neglects potential influence from the organic carbon cycle, and that the link between weathering and climate is parametrized in a relatively simple way. This could change the response of atmospheric CO_2 concentration over time, following anthropogenic emissions. Additionally, neglecting the role of the organic carbon cycle does not allow to reproduce past $\delta^{13}C$ data, that exhibit oscillations on different timescales, 400 kyr as well as much longer multi-million year cycles [Kocken et al., 2019, Boulila et al., 2012, Martinez and Dera, 2015].

Additionally to studies on the long term fate of atmospheric carbon dioxide, studies exist on the climate (in terms of global temperature and ice volume) over the next million year (the BIOCLIM project, Lord et al. [2019], Talento and Ganopolski [2021]). For instance, Talento and Ganopolski [2021] have developed a reduced-complexity model in order to assess the impact of anthropogenic CO_2 emissions on future glacial cycles. Their model is based on three equations representing the evolution of ice volume, temperature and CO_2. The sole forcing of the model

are the insolation and cumulative anthropogenic emissions. In the future, an anthropogenic CO_2 component is added. The anthropogenic CO_2 component is computed through the use of the impulse response function of Lord et al. [2016]. The model parameters are calibrated using both paleo reconstructions over the Quaternary and outputs from the CLIMBER-2 model. The model represents qualitatively well the glacial-interglacial ice volume evolution over the last million years. The authors find that even for low (already achieved) emission scenarios of 500 PgC, the behaviour of the climate is affected for a very long period of time, the next glaciation being very unlikely until 120 kyr AP, while several studies estimate that it would take place in 50 kyr AP in a natural case. They find that cumulative emissions of 3 000 PgC will most likely lead to Northern Hemisphere Ice free conditions for the next half million year. One key assumption of their work is that ice volume is equal or higher than pre-industrial levels at all time, and the model parameters were calibrated on past glacial cycles, corresponding to variations of the Northern Hemisphere ice sheet, but where a stable Antarctic ice sheet remained. Therefore, the authors warn that their approach is not applicable for cases where anthropogenic emissions lead to a substantial melting of the Antarctic ice sheet. Additionally, their anthropogenic CO_2 component is derived from the impulse response function of Lord et al. [2016] that neglects processes that could be of importance for the long term carbon cycle, such as organic matter burial.

To sum up, studies on the timescale of a million year agree that anthropogenic fossil fuel emissions will impact climate on long timescale, with stronger impacts for higher cumulated emissions. However, most studies on the long term fate of carbon rely on the assumption that silicate weathering is the ultimate CO_2 sink, and neglect the influence of organic processes of the carbon cycle. Conceptual models are often used to project the ice evolution in the future. However, these conceptual models are calibrated on past glacial-interglacial cycles and cannot be used to project a complete Greenland ice sheet disappearance or a substantial Antarctic ice sheet retreat, that can be expected over the next millenia under high emission scenarios [Clark et al., 2016, Van Breedam et al., 2020, Winkelmann et al., 2015].

This is what motivates our study. The objective of this thesis is to broaden the scope of existing studies on the climate of the next million year. We explore the potential melt of the Antarctic ice sheet due to increased CO_2 concentration. Additionally, we develop a conceptual model for the geological carbon cycle that includes the role of organic matter burial, and can produce multi-million years oscillations in the $\delta^{13}C$, in coherence with the data.

In the first chapter, we review important elements of context and existing studies on the climate of the next million years.

In the second chapter, we investigate what can be said about the terrestrial ice volume in the next million years in a "natural" case, without anthropogenic emissions. To do so, we have developed a conceptual model able to represent past

glacial-interglacial ice volume variation, as a response to summer insolation variations. We have studied the influence of the choice of summer insolation used as input, and of one important model parameter, the deglaciation threshold, on the model results. Finally, the conceptual model is used over the next million years. In this chapter, the ice volume evolution is studied in a case without anthropogenic emissions. However, current and future anthropogenic emissions can lead to the partial or total retreat of currently existing ice sheets : Greenland and Antarctica. Currently, less work has been performed on the Antarctic ice sheet, as it is susceptible to higher levels of warming than the Greenland ice sheet.

Therefore, we have decided to investigate the behaviour of the Antarctic ice sheet under higher atmospheric CO_2 concentrations. To do so, we use the atmosphere-ocean-vegetation model of reduced complexity iLOVECLIM, coupled to the GRISLI Antarctic ice sheet model. The models used are presented in Chapter 3. Chapter 3 also details the coupled setting and the model calibration performed in order to obtain the reference configuration from which simulations with higher CO_2 levels are started : an equilibrated present-day ice sheet under pre-industrial CO_2 levels.

In chapter 4, we apply increasing CO_2 levels to the Antarctic ice sheet until it melts entirely. It is known that ice sheets exhibits an hysteresis behaviour [Pollard and DeConto, 2005, Garbe et al., 2020, Robinson et al., 2012]. Therefore, we also study the behaviour of the ice sheet regrowth, by lowering the CO_2 levels applied until the ice sheet regrows. The sensitivity of the results to the insolation is investigated. In addition, we investigate the role of the albedo feedback, as our coupled setting allows to take it into account, while it was not in previous modelling studies of the Antarctic ice sheet long term fate [Garbe et al., 2020, Winkelmann et al., 2015]. The simulations carried out in Chapter 4 are equilibrium simulations, performed for a fixed level of atmospheric CO_2 and a fixed insolation. In the next million years, the insolation will vary. The insolation changes at the scale of one million years are accurately known [Laskar et al., 2004]. However, the evolution of the atmospheric CO_2 concentration on this timescale is much more uncertain. It will depend on the cumulative CO_2 emissions, and on the efficiency of different processes to remove atmospheric CO_2. Currently existing long term CO_2 scenarios do not take into account organic matter burial, and do not permit to reproduce past $\delta^{13}C$ data.

Therefore, in Chapter 5, we develop a new conceptual model for the geological carbon cycle, that includes organic matter burial. In our model, there are different possible equilibria in the carbon system. This non linearity allows us to produce multi-million year cycles in $\delta^{13}C$, as are seen in the data [Boulila et al., 2012, Martinez and Dera, 2015]. Finally, we look at different idealized scenarios to illustrate the impact of the possible presence of multiple equilibria in the carbon cycle on future atmospheric CO_2 concentrations, following emissions.

In a last part, we discuss which insights our results bring to the questions : how

will anthropogenic greenhouse gas emissions impact the climate on a timescale up to a million year ? Is a end of the Quaternary in the future possible? With a disappearance of Northern Hemisphere glaciations, but also a disappearance of the Antarctic ice sheet ?

1 - Context and state of the art

Chapter aims:

1. Present existing knowledge on the carbon cycle on long timescales, and its modelling.
2. Present generalities about ice sheets, and review current work on their modelling on a multi-millenia timescale.
3. Present existing studies on the climate of the next million years.

Highlights:

↪ Existing modelling studies on the carbon cycle on a timescale of a million years are based on the assumption that CO_2 levels come back to their pre-industrial value, ultimately due to CO_2 removal via silicate weathering.

↪ Modelling studies on the climate of the next million years do not consider a partial or total retreat of the Antarctic ice sheet, while studies on a timescale of a few millenia have shown that a large retreat of the Antarctic ice sheet is possible under high emission scenarios.

In this first chapter, we discuss existing knowledge on the two major Earth System components on long timescales, that are the focus of this thesis : carbon cycle and ice sheets. First, we review existing knowledge on the carbon cycle at present and in the past, as well as modelling studies on its long term response to the anthropogenic greenhouse gas release. Then, we discuss existing studies on ice sheet modelling on long timescale (several millenia). Finally, we review existing studies on the climate of the next million years, discuss their limitations and the novelty of this thesis compared to previous studies.

1.1 . Carbon cycle on long time scales

1.1.1 . Global view of the current carbon cycle

Carbon cycle is made of reservoirs that contain carbon and of the exchanges taking place between these reservoirs. The current emissions of fossil fuel CO_2 due to human activities is modifying the carbon cycle. A schematic of the carbon cycle is presented in Figure 1.1.

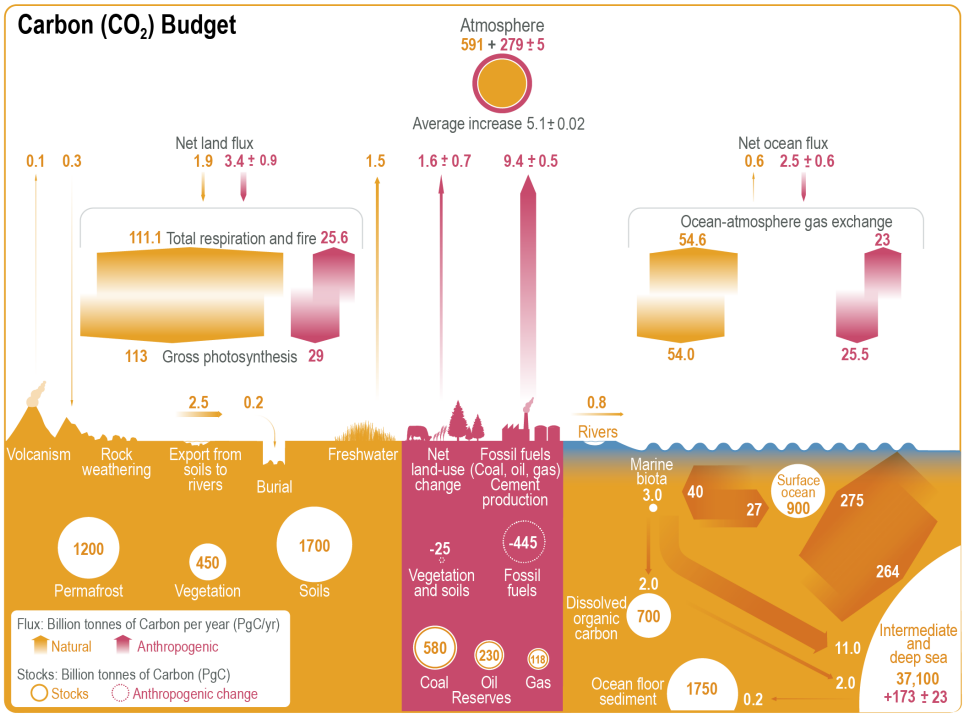

Figure 1.1: Global carbon (CO_2) budget (2010–2019). Yellow arrows represent annual carbon fluxes (in PgC yr^{-1}) associated with the natural carbon cycle, estimated for the time prior to the industrial era, around 1750. Pink arrows represent anthropogenic fluxes averaged over the period 2010–2019. The rate of carbon accumulation in the atmosphere is equal to net land-use change emissions, including land management plus fossil fuel emissions, minus land and ocean net sinks. Circles with yellow numbers represent pre-industrial carbon stocks in PgC. Circles with pink numbers represent anthropogenic changes to these stocks (cumulative anthropogenic fluxes) since 1750. In this thesis we will focus on the geological, long term fluxes : volcanism, rock weathering and burial. Figure from Canadell et al. [2021]. Legend adapted from Canadell et al. [2021].

The surface carbon reservoir is constituted of :

- the atmosphere : at the pre-industrial era, the atmosphere contained 600 GtC, corresponding to a CO_2 concentration of 280 ppm. The carbon contained in the atmosphere has a major effect on climate, through the radiative effect of CO_2.
- the biosphere, that includes soils and vegetation is estimated to contain 2000 - 3000 GtC
- the ocean : it is a very big carbon reservoir, with approximately 39 000 GtC, $\sim$60 times the quantity of carbon in the atmosphere.

On short timescale, these surface reservoirs (atmosphere, biosphere, ocean) interact with each other. For instance, CO_2 is exchanged between the atmosphere and biosphere through photosynthesis and respiration. CO_2 is exchanged at the interface between the atmosphere and the ocean : atmospheric CO_2 dissolves into the ocean if the partial pressure of CO_2 of water locally is lower than the local atmospheric partial pressure of CO_2.

On geological timescales, the atmospheric, oceanic and biospheric reservoirs interact with the geological reservoirs : sediments and rocks. The fluxes are very small and exchanges take place on much longer timescale.

This is depicted in the (even more) simplified schematic carbon cycle of Figure 1.2.

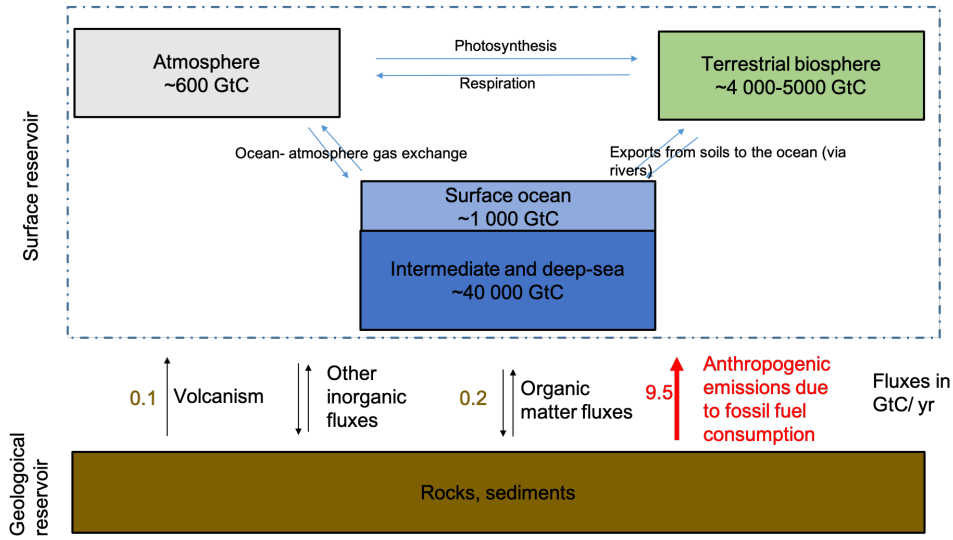

Figure 1.2: Simplified schematic of the global carbon cycle. Stocks are in the coloured squares and fluxes between the different reservoirs are depicted by arrows. Please note that processes are missing in this simplified view, and that the objective is not to be exhaustive.

Schematically, the quantity of carbon in the atmosphere depends on :

- the total quantity of carbon in the surface reservoir (atmosphere, terrestrial biosphere, and ocean). The more there is carbon globally in the surface reservoir, the more likely it is to have high CO_2 quantity in the atmosphere.
- the exchange between atmosphere, biosphere, and ocean. For a same total surface carbon quantity C, the CO_2 content can be lower or higher depending on the "efficiency" of the two other reservoirs, the biosphere and the ocean. For instance, the atmosphere interacts with the surface ocean, and carbon can be exported through several mechanisms at the ocean depth, before being brought back to the surface by oceanic circulation. At a time where more carbon is stored at depth, this reduces the carbon at the surface ocean and the ocean can uptake more of the atmospheric CO_2. Similarly, in case of a growing biosphere, the biosphere will store more atmospheric carbon due to photosynthesis. This can explain transient changes in the atmospheric CO_2 concentrations on timescales of a few decades to millenia (timescale of the oceanic circulation).

During the glacial-interglacial cycles of the Quaternary, the atmospheric CO_2 concentration was much lower during glacial time. A different repartition of carbon between the oceanic and atmospheric reservoirs at that time is the leading hypothesis to explain the atmospheric CO_2 differences on these timescale ($\sim$ 1 000 yrs) [Bouttes et al., 2011].

However, on geological timescale, the atmospheric CO_2 content is also determined by the exchanges with the geological reservoirs (with fluctuations owing to the repartition with the different surface carbon reservoirs). For instance, volcanism is a CO_2 source. Fluxes due to volcanism are currently estimated between 0.04 and 0.175 GtC $yr^{-}1$ [Burton et al., 2013]. There are also fluxes of inorganic matter as well as organic matter to and from rocks and sediments. They will be further detailed in the following and Chapter 5. Although a precise estimate of these fluxes is a difficult task, they are of the same order of magnitude as volcanism, and much lower than the current flux due to anthropogenic consumption of fossil fuels (around 9.5 GtC/yr).

As the ocean has a particularly important role in the carbon cycle, acting on both short and longer timescales, we detail some processes here. The oceanic carbon cycle consists of both, organic and inorganic carbon.

- organic carbon

  With lights and nutrients, marine phytoplanktons perfom photosynthesis in surface waters, through the reaction :

$$106CO_2 + 16NO_3^- + H_2PO_4^- + 17H_3O^+ + 105H_2O + light$$
$$\rightarrow (CH_2O)_{106}(NH_3)_{16}(H_3PO_4) + 138O_2 \quad (1.1)$$

  This reaction consumes CO_2 and produces organic carbon. When the plancton dies, it sinks to the bottom of the ocean. During its way in the water column, most of the carbon is remineralized and only a small fraction of it ($\sim$1% or less) is buried into sediments. The fact that CO_2 of surface waters is used to form organic carbon that sinks, and is remineralized at depths constitutes a carbon sink for the atmosphere on millenial timescale, as there is less CO_2 on surface waters, able to interact with the atmosphere. It is called the "soft tissue" pump.

- inorganic carbon

  In the ocean, the dissolved CO_2 reacts following the reaction :

$$CO_2(aq) + CO_3^{2-} + H_2O \leftrightarrow 2HCO_3^- \quad (1.2)$$

  This increases the concentration of bicarbonate ions (HCO_3^-) and decreases the concentration of carbonate ions (CO_3^{2-}). This also decreases ocean pH. A part of atmospheric CO_2 dissolves in seawater and the surface CO_2 enriched waters are brought at depth by the oceanic circulation. This is especially true in polar regions, zones of deep water formation and where the water at the surface is colder and thus CO_2 more soluble.

  Additionally, the biology also produces inorganic carbon. This is the case of calcifying planktons, planktons that form a calcite shell, such as coccoliths or foraminifera. They produce $CaCO_3$ in surface water, through the reaction :

$$Ca^{2+} + CO_3^{2-} \rightarrow CaCO_3 \quad (1.3)$$

  A non negligeable portion of it is buried into sediments ($\sim$25%), while the rest is remineralized.

A particularly relevant question to the study of climate is : following an initial carbon release due to anthropogenic activities (fossil fuel consumption or land use change), how much carbon will stay in the atmosphere, and for how long ?

On a timescale of a few centuries, the anthropogenic CO_2 emissions released into the atmosphere equilibrate between the reservoirs of the atmosphere, ocean and terrestrial biosphere. For instance, it is estimated that of the CO_2 emitted during the decade 2010–2019, 46% accumulated in the atmosphere, while 31%

was stored by vegetation in terrestrial ecosystems and 23% was taken up by the ocean [Canadell et al., 2021]. After the initial equilibrium between the atmosphere, ocean and vegetation reservoir, a sizeable fraction of atmospheric CO_2 remains, and the processes allowing for a further decrease of CO_2 (that will be discussed below) operate on longer timescales (thousands to ten of thousands of years).

Therefore, anthropogenic carbon emissions can interact with components of the climate system that have a slow response time, such as ice sheets [Winkelmann et al., 2015], and impact the climate on very long timescales.

In the following, I start by reviewing our current state of knowledge on the carbon cycle in the past, more specifically the estimates of atmospheric CO_2 and carbon isotopes (section 1.1.2). Then, I present existing studies on the lifetime of atmospheric CO_2 (section 1.1.3). Finally, I outline some processes that are not taken into account in these studies and that could be of importance (section 1.1.4).

1.1.2 . What do proxies tell us about carbon cycle in the past ?

Due to the radiative effect of atmospheric CO_2, its concentration in the past is a key information for the study of paleoclimate.

Insights into greenhouse gases (CO_2, CH_4, N_2O) concentrations over the last 800 kyr period are available by analysing the composition of the air trapped in ice cores in the past [Lüthi et al., 2008, Bereiter et al., 2015, Loulergue et al., 2008, Spahni et al., 2005]. For instance, it is known that over the last 800 kyr, CO_2 oscillated between 180-200 ppm in cold periods and 240-280 ppm in warmer periods, as visible in Figure 1.3. This will be further detailed in Chapter 2.

However, for periods of time older than 800 kyr ago, direct measurements of past CO_2 concentrations do not exist, and different proxies are used to reconstruct past CO_2 variations several million years in the past. These proxies are associated with a much larger uncertainty than ice core measurements, but much progress has been made in the last decades to improve theses proxies [Beerling and Royer, 2011, Rae et al., 2021]. They consist for instance of : carbon isotopes in organic matter alkenones [Zhang et al., 2013], boron isotopes in planktic foraminifera [Hönisch et al., 2009], carbon isotopic composition of paleosol carbonate nodules [Cerling, 1992], stomatal indices of fossil leaves [Retallack, 2009].

CO_2 reconstructions over the Cenozoic (last 66 Myr) have mostly a coherent behaviour with reconstructions of deep sea temperatures, with warm, ice-free periods associated with higher CO_2 levels and conversely [Beerling and Royer, 2011, Rae et al., 2021]. A reconstruction of CO_2 levels (from a recent review [Rae et al., 2021] using boron isotopes of carbonate and carbon isotopes of organic matter estimates), as well as surface temperature and sea level is shown in Figure 1.4.

The CO_2 levels reached during the early Eocene were around $\sim$ 1500 ppm [Rae et al., 2021]. This corresponds to the "Hothouse" [Westerhold et al., 2020] period, a period of extreme global warmth with global temperatures more than 10°C higher than today and where no ice sheets were present. Falling CO_2 is

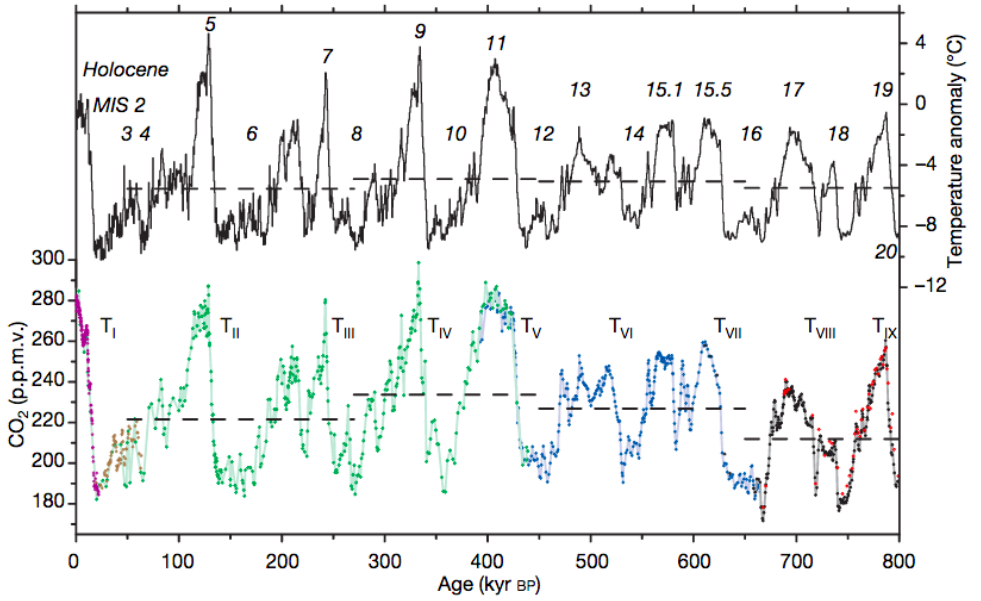

Figure 1.3: Compilation of CO_2 records and EPICA Dome C temperature anomaly over the past 800 kyr. Figure from Lüthi et al. [2008]

associated with a cooling to the middle and late Eocene "Warmhouse" period with CO_2 levels around $\sim$ 1000 ppm and surface temperatures more than 5°C higher than today. The start of Antarctic glaciation at the Eocene-Oligocene boundary (33-34 Myr BP) follows a sharp drop in CO_2 [Beerling and Royer, 2011], with CO_2 levels being around $\sim$ 800 ppm. The "Coolhouse" climates of the Oligocene and early Miocene correspond to CO_2 concentrations around 600 ppm. At the Miocene Climatic Optimum (18 - 14 Myr BP), a significant retreat of the Antarctic ice sheet took place, and it is associated with peak CO_2 levels [Foster et al., 2012]. Then, CO_2 levels decreased again. There is a slight CO_2 rise during the mid-Pliocene Warm period (~ 400 ppm), before CO_2 falls again in the Plio-Pleistocene ($\sim$180 - 300 ppm). This corresponds to a "Ice house" state with glaciations taking place in both Hemispheres. For all past CO_2 estimations, a large spread in estimations remains. For instance, there is a large spread when using the same proxy as visible in panel (c) of Figure 1.4. Additionally, Steinthorsdottir et al. [2016] highlighted that reconstructed CO_2 values with terrestrial proxies are significantly lower than when using marine proxies (such as in Rae et al. [2021], from which the values are given above). For instance, Steinthorsdottir et al. [2016] found that CO_2 levels were around $\sim$410 ppm at the Eocene-Oligocene boundary (in the contrary to a drop from around $\sim$1000ppm to $\sim$800ppm at this period in Rae et al. [2021]). This highlights the fact that CO_2 reconstructions differ widely among proxies used. Also, it cannot be excluded that CO_2 varied on orbital timescale, as observed in the Quaternary, in addition to the decreasing trend from the Eocene to the Oligocene.

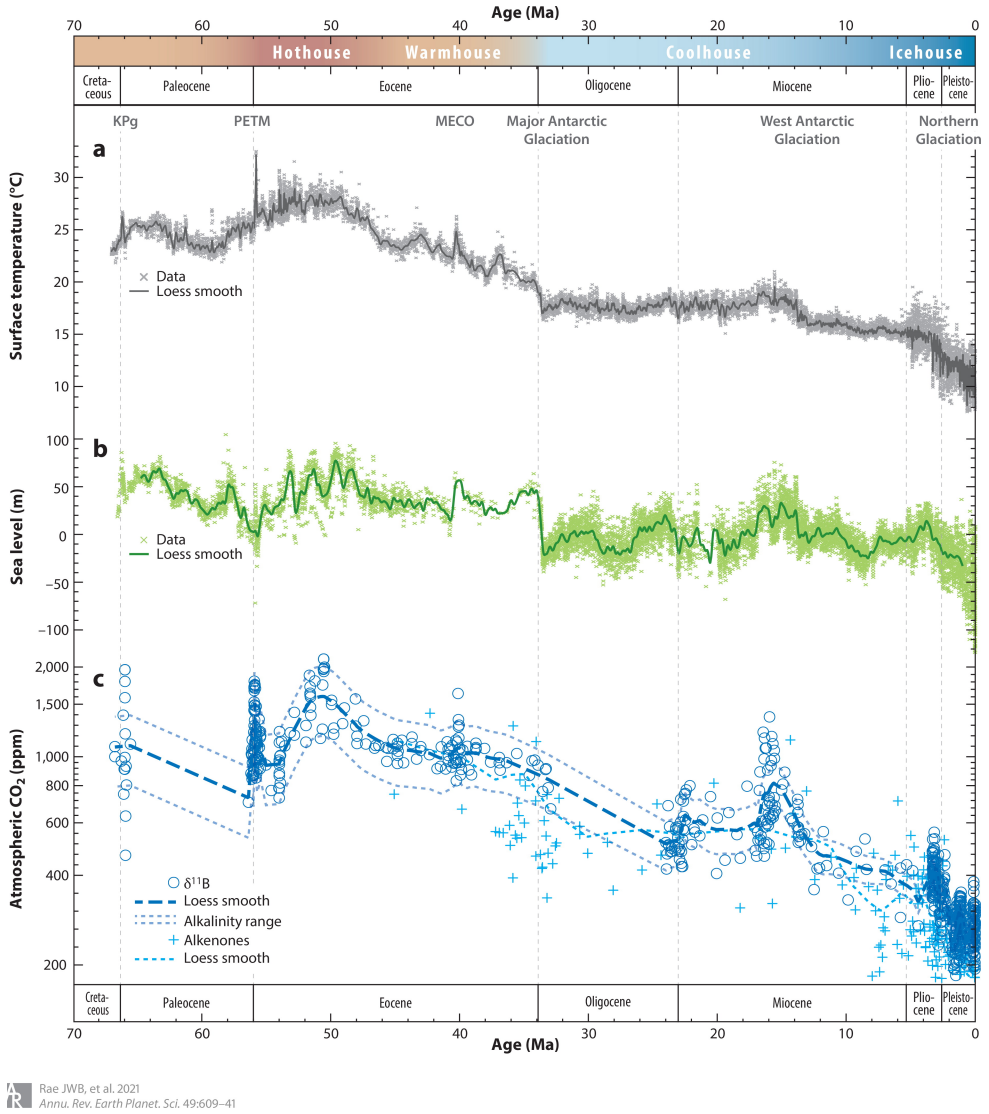

Figure 1.4: Cenozoic CO_2 and global climate. (a) Surface temperature estimated from the benthic $\delta^{18}O$ stack of Westerhold [2020]. (b) Sea level estimates from Miller et al. [2020] (c) Atmospheric CO_2 reconstructions from boron isotopes and alkenones. Figure from Rae et al. [2021] (adapted legend)

The Earth's has experienced very different CO_2 levels over the Cenozoic, with higher CO_2 levels associated with warmer temperatures and less ice. The extension of the SSP scenarios from the IPCC to the year 2500 [Meinshausen et al., 2020] show that CO_2 levels of $\sim$ 2000 ppm, similar to high values of the Eocene could be reached in a few centuries.

Despite advances in the reconstruction of past CO_2 levels, records remain

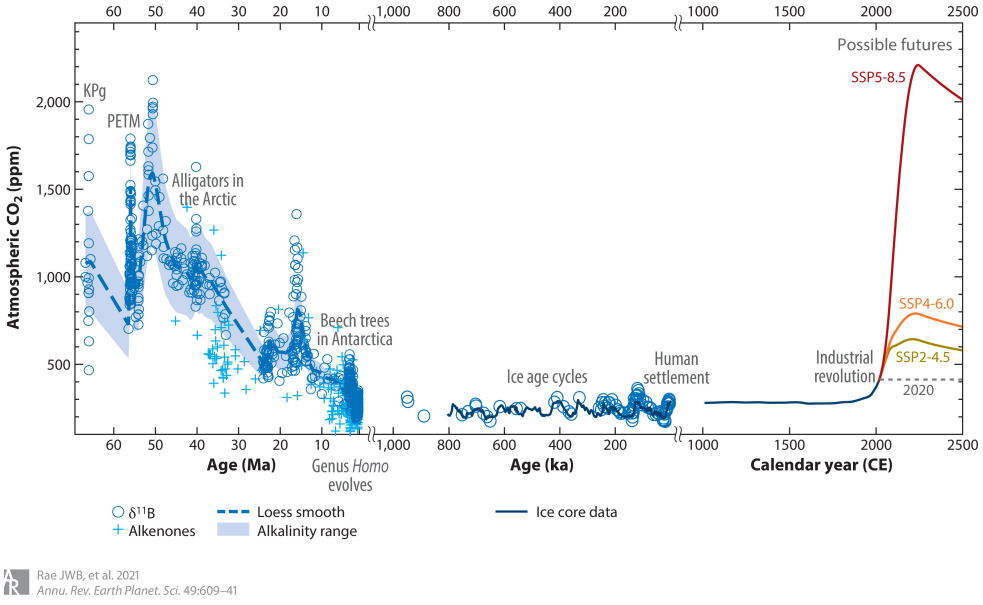

Figure 1.5: Paleo-CO_2 compared with future CO_2 change under the different scenarios used in the Intergovernmental Panel on Climate Change Sixth Assessment Report. The scenarios are shared socioeconomic pathways (SSPs) SSP2-4.5, SSP4-6.0, and SSP5-8.5 from Meinshausen et al. [2020]. SSP2-4.5 corresponds to moderate emissions and SSP5-8.5 corresponds to high emissions. Figure from Rae et al. [2021]

discontinuous and uncertain on the Cenozoic. More robust informations can be obtained on the carbon cycle from the analysis of the carbon isotopic composition of deep sea benthic foraminifera.

There are three isotopes of carbon : ^{12}C,^{13}C and ^{14}C. ^{12}C constitutes the dominant proportion (∼99%), followed by ^{13}C (∼1%). ^{14}C constitutes a negligible portion of total carbon atoms. The relative proportion of carbon 12 isotopes (^{12}C) to carbon 13 isotopes (^{13}C) is usually expressed with $\delta^{13}C$, expressed in ‰. $\delta^{13}C$ compares the ratio of ^{13}C to ^{12}C in a sample, to a reference :

$$\delta^{13}C = 1000 \cdot [\frac{^{13}C/^{12}C_{sample}}{^{13}C/^{12}C_{reference}} - 1] \tag{1.4}$$

If we neglect isotopic fractionation during carbonate precipitation, meaning that the proportion of ^{13}C in the produced carbonate is the same as the one of the surrounding ocean, analysis of ^{13}C of foraminifera informs us on the evolution of ^{13}C proportion in the ocean in the past.

Westerhold et al. [2020] presented a highly resolved and well-dated record of benthic carbon for the past 66 million years. They analyse at the same time carbon isotope compositions of foraminifera, that give informations on the carbon cycle, and oxygen isotopes that give informations on global temperatures. The record is

shown in Figure 1.6.

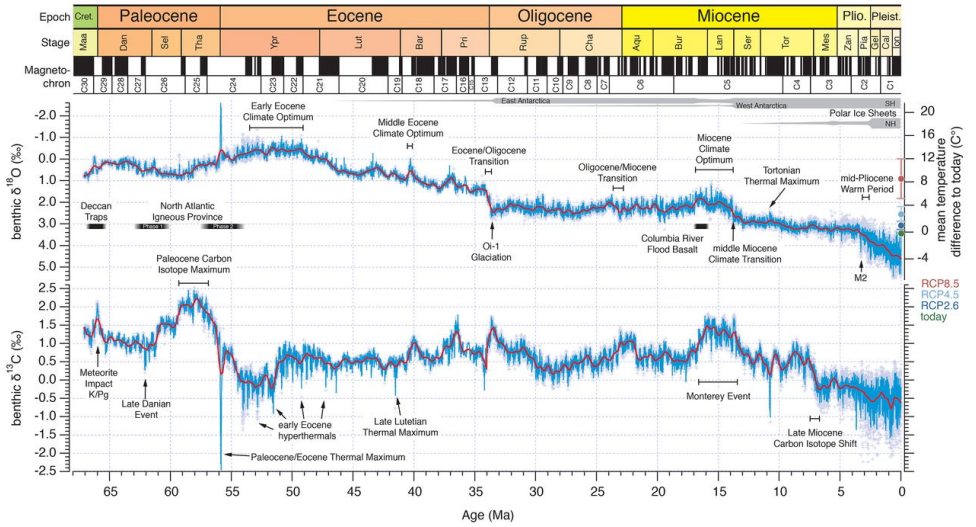

Figure 1.6: Cenozoic Global Reference benthic foraminifer carbon and oxygen Isotope Dataset (CENOGRID) from ocean drilling core sites spanning the past 66 million years. Figure from Westerhold et al. [2020].

The $\delta^{13}C$ record exhibits shorter and longer term oscillations. Organic matter is largely ^{12}C-enriched compared to its environment as lighter, ^{12}C atoms, are favourably taken in the photosynthesis process (in other words, organic matter has a large fractionation factor). Due to its large fractionation factor, organic matter fluxes to and from the geological reservoir are the most likely candidate to explain past $\delta^{13}C$ variations. Indeed, organic matter burial removes ^{12}C -rich matter from the surface system, thus increasing the ^{13}C proportion of the surface system, and thus its $\delta^{13}C$. This will be further discussed in Chapter 5.

1.1.3 . Classical modelling studies of the long term carbon cycle

In this part, I present the different mechanisms commonly taken into account in several studies estimating the atmospheric lifetime of CO_2. Processes acting on several timescales to remove atmospheric CO_2, as described in various studies [Archer et al., 1997, 1998, Archer, 2005, Archer et al., 2009, Lord et al., 2016] are depicted in Figure 1.7 and consist of :

- air-sea gas exchange, taking place on a timescale of 1-10 years (panel (a) of Figure 1.7). CO_2 is a soluble gas and is transferred accross the air-sea interface. It increases the $CO_2(aq)$ concentration. Soluble CO_2 reacts following the reaction of equation 1.2. This increases the concentration of bicarbonate ions (HCO_3^-) and decreases the concentration of carbonate

ions (CO_3^{2-}). This also decreases ocean pH and thus the buffering capacity of the ocean.

- ocean invasion, taking place on a timescale of 10-100 years (depicted in panel (b) of Figure 1.7). The CO_2 enriched surface water are transported into the ocean interior.

- seafloor $CaCO_3$ neutralization, taking place on a timescale of thousand years (panel (c) of Figure 1.7). Marine sediments become in contact with CO_2 enriched and thus CO_3^{2-} depleted waters. This leads to dissolution of previously deposited $CaCO_3$ on the sea floor, in order to restore the CO_3^{2-} concentration. Schematically, $CaCO_3 \leftrightarrow Ca^{2+} + CO_3^{2-}$. Combined with equation 1.2, this gives :

$$CO_2 + H_2O + CaCO_3 \leftrightarrow Ca^{2+} + 2HCO_3^- \tag{1.5}$$

  Seafloor $CaCO_3$ dissolution allows to partially restore the buffering capacity of the deep water, and to allow further atmospheric CO_2 uptake when these water return to the surface.

- terrestrial $CaCO_3$ neutralization, taking place on timescale of ten of thousands of years, and depicted in panel (d) of Figure 1.7. Weathering of carbonate rocks take place on land, following the equation :

$$CO_2 + H_2O + CaCO_3 \rightarrow Ca^{2+} + 2HCO_3^- \tag{1.6}$$

  This weathering reaction thus consumes atmospheric CO_2. Then, the formed bicarbonate ions are transported to the sea via river, where biogenic carbonate can precipitate and be buried on the seafloor. This reaction produces CO_2 :

$$Ca^{2+} + 2HCO_3^- \rightarrow CO_2 + H_2O + CaCO_3 \tag{1.7}$$

  It is usually assumed that these processes are in equilibrium on very long timescales and thus the weathering of terrestrial carbonate rocks does not remove carbon from the atmosphere and ocean system, as each mole of carbon taken from the atmosphere through the weathering reaction is then returned to the ocean through the precipitation of biogenic $CaCO_3$. However, seafloor $CaCO_3$ dissolution (seafloor $CaCO_3$ neutralization) decreases the burial rate of marine $CaCO_3$, the CO_2 consumed by the weathering reaction is no longer balanced by the precipitation and burial of biogenic $CaCO_3$ This allows additional CO_2 drawdown.

- silicate rock weathering, taking place on timescale of hundred of thousand years. As carbonate minerals, silicate minerals on land can be broken down by the dissolution of CO_2 in rainwater, following reactions similar to :

$$2CO_2 + 3H_2O + CaAl_2Si_2O_8 \rightarrow Ca^{2+} + 2HCO_3^- + Al_2Si_2O_5(OH)_4 \tag{1.8}$$

The formed bicarbonate ions are transported to the sea via river, where biogenic carbonate can precipitate and be buried on the seafloor,

$$Ca^{2+} + 2HCO_3^- \rightarrow CO_2 + H_2O + CaCO_3 \tag{1.9}$$

The difference between terrestrial carbonate weathering and silicate weathering (followed by calcium carbonate formation in the ocean), is that in the case of carbonate weathering, consumed CO_2 from the atmosphere is returned to the ocean, therefore not changing carbon in the (atmosphere + ocean) system; while in the case of silicate weathering the uptake of two moles of atmospheric CO_2 results in only one mole of carbon returned to the ocean, thus decreasing the amount of carbon in the (atmosphere + ocean) system. The silicate weathering reaction can differ according to the type of silicate weathered, but this does not change the fact that on long timescale, for two moles of atmospheric CO_2 consumed, only one is released to the ocean, while the other is buried into sediments in the form of $CaCO_3$. This constitutes a net long term CO_2 drawdown.

Since the work of Walker et al. [1981], it is assumed that the strength of silicate weathering varries with climate. Indeed, weathering is facilitated in a warmer, wetter climate. This produces a negative feedback for the carbon cycle, as an increased CO_2 concentration results in a warmer climate, leading to an increase in silicate weathering and thus to more CO_2 drawdown. This is usually referred to as the "weathering thermostat", and it is often assumed to be the reason of relatively stable climate condition on Earth (presence of liquid water except during certain 'Snowball Earth' episodes in the Proterozoic), as CO_2 increases in the atmosphere are damped by increased silicate weathering, and conversely for CO_2 decrease [Foster et al., 2017, Kasting, 2019].

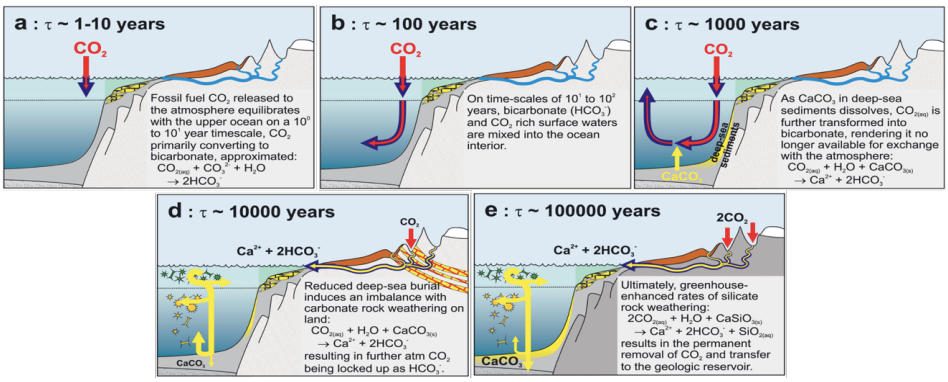

Figure 1.7: Primary natural mechanisms of CO_2 sequestration from the atmosphere. Figure and legend adapted from Lord et al. [2016]

Using an ocean and sediment carbon cycle model, Archer et al. [1997] simulated the response of the carbon cycle to a range of anthropogenic CO_2 release scenarios. They derived multiple timescales associated with each processes and computed the fraction of atmospheric CO_2 consumed by each process. They found that 70-80% of the CO_2 release was dissolved in the ocean on the timescale of several hundred of years. Sea floor $CaCO_3$ neutralization permitted to account for an additional 9-15% decrease of the CO_2 concentration on a time scale of 5.5 - 6.8 kyr. Terrestrial $CaCO_3$ neutralization accounted for an additional 3-8% decrease of the CO_2 concentration on a time scale of 8.2 kyr. The remaining CO_2 in the atmosphere (7-8 %) is consumed via silicate weathering. However, silicate weathering was not implemented in their model, and for this process they directly assumed a timescale of 200 kyr. From the CO_2 relased (3000 GtC), they were able to derive a simple function allowing to compute the evolution of atmospheric CO_2 as a function of time (sum of exponentials) :

$$CO_2(t) = CO_2(t=0) + 3000GtC[0.75e^{\frac{-t}{365yr}} + 0.135e^{\frac{-t}{5.5kyr}} + 0.035e^{\frac{-t}{8.2kyr}} + 0.08e^{\frac{-t}{200kyr}}] \quad (1.10)$$

Due to its simplicity, this function was used in studies of climate of the next million years, such as the BIOCLIM project (see section 1.3 for details).

In a following study, Archer [2005] took into account a feedback not taken into account in the previous study : a warming climate reduces the solubility of CO_2 in seawater, thus limiting the immediate CO_2 drawdown. This results in an increase of the percentage of remaining CO_2 in the atmosphere. For instance, the remaining fraction after 100 kyr increased from 5.8% to 6.7% in the low emission scenario (300 PgC), when taking into account the temperature feedback. However, in this study the timescale of silicate weathering was once again assumed, rather than modelled. It was assumed to be 400 kyr.

Lord et al. [2016] used the cGENIE Earth System Model model to carry out several simulations following various carbon emission scenarios (from 1000 PgC to 20 000 PgC) on a million year timescale. The cGENIE model allows to take into account first order CO_2 climate feedbacks on ocean temperatures and circulation. A major difference to previous studies ([Archer et al., 1997, 1998, Archer, 2005]) is that the timescale associated with silicate weathering is not anymore assumed but modelled. However, as stated by Lord et al. [2016], this relies on a relatively simple and global mean function linking weathering rates and climate. The terrestrial carbonate weathering is calculated as :

$$F_{CaCO_3} = F_{CaCO_3,0}(1 + k_{Ca}(T - T_0)) \quad (1.11)$$

The silicate weathering flux is calculated as :

$$F_{CaSiO_3} = F_{CaSiO_3,0}e^{\frac{1000E_a}{RT_0^2}(T-T_0)} \quad (1.12)$$

where T is the mean annual global land surface temperature, the 0 subscript represents an initial value of the parameter, k_{Ca} is an empirical constant (0.049), E_a is the activation energy for dissolution, and R is the molar gas constant. The temperature dependence of $CaCO_3$ weathering (equation 1.11) follows the one used by Berner [1994], derived by correlating temperatures and bicarbonate concentrations of groundwater. The temperature dependence of silicate weathering (equation 1.12) is based on laboratory studies of the impact of temperature on the dissolution of Ca and Mg silicates [Brady, 1991].

Lord et al. [2016] found that for shorter timescales (less than a millenia), the fraction of CO_2 removed depends strongly, and in a non linear way on total emissions. This is due to the fact that the buffering capacity of the ocean progressively saturates with increasing total emission. This difference in removal is compensated by an increase in the fraction removed due to carbonate weathering and burial, but this operates at a much longer timescale. After 500 kyr, atmospheric CO_2 has not returned to its preindustrial value. In the case of the 1000 PgC emission scenario, the atmospheric CO_2 concentration after 500 kyr is 283 ppm, not much higher than the pre-industrial one. However, for the 20 000 PgC emission scenario, the atmospheric concentration after 500 kyr is 360 ppm, still largely higher than pre-industrial values. The evolution of CO_2 over time depending on the initial emissions is shown in Figure 1.8. From these simulations, Lord et al.

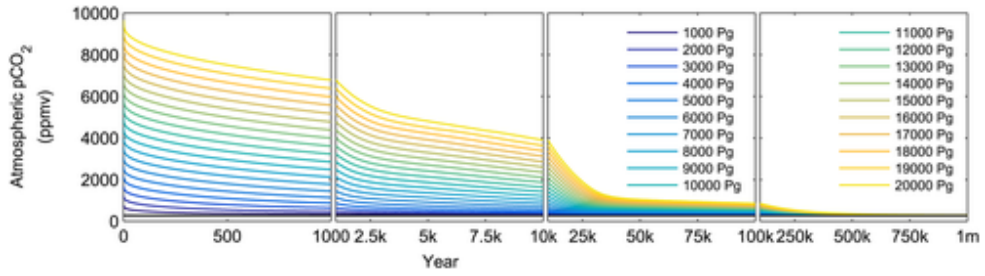

Figure 1.8: Atmospheric pCO_2 predicted by cGENIE for the pulse series scenarios (1000–20,000 Pg C). Pre-industrial CO_2 concentrations are shown in black. Figure and legend are from Lord et al. [2016]

[2016] derived a response impulse function, from fitting to several exponentials. The response impulse function reproduces the modelled atmospheric CO_2 concentration over time, following emission. As this provides a simple tool to project the CO_2 concentration over time depending on the emissions, this was used in studies of the climate of the next million year, such as Lord et al. [2019], Williams et al. [2022], Talento and Ganopolski [2021] (see section 1.3 for details).

1.1.4 . A broader view of the long term carbon cycle

The studies presented in the previous section show unambiguously that anthropogenic CO_2 release will continue to affect the atmospheric CO_2 concentration, and thus climate, far in the future. As summed up by Archer et al. [2009] "[...] Generally accepted modern understanding of the global carbon cycle indicates that climate effects of CO_2 releases to the atmosphere will persist for tens, if not hundreds, of thousands of years into the future". However, these studies neglect a number of processes, that could be of importance on long timescales.

Indeed, these studies focus mostly on the inorganic part of the carbon cycle and neglect possible variations in the organic carbon cycle. This is probably due to the fact, that it is easier to model the behaviour of the inorganic carbon cycle. In addition, it is difficult to quantify the evolution of the organic carbon cycle in conditions different from today. These studies all rely on increased silicate weathering to explain the ultimate removing of the reminder airborne fraction. However, as stated by Lord et al. [2016] "Removal of added carbon from the ocean and atmosphere need not exclusively take place via increased silicate weathering, and other feedbacks may be important". Hilton and West [2020] have reviewed important processes removing or adding CO_2 to the atmosphere on geological timescale, influenced by erosion. They emphasize that one should "look[..] beyond silicate weathering" and "advocate for a more holistic view of the geological C cycle", that includes all CO_2 sources and sinks.

Among these other possible processes, is the burial of organic carbon in marine sediments. Enhanced marine productivity due to higher nutrient supply could enhance organic matter burial. However, this idea is debatted and others think that an enhanced marine productivity does not necessarily leads to an enhanced burial, as most of the production is remineralized. An enhanced burial of marine organic carbon can be obtained under reduced ocean oxygenation. A warmer climate increases ocean stratification and decrease the solubility of O_2 in surface water [Bopp et al., 2002] and could thus increase organic carbon burial into sediments.

Additionally to marine organic matter burial, erosion of biospheric particulate organic carbon can provide a CO_2 sink. The biosphere produces organic matter through photosynthesis. This consumes atmospheric CO_2 and produces O_2. Particulate organic carbon can be eroded and exported from forests to rivers. Terrestrial organic matter has a higher preservation efficiency (10-30%) than marine organic matter ($\sim$1%) [Burdige, 2005]. If the eroded terrestrial organic carbon is replaced through new photosynthesis production and the eroded particulate organic carbon is buried into sediments (in lake or into the ocean), this results in a long term CO_2 drawdown [Berhe et al., 2007, Galy et al., 2007].

An enhanced organic carbon burial into marine sediments can thus act in tandem with silicate weathering to reduce atmospheric CO_2 on long timescales.

However, other processes implying organic matter act as a CO_2 source on long timescales. For instance, organic carbon oxidation can happen as sedimentary

rocks, containing petrogenic organic carbon are exhumed [Petsch et al., 2005], following the reaction :

$$CH_2O + O_2 \rightarrow CO_2 + H_2O \tag{1.13}$$

Additionally, sulfide minerals (such as pyrite, FeS_2) can form sulfuric acid (H_2SO_4) that can in turn weather carbonate minerals, through the reaction :

$$CaCO_3 + H_2SO_4 \leftrightarrow CO_2 + H_2O + Ca^{2+} + SO_4^{2-} \tag{1.14}$$

This releases CO_2 and acts as a CO_2 source [Torres et al., 2014].

Current estimates of CO_2 sources and sinks are :

- CO_2 release by volcanism : 40 - 175 MtC yr^{-1} Burton et al. [2013]
- CO_2 drawdown by silicate weathering : 90-140 MtC yr^{-1} [Gaillardet et al., 1999, Moon et al., 2014]
- CO_2 drawdown by erosion of particulate biospheric organic carbon and its burial into ocean sediments : 40-80 MtC yr^{-1} [Burdige, 2005, Galy et al., 2007]
- CO_2 release by oxidation of petrogenic organic carbon : 40 - 100 MtC yr^{-1} [Petsch, 2014].
- CO_2 release associated with sulfide oxidation : $\sim$ 40 MtC yr^{-1} [Torres et al., 2016, Burke et al., 2018a]

Despite the large uncertainties, these estimates show that CO_2 sources and sinks not considered by most studies are of the same order of magnitude than silicate weathering, and therefore need to be taken into account.

These processes all increase with erosion rate [Hilton and West, 2020]. Thus, they might vary with climate, for instance through climate influence on weathering rates. Additionaly, climate can influence organic carbon burial. This provides additional positive or negative feedbacks to the carbon cycle. However, these processes are poorly constrained at present, and this is probably why they are not taken into accounted in the studies presented earlier. Though, taking them into account could change the qualitative behaviour of the evolution of atmospheric CO_2 through time, following emissions.

Additionally, taking into account organic matter fluxes is key to explain the $\delta^{13}C$ variations exhibited by marine carbonates records (see Figure 1.6). Indeed, organic matter is particularly rich in ^{12}C carbon. For instance, δ^{13}C values of C3 plants range from -20 to -37 ‰ [Kohn, 2010]. Therefore, comparatively to other inorganic processes, for a same flux, burial or oxidation of organic matter has a larger impact on the $\delta^{13}C$ of the surface reservoir. In other words, for a same impact on surface carbon, the impact on the surface $\delta^{13}C$ is higher with organic

matter burial or oxydation than with inorganic processes. Explaining the same $\delta^{13}C$ variations solely with inorganic fluxes would require much larger fluxes, and thus larger surface carbon variations. In as study over the Quaternary, the only period for which direct records are available for both CO_2 and $\delta^{13}C$, Russon et al. [2010] showed that it was not possible to explain the relatively large $\delta^{13}C$ variations ($> 0.4‰$) with silicate weathering only while remaining in the the observed range for atmospheric CO_2.

In summary, current modelling studies on the long term fate of atmospheric CO_2 rely on three hypothesis that need to be challenged.

- The assumption is made that the atmospheric CO_2 concentration comes back to pre-industrial levels. There is no real basis for such an assumption, and the past CO_2 records show us that the Earth has already experienced CO_2 levels far from the pre-industrial value of 280 ppm.

- The assumption is made that the ultimate CO_2 sink is silicate weathering. No organic matter fluxes variations are considered. However, this assumption does not allow to reproduce past $\delta^{13}C$ variations. Additionally, other processes removing and releasing CO_2, estimated to be of the same order of magnitude than silicate weathering, are not taken into account.

- In many earlier studies, the timescale associated with silicate weathering, assumed to be the ultimate inorganic process to remove CO_2 was simply assumed : 200 kyr in Archer et al. [1997, 1998] and 400 kyr in Archer [2005]. In a more recent study, the timescale was calculated [Lord et al., 2016]. However, this relies on a relatively simple and global mean function linking weathering rates and climate.

1.2 . Ice sheets in the climate system

In this part, I will present some generalities about ice sheets. Then I will present how climate and ice sheets interact and discuss how these interactions are modelled. Finally, I will review existing studies on the long term fate of the Greenland and Antarctic ice sheets.

1.2.1 . Generalities about ice sheets

Ice sheets are masses of ice, that cover at least 50 000 km^2. They form due to presence of snow packs that persist through summer and, due to continuous accumulation, are compacted into ice. Currently, there are two ice sheets on Earth : the Greenland and Antarctic ice sheets, shown in Figure 1.9. They represent the largest reservoir of freshwater. If the Antarctic ice sheet disappeared entirely, this would correspond to a sea level rise of ∼58 m [Fretwell et al., 2013], and ∼7 m in the case of the Greenland ice sheet [Bamber et al., 2013]. The ice thickness in the central regions of the Antarctic ice sheet varies between 2000 and 4000 m, due to the bedrock that is mountainous (the bed topography varies spatially by more than a vertical kilometre over just a few kilometres [Fretwell et al., 2013]). The ice elevation (altitude at the top of the ice sheet) and ice thickness of the Antarctic ice sheet are depicted in Figures 1.10 and 1.11.

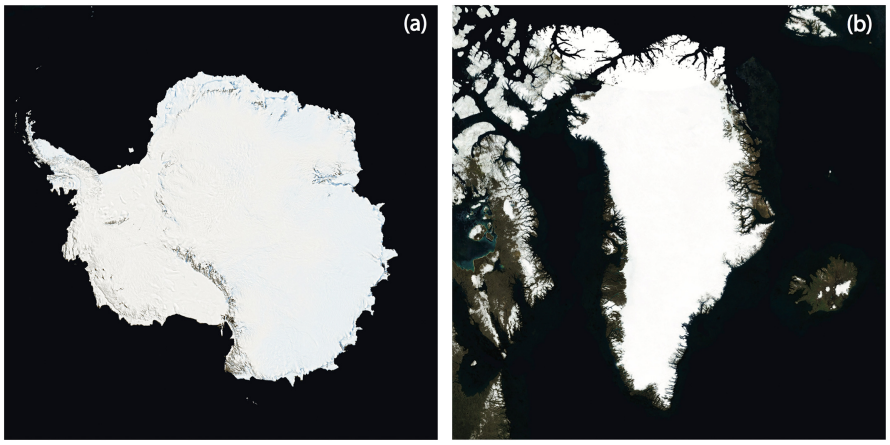

Figure 1.9: (a) Antarctic ice sheet (∼58 m of sea level equivalent [Fretwell et al., 2013]); (b) Greenland ice sheet (∼7 m of sea level equivalent) Bamber et al. [2013]-. Cloud-free imagery courtesy of National Aeronautics and Space Administration Worldview (worldview.earthdata.nasa.gov). Figure and legend from Fyke et al. [2018]

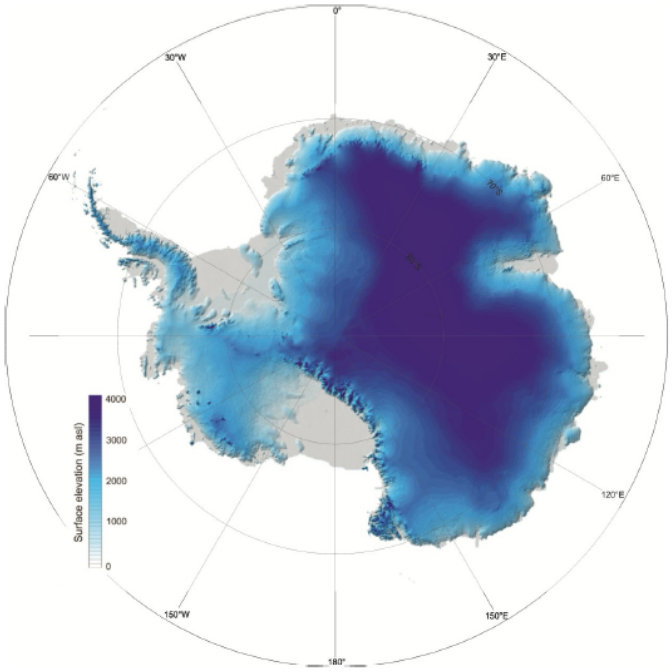

Figure 1.10: Antarctic ice surface elevation. Figure from Fretwell et al. [2013]

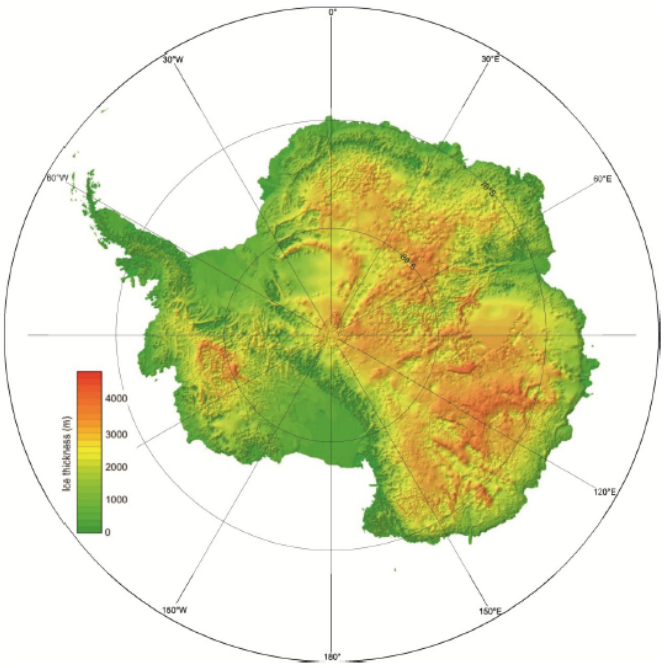

Figure 1.11: Antarctic ice sheet thickness. Figure from Fretwell et al. [2013]

The shape of ice sheets and their evolution depends at the same time of the internal ice dynamics and on the boundary conditions (influence of the solid Earth and of the climate surrounding the ice sheet : atmosphere and ocean).

Ice is a fluid with a very high viscosity. The ice flow is determined by internal deformations and stress at the interface with the bedrock (boundary condition). Schematically, ice flows towards lower elevation under the effect of gravity. Ice is a non Newtonian fluid, and its viscosity depends on the stress applied : the higher the stress applied, the lower the viscosity. In addition, ice viscosity depends non linearly on its temperature : ice is less viscous at higher temperatures. The rate of ice deformation is thus a highly nonlinear function of temperature. Conversely, the ice temperature is influenced by ice deformation, as it produces heat (thermo mechanical coupling). At the base of the ice sheet, the friction between ice and the bedrock slows the ice flow. In cold based areas (temperature at the base lower than the melting point), the ice has an almost zero velocity at the base. Where the temperature reaches the melting point (that depends on pressure), the ice sheet can slide on the bedrock. When waterlogged sediments are present at the base, they can deform, which facilitates the sliding of the ice. However, the mechanics of basal friction remains largely unknown and is one of the source of uncertainty in ice sheet modeling [Pattyn and Morlighem, 2020]. The ice velocity of the Greenland and Antarctic ice sheet is depicted in Figure 1.12.

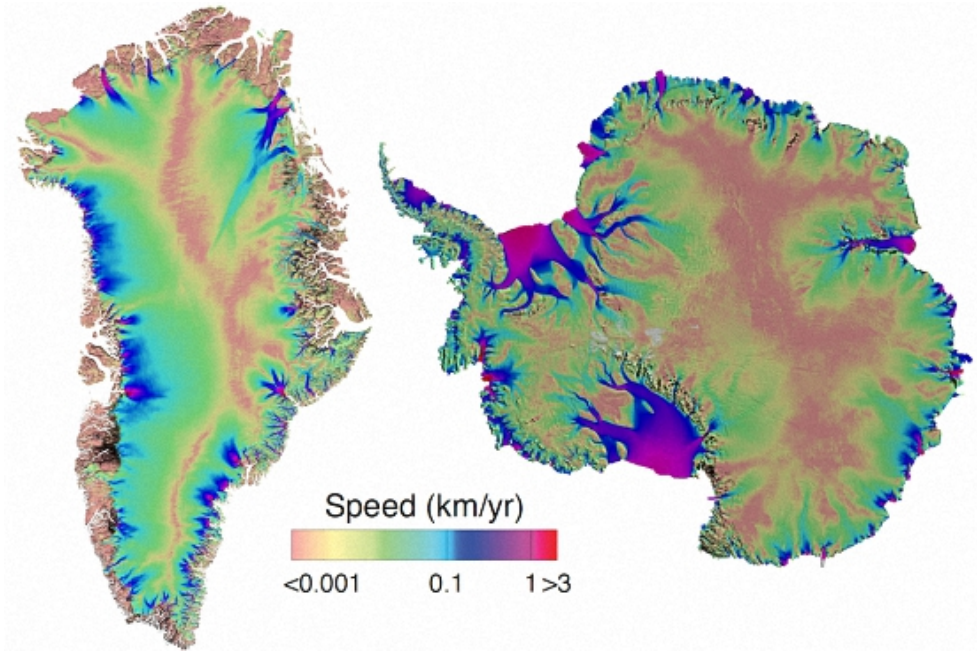

Figure 1.12: Ice velocity in Greenland and Antarctic ice sheets. Figure from Mouginot et al. [2017]

Generally, the ice velocity on grounded parts of the ice sheet (parts that rest on the bedrock, and not the sea) is very low ($<$ 5-10 m/yr). However, there are "ice streams", where ice flows much faster. Ice streams velocities can be of hundreds of meter per years. Most of the ice is evacuated from the center of the ice sheet towards the edges through these ice streams.

As ice flows towards the sea, it can form ice shelves. Ice shelves is the denomination for floating ice that are mostly fed by the flow coming from the grounded ice. The separation between the grounded ice and ice shelves is called the grounding line. The velocity of ice shelves is much higher than the velocity of grounded ice, sometime reaching velocities up to 1km/ year. These much higher velocities are due to the fact that ice shelves rest on water, leading to a negligible friction at the base. Grounded ice and ice shelves have widely different behaviour in response to normal stresses : grounded ice is characterized by vertical shears, while ice shelves and ice streams are characterized by longitudinal stresses.

In addition to the bedrock, ice sheets interact with the atmosphere and ocean. Atmospheric temperature at the ice sheet surface is a boundary condition for temperature evolution in the ice sheet. Warmer temperature at the surface of the ice sheet lead (through heat advection and diffusion) to warmer temperatures inside the ice sheet, thus facilitating deformation, and leading to faster ice flow. In addition, ice sheet gains mass through the accumulation of snow, and loses mass due to surface processes : surface meltwater runoff by surface melt, snow erosion or sublimation of surface snow or blowing snow. In the case of floating ice shelves, mass is also lost due to ocean submarine melt, or iceberg calving [Fyke et al., 2018].

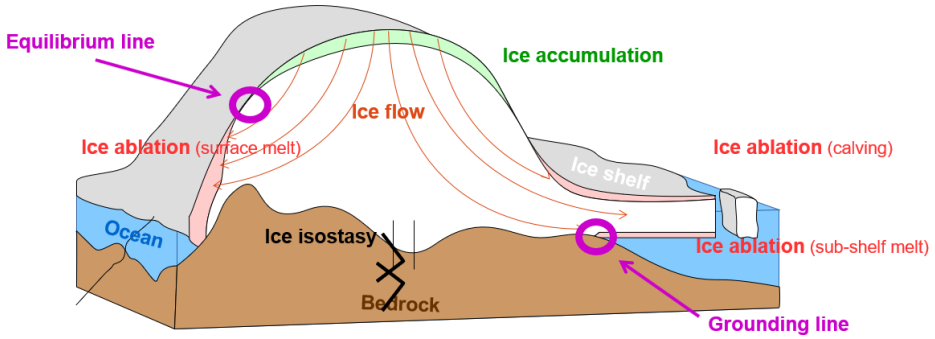

Figure 1.13: Schematic representation of an ice sheet. Figure from A. Quiquet.

The limit between the part of the surface loosing ice, the "ablation area" (usually at lower altitude, that corresponds to warmer temperatures) and the one gaining ice, the "accumulation area", is called the equilibrium line. It is depicted in Figure 1.13. Currently, the temperature are so cold over Antarctica that there is

very limited surface melt, limited to flat, low-lying ice shelves in peak austral summer [Fyke et al., 2018]. At the center of the Antarctic ice sheet, the accumulation rate is very low; around 10 - 50 mm of water equivalent per year [Van Wessem et al., 2014].

Surface accumulation or ablation, and ocean submarine melt, or iceberg calving are affected and modulated by climate (here meant mostly as the atmospheric and oceanic circulations) and thus climate has a major influence on ice sheets. On the other side, ice sheets influence the climate. For instance, the ice sheet topography can impact the atmospheric circulation. These two sides interaction give rise to multiple possible feedbacks, positive (amplifying) or negative (dampening). This will be discussed in Section 1.2.2.

The Antarctic Ice Sheet (AIS) is comprised of two main grounded ice sheets: the West Antarctic Ice Sheet (WAIS) and the East Antarctic Ice Sheet (EAIS), that are separated by the Transantarctic Mountains [McMillan et al., 2018]. A map of Antarctica is provided in Figure 1.14.

Figure 1.14: Map of Antarctica. Figure from https://gisgeography.com/antarctica-map-satellite-image/. Ice free rock is in brown, grounded ice sheet in white and ice shelves are in grey.

More than 90% of the coastline of the AIS has marine margins (their majority consist of ice-shelves or fast flowing glaciers) [Fretwell et al., 2013, Bindschadler et al., 2011] that interact directly with the ocean, either at a calving front or

through floating ice shelves. Ice shelves represent ∼12% of the AIS area [Fretwell et al., 2013], and can melt through their contact with the ocean (sub-shelf melting). Icebergs calve from the marine margins of ice shelves, where ice thickness is usually 250-300 m. As there is almost no surface mass loss in Antarctica currently, the mass loss thus entirely comes from sub-shelf melting and iceberg calving, each process representing approximately half of the mass loss [Rignot et al., 2013, Depoorter et al., 2013, Greene et al., 2022].

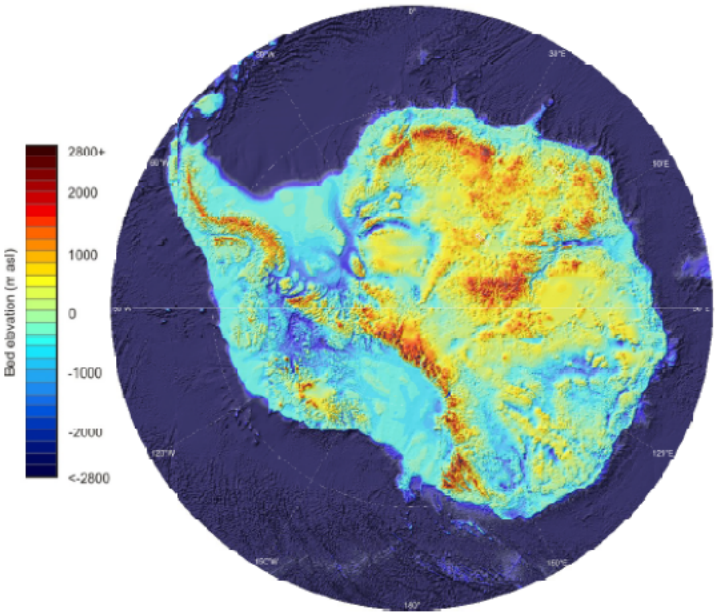

Figure 1.15: Antarctic bedrock elevation. Figure from Fretwell et al. [2013]

A large part of the AIS bedrock lies below see level, as is visible with the blue colors in Figure 1.15. This is particularly the case in the West part of the Antarctic ice sheet (WAIS). The two largest ice shelves of Antarctica, the Filcher-Ronne and Ross ice shelves are located in the marine-based WAIS. As ice shelves are floating, the thinning or removal of these ice shelves by either sub-shelf melt or iceberg calving does not directly contribute to sea level rise. If the WAIS was to disappear entirely, it would contribute ∼4.3 m to global sea level. Most of the East Antarctic Ice Sheet (EAIS) lies on bedrock above sea level (visible with the yellow colors in Figure 1.15). However, approximately one-third of the EAIS is grounded below sea level [Fretwell et al., 2013]. The largest EAIS basins with marine-based ice are the Recovery Subglacial Basin (Weddell Sea sector), the Wilkes and Aurora Subglacial Basins, with a smaller basin existing in the Prydz Bay region (Lambert Trough). If the marine-based part of EAIS ice sheet melted entirely, it would contribute ∼19.2 m to global sea level [Fretwell et al., 2013].

While the terrestrial parts of the Antarctic Ice Sheet are expected to be relatively stable, it has long been acknowledged that the marine-based sectors could be susceptible to retreat or collapse under only moderate climate warming [Weertman, 1974, Mercer, 1978]. The transition between the grounded ice sheet and the ice shelves (grounding line) plays a crucial role in marine ice sheet dynamics, as it determines the rate at which ice flows out of the grounded part of the ice sheet. Two important processes are thought to be critical for retreat of marine based ice sheets. First, when marine-based ice sheets rest on a reverse sloping bed that deepens inland, they are susceptible to Marine Ice Sheet Instability (MISI). MISI is a positive feedback that enables rapid retreat following an initial perturbation [Schoof, 2007, Weertman, 1974]. This is due to the fact that ice discharge through the grounding line increases sharply with ice thickness at the grounding line. On a retrograde slope, an initial grounding line retreat leads to an increased ice thickness at the grounding line and thus ice discharge at the grounding line, leading to further shrinkage.

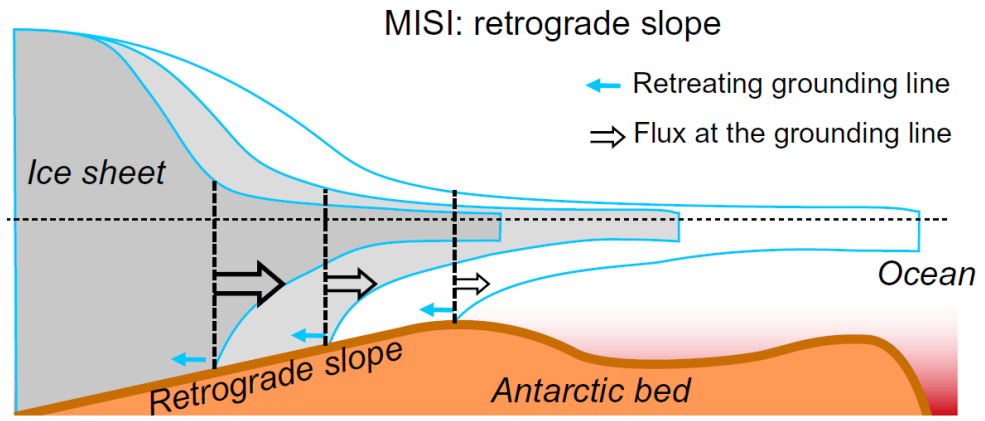

Figure 1.16: Schematic representation of Marine Ice Sheet Instability. Figure from Pattyn [2017]

Observations and modelling studies suggest that MISI is already underway in part of West Antarctica such as Pine Island and Thwaites Glacier [Favier et al., 2014, Joughin et al., 2014].

A second important process is that most ice streams are significantly supported by buttressing ice shelves. Although the thinning or removal of ice shelves does not directly contribute to sea level rise as they float, ice shelves induce buttressing and thus indirectly control upstream grounded ice speed and subsequent sea level rise contribution. The thinning or removal of ice shelves by either sub-shelf melt or iceberg calving can reduce the back-stress on the ice and accelerate upstream ice sheet flow [Dupont and Alley, 2005, Gagliardini et al., 2010, Fürst et al., 2016].

1.2.2 . Modelling climate / ice sheet interactions

Ice sheet behaviour and dynamics are affected by the solid Earth, ocean and the atmosphere. In turn, ice sheet evolution affects the solid Earth, as well as atmospheric and oceanic circulation. These two sides interaction give rise to multiple possible feedbacks, positive (amplifying) or negative (dampening). The multiple feedbacks taking place between ice sheets and the rest of the climate system have been thoroughly reviewed by Fyke et al. [2018], and the major feedbacks are detailed in the following. Positive feedbacks are marked with a (+) and negative feedbacks with a (-).

Ice sheet / atmosphere feedbacks

As the ice sheet geometry changes, this leads to atmospheric changes and potential feedbacks.

- elevation / SMB feedback, also called height feedback (+) : in the case of an initial externally forced increase in ablation, the surface elevation of the ablation area will decrease. The ice surface will thus experience warmer temperature, leading to additional melting.

- ice sheet topography - precipitation feedback (+/-) : changes in the AIS topography can lead to regional precipitation changes, and thus to changes in SMB and ice volume. The direction of this feedback is not easily estimated. Nowadays, orographic precipitation dominate over the AIS. All other things being equal, surface lowering would tend to reduce precipitation in the coastal area and increase moisture transport towards the interior and precipitations in the interior.

- albedo / melt (+) : warmer snow has a lower albedo. When snow at the surface of the ice sheet is melting, the albedo is reduced leading to further solar radiation absorption and melting. Furthermore, it has been shown over Greenland, where surface melt takes place, that the exposed underlying ice often has a lower albedo. This effect can be enhanced locally, by supraglacial lake formation (that have a low albedo). Additionnaly to the local albedo effects of the melt, retreat of the ice sheet and replacement of snow or ice by soil, rocks or vegetation that have a lower albedo further enhances regional warming.

Ice sheet / ocean feedbacks

Ice sheet ocean feedbacks are curently much less understood than atmosphere ice sheet feedbacks [Fyke et al., 2018].

- meltwater feedback (+) : Meltwater impact vertical mixing of heat in the coastal oceans of Antarctica [de Lavergne et al., 2014]. If freshwater input increase, this would enhance vertical stratification and reduce vertical

mixing, leading to cooling of the surface and warming at depth, potentially leading to warmer water into ice shelf cavities and more basal melt [Fogwill et al., 2015].

- feedbacks taking place in cavities are currently poorly represented in models as cavities under the ice shelves are often not represented [Fyke et al., 2018]. A possible feedback taking place in cavities is the ice pump mechanism (+) : the salinity and pressure dependence of the freezing point of water (and thus, ice melting temperature) favors melting at depth in the ice shelf cavities. This gives rise to buoyant turbulent plumes that drive warm water from below to intermediate depths of the ice shelf, leading to additional melt that would have not taken place in immobile waters.

Ice sheet / solid Earth feedback

- Glacial Isostatic Adjustment feedback (-) : when an ice sheet melts, the lithosphere will rebound and raise to adjust to the load loss. This will lead to higher ice sheet elevation, and a higher surface mass balance. For marine ice sheet, this process might reduce Marine Ice Sheet Instabilities. As the bedrock rises, the ocean depth decreases and a part of the ice that was floating start to rest on the bedrock. The grounding line moves to a position where the ice is thinner, counterbalancing the MISI.

- gravity feedbacks (-) : ice volume changes lead to local gravity change that affect the sea level locally. Ice loss leads to a locally lower sea level, potentially reducing MISI.

Modelling ice sheet climate interactions

Equilibrium simulations of past climates, such as the Last Glacial Maximum [Kageyama et al., 2017] or the Last Interglacial [Otto-Bliesner et al., 2017] as well as transient simulations for the last deglaciation [Ivanovic et al., 2016] are often performed with imposed ice sheets and prescribed meltwater fluxes. Future climate simulations for the next centuries performed within the CMIP6 project also mostly have fixed ice sheets [Eyring et al., 2016]. Conversely, simulations of ice sheet evolution in the next centuries, such as in the Ice Sheet Model Intercomparison Project ISMIP6 are mostly performed with ice sheet models run independently from the climate models used to perform the climate projections (the climate applied as boundary condition to the ice sheet model is computed beforehand, and is not affected by the ice sheet evolution) [Nowicki et al., 2016, Seroussi et al., 2020, Nowicki et al., 2020]. This is due to computational cost arising from the difference in timescales between the rapid atmospheric variations and much slower ice sheet variations [Pollard, 2010]. Running a GCM coupled to an ice sheet model during several millenia would be too expensive, due to the computational costs of GCMs. However, ice sheets and the atmospheric and oceanic circulations are known to

interact, which can give rise to several feedbacks, as explained previously. Climate simulations with fixed ice sheets, or ice sheets simulation with a pre-computed climate not affected by ice sheet variations, do not allow to take into account these ice sheet and ocean / atmosphere interactions. Coupling between GCMs and ice sheet model is very new [Smith et al., 2021, Muntjewerf et al., 2020, Gregory et al., 2020]. In the last decades, much work has been performed in order to model ice sheet-climate feedbacks, and alternative methods to a direct GCM - ice sheet model coupling have been developed. These methods are :

- GCM lookup table : different GCM runs are performed, corresponding to different boundary conditions, that span the space of possible states expected. Then, the ice sheet model is run (for a long integration) and the corresponding temperature and precipitation fields at each time are interpolated from the GCM lookup-table. There are different degree of complexity of this method. The "glacial index" method that has been used over the last glacial cycle [Zweck and Huybrechts, 2005, Charbit et al., 2007] interpolates the climate between two extreme climates (in this case, LGM and modern). The weight of each extreme state in the interpolation is based on a "glacial index", such as $\delta^{18}O$, pCO_2 or ice core isotopes. A more developed method is the "climate matrix method". In this case, GCM simulations are performed for different values of long term drivers of climate (such as insolation, ice sheet geometry and pCO_2 levels). During the ice sheet simulation, the climate is interpolated from these GCM runs, depending on the current insolation, ice sheet volume and CO_2 level [Pollard, 2010]. This method has been used over various time periods such as the last deglaciation [Berends et al., 2018], the Eocene - Oligocene transition [DeConto and Pollard, 2003a, Ladant et al., 2014], the Miocene [Stap et al., 2022].

- Gaussian process emulator. This is a statistical representation of a climate model (the simulator) [Van Breedam et al., 2021]. A small number of climate runs (with different climate forcings) are performed and the emulator is calibrated on them, in order to predict the climate for any given combination of climatic forcing. The climatic forcing can be the orbital paramaters, CO_2 concentration and ice sheet size and / or extent [Van Breedam et al., 2021]. This method allows to run multi-million year simulations and has been used over the late Eocene to investigate the presence of continental-scale ice sheets prior to the Eocene-Oligocene transition [Van Breedam et al., 2022].

- Coupling between EMIC and ice sheet model. EMICs have a lower computation time than GCM. This allows to perform coupled climate-ice sheet simulations over multi-millenial timescale. Different EMICs or Energy balance models have been coupled to model past or future periods. For instance, Berger and Loutre [2002] used an energy balance model coupled to an ice sheet model to investigate the start of the next glaciation. Some periods of

the Quaternary have been modelled with coupled EMICs-ice sheet models, such as the last interglacial [Goelzer et al., 2016], MIS 7 [Choudhury et al., 2020], the last deglaciation [Quiquet et al., 2021, Heinemann et al., 2014, Philippon et al., 2006]. The CLIMBER-2 model [Ganopolski and Brovkin, 2017, Willeit et al., 2019] and a simpler energy balance model [Stap et al., 2014] have been used to model several past glacial-interglacial cycles. To save computation time, asynchronous coupling are sometimes used [Heinemann et al., 2014, Choudhury et al., 2020, Quiquet et al., 2021]. Some of these coupled climate-ice sheet models have been used for future projections of the Greenland Ice sheet [Robinson et al., 2012, Van Breedam et al., 2020], and the Antarctic ice sheet [Van Breedam et al., 2020].

In this study, we take advantage of the low computation time of the model of intermediate complexity iLOVECLIM (atmosphere-ocean-vegetation model that will be further described in Section 3.1) to perform coupled simulations with the GRISLI Antarctic ice sheet model (described in Section 3.2).

1.2.3 . Future long term fate of current ice sheets : review of existing studies

The disappearance of the Greenland and Antarctic ice sheet can have large consequences on human population, due to their contribution to sea level rise ($\sim$7 m for Greenland and $\sim$58 m for Antarctica [Bamber et al., 2013, Fretwell et al., 2013]. As for climate, most of the focus is being set on ice sheet changes in the next century, or up to the year 2300. Fewer studies assess the behaviour of ice sheets on timescales longer than a millenia. In this section, we review some of the existing studies on the long term (more than a millenia) fate of the Greenland and Antarctic ice sheets. For the Antarctic ice sheet, we set a particular focus on studies of higher end projection. Current existing studies on the climate of the next million years ignore possible important changes in the Antarctic ice sheet (see section 1.3). We want to broaden this scope and therefore emphasize on studies that have shown that large to complete Antarctic ice sheet retreat due to anthropogenic emissions cannot be excluded.

The Greenland ice sheet

Gregory et al. [2020] used a coupled ice sheet - atmosphere general circulation model and carried out multi-millenial simulation of the Greenland ice sheet. Their results show that if a climate that gives the recently observed surface mass balance was maintained, global-mean sea level rise would reach 0.5–2.5m. For any global warming exceeding 3°C, the contribution to sea level rise exceeds 5m. And for the largest global warming considered (around 5°C), only a small ice cap remains, resulting in over 7m of sea level rise.

Van Breedam et al. [2020] used a coupled EMIC-ice sheet model (LOVE-

CLIMv1.3) to carry out multi-millenial simulation of both the Greenland and Antarctic ice sheet. In their results, the Greenland ice sheet nearly disappears for all forcing scenarios, with a faster retreat for stronger emission scenarios. The melting of the Greenland ice sheet takes 10 000 years when Greenland temperature anomalies are around 2°C respective to 1970-2000 (low emission scenario) and 2000 years when Greenland temperature anomalies are around 10°C (highest forcing scenario).

Clark et al. [2016] estimated that complete loss of the Greenland ice sheet would take around 8000 years at 5.5°C of warming, and around 3000 years at 8.6°C. The IPCC AR 6 [Fox-Kemper et al., 2021] confirmed the assessment previously made in the AR5 report and SROCC [Meredith et al., 2019] : "complete loss of Greenland ice, contributing about 7m to sea level over a millenium or more would occur for a sustained global mean surface temperature between 1°C (low confidence) and 4°C (medium confidence) above pre-industrial levels."

The Antarctic ice sheet

Chambers et al. [2022] studied the Antarctic mass loss around one millenia from now (up to the year 3000) by forcing an ice sheet model with climate scenarios up to 2100 and applying no trend afterwards. They found that for the unabated warming path simulations, West Antarctica suffers a much more severe ice loss than East Antarctica. The mass loss amounts to an ensemble average of ∼3.5 m sea-level equivalent by the year 3000 and ∼5.3 m for the most sensitive experiment.

Van Breedam et al. [2020] carried 10 000 years long coupled EMIC-ice sheet simulations and found that in the case of a low forcing scenario (∼ 460 GtC emitted from the pre-industrial period) the Antarctic ice sheet contributes only about 1.6m to sea level with a limited retreat of the grounding line in West Antarctica. However, for a higher forcing scenario (cumulative emissions of ∼ 5900 GtC relative to the pre-industrial period), the marine basins of the East Antarctic Ice Sheet also become ice free, resulting in a sea-level rise of up to 27m. When using a different model version in a sensitivity experiment (different parameter set for the climate model, that led to a stronger climate sensitivity, ∼3K instead of ∼2K) the Antarctic ice sheet disappears entirely in 10 000 years for the higher forcing scenario, due to a strong albedo-temperature feedback that initiates once a significant part of the ice sheet has retreated on land.

Winkelmann et al. [2015] showed that burning the current attainable fossil fuel resources is sufficient to eliminate the Antarctic ice sheet. With cumulative fossil fuel emissions of 10 000 GtC, the Antarctica is projected to become virtually ice free on a timescale of 10 kyr. The West Antarctic ice sheet becomes unstable for 600-800 GtC cumulative emissions. The Wilkes grounding line retreats significantly under fossil fuel carbon emissions of 1000 GtC or more. The Antarctic ice sheet state after 10 000 years under the different cumulative emissions scenarios is shown in Figure 1.17.

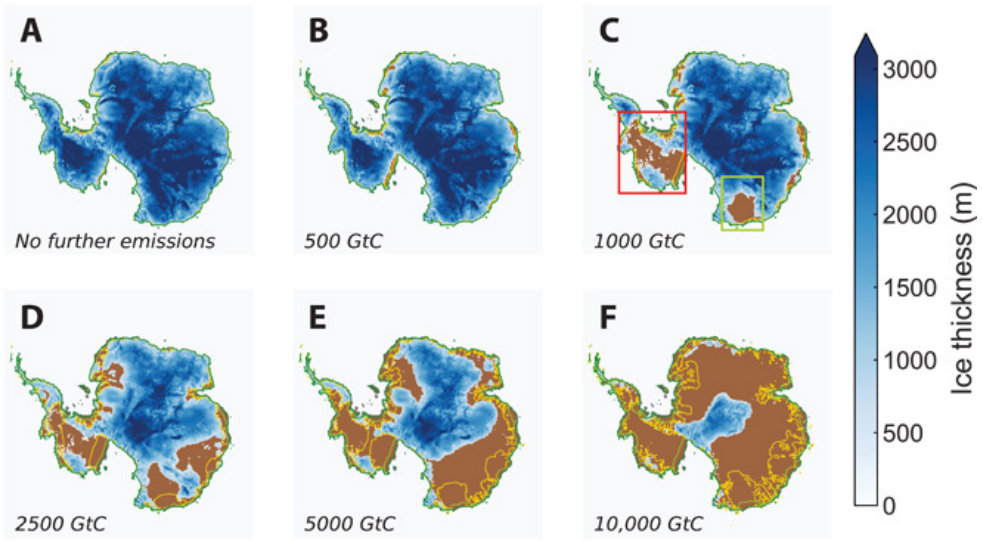

Figure 1.17: States of the Antarctic Ice Sheet after 10,000 years in the simulations from Winkelmann et al. [2015]. Shown is the ice thickness for (A) present-day Antarctica and the states of the ice sheet after forcing it for 10,000 years with cumulative emissions of (B) 500 GtC, (C) 1000 GtC, (D) 2500 GtC, (E) 5000 GtC, and (F) 10,000 GtC, simulated with the ice-sheet model PISM. Ice-free bedrock is shown in brown. In the 1000 GtC scenario, both the West Antarctic Ice Sheet (red rectangular) and the Wilkes Basin (green rectangular) become unstable. For the 10,000 GtC scenario, the Antarctic continent is almost ice-free. Figure from Winkelmann et al. [2015] (legend adapted).

Garbe et al. [2020] applied different warming levels to the same ice sheet model (PISM) and found that at global warming levels around 2°C above pre-industrial levels, West Antarctica is committed to long term partial collapse due to the marine ice sheet instability. At 6-9°C of warming above pre-industrial levels, the loss of more than 70% of the present day Antarctic ice sheet volume is triggered, mainly due to the surface elevation feedback. At more than 10°C of warming above pre-industrial levels, the Antarctic ice sheet is committed to become virtually ice free. They show that the Antarctic ice sheet exhibits hysteresis behaviour : once the ice sheet is lost, temperatures need to decrease to temperatures lower than pre-industrial levels to return to the present-day ice volume (see Figure 1.18).

The studies of Van Breedam et al. [2020], Winkelmann et al. [2015] and Garbe et al. [2020] show that major loss of the Antarctic ice sheet can occur for cumulative emissions of 2 500 -6 000 GtC or 6-9°C global mean warming, with Antarctica becoming virtually ice free for cumulative emissions of 10 000 GtC, or global mean warming levels around 10°C. Winkelmann et al. [2015] used emission scenarios (in terms of cumulative emissions). This was converted into global mean temperature increase using the GENIE model. Garbe et al. [2020] did not use emission scenar-

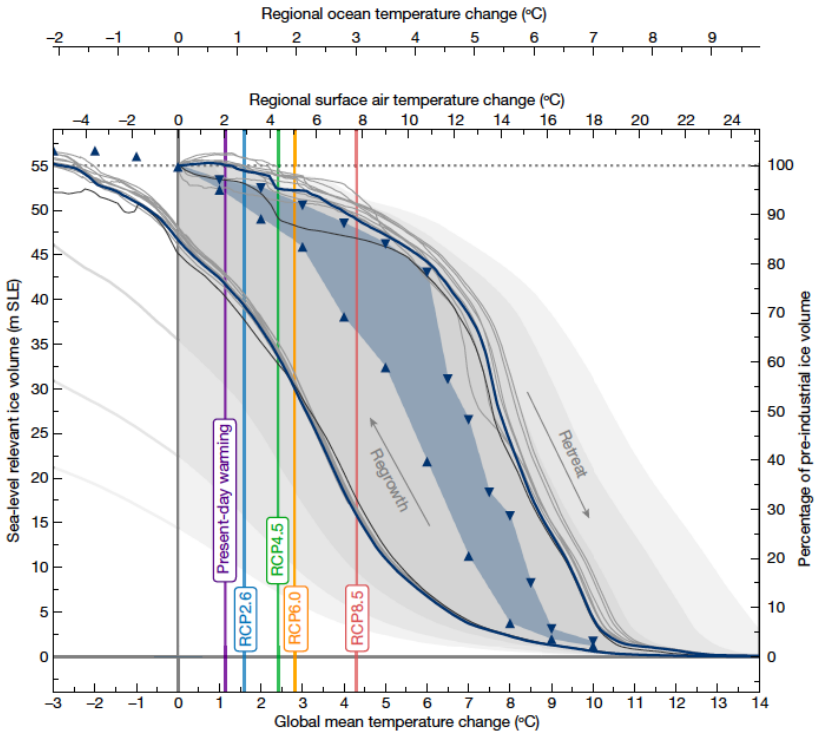

Figure 1.18: Hysteresis of the Antarctic Ice Sheet in the study of Garbe et al. [2020]. Sea level equivalent ice volume is shown for the quasi-static reference simulations (blue curve) as well as the corresponding equilibrium states at discrete temperature levels (blue triangles). The blue filled area marks the hysteresis gap, that is, the equilibrium volume difference between the upper and lower hysteresis branches. Figure from Garbe et al. [2020], legend adapted from Garbe et al. [2020]

ios and directly applied global mean temperature changes. However, a common point to their approach is that they force the PISM ice sheet model with global mean temperature increase. More specifically, global mean temperature increase (obtained with GENIE in Winkelmann et al. [2015] or levels directly assumed in Garbe et al. [2020]) is scaled to regional atmospheric Antarctic temperature change and oceanic Antarctic temperature change, using constant proportionality factors. The changes in oceanic temperature are used to compute basal melt rates using the PICO model [Reese et al., 2018]. The changes in atmospheric temperature in Antarctica are used to compute the surface mass balance, through a Positive Degree Days (PDD) scheme [Reeh, 1991]. In this approach the elevation / surface mass balance feedback (see section 1.2.2) is taken into account via the use of an atmospheric lapse rate. However, the PDD formulation does not depend on albedo. And the factor scaling global mean temperature change to Antarctic temperature change remains constant, independently of the ice sheet changes. When

the ice sheet retreats, this leads to albedo changes that promotes further melt (albedo-melt feedback, see section 1.2.2), and this is not taken into account in their studies.

Armstrong McKay et al. [2022] reviewed potential tipping points in the climate system, ie thredhold in a forcing control parameter at which a small additional perturbation causes a qualitative change in the future state of the system. They estimated the temperature threshold for the stability of the West Antarctic Ice Sheet to be $\sim$1.5°C (1 to 3°C) on a timescale of 2 kyr. They estimated the East Antarctic Ice Sheet tipping threshold to be of $\sim$7.5°C (5 to 10°C), on timescales larger than 10 kyr.

To sum up, studies show that complete disappearance of the Greenland ice sheet can occur between 1-4°C of warming, levels that can be expected to be reached under high emission scenarios. Loss of parts of the West Antarctic ice sheet is expected for relatively low temperature difference to pre-industrial levels (1 to 3°C), and a significant loss of the Antarctic Ice sheet, including part of the East Antarctic Ice Sheet cannot be excluded for high emission scenarios (for instance, 5000 GtC cumulative emissions) and high global mean temperature rise (5 to 10°C).

1.3 . Existing studies on the climate of the next million years

Climate studies on the timescale of the next million years are very rare. Indeed, much of the work on future climate focuses on the next century, or the next few centuries. Most studies carried out on the million years timescales are being requested by nuclear waste management agencies. Indeed, the timescale involved in the radioactivity decay of high level long lived waste (HLW) to safe levels is of order one million year. Current solutions envisaged for HLW management includes geological storage. Climatic conditions can affect the geological storage and possible climate scenarios over the next million years are therefore needed, in order to evaluate the robustness against possible climatic sites at the storage site. Before years 2000, benchmarks on future climate performed by nuclear agencies were limited to an extrapolation of the glacial interglacial cycles of the Quaternary, without taking into account the influence of anthropogenic carbon emissions. A pioneering initiative in taking into account the impact of human emissions on future climate on very long timescales is the BIOCLIM project launched in 2000 and coordinated by ANDRA. Since then, few other studies on the timescale of the next million years have been performed, and are reviewed here. Due to the timescales involved, these studies use a wide range of modelling approach. For instance, conceptual models are being used, along with EMICs for transient simulations and GCMs for snapshots simulations. Please note that several studies have also been performed on the timescale of a 100 000 - 200 000 years, mainly focussing on the assement of the start of the next glaciation, but are not reviewed here for conciseness.

1.3.1 . The BIOCLIM project

The BIOCLIM project used simple models such as the LLN 2-D NH model and conceptual thresholds models to simulate the overall long-term evolution of the global climate. The LLN 2-D is relatively simple (2D) but includes a Northern Hemisphere Ice sheet component. Global coupled ocean-atmosphere simulations with the IPSL_CM4_D model were performed for different snapshots, based on the results of the LLN 2D HN and conceptual models.

- Different CO_2 scenarios over the next million years were performed. They resulted from the addition (or the scaling) of a natural CO_2 contribution and an anthropogenic CO_2 contribution. The natural CO_2 contribution was either calculated following a regression to insolation, developed by Burgess [1998] by linking past insolation and atmospheric CO_2 (Vostok record), or based on the threshold model developed by Paillard [1998]. The anthropogenic CO_2 contribution was calculated from emission scenarios using the response function of Archer et al. [1997], described in Section 1.1.3.

- The LLN 2D HN model as well as the Paillard [1998] conceptual threshold model were run over the next million years, forced by insolation and the

computed changes in the atmospheric concentration of CO_2, in order to compute global ice volume evolution.

The climate evolutions obtained differed widely depending on the CO_2 scenario used. A caveat of this approach is that the conceptual model used to simulate global ice volume was calibrated on glacial-interglacial cycles of the past million years, and thus the alternance of large to smaller ice sheets in the Northern Hemisphere. Therefore, this model has not been calibrated on periods where the Greenland ice sheet melts completely nor where the Antarctic ice sheet melts, and is therefore unlikely to be able to reproduce these features. However, studies show that the complete disappearance of the Greenland ice sheet and at least, partial disappearance of the Antarctic ice sheet can be expected over the next millenia, if emissions continue unabated (see section 1.2.3). Additionally, as discussed in Section 1.1.3, with the use of the response function of Archer et al. [1997] it is assumed that CO_2 levels come back to pre-industrial levels, ultimately due to silicate weathering, from which the characteristic timescale (200 kyr) is directly assumed. This assumption does not allow to reproduce past $\delta^{13}C$ data, and neglects other processes that could be of similar importance.

1.3.2 . Other studies

Archer and Ganopolski [2005] also used the conceptual model previously developed by Paillard [1998] that simulates ice volume evolution over glacial interglacial cycles, as a response to insolation forcing, and more specifically summer insolation in the Northern Hemisphere. The Paillard [1998] model is based on insolation thresholds. For instance, glaciations only initiate if the insolation drops below a certain threshold. In its original version, the threshold for glaciation was fixed. Archer and Ganopolski [2005] made the insolation glaciation threshold depend on the pCO_2 levels, based on a relationship obtained with the CLIMBER-2 model (the higher the CO_2, the lower the insolation threshold, and the lower the insolation has to drop in order for the glaciation to initiate). The CO_2 levels are computed from carbon emissions scenarios, following the model of Archer [2005], previously described in section 1.1.3. They found that a carbon release of 5000 GtC could prevent glaciation for the next 500 000 years. The limitations of this approach are similar to those of the BIOCLIM study. Indeed, the conceptual model used to simulate global ice volume [Paillard, 1998] is the same as in BIOCLIM. Additionally, the atmospheric CO_2 scenarios are computed from the Archer [2005] model, and it only slightly differs from the Archer et al. [1997] model. In both cases, the ultimate process to remove atmospheric CO_2 is silicate weathering and the timescale is simply assumed (400 kyr in Archer [2005], compared to 200 kyr in Archer et al. [1997]).

Talento and Ganopolski [2021] have developed a reduced-complexity model in order to assess the impact of anthropogenic CO_2 emissions on future glacial cycles. Their model is based on three equations representing the evolution of ice volume,

temperature and CO_2. The sole forcing of the model are the insolation and cumulative anthropogenic emissions. The global mean surface temperature depends on ice volume and CO_2 concentrations. The past CO_2 evolution depends on temperature, ice volume evolution. In the future, an anthropogenic CO_2 component is added. This anthropogenic CO_2 component is computed through the use of the impulse response function of Lord et al. [2016], described in 1.1.3. The ice volume evolution depends on ice volume itself, orbital forcing and CO_2 concentrations. The model parameters are calibrated using both paleo reconstructions over the Quaternary and outputs from the CLIMBER-2 model. The model represents qualitatively well the glacial-interglacial cycle of the last million years. For low, already achieved, emission scenarios of 500 PgC, the behaviour of the climate is affected for a very long period of time, the next glaciation being very unlikely until 120 kyr AP, whereas it would be expected to take place in 50 kyr AP in a natural case. Cumulative emissions of 3000 PgC most likely lead to Northern Hemisphere Ice free conditions for the next half million year. Their work is based on the assumption that ice volume is equal or higher than pre-industrial levels at all time and the authors warn that their approach is not applicable for cases where anthropogenic emissions lead to a substantial melting of the Antarctic ice sheet. In their work, the anthropogenic CO_2 component is derived from the impulse response function of Lord et al. [2016] that neglects processes that could be of importance for the long term carbon cycle, such as organic matter burial (see section 1.1.3).

1.3.3 . SKB studies

The most recent studies performed by SKB are the reports released in 2019 and 2022, respectively : "Modelling changes in climate over the next 1 million years" [Lord et al., 2019] and "Uncertainties in modelled climate changes at Forsmark over the next 1 million years" [Williams et al., 2022].

Both reports follow the same methodology. The second one is an extension of the first one, where simulations are performed for a larger number of model parameters in order to assess climate uncertainty. Climate scenarios are performed over the next million years, and temperature and precipitations are downscaled at the site of interest (Forsmark, in Sweden).

Their methodology consists in several steps :

- First, they translate carbon emission scenarios from the IPCC into carbon concentration scenarios over the next million years, via the use of the carbon impulse response function described of Lord et al. [2016], described in 1.1.3.
- The CO_2 concentration over the next million years previously obtained and the insolation (orbital parameters) over the next million years (obtained through the La04 solution [Laskar et al., 2004] are used as forcing to a conceptual model of future changes in global sea level, in order to obtain ice volume changes over the next million years. The conceptual global sea level

model is based on the model of Archer and Ganopolski [2005], described in the previous section.

- The ice sheet volume changes obtained with the conceptual global sea level model, as well as the CO_2 concentration and orbital parameters are used to force a statistical climate emulator [Lord et al., 2017] over one million year. The statistical emulator produces the evolution of climatic variables such as temperature and precipitation.

- Lastly, a bias-correction downscaling technique is used, in order to increase the resolution of the climatic fields in the region of interest (around Forsmark, Sweden).

The conceptual global sea level model is based on the model of Archer and Ganopolski [2005]. The same caveats therefore apply to this study : the model was calibrated on past glacial interglacial cycles, and is not able to simulate a disappearance of the Antarctic ice sheet. The carbon impulse response function used is the one of Lord et al. [2016]. As has been mentioned before (see section 1.1.3), this does not take into account the role of organic matter burial on the long term response.

1.3.4 . Conclusion

Despite their scarcity, studies on impacts of anthropogenic emission on timescales of several millenia are essential. Indeed, the extremely long lifetime of CO_2 and the timescales associated with ice sheet imply that the impact of anthropogenic CO_2 emissions will last for much longer than a century. For instance, studies suggest that this could delay the next glaciation [Archer and Ganopolski, 2005, Talento and Ganopolski, 2021]. However, these studies present some limitations. In most cases, conceptual models are used to project ice volume evolution in the future. However, these conceptual models are calibrated on past glacial interglacial cycles and cannot be used to project a complete Greenland ice sheet disappearance or a substantial Antarctic ice sheet retreat. However, studies using spatially resolved ice sheet and climate model show that the complete disappearance of the Greenland ice sheet and at least, partial disappearance of the Antarctic ice sheet can be expected over the next millenia, if emissions continue unabated (see section 1.2.3). Also, the atmospheric CO_2 long term concentration is always computed based on the assumption that the ultimate removal of atmospheric CO_2 is silicate weathering, and that CO_2 levels come back to their pre-industrial value.

In this study, although we definitely do not aim at predicting the climate of the next million year, we want to broaden the scope of currently existing scenarios, by considering processes that are not yet included. We have decided to set our focus mostly on the Antarctic ice sheet, whose potential partial or complete disappearance is currently overlooked in studies on the next million years. Additionally,

we develop a conceptual model for the long term carbon cycle, that does not rely on silicate weathering only, but also includes organic matter fluxes. In the next chapter, we start by investigating what can be said about the climate of the next million years in a "natural" case, where the impact of anthropogenic emissions is not taken into account.

2 - Climate without anthropogenic influence

Chapter aims:

1. Present the main features of the Quaternary climate.
2. Develop a conceptual model able to reproduce the ice volume evolution over the Quaternary.
3. Study the influence of the insolation forcing used on the model results.
4. Discuss the use of ice volume conceptual models on future climates.

Highlights:

↪ Our model is able to represent qualitatively the main features of Quaternary ice volume evolution for each insolation forcing, with 41 kyr cycles dominating in the Early Pleistocene and ∼100 kyr cycles in the Late Pleistocene, provided the model deglaciation threshold (limit on insolation and ice volume that initiates the start of the deglaciation) increases over time.

↪ Insolation forcing and model parameters leading to similar behaviour in the past can produce widely different behaviours in the future.

↪ Conceptual models for ice volume evolution based on Northern Hemisphere glaciation are not suitable to study a potential Antarctic ice sheet melting due to anthropogenic forcing.

In this second chapter, we investigate what can be said about the climate of the next million years in a "natural" case, where the impact of anthropogenic emissions is not taken into account. This is done with the use of a conceptual model.

The climate of the last 2.6 Million year, the Quaternary, being mainly characterized by the alternance of "cold" and "warm" periods associated to Northern Hemisphere ice sheet build up and retreat, known as the glacial-interglacial cycles [Paillard, 2001], we focused on modeling the evolution of ice volume in the past. The alternance of glacial-interglacial cycles is expected to continue in the future in a case without anthropogenic forcing. Therefore, modelling the ice evolution over the Quaternary is critical to make scenarios about the ice volume evolution in the future in the case of a natural scenario.

In the first part, we present the main features of the Quaternary climate and review existing modeling studies over this period. In a second part, we develop a simple conceptual model representing the global ice volume evolution as a response

to the insolation forcing. This model is able to reproduce the ice volume evolution over the Quaternary. We study the impact of one of the model parameters and of the insolation forcing used on the model results. This study was published in Climate of the Past in 2022 ([Leloup and Paillard, 2022]) and the key points are summarized in this part. In the third part, we run the model on the future, with the optimal parameters identified in the previous part, and discuss its implications for a natural climate scenario. We compare our results to other modeling studies on future long term climate in a natural scenario.

2.1 . Ice sheets over the Quaternary : a short overview of existing data and modelling studies

The Quaternary period, that started ∼2.6 Million years ago, is characterized by the alternance of the build up and retreat of Northern continental ice sheets. We are currently in an interglacial state (the Holocene), and ice sheets in the Northern Hemisphere are limited to a single one, over Greenland. Around 21 000 years ago, at the last glacial Maximum, Northern Hemisphere ice sheets extended over the north of Europe and America (as depicted in Fig 2.1) leading to a sea level approximately 120m lower than today [Clark et al., 2009, Lambeck et al., 2014]. The global temperature was around 4-6°C colder than in the pre-industrial era [Annan and Hargreaves, 2013, Tierney et al., 2020b, Annan et al., 2022].

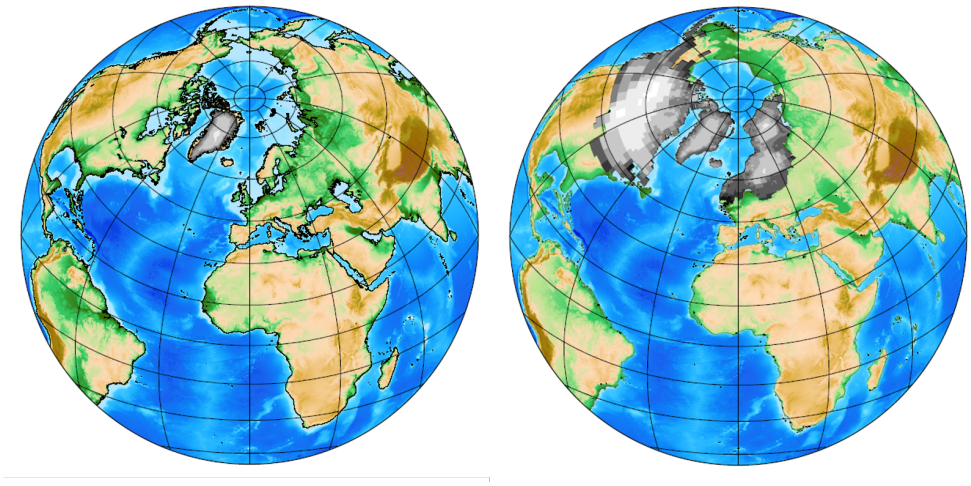

Figure 2.1: Northern Hemisphere ice sheets at present day (left panel, limited to the Greenland ice sheet) and at the Last Glacial Maximum (right panel). Figure from C. Dumas.

Benthic $\delta^{18}O$ records [Lisiecki and Raymo, 2005, Ahn et al., 2017] exhibit oscillations over the Quaternary and are used as a proxy for sea level variations, although it is also influenced by deep sea temperature [Raymo et al., 2018].

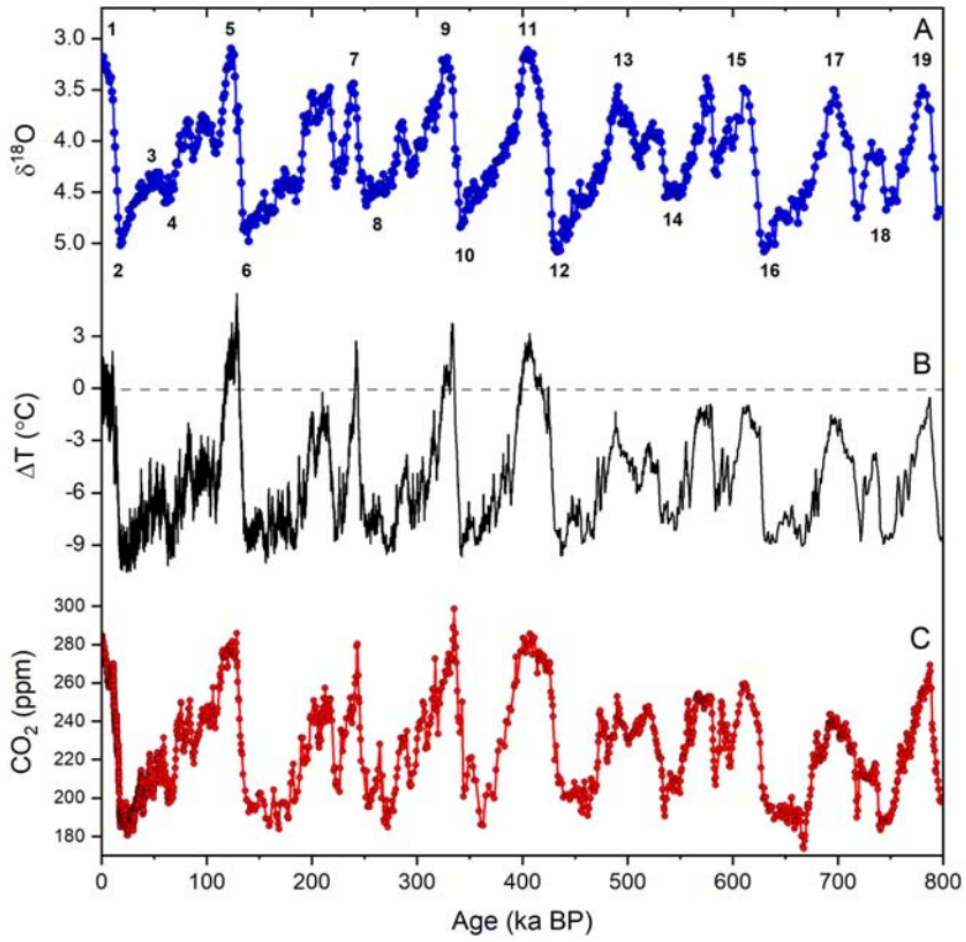

Figure 2.2: Marine and ice core records of late Pleistocene climate variability. (A) 'LR04' benthic foraminiferal oxygen isotope ($\delta^{18}O$) stack ([Lisiecki and Raymo, 2005]). (B) Antarctic ice core temperature reconstruction (ΔT, difference from the mean of the last millennium) based on deuterium isotopes (δD_{ice}) in EPICA Dome C ([Jouzel et al., 2007]). (C) Atmospheric carbon dioxide (CO_2) concentrations from Antarctic ice cores ([Bereiter et al., 2015]). Marine Isotope Stage (MIS) numbers are shown in (A). Note (1) the strong connection between Antarctic temperatures, benthic foraminiferal $\delta^{18}O$ values and atmospheric CO_2; (2) the dominance of quasi 100-kyr cycles for the last 800 kyr; and (3) the enhanced warmth and elevated atmospheric CO_2 of Antarctic interglacials since MIS 11 (i.e. the Mid-Brunhes Event at $\sim$430 ka). The legend and Figure are taken from Wilson et al. [2021].

Antarctic ice cores also provide information about past climate. The analysis of deuterium of the ice reveals information on the evolution of the local Antarctic

temperature [Jouzel et al., 2007]. Analysis of the air trapped in the ice core provides insights into greenhouse gases concentrations (CO_2, CH_4, N_2O) in the past [Lüthi et al., 2008, Bereiter et al., 2015, Loulergue et al., 2008, Spahni et al., 2005]. Both temperature and greenhouse records exhibit oscillations that are highly correlated to the global ice volume evolution, as is visible in Figure 2.2. The longest ice core currently available goes back until about 800 kyr BP [community members, 2004], and cannot provide information for oldest periods.

Marine cores extend further back in time (around 5 Myr BP for the Lisiecki and Raymo [2005] record). The analysis of $\delta^{18}O$ of marine cores reveals two differences between the last million year and the earlier part of the Quaternary. In the last million year, glacial-interglacial cycles have a periodicity around 100 kyr, and the cycles are strongly asymmetric, with short deglaciations following long glaciations. However, in the earliest part of the Quaternary, the cycles exhibit a period of 41 kyr, and are more symmetrical. This is depicted in Figure 2.3. The shift from a 41 kyr dominated record to a 100 kyr dominated record occurring approximately 1 Myr BP is known as the Mid-Pleistocene Transition (MPT) [Clark et al., 2006, Berends et al., 2021].

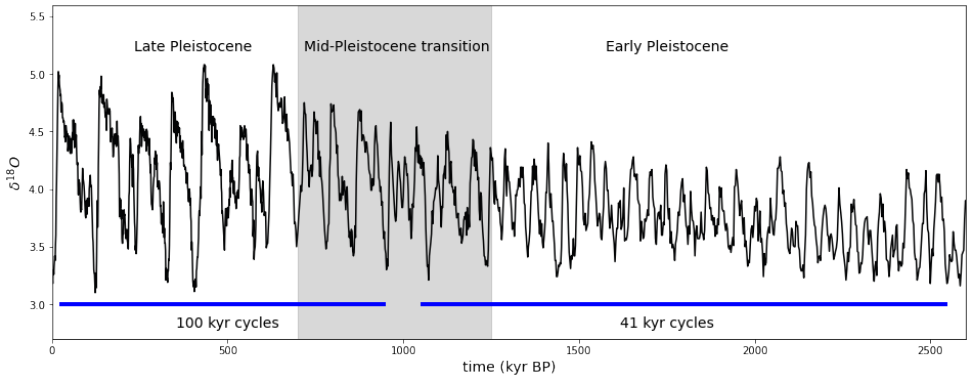

Figure 2.3: $\delta^{18}O$ record of Lisiecki and Raymo [2005] over the Quaternary. The more recent part of the record (Late Pleistocene) displays $\sim$ 100 kyr oscillations, while there are of 41 kyr in the Early Pleistocene.

Spectral analysis demonstrated that astronomical frequencies are present in the ice volume record [Hays et al., 1976]. This hints at a link between insolation and the glacial-interglacial ice volume variations. However, questions remain : how are the insolation variations translated into ice volume variations ? How are the 100 kyr oscillations obtained, as the 100 kyr frequency is very weak in the forcing ? How to explain the shift from 41 kyr to 100 kyr cycles ?

Milankovitch [1941] popularized the idea that the crucial element for Northern Hemisphere ice sheet growth, was the summer insolation at typical latitudes for ice sheets (65°N). A cold summer, linked to reduced summer insolation, favors ice sheet growth. Since then, glacial interglacial cycles ice volume evolution has

been modelled over different time periods, ranging from an ice age cycle to the whole Quaternary, with a wide range of models; conceptual models as well as more complex models.

The first conceptual model linking insolation and ice volume variations was developed by Calder [1974] : if the insolation is below a threshold, the ice volume increases linearly with the insolation, and conversely if insolation is above the threshold, the ice volume decreases linearly with insolation (with a different proportionality constant). MacAyeal [1979] developed a model where global ice volume variation is not only controlled by the insolation fluctuations, but also by a second control parameter that allows to differentiate between fast and slow glaciological response mechanisms. The model of Imbrie and Imbrie [1980] used different rates of ice volume change depending on the climate state (warming or cooling). Paillard [1998] represented glacial interglacial cycles as relaxation oscillations between multiple equilibria, a glaciation and deglaciation state. This idea was carried on by Parrenin and Paillard [2003, 2012] with slightly different model formulations. These conceptual models were able to produce 100 kyr cycles as a response to insolation.

Energy balance models coupled to simplified ice-sheet models have been able to perform 100 kyr oscillations in the ice volume in response to the insolation forcing [Pollard, 1983, DeBlonde and Peltier, 1991, Tarasov and Peltier, 1997, Berger et al., 1999, Stap et al., 2014]. Earth system Model of Intermediate Complexity (EMIC) have also been coupled to ice sheet models and were able to represent 100 kyr oscillations as a direct response to the insolation forcing [Ganopolski and Calov, 2011, Ganopolski and Brovkin, 2017] as well as a transition from 41 kyr cycles to 100 kyr cycles [Willeit et al., 2019]. Ice sheet models using climate parametrization for the ice sheet based on timeslice runs of GCM have also been used to produce 100 kyr oscillations [Abe-Ouchi et al., 2013].

Many feedbacks from the climate -cryosphere system can amplify the response to the astronomical forcing and explain the non linear response of ice sheet to insolation forcings : delayed isostatic rebound, albedo, dust, carbon cycle and ocean feedbacks. While in conceptual model the link between ice volume variation and insolation is parametrized, the use of EMIC or General Circulation Model (GCM) allows to model more explicitly the different processes that can give rise to positive and negative feedbacks. For example rapid glacial terminations could be explained by the dust albedo feedback with large ice sheets and glacial conditions being associated with high rates of dust deposition over the ice sheets [Ganopolski and Calov, 2011]. This reduces the ice sheet albedo and therefore enhances its response to insolation. Stap et al. [2014] have shown that the ice-albedo feedback is crucial in amplifying ice sheet growth and decay. Feedbacks due to the carbon cycle have also been suggested. For instance, oceanic circulation changes due to insolation changes can impact the carbon cycle [Paillard and Parrenin, 2004], and thus amplify the ice sheet's response to insolation variations. Others [Pollard, 1982,

Oerlemans, 1980, Abe-Ouchi et al., 2013] have suggested that the fast retreat of ice sheets was driven by delayed isostatic rebound : when the ice sheet melt and has not yet rebound, this lowers the surface elevation and increases the ice ablation.

Due to their simplicity, conceptual models are much less computationally expensive than EMIC or GCM simulation. Their aim is not to represent the physical system explicitly, but they allow us to understand important aspects of the climate system. As they are computationally inexpensive, it is possible to make different scenarios for the future, with different model parameter values. Therefore, in the following we have developed a conceptual model, able to represent the ice volume evolution over the Quaternary. Afterwards, we run it on the future and discuss about the use of conceptual models in future long term projections.

2.2 . A conceptual model for representing ice volume evolution over the glacial-interglacial cycles

In this part, we develop a simple conceptual model representing the global ice volume evolution as a response to the insolation forcing. We study the impact of the model parameters and of the insolation forcing used as input on the model results. The model is quickly presented, followed by a more detailed study in the article. The key results of the article are summarized.

Our model is a simplified version of the Parrenin and Paillard [2003] model. As in Parrenin and Paillard [2003], we represent the climate system by relaxation oscillations between two states : glaciation and deglaciation. The model's only external forcing is the summer insolation at 65°N (I). In our model, the ice volume (v) evolution is represented by two different equations : one for the "glaciation" (g) and another for the "deglaciation" (d) state. These equations are composed of two terms. The first term, common in both the glaciation and deglaciation state, is a linear relation to the insolation forcing. When the insolation is high, the ice volume decreases and conversely. We make the assumption that the global ice volume changes are mainly driven by the Northern Hemisphere ice sheet volume changes, and we neglect Antarctic ice volume changes. This seems reasonable as most recent studies suggest that the Antarctic ice sheet contribution to the $\sim$120 m sea level drop since the LGM is around 10m sea level equivalent [Briggs et al., 2014, Golledge et al., 2013, 2014, Whitehouse et al., 2012, Simms et al., 2019, Wilson et al., 2021].

The second term of the equations depends on the state glaciation or deglaciation. In the glaciation state, there is a slow glaciation trend, while there is a rapid ice volume decrease trend in the deglaciation state. In comparison to the Parrenin and Paillard [2003] model, there are only two terms in the equation driving the ice volume evolution. The Parrenin and Paillard [2003] model included a third term : a direct dependance to obliquity, additionally to the dependance to the summer insolation forcing (having contributions from both, precession and obliquity). Here,

we have discarded the direct dependency to obliquity term as it was possible to obtain good results without it. The equations of our model are therefore :

$$\begin{cases} (g)\ \frac{dv}{dt} = -\frac{I}{\tau_i} + \frac{1}{\tau_g} \\ (d)\ \frac{dv}{dt} = -\frac{I}{\tau_i} - \frac{v}{\tau_d} \end{cases} \tag{2.1}$$

where v is the normalized ice volume, τ_i,τ_d, τ_g are time constants, I is the normalized summer insolation forcing at 65°N.

In the Parrenin and Paillard [2003] study, the summer insolation was taken equal to the summer solstice insolation. However, different definitions can be taken for the summer insolation, and their influence on the model results has rarely been studied, as will be discussed afterwards.

We emphasize that following our assumption of global ice volume variations being mainly driven by Northern Hemisphere ice sheets variations, our model is not applicable to cases where the Antarctic ice sheet melts substantially.

The switch from the glaciation to deglaciation state and conversely in our model are similar to the Parrenin and Paillard [2003] model. On one hand, the switch from the deglaciation (d) to the glaciation (g) state happens when the insolation forcing becomes low enough, lower than the glaciation threshold I_0. On the other hand, the switch from glaciation (g) to deglaciation (d) state happens when not only the insolation, but the combination of insolation and ice volume becomes high enough, higher than the deglaciation threshold V_0.

$$\begin{cases} (d)\ to\ (g)\ : I < I_0 \\ (g)\ to\ (d)\ : I + v > V_0 \end{cases} \tag{2.2}$$

Within the scope of conceptual models, the choice of the astronomical forcing differs. Milankovitch used caloric seasons at 65°N. Imbrie and Imbrie [1980] used the July insolation. Paillard [1998, 2001] used the summer solstice insolation. Parrenin and Paillard [2012] and Imbrie et al. [2011] have used a combination of orbital parameters. However, these studies did not consider different insolation forcings and the influence of the insolation forcing on the model results. Therefore, in the following, we will consider different definitions of the summer insolation and study its impact on the model results.

In the article, we define different types of summer insolation : the summer solstice insolation, the caloric season and the integrated summer insolation above two different thresholds. We use these four different summer insolation as model forcing and study the impact on the model results. The goal is to assess the robustness of the model relative to the choice of definition for the summer insolation. Indeed, conceptual models are more relevant if they are not too sensitive to parameter choices. This has rarely been done in previous modelling studies using conceptual models, where only one type of insolation forcing is considered. We also consider

how the deglaciation threshold must evolve with time in order to represent the past volume variations, and more specifically, the Mid-Pleistocene transition.

Clim. Past, 18, 547–558, 2022
https://doi.org/10.5194/cp-18-547-2022

Climate of the Past
Open Access
EGU

Influence of the choice of insolation forcing on the results of a conceptual glacial cycle model

Gaëlle Leloup[1,2] **and Didier Paillard**[2]

[1]Agence Nationale pour la gestion des déchets radioactifs (ANDRA), 1 Rue Jean Monnet, 92290 Châtenay-Malabry, France
[2]Laboratoire des Sciences du Climat et de l'Environnement, LSCE/IPSL, CEA-CNRS-UVSQ-Université Paris-Saclay, 91198 Gif-sur-Yvette, France

Correspondence: Gaëlle Leloup (gaelle.leloup@lsce.ipsl.fr)

Received: 6 September 2021 – Discussion started: 13 September 2021
Revised: 11 February 2022 – Accepted: 18 February 2022 – Published: 25 March 2022

Abstract. Over the Quaternary, ice volume variations are "paced" by astronomy. However, the precise way in which the astronomical parameters influence the glacial–interglacial cycles is not clear. The origin of the 100 kyr cycles over the last 1 million years and of the switch from 40 to 100 kyr cycles over the Mid-Pleistocene Transition (MPT) remain largely unexplained. By representing the climate system as oscillating between two states, glaciation and deglaciation, switching once glaciation and deglaciation thresholds are crossed, the main features of the ice volume record can be reproduced (Parrenin and Paillard, 2012). However, previous studies have only focused on the use of a single summer insolation as input. Here, we use a simple conceptual model to test and discuss the influence of the use of different summer insolation forcings, having different contributions from precession and obliquity, on the model results. We show that some features are robust. Specifically, to be able to reproduce the frequency shift over the MPT, while having all other model parameters fixed, the deglaciation threshold needs to increase over time, independently of the summer insolation used as input. The quality of the model–data agreement however depends on the chosen type of summer insolation and time period considered.

1 Introduction

Palaeoclimate records over the Quaternary (last 2.6 Myr), such as ice cores (Jouzel et al., 2007) or marine cores (Lisiecki and Raymo, 2005) show a succession of oscillations. These oscillations are due to the build-up and retreat of northern continental ice sheets, corresponding to respectively cold and warm periods known as the glacial–interglacial cycles. Over the last 1 million years, there is an alternation of long glaciations followed by quick deglaciations, leading to cycles of a period of 100 kyr. Yet, in the earliest part of the record, glacial–interglacial cycles are mostly dominated by a frequency of 41 kyr with lower amplitudes. Spectral analysis of the record (Hays et al., 1976) has revealed that astronomical frequencies are imprinted into the ice volume record, suggesting a strong link between insolation and the glacial–interglacial cycles.

The nature and physics of this link has been a central question since the discovery of previous warm and cold periods, and long before the obtention of continuous $\delta^{18}O$ records. It is known that the variations of annual total energy are of too-low an amplitude to explain such changes (Croll, 1864). Therefore, focus has been set on seasonal variations. Croll (1864) assumed that glaciations were linked to colder winters. In contrast, the idea that the decisive element for glaciation was the presence of cold summers, due to reduced summer insolation, at latitudes of the Northern Hemisphere critical for ice sheet growth (65° N), was taken up by Milankovitch, who made it the key element of his ice age theory (Berger, 2021). For conceptual models, this raises the question of which insolation to use as input. When summer insolation is used, this questions the definition of summer: should it be defined as a specific single day, like the summer solstice; the astronomical summer between the two equinoxes; or a fixed number of days around the solstice? The choice leads to very different forcings with different contributions from obliquity and precession. For Earth system models and

climate models, insolation is computed at each time step for each grid area, and such choice of the input forcing is not needed. However, other modelling choices have to be made. For instance, several parameterizations are used to represent ice sheet surface melt (Robinson et al., 2010), like the positive degree day (PDD) method (Reeh, 1991), in which surface melt depends solely on air temperature, or the insolation temperature melt (ITM) method (Van den Berg et al., 2008), which takes into account the effect of both temperature and insolation. In both cases, the translation of insolation local and seasonal variations into ice sheet changes and ice age cycles remains an open modelling question.

The obtention of 100 kyr cycles is not possible with a linear theory like that of Milankovitch (Hays et al., 1976; Imbrie and Imbrie, 1980), and a form of non-linearity is needed. Indeed, there is no simple relation between insolation extrema and ice volume extrema. One of the largest deglaciations (termination V) occurred when insolation variations were minimal. Conversely, insolation variations were maximal at termination III, whereas the transition was rather small. In addition, the amplitude of summer insolation variations is maximal every 400 kyr, but this frequency is absent from the palaeoclimatic records. The 100 kyr cycles have been proposed to be linked to either eccentricity-driven variations of precession (Raymo, 1997; Lisiecki, 2010), obliquity (Huybers and Wunsch, 2005; Liu et al., 2008), or both (Huybers, 2011; Parrenin and Paillard, 2012), to internal oscillations phase locked to the astronomical forcing (Saltzman et al., 1984; Paillard, 1998; Gildor and Tziperman, 2000; Tziperman et al., 2006), to internal oscillations independent of the astronomical forcing (Saltzman and Sutera, 1987; Toggweiler, 2008) or to period-doubling bifurcation (Verbitsky et al., 2018). Additionally, the Mid-Pleistocene Transition (MPT) and the switch from a 41 kyr dominated record to a 100 kyr one remain mostly unexplained.

Several conceptual models have been developed to try to solve these questions. Calder (1974) was the first to develop a simple conceptual model, linking insolation and ice volume variations. Imbrie and Imbrie (1980) also developed a conceptual model, where the rate of change was different in the case of a warming or cooling climate. Paillard (1998) developed the idea that the glacial–interglacial cycles can be seen as relaxation oscillations between multiple equilibria, like a glaciation and a deglaciation state. It was suggested that the criteria to trigger a deglaciation depends on both insolation and ice volume, whereas insolation alone seems able to trigger glaciation (Parrenin and Paillard, 2003). Here, we adapt and simplify the model of Parrenin and Paillard (2003) and extend it over the whole Quaternary.

One of the critical questions for conceptual models is to decide which insolation to use as input. Milankovitch's work utilized "caloric seasons" at 65° N, the half-year with the highest insolation. This was also the case in Calder's model, which used caloric seasons at 50° N as input. Imbrie and Imbrie (1980) used the July insolation. The use of summer insolation gradually shifted towards the use of the summer solstice insolation, most probably as it is easier to compute thanks to the tables provided by Berger (1978) and allows one to obtain better fits for the more recent part of the records (Paillard, 2015). More recently, Huybers (2006) suggested that the integrated summer insolation (ISI) over a certain threshold could be better, as it would more closely follow PDDs, an important metric for ice sheet mass balance. Others have also used combinations of orbital parameters as a forcing (Imbrie et al., 2011; Parrenin and Paillard, 2012). However, most models only use one type of insolation forcing and do not consider the influence of other insolation forcing types on the model results.

In our work, we will consider several summer insolation forcings at 65° N (summer solstice insolation, caloric season and ISI over two different threshold values) in order to study their influence on the model results. These different summer insolation forcings have similar shape, but the respective contribution of obliquity and precession differ. The different insolation forcings have different performances in matching the data, depending on the time period considered. However, we show that some features are independent of the insolation forcing used as input. In particular, we are able to reproduce a switch from 41 kyr oscillations before the MPT to 100 kyr cycles afterwards, in agreement with the records for all insolation forcings, by varying a single parameter: the deglaciation threshold V_0, and keeping all the other model parameters constant. This is similar to the results of Paillard (1998), who obtained a frequency shift on the glacial cycles by using a linearly increasing deglaciation threshold. This is also coherent with the more recent results of Tzedakis et al. (2017), who demonstrated that the particular sequence of interglacials that happened over the Quaternary and the frequency shift from 41 to 100 kyr could be explained with a simple rule, taking into account a deglaciation threshold that increases over time, leading to "skipped" insolation peaks and longer cycles.

2 Conceptual model and methods

2.1 Conceptual model

The model used in our study is an adapted and simplified version of the conceptual model of Parrenin and Paillard (2003). For the glacial–interglacial cycles, it is not a new idea that the climate system can be represented by relaxation oscillations between multiple equilibria, like a glaciation and a deglaciation state (Paillard, 1998; Parrenin and Paillard, 2003, 2012). The aim of conceptual models is not to explicitly model and represent physical processes but rather to help us understand critical aspects of the climate system. Here, we do not intend to explicitly represent the numerous physical processes involved in ice sheet volume evolution, affecting surface mass balance, ice discharge to the ocean and bottom melt of grounded ice. Instead, we represent the climate

system with two distinct states of evolution: the "glaciation state" (g) and "deglaciation state" (d). We make the assumption that the evolution of the ice sheet volume in these two states can be simply described by two terms. The first one, common to the glaciation and deglaciation states, is a linear relation to the summer insolation: when the insolation is above average, the ice sheet melts, whereas when the insolation is low enough, the ice sheet grows. The second term, specific to the system state, represents an evolution trend linked to the system state: a slow glaciation in (g) state and a rapid deglaciation in (d) state.

In our model, the evolution of the ice volume in these two states is described by

$$\begin{cases} (g)\ \frac{\mathrm{d}v}{\mathrm{d}t} = -\frac{I}{\tau_\mathrm{i}} + \frac{1}{\tau_g} \\ (d)\ \frac{\mathrm{d}v}{\mathrm{d}t} = -\frac{I}{\tau_\mathrm{i}} - \frac{v}{\tau_d} \end{cases}, \tag{1}$$

where v represents the normalized ice volume. τ_i, τ_d and τ_g are time constants. I is the normalized summer insolation forcing at 65° N. The implicit assumption is made that the global ice volume changes are mainly driven by the Northern Hemisphere ice sheet waning and waxing, as we focus on the effect of insolation changes at high northern latitudes. This is not a limiting assumption as data suggest much lower sea level variations due to the Antarctic ice sheet than due to those of the Northern Hemisphere over glacial–interglacial timescales. For example, the contribution of the Antarctic ice sheet to the $\sim$ 120 m Last Glacial Maximum sea level drop is estimated to be between 10 and 35 m sea level equivalent (Lambeck et al., 2014). Other effects like thermal expansion, small glaciers and ice caps are estimated to be around 3 to 4 m sea level equivalent. Furthermore, it has been suggested (Jakob et al., 2020) that the growth of larger Northern Hemisphere ice sheets since the start of the Quaternary and the associated sea level drop has a stabilizing effect on the East Antarctic ice sheet, as it limits its exposure to warm ocean waters.

A critical point is to define the criteria for the switch between the glaciation and deglaciation states. To enter the deglaciation state, both ice volume and insolation seem to play a role (Raymo, 1997; Parrenin and Paillard, 2003, 2012), as terminations occur after considerable build-up of ice sheet over the last 1 million years. To represent the role of both ice volume and insolation in the triggering of deglaciations, the condition to switch from (g) to (d) state uses a linear combination of ice volume and insolation. The deglaciation is triggered when the combination crosses a defined threshold V_0: the deglaciation threshold. As in the work of Parrenin and Paillard (2003), this allows transitions to occur with moderate insolation when the ice volume is large enough and reciprocally. Conversely, glacial inception seems to depend on orbital forcing alone (Khodri et al., 2001; Ganopolski and Calov, 2011). Therefore, the condition to switch from the deglaciation state to the glaciation state is based on insolation only: it is possible to enter glaciation when the insolation becomes low enough.

$$\begin{cases} (d) \text{ to } (g)\ : I < I_0 \\ (g) \text{ to } (d)\ : I + v > V_0 \end{cases} \tag{2}$$

The idea that the deglaciation threshold is linked to both insolation and ice volume is not new (Parrenin and Paillard, 2003, 2012), and is similar to that developed by Tzedakis et al. (2017), where the threshold for a complete deglaciation decreases with time as the system accumulates instability, with ice sheets becoming more sensitive to insolation increase. As the ice sheet grows and extends to lower latitudes, the insolation needed to reach a negative mass balance decreases. This idea has been confirmed with modelling studies (Abe-Ouchi et al., 2013). Several reasons can explain this increase of instability over time: delayed bedrock rebound and exposure to higher temperature as the ice sheet sinks (Oerlemans, 1980; Pollard, 1982; Abe-Ouchi et al., 2013), increase in basal sliding as the ice sheet grows and the base becomes warmer as it is more isolated from the cold surface temperature (MacAyeal, 1992; Marshall and Clark, 2002), ice sheet margin calving (Pollard, 1982), decrease of the ice sheet albedo due to either snow ageing (Gallée et al., 1992) or increase of dust deposition as the ice sheet expands (Peltier and Marshall, 1995; Ganopolski and Calov, 2011) and increase of atmospheric CO_2 due to the release of deep ocean carbon when the Antarctic ice sheet extends over the continental shelves (Paillard and Parrenin, 2004; Bouttes et al., 2012).

2.2 Summer insolation

The conceptual model defined previously uses summer insolation as input. It is therefore important to consider which insolation should be used. Insolation is usually taken at 65° N, a typical latitude for Northern Hemisphere ice sheets. Several articles have used the summer solstice daily insolation at 65° N as input insolation forcing (Paillard, 1998; Parrenin and Paillard, 2003). Others (Tzedakis et al., 2017) have used the caloric season, as defined by Milankovitch (1941), defined as the half-year with the highest insolation. It is also possible to use as input a linear combination of orbital parameters (Imbrie et al., 2011; Parrenin and Paillard, 2012). Huybers (2006) also defined the integrated summer insolation (ISI) above a threshold.

Here, for the first time, we want to examine the effect of this choice on the dynamics of a conceptual model. We therefore use four different summer insolation forcings, and compare the model results obtained with each of them. We use the summer solstice insolation, the caloric season and ISI above two different thresholds (300 and 400 W m^{-2}). Experiments were also conducted for the summer solstice insolation at 50° N instead of 65° N, but these are not presented here as they do not change the conclusions obtained with the forcings at 65° N. We refer the reader to Sect. S1 in the Supplement for information on these experiments.

These four insolation forcings differ, and have different contributions from precession and obliquity, as can be seen in Fig. 1. For example, the summer solstice insolation has a low contribution from obliquity (41 kyr) compared to the caloric season, or ISI above 300 W m^{-2}. The summer solstice insolation and the caloric season were computed using the AnalySeries software (Paillard et al., 1996). The ISI for a threshold τ (noted as ISI above τ, or ISI(τ) in this article) was defined by Huybers (2006) as the sum of the insolation on days exceeding this threshold.

$$\mathrm{ISI}(\tau) = \sum_i \beta_i (W_i \cdot 86\,400)$$

Here, W_i is the mean insolation of day i in W m^{-2} and β_i equals one if $W_i > \tau$ and zero otherwise.

To compute ISI(τ), one first needs to compute the daily insolation on day i, and then sum over the year for the days exceeding the threshold. Here, we developed a Python code based on the MATLAB code provided by Huybers (2006). Unlike the insolation files provided by Huybers (2006), which used the solution from Berger and Loutre (1991), we use the orbital parameter value of the Laskar et al. (2004) solution for the calculation. This results in slightly different results for deeper time periods as the calculation of orbital parameters also differ with these two estimations.

2.3 Optimal model parameters

The conceptual model relies on a small number of model parameters: τ_i, τ_g, τ_d and the two thresholds for the switch from a glaciation state to a deglaciation state and the inverse: V_0 and I_0. For all the simulations performed, we kept $\tau_i = 9$ kyr, $\tau_g = 30$ kyr, $\tau_d = 12$ kyr and $I_0 = 0$, as these parameters gave correct behaviour in previous studies (Parrenin and Paillard, 2003). No attempt was made to tune these parameters to obtain a behaviour closer to the data: on the contrary, focus was set more towards the influence of the deglaciation threshold parameter, V_0, on the model results. To compare our model results to the data, we used the benthic δ^{18}O stack "LR04" (Lisiecki and Raymo, 2005) as a proxy for ice volume, considering that most of the δ^{18}O changes of benthic foraminifera represent changes in continental ice (Shackleton, 1967; Shackleton and Opdyke, 1973). Lower δ^{18}O values correspond to lower ice volume. The model results and the LR04 curve were normalized to facilitate their comparison. In the following, "data" refers to the normalized δ^{18}O stack curve LR04.

To estimate which model parameters lead to model results closer to the data, the definition of an objective criteria is needed. The choice of such a criteria is not straightforward, and the use of different criteria could have led to slightly different results. Our model is simple and does not aim at precisely reproducing the ice volume evolution, but rather at reproducing the main qualitative features, such as the shape and frequency of the oscillations. Therefore, we used a criteria based on the state of the system: glaciation or deglaciation. Similar results can be obtained using a simple correlation coefficient (see Sect. S2). The definition of the deglaciation state in the data is explained in Sect. 2.4. A critical point is that our model should be able to deglaciate at the right time, when a deglaciation is seen in the data. Conversely, the model should not produce deglaciation at periods where the data do not show deglaciation.

We defined a criteria for each of these two conditions, and assembled them in a global criteria. To determine if deglaciation is well reproduced by our model, we look at the state of the model (glaciation or deglaciation) at the time halfway between the start of the deglaciation and the end of the deglaciation. If the model state at that time is deglaciation, the deglaciation is considered as correctly reproduced. Otherwise, it is considered as a "missed" deglaciation. We simply defined the criteria c_1 as the fraction of deglaciations correctly reproduced. This criteria equals one when all the deglaciations take place at the right time, meaning that the model produces a deglaciation state every time deglaciation is seen in the data. To ensure that the model does not deglaciate too often, we looked at insolation maxima that are not associated with deglaciation in the data and ensured the corresponding model state was glaciation. We decided to look specifically at insolation maxima, as they are where the model is the most likely to deglaciate when it should not. A deglaciation seen in the model at a place where no deglaciation is seen in the data is considered as a "wrong transition". We defined the criteria c_2 as $c_2 = 1 - w$, with w the fraction of wrong transitions. The c_2 criteria equals one when the model does not deglaciate when it should not. To take into account these two conditions, the overall accuracy criteria c is defined as $c = c_1 \cdot c_2$. It is equal to one when all the deglaciations are correctly placed and when no additional deglaciation compared to the data take place.

In order to study the evolution of the optimal deglaciation threshold V_0 over the Quaternary, it was divided into five 500 kyr periods. The V_0 values that maximize the accuracy criteria for each time period and insolation forcing are called "optimal V_0". To determine the optimal V_0 threshold corresponding to each period and insolation forcing, several simulations were carried out and the parameter values maximizing the accuracy criteria c were selected. More precisely, for each insolation and period, 3500 simulations corresponding to different V_0 thresholds (from $V_0 = 1.0$ to $V_0 = 8.0$ with a step of 0.1) and different initial conditions (initial volume V_{init} ranging from 0.0 to 5.0 with a step of 0.2, and the two possible initial states – glaciation or deglaciation) were performed. The numerical integration of the model equations was done with a fourth-order Runge–Kutta scheme.

For each insolation forcing, the best fit over the Quaternary is defined as the simulation over the whole Quaternary (0 to 2500 ka) with V_0 changing with time that is equal to the corresponding optimal V_0 at each time period. Addition-

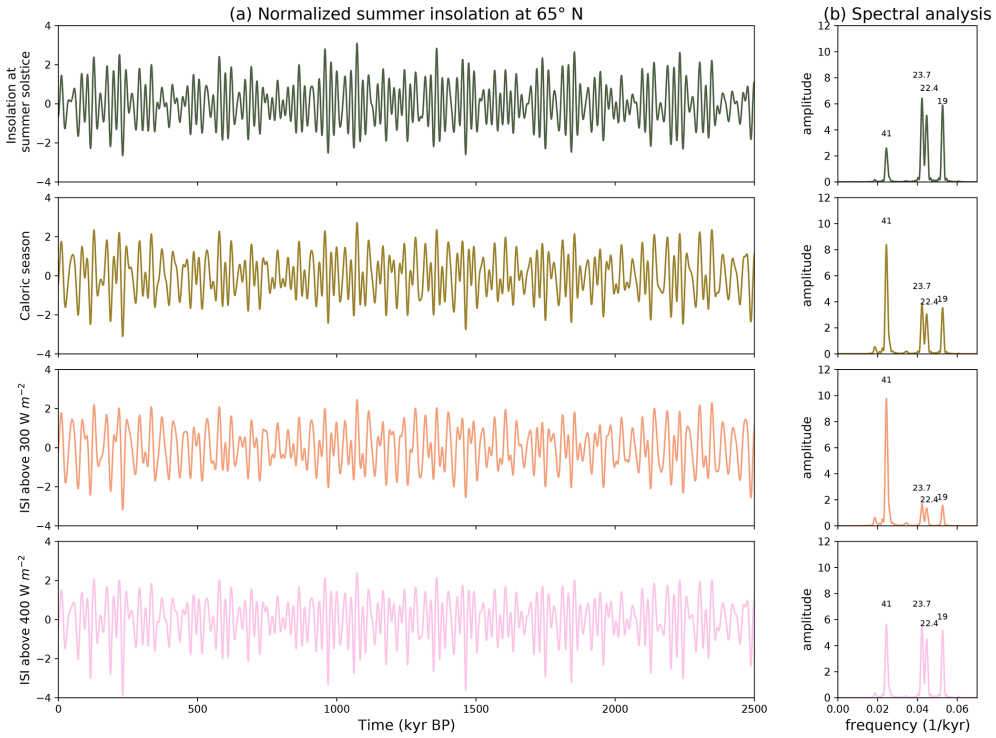

Figure 1. **(a)** The four different summer insolation forcings at 65° N (summer solstice, caloric season, ISI above 300 W m^{-2} and ISI above 400 W m^{-2}) displayed over the Quaternary. The insolation forcings are centred and normalized by their standard deviation. **(b)** Corresponding spectral analysis over the Quaternary, normalized by standard deviation.

ally, simulations were performed to determine the optimal V_0 threshold obtained when the optimization procedure is carried out over the whole Quaternary. It is called V_0^{Q} in the following.

2.4 Definition of the deglaciation state in the data

To calculate our accuracy criteria c and therefore determine the optimal V_0 threshold over a given period, a definition of the deglaciation in the data is needed. We based our definition on the interglacial classification developed by Tzedakis et al. (2017). Tzedakis et al. (2017) differentiates interglacials, continued interglacials and interstadials based on a detrended version of the LR04 stack curve. A period is considered as an interglacial if its isotopic δ^{18}O is below a threshold (3.68 ‰). Two interglacials are considered to be separated if they are separated by a local maximum above a threshold (3.92 ‰). This definition differs from the usual characterization of terminations, sometimes leading to several interglacials in the same isotopic stage. The definition of Tzedakis et al. (2017) is for interglacials, and as our focus is not on interglacial periods but rather on deglaciations, we adapted it. We defined deglaciations as periods of decreasing δ^{18}O (and thus, ice volume, in our assumptions) preceding the interglacials. The start of the deglaciation is taken as the last local maxima above the threshold of 3.92 ‰, and the end of the deglaciation is taken as the first local minima below the interglacial threshold of 3.68 ‰. The deglaciation periods in the data corresponding to the time between the deglaciation starts and deglaciation ends are displayed with blue shading in Figs. 4 and 5.

3 Results and discussion

3.1 Optimal deglaciation threshold V_0 and corresponding accuracy

For each insolation, we computed the deglaciation threshold V_0 maximizing the accuracy for each of the five 500 kyr periods and the fixed V_0^{Q} value maximizing the accuracy over the whole Quaternary. The results are displayed in Fig. 2.

In some cases, several values of the deglaciation threshold V_0 lead to the same accuracy criteria, whereas in others there is only one V_0 value maximizing the accuracy. When several V_0 values are equivalent, the mean value was plotted and the other possible values are represented with error bars.

Over the same time period, different insolation values lead to slightly different optimal V_0 thresholds. But the most striking feature is the increase of the optimal V_0 threshold over time, and more specifically for the last 1 million years, after the MPT. This feature is valid regardless of the insolation type. The optimal V_0 over the whole Quaternary V_0^{Q} is between 3.4 and 4 for each insolation type. It is a value in the

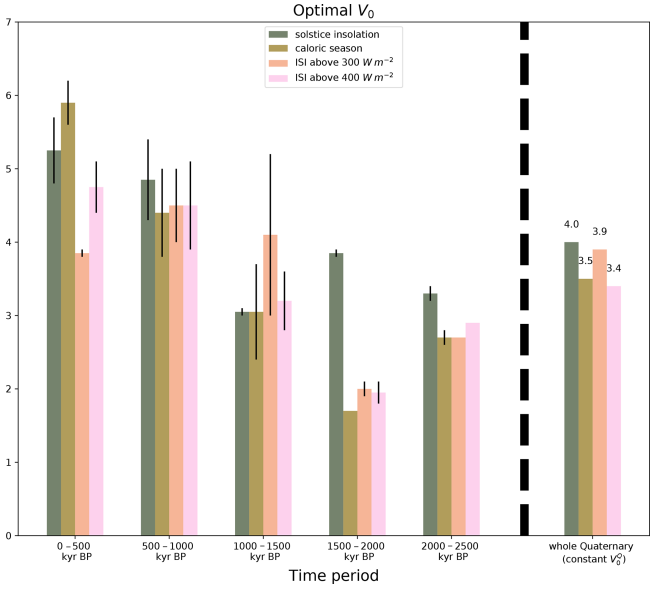

Figure 2. Optimal deglaciation threshold V_0 over the five 500 kyr periods for the four different summer insolation forcings at 65° N and optimal constant V_0 threshold obtained when the optimization procedure is done over the whole Quaternary (V_0^Q). When several values of the deglaciation threshold V_0 maximize the accuracy criteria, the mean value is plotted and the other possible values are represented with error bars.

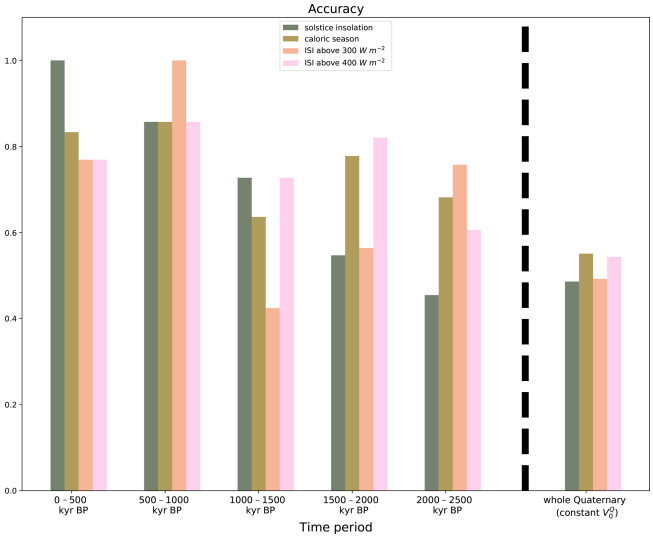

Figure 3. Accuracy over the five 500 kyr periods for the four different summer insolation forcings at 65° N, and accuracy criteria over the Quaternary when the optimization procedure is done over the whole Quaternary (constant V_0^Q).

middle of the highest values that best fit the latter part of the record and the lowest values that best fit the earliest part of the record.

For each insolation, the accuracy corresponding to the optimal V_0 threshold for each time period as well as to the fixed V_0^Q value maximizing the accuracy over the whole Quaternary is displayed in Fig. 3.

It is first noticeable that the accuracy is higher over the last 1 million-year period, regardless the input summer insolation used. In the last 1 million years, the summer solstice insolation as input produces the best results. However, this is no longer the case for older time periods: the solstice insolation gives the worst results at the start of the Quaternary. The accuracy obtained for the whole Quaternary period (fixed V_0^Q value) is globally lower than the accuracy for each time period. This is due to the fact that the V_0^Q values obtained are lower than the optimal V_0 values in the later part of the Quaternary and higher than the optimal V_0 values in the earliest part of the Quaternary, leading to a poorer representation of both of these periods.

In the earlier part of the Quaternary (periods earlier than 1.5 Ma), the results are less robust. This is due to increased uncertainties in the LR04 record, and the associated definition of interglacial periods, which affects our accuracy criteria. In their classification, Tzedakis et al. (2017) stated that the definition of the valley depth needed to separate several interglacials was quite straightforward in the earlier part of the record, whereas for earlier time periods (ages older than 1.5 Ma), their method led to several "borderline cases". Additionally, slightly different choices for the interglacial and interstadial thresholds would have led to a different population of interglacial. For us, this would lead to a different definition of deglaciation, and thus a different accuracy criteria. In addition, the resolution of the LR04 curve decreases with increasing age (Lisiecki and Raymo, 2005), and for periods with lower resolution or more uncertain age matching, the amplitude of the peaks might be reduced (Tzedakis et al., 2017).

Moreover, the δ^{18}O LR04 curve includes at the same time an ice volume and deep water temperature component. Ice volume and sea level reconstructions do exist (Bintanja et al., 2005; Spratt and Lisiecki, 2016), but are however limited to the more recent part of the Quaternary and do not allow for the investigation of the pre-MPT period. The use of δ^{18}O as an ice volume proxy has already been largely debated (Shackleton, 1967; Chappell and Shackleton, 1986; Shackleton and Opdyke, 1973; Clark et al., 2006), and recent studies (Elderfield et al., 2012) have shown that the temperature component may be as large as 50 %. Furthermore, the stack was tuned to insolation (Lisiecki and Raymo, 2005). We refer the reader to Raymo et al. (2018) for a review of possible biases in the interpretation of the LR04 benthic δ^{18}O stack as an ice volume and sea level reconstruction. All these reasons encourage us to remain at a qualitative level to fit the data.

The increase in the optimal deglaciation threshold V_0 over the MPT is however a robust feature that does not depend on the input summer insolation forcing used. This is coherent with the work of Paillard (1998) and Tzedakis et al. (2017),

who obtained a frequency shift from 41 to 100 kyr cycles with an increasing deglaciation threshold. The classical hypothesis and possible physical meanings of the rise of the V_0 threshold often imply a gradual cooling, due to lower pCO_2 (Raymo, 1997; Paillard, 1998; Berger, 1978), but this idea is not supported by more recent data, which do not show a gradual decrease in the pCO_2 trend, but rather only a decrease in minimal pCO_2 values (Hönisch et al., 2009; Yan et al., 2019). Other hypothesis imply a gradual erosion of a thick regolith layer that exposed the ice sheet to a higher friction bedrock, allowing for a thicker ice sheet to develop (Clark and Pollard, 1998; Clark et al., 2006), or a sea ice switching mechanism (Gildor and Tziperman, 2000).

The overall lowest accuracy in the older part of the record suggests that our non-linear threshold model is less adapted for this time period. Indeed, the ice volume might respond more linearly to the insolation forcing before the MPT, as some studies suggest (Tziperman and Gildor, 2003; Raymo and Nisancioglu, 2003). In contrast, others (Ashkenazy and Tziperman, 2004) have shown that the 41 kyr pre-MPT oscillations are in fact significantly asymmetric and therefore suggested that oscillations both before and after the MPT could be explained as the self-sustained variability of the climate system, phase locked to the astronomical forcing. In our model, the deglaciation threshold V_0 changes over time, leading to an amplitude change of the cycles. However, it cannot be excluded that the mechanisms behind the pre- and post-MPT glacial cycles are structurally different, and that they cannot be explained with the same physics and the same equations in our model. Moreover, this kind of conceptual model has mainly been constructed in order to explain the non-linear features of the 100 kyr cycles, and it is therefore not surprising that its agreement with the data on the pre-MPT period is less satisfying.

3.2 Best fit over the Quaternary

Our conceptual model is able to reproduce qualitatively well the data (LR04 normalized curve) over the whole Quaternary. The model's best fit over the Quaternary for each insolation forcing, as defined in Sect. 2.3, is displayed in Fig. 4. It is able to reproduce the frequency shift from a dominant 41 kyr period before 1 Ma to longer cycles afterwards, as observed in the data, and thus by varying only one parameter during the whole simulation length: the deglaciation threshold V_0. Like the previous model of Parrenin and Paillard (2003), from which our model is adapted, ours quickly looses its sensitivity to the initial conditions (after no more than 200 kyr). For every input forcing, longer cycles are obtained in the last part of the Quaternary (last Myr). Figure 4 displays the results over the whole Quaternary with the V_0 threshold being set to its optimal value for each 500 kyr period, while Fig. 5 displays the results over the last 1 million years with the V_0 threshold being set to its optimal value for the [0–1000] ka period.

For the last 1 million years, it is possible to reproduce all terminations with the right timing, apart from the last deglaciation, for all insolation forcings, by using a single value of the V_0 threshold over this period. Some differences are however noticeable between the different forcings. In particular the agreement for the ISI above 300 W m^{-2} forcing is not as good as for the other forcings: termination V (around 420 ka) is triggered later compared to in the data, while termination III (around 240 ka) is triggered too early. For the ISI above 300 W m^{-2} forcing, the range of V_0 values that allow us to correctly reproduce most of the terminations during the last 1 million years is reduced (only values of $V_0 = 3.9$–4.0), whereas the results are more robust for the three other insolation forcings, with a broader range of working V_0 values. The ISI above 300 W m^{-2} forcing has a low precession component, which explains why it is less successful in reproducing the data over the last 1 million years. Experiments with our model setup have shown that a summer forcing with no precession component could not successfully reproduce the data over the post-MPT period as accurately as the four forcings presented here that contain both precession and obliquity (see Sect. S3).

Despite the accurate timing of terminations, the spectral analysis of the model results over the last 1 million years differs from the spectral analysis of the data. For all forcings except the summer solstice insolation, obliquity continues to dominate after the MPT. The spectral analysis shows secondary and third peaks of lower frequency, but does not show a sharp 100 kyr cyclicity as in the LR04 record. Compared to the data, all the model outputs over the post-MPT period have a more pronounced obliquity and precession component and a less pronounced 100 kyr component. This feature is most probably due to the model formulation, and more specifically the direct dependence of ice volume evolution to insolation via the $\mathrm{d}V/\mathrm{d}t = -I/\tau_\mathrm{i}$ term. This is one of the limits of our conceptual model. While the criteria on the switch to deglaciations allow us to reproduce the deglaciations at the right timing, the direct dependance of ice volume change to the insolation forcing is definitely too simplistic and probably produces an overestimated dependency of the ice evolution to the astronomical forcing for the latter part of the record.

In the first part of the Quaternary (2.6 to 1 Ma), the spectral analysis of the data is dominated by a 41 kyr (obliquity) peak. It is also the case for the model results, for each type of insolation. However, the model outputs also show a precession component (19 to 23 kyr), especially for the summer solstice and the ISI above 400 W m^{-2} forcings, which does not exist on the data. Although our model reproduces the features of the record qualitatively well, there are some noticeable model–data mismatches that occur for all insolation types around 1100 and 2030 ka. Additionally, the amplitude of the oscillations produced is slightly too high in the older part of the Quaternary, especially when the ISI above 300 W m^{-2} is used.

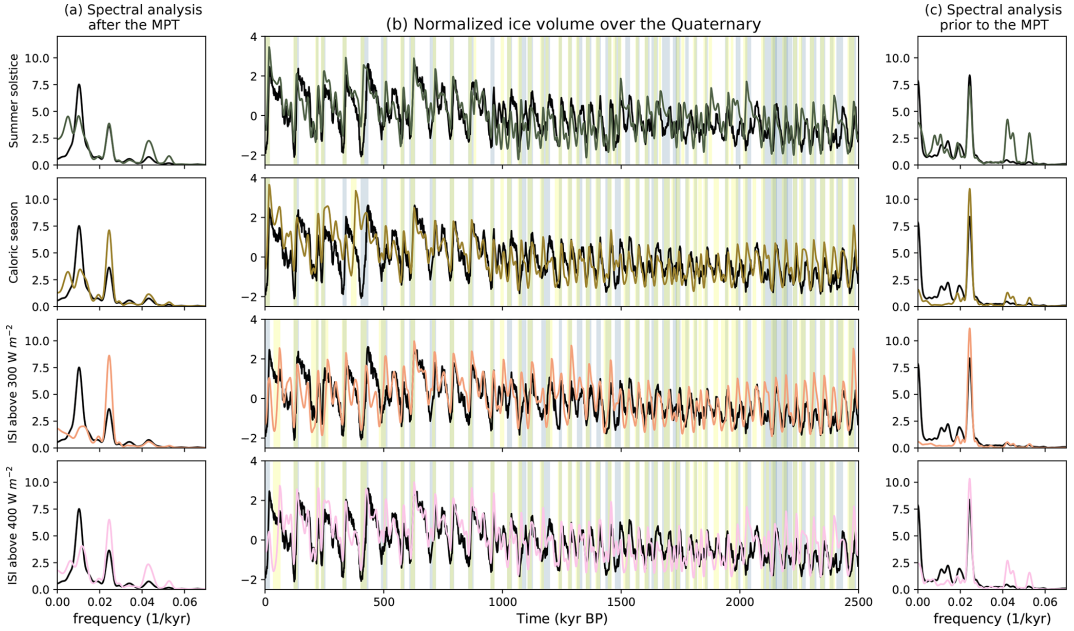

Figure 4. Best model fit over the whole Quaternary and corresponding spectral analysis. **(b)** presents the best fit of the model for the different summer insolation used as input, compared to the data. The results for the summer solstice insolation, caloric season, ISI above 300 and ISI above 400 W m^{-2} are displayed. The data (normalized LR04 curve) are in black. The blue shading presents deglaciation periods in the data and the yellow shading deglaciation periods in the model. This results in a green shading when deglaciations are seen in the model and data at the same time. **(a)** presents the spectral analysis of the best fit solution over the last 1 million years. **(c)** presents the spectral analysis over the older part of the Quaternary (before 1 Ma).

On the oldest part of the Quaternary, the caloric season forcing and the ISI above 300 W m^{-2} seem to perform better in reproducing the frequency of the oscillations than the summer solstice insolation and ISI above 400 W m^{-2}. They correspond to the forcing with the strongest obliquity (41 kyr) component, which might explain why they more successfully represent this part of the record, which is dominated by obliquity.

Over the last 1 million years, the highest accuracy is obtained with the summer solstice insolation as input forcing ($c = 0.92$ for the summer solstice insolation, $c = 0.82$ for the caloric season and ISI above 400 W m^{-2} and $c = 0.87$ for the ISI above 300 W m^{-2}). This is mainly due to the fact that for the three other forcings (caloric season, ISI above 300 and ISI above 400 W m^{-2}), the last deglaciation occurs one insolation peak too early, around 50 ka. However, if one computes the accuracy over the last 1 million years excluding the last 100 kyr (period from 100 ka to 1000 ka), the accuracy is similar for all four forcings (0.92 for summer solstice, caloric season and ISI above 400 W m^{-2} and 0.89 for ISI above 300 W m^{-2}). Figure 5 displays two different alternatives. For the first one (full line), the optimal V_0 is calibrated over the [100–1000] ka period and maintained for the whole simulation ($V_0 = 5.0$ for the summer solstice insolation, 4.5 for the caloric season, 4.0 for the ISI above 300 W m^{-2} and 4.6 for the ISI above 400 W m^{-2}). Except with the summer solstice insolation as input, the three other insolation forcings fail to accurately reproduce the last deglaciation, as the last deglaciation occurs one insolation peak too early. The second alternative (dashed line) is to raise the deglaciation threshold V_0 over the last cycle (raised to $V_0 = 5.5$ from 100 ka onward). In this case, the model does accurately reproduce the last deglaciation for all insolation forcings. This suggests that we might need to further raise the V_0 threshold in order to model a theoretical "natural" future (without anthropogenic influence) with longer cycles. A cycle is not enough to conclude about a trend, but this should be envisaged for future natural scenarios. This is coherent with the idea of Paillard (1998), who used a linearly increasing deglaciation threshold over the Quaternary.

3.3 Reflections about the future

To model future natural evolutions of the climate system, possible evolutions of the V_0 threshold should be considered. However, we do not exclude the fact that variations of other parameters, which were kept constant in this study, could vary in the future. For instance, different I_0 thresholds have to be considered. The fate of the next thousands of years in a natural scenario cannot be ascertained with our conceptual model. Indeed, this depends on the onset (or not) of a glaciation, which is determined by the I_0 parameter. In our model, a broad range of I_0 parameter values lead to satisfying results over the last 1 million years. These different values pro-

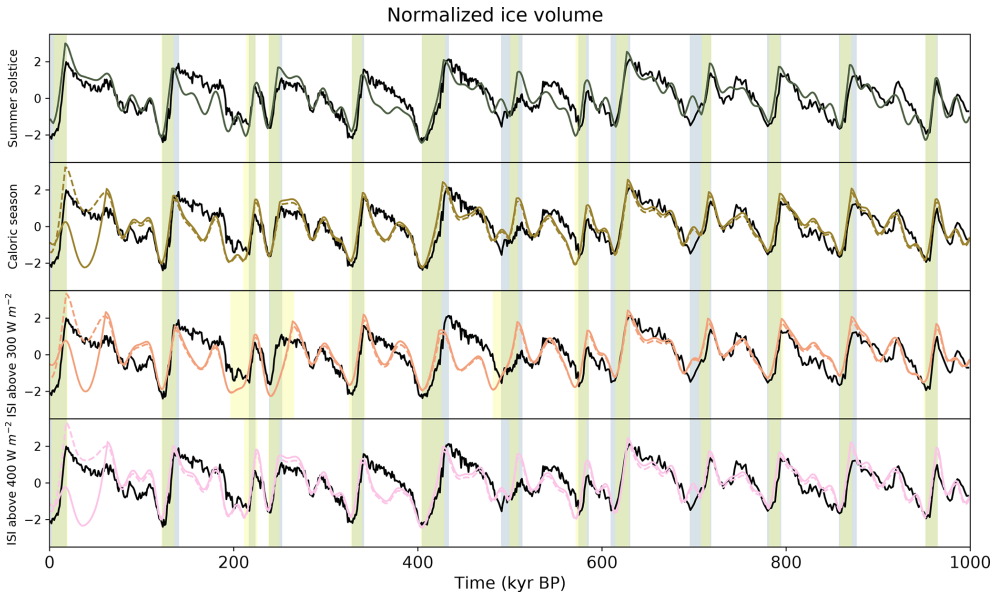

Figure 5. Normalized model results over the last 1 million years, with the different summer insolation forcings: insolation at the summer solstice, caloric season, ISI above 300 W m^{-2} and ISI above 400 W m^{-2}. The full coloured lines are the best fit computed over the 100–1000 ka period for each input insolation. The dashed lines represent the same solution, but with an increased V_0 threshold for the last deglaciation. The data (normalized LR04 stack curve) are in black. The blue shading represents deglaciation periods in the data. The yellow shading represents deglaciation periods in the model outputs (case of the increased V_0 threshold). This results in a green shading when deglaciations are seen in the model and data at the same time.

jected into the future lead either to, in one case, a glaciation start at present, or, in the other case, a continued deglaciation, switching to a glaciation state only around 50 kyr after present at the next insolation minima. This is due to the current particular astronomical configuration, with very low eccentricity, which leads to high summer insolation minima, where the threshold for glaciation might not be reached. This is coherent with previous studies (Berger and Loutre, 2002; Paillard, 2001), which suggested that without anthropogenic forcing, the present interglacial might have lasted 50 kyr.

However, this exercise is purely academic, as we are not taking into account the role of anthropogenic CO_2, which would affect the glaciation and deglaciation thresholds (Archer and Ganopolski, 2005; Talento and Ganopolski, 2021). Furthermore, our conceptual model cannot be extended outside the Quaternary, as the ice volume variations considered are exclusively those of the Northern Hemisphere, and our model is, by construction, unable to represent projected future Antarctic ice sheet mass loss.

4 Conclusions

We have used a conceptual model with very few tunable parameters that represents the climatic system with multiple equilibria and relaxation oscillation. Only one parameter was varied, the deglaciation threshold parameter V_0. We used different summer insolation as input for our conceptual model: the summer solstice insolation, the caloric season and ISI over two different thresholds. With all these forcings, which have different contributions from obliquity and precession, we are able to reproduce the features of the ice volume over the whole Quaternary. More specifically, we are able to represent the MPT and the switch from a 41 kyr dominated record to larger cycles by raising the deglaciation threshold and keeping the other model parameters constant. This rise in the deglaciation threshold is valid regardless of the type of summer insolation forcing used as input. However, the data agreement is less satisfying before the MPT. This suggests the possibility that climate mechanisms might be structurally different before and after the MPT, with a more linear behaviour in pre-MPT conditions. This highlights that models are designed to answer rather specific questions, and a model built specifically to explain 100 kyr cycles might be less efficient in a more linear setting. More generally, this kind of glacial–interglacial conceptual model is designed to explain the main features of the Quaternary time period characterized by the waning and waxing of Northern Hemisphere ice sheets under the influence of changing astronomical parameters. In our case, this raises the question of which physical phenomena are responsible for making deglaciations "harder" to start in the latest part of the Quaternary compared to the earliest part. This kind of model is however unlikely to be directly applicable in a more general context, like during the Pliocene and earlier periods, or in the context of future climates under the long-term persistence of anthropogenic CO_2 (Archer and Ganopolski, 2005; Talento and Ganopolski, 2021). In order

to tackle such questions, it would be critical to gain a deeper understanding of the natural evolution of the other forcings involved in the climate system and most notably of the dynamics of the carbon cycle. Conceptual models are likely to pave the way in this direction (Paillard, 2017). Indeed, just as in the case of the Quaternary, a full mechanistic simulation of the many processes at work is currently out of reach and modelling work can only be very exploratory. Here, we have shown that some robust features are required to explain Quaternary ice age cycles. Similar conceptual modelling on a wider temporal scope over the Cenozoic could help better explain the connections between astronomical forcing, the carbon cycle, ice sheets and the climate. This would help us imagine what the Anthropocene might be like.

Code and data availability. The model code, insolation input files, spectral analysis and code needed to reproduce the figures are available for download: https://doi.org/10.5281/zenodo.6045532 (Leloup, 2022).

Supplement. The supplement related to this article is available online at: https://doi.org/10.5194/cp-18-547-2022-supplement.

Author contributions. GL and DP designed the study. GL performed the simulations, and also wrote the manuscript under the supervision of DP.

Competing interests. The contact author has declared that neither they nor their co-author has any competing interests.

Disclaimer. Publisher's note: Copernicus Publications remains neutral with regard to jurisdictional claims in published maps and institutional affiliations.

Special issue statement. This article is part of the special issue "A century of Milankovic's theory of climate changes: achievements and challenges (NPG/CP inter-journal SI)". It is not associated with a conference.

Acknowledgements. We acknowledge the use of the LSCE storage and computing facilities. We also thank the reviewers for their helpful comments and suggestions.

Financial support. This research has been supported by ANDRA (contract no. 20080970).

Review statement. This paper was edited by Marie-France Loutre and reviewed by Mikhail Verbitsky, Andrey Ganopolski, and one anonymous referee.

References

Abe-Ouchi, A., Saito, F., Kawamura, K., Raymo, M., Okuno, J., Takahashi, K., and Blatter, H.: Insolation-driven 100,000-year glacial cycles and hysteresis of ice-sheet volume, Nature, 500, 190–193, https://doi.org/10.1038/nature12374, 2013.

Archer, D. and Ganopolski, A.: A movable trigger: Fossil fuel CO_2 and the onset of the next glaciation, Geochem. Geophy. Geosy., 6, Q05003, https://doi.org/10.1029/2004GC000891, 2005.

Ashkenazy, Y. and Tziperman, E.: Are the 41 kyr glacial oscillations a linear response to Milankovitch forcing?, Quaternary Sci. Rev., 23, 1879–1890, https://doi.org/10.1016/j.quascirev.2004.04.008, 2004.

Berger, A.: Long-term variations of daily insolation and Quaternary climatic changes, J. Atmos. Sci., 35, 2362–2367, 1978.

Berger, A.: Milankovitch, the father of paleoclimate modeling, Clim. Past, 17, 1727–1733, https://doi.org/10.5194/cp-17-1727-2021, 2021.

Berger, A. and Loutre, M.-F.: Insolation values for the climate of the last 10 million years, Quaternary Sci. Rev., 10, 297–317, https://doi.org/10.1016/0277-3791(91)90033-Q, 1991.

Berger, A. and Loutre, M.-F.: Climate: An Exceptionally Long Interglacial Ahead?, Science, 297, 1287–1288, https://doi.org/10.1126/science.1076120, 2002.

Bintanja, R., van de Wal, R., and Oerlemans, J.: Modelled atmospheric temperatures and global sea levels over the past million years, Nature, 437, 125–128, https://doi.org/10.1038/nature03975, 2005.

Bouttes, N., Paillard, D., Roche, D. M., Waelbroeck, C., Kageyama, M., Lourantou, A., Michel, E., and Bopp, L.: Impact of oceanic processes on the carbon cycle during the last termination, Clim. Past, 8, 149–170, https://doi.org/10.5194/cp-8-149-2012, 2012.

Calder, N.: Arithmetic of ice ages, Nature, 252, 216–218, https://doi.org/10.1038/252216a0, 1974.

Chappell, J. and Shackleton, N. J.: Oxygen isotopes and sea level, Nature, 324, 137–140, 1986.

Clark, P. and Pollard, D.: Origin of the Middle Pleistocene Transition by ice sheet erosion of regolith, Paleoceanography, 13, 1–9, https://doi.org/10.1029/97PA02660, 1998.

Clark, P., Archer, D., Pollard, D., Blum, J. D., Rial, J., Brovkin, V., Mix, A., Pisias, N., and Roy, M.: The middle Pleistocene transition: characteristics, mechanisms, and implications for long-term changes in atmospheric pCO_2, Quaternary Sci. Rev., 25, 3150–3184, https://doi.org/10.1016/j.quascirev.2006.07.008, 2006.

Croll, J.: XIII. On the physical cause of the change of climate during geological epochs, The London, Edinburgh, and Dublin Philosophical Magazine and Journal of Science, 28, 121–137, https://doi.org/10.1080/14786446408643733, 1864.

Elderfield, H., Ferretti, P., Greaves, M., Crowhurst, S., Mccave, I. N., Hodell, D., and Piotrowski, A. M.: Evolution of Ocean Temperature and Ice Volume Through the Mid-Pleistocene Climate Transition, Science, 337, 704–709, https://doi.org/10.1126/science.1221294, 2012.

Gallée, H., Van Yperselb, J. P., Fichefet, T., Marsiat, I., Tricot, C., and Berger, A.: Simulation of the last glacial cycle by a cou-

pled, sectorially averaged climate-ice sheet model: 2. Response to insolation and CO_2 variations, J. Geophys. Res.-Atmos., 97, 15713–15740, https://doi.org/10.1029/92JD01256, 1992.

Ganopolski, A. and Calov, R.: The role of orbital forcing, carbon dioxide and regolith in 100 kyr glacial cycles, Clim. Past, 7, 1415–1425, https://doi.org/10.5194/cp-7-1415-2011, 2011.

Gildor, H. and Tziperman, E.: Sea ice as the glacial cycles' Climate switch: role of seasonal and orbital forcing, Paleoceanography, 15, 605–615, https://doi.org/10.1029/1999PA000461, 2000.

Hays, J., Imbrie, J., and Shackleton, N. J.: Variations in the Earth's Orbit: Pacemaker of the Ice Ages, Science, 194, 1121–1132, https://doi.org/10.1126/science.194.4270.1121, 1976.

Hönisch, B., Hemming, N. G., Archer, D., Siddall, M., and McManus, J. F.: Atmospheric Carbon Dioxide Concentration Across the Mid-Pleistocene Transition, Science, 324, 1551–1554, https://doi.org/10.1126/science.1171477, 2009.

Huybers, P.: Early Pleistocene glacial cycles and the integrated summer insolation forcing, Science, 313, 508–511, https://doi.org/10.1126/science.1125249, 2006.

Huybers, P.: Combined obliquity and precession pacing of late Pleistocene deglaciations, Nature, 480, 229–232, https://doi.org/10.1038/nature10626, 2011.

Huybers, P. and Wunsch, C.: Obliquity pacing of the late Pleistocene glacial terminations, Nature, 434, 491–494, https://doi.org/10.1038/nature03401, 2005.

Imbrie, J. and Imbrie, J. Z.: Modeling the Climatic Response to Orbital Variations, Science, 207, 943–953, https://doi.org/10.1126/science.207.4434.943, 1980.

Imbrie, J. Z., Imbrie-Moore, A., and Lisiecki, L. E.: A phase-space model for Pleistocene ice volume, Earth Planet. Sci. Lett., 307, 94–102, 2011.

Jakob, K. A., Wilson, P. A., Pross, J., Ezard, T. H. G., Fiebig, J., Repschläger, J., and Friedrich, O.: A new sea-level record for the Neogene/Quaternary boundary reveals transition to a more stable East Antarctic Ice Sheet, P. Natl. Acad. Sci. USA, 117, 30980–30987, https://doi.org/10.1073/pnas.2004209117, 2020.

Jouzel, J., Masson-Delmotte, V., Cattani, O., Dreyfus, G., Falourd, S., Hoffmann, G., Minster, B., Nouet, J., Barnola, J., Chappellaz, J., Fischer, H., Gallet, J.-C., Johnsen, S., Leuenberger, M., Loulergue, L., Lüthi, D., Oerter, H., Parrenin, F., Raisbeck, G., and Wolff, E.: Orbital and Millennial Antarctic Climate Variability over the Past 800,000 Years, Science, 317, 793–796, https://doi.org/10.1126/science.1141038, 2007.

Khodri, M., Leclainche, Y., Ramstein, G., Braconnot, P., Marti, O., and Cortijo, E.: Simulating the amplification of orbital forcing by ocean feedbacks in the last glaciation, Nature, 410, 570–574, 2001.

Lambeck, K., Rouby, H., Purcell, A., Sun, Y., and Sambridge, M.: Sea level and global ice volumes from the Last Glacial Maximum to the Holocene, P. Natl. Acad. Sci. USA, 111, 15296–15303, https://doi.org/10.1073/pnas.1411762111, 2014.

Laskar, J., Robutel, P., Joutel, F., Gastineau, M., Correia, A., and Levrard, B.: A long-term numerical solution for the insolation quantities of the Earth, Astron. Astrophys., 428, 261–285, 2004.

Leloup, G.: Data and code for results and figures in Climate of the Past "Influence of the choice of insolation forcing on the results of a conceptual glacial cycle model", Zenodo [code and data set], https://doi.org/10.5281/zenodo.6045532, 2022

Lisiecki, L. E.: Links between eccentricity forcing and the 100,000-year glacial cycle, Nat. Geosci., 3, 349–352, https://doi.org/10.1038/ngeo828, 2010.

Lisiecki, L. E. and Raymo, M. E.: A Pliocene-Pleistocene stack of 57 globally distributed benthic $\delta^{18}O$ records, Paleoceanography, 20, PA1003, 2005.

Liu, Z., Cleaveland, L., and Herbert, T.: Early onset and origin of 100-kyr cycles in Pleistocene tropical SST records, Earth Planet. Sci. Lett., 265, 703–715, https://doi.org/10.1016/j.epsl.2007.11.016, 2008.

MacAyeal, D. R.: Irregular oscillations of the West Antarctic ice sheet, Nature, 359, 29–32, https://doi.org/10.1038/359029a0, 1992.

Marshall, S. J. and Clark, P. U.: Basal temperature evolution of North American ice sheets and implications for the 100-kyr cycle, Geophys. Res. Lett., 29, 67-1–67-4, https://doi.org/10.1029/2002GL015192, 2002.

Milankovitch, M.: Kanon der Erdbestrahlung und seine Anwendung auf das Eiszeitenproblem, Royal Serbian Academy Special Publication, 133, 1–633, 1941.

Oerlemans, J.: Model experiments on the 100,000-yr glacial cycle, Nature, 287, 430–432, https://doi.org/10.1038/287430a0, 1980.

Paillard, D.: The timing of Pleistocene glaciations from a simple multiple-state climate model, Nature, 391, 378–381, https://doi.org/10.1038/34891, 1998.

Paillard, D.: Glacial cycles: toward a new paradigm, Rev. Geophys., 39, 325–346, https://doi.org/10.1029/2000RG000091, 2001.

Paillard, D.: Quaternary glaciations: from observations to theories, Quaternary Sci. Rev., 107, 11–24, https://doi.org/10.1016/j.quascirev.2014.10.002, 2015.

Paillard, D.: The Plio-Pleistocene climatic evolution as a consequence of orbital forcing on the carbon cycle, Clim. Past, 13, 1259–1267, https://doi.org/10.5194/cp-13-1259-2017, 2017.

Paillard, D. and Parrenin, F.: The Antarctic ice sheet and the triggering of deglaciations, Earth Planet. Sci. Lett, 227, 263–271, https://doi.org/10.1016/j.epsl.2004.08.023, 2004.

Paillard, D., Labeyrie, L., and Yiou, P.: Macintosh Program performs time-series analysis, Eos Transactions, AGU, 77, 379–379, https://doi.org/10.1029/96EO00259, 1996.

Parrenin, F. and Paillard, D.: Amplitude and phase of glacial cycles from a conceptual model, Earth Planet. Sci. Lett., 214, 243–250, https://doi.org/10.1016/S0012-821X(03)00363-7, 2003.

Parrenin, F. and Paillard, D.: Terminations VI and VIII ($\sim$ 530 and $\sim$ 720 kyr BP) tell us the importance of obliquity and precession in the triggering of deglaciations, Clim. Past, 8, 2031–2037, https://doi.org/10.5194/cp-8-2031-2012, 2012.

Peltier, W. R. and Marshall, S.: Coupled energy-balance/ice-sheet model simulations of the glacial cycle: A possible connection between terminations and terrigenous dust, J. Geophys. Res.-Atmos., 100, 14269–14289, https://doi.org/10.1029/95JD00015, 1995.

Pollard, D.: A simple ice sheet model yields realistic 100 kyr glacial cycles, Nature, 296, 334–338, https://doi.org/10.1038/296334a0, 1982.

Raymo, M.: The timing of major climate terminations, Paleoceanography, 12, 577–585, https://doi.org/10.1029/97PA01169, 1997.

Raymo, M. E. and Nisancioglu, K. H.: The 41 kyr world: Milankovitch's other unsolved mystery, Paleoceanography, 18, 1011, https://doi.org/10.1029/2002PA000791, 2003.

Raymo, M. E., Kozdon, R., David, E., Lisiecki, L., and Ford, H. L.: The accuracy of mid-Pliocene δ^{18}O-based ice volume and sea level reconstructions, Earth-Sci. Rev., 177, 291–302, https://doi.org/10.1016/j.earscirev.2017.11.022, 2018.

Reeh, N.: Parameterization of Melt Rate and Surface Temperature on the Greenland Ice Sheet, Polarforschung, 59, 113–128, 1991.

Robinson, A., Calov, R., and Ganopolski, A.: An efficient regional energy-moisture balance model for simulation of the Greenland Ice Sheet response to climate change, The Cryosphere, 4, 129–144, https://doi.org/10.5194/tc-4-129-2010, 2010.

Saltzman, B. and Sutera, A.: The Mid-Quaternary Climatic Transition as the Free Response of a Three-Variable Dynamical Model, J. Atmos. Sci., 44, 236–241, https://doi.org/10.1175/1520-0469(1987)044<0236:TMQCTA>2.0.CO;2, 1987.

Saltzman, B., Hansen, A., and Maasch, K.: The Late Quaternary Glaciations as the Response of a Three-Component Feedback System to Earth-Orbital Forcing, J. Atmos. Sci., 41, 3380–3389, https://doi.org/10.1175/1520-0469(1984)041<3380:TLQGAT>2.0.CO;2, 1984.

Shackleton, N.: Oxygen Isotope Analyses and Pleistocene Temperatures Re-assessed, Nature, 215, 15–17, https://doi.org/10.1038/215015a0, 1967.

Shackleton, N. J. and Opdyke, N. D.: Oxygen isotope and palaeomagnetic stratigraphy of Equatorial Pacific core V28-238: Oxygen isotope temperatures and ice volumes on a 105 year and 106 year scale, Quaternary Res., 3, 39–55, https://doi.org/10.1016/0033-5894(73)90052-5, 1973.

Spratt, R. M. and Lisiecki, L. E.: A Late Pleistocene sea level stack, Clim. Past, 12, 1079–1092, https://doi.org/10.5194/cp-12-1079-2016, 2016.

Talento, S. and Ganopolski, A.: Reduced-complexity model for the impact of anthropogenic CO_2 emissions on future glacial cycles, Earth Syst. Dynam., 12, 1275–1293, https://doi.org/10.5194/esd-12-1275-2021, 2021.

Toggweiler, J. R.: Origin of the 100,000-year timescale in Antarctic temperatures and atmospheric CO_2, Paleoceanography, 23, PA2211, https://doi.org/10.1029/2006PA001405, 2008.

Tzedakis, P., Crucifix, M., Mitsui, T., and Wolff, E. W.: A simple rule to determine which insolation cycles lead to interglacials, Nature, 542, 427–432, https://doi.org/10.1038/nature21364, 2017.

Tziperman, E. and Gildor, H.: On the mid-Pleistocene transition to 100-kyr glacial cycles and the asymmetry between glaciation and deglaciation times, Paleoceanography, 18, 1-1–1-8, https://doi.org/10.1029/2001pa000627, 2003.

Tziperman, E., Raymo, M. E., Huybers, P., and Wunsch, C.: Consequences of pacing the Pleistocene 100 kyr ice ages by nonlinear phase locking to Milankovitch forcing, Paleoceanography, 21, PA4206, https://doi.org/10.1029/2005PA001241, 2006.

Van den Berg, J., van de Wal, R., and Oerlemans, H.: A mass balance model for the Eurasian Ice Sheet for the last 120,000 years, Global Planet. Change, 61, 194–208, https://doi.org/10.1016/j.gloplacha.2007.08.015, 2008.

Verbitsky, M. Y., Crucifix, M., and Volobuev, D. M.: A theory of Pleistocene glacial rhythmicity, Earth Syst. Dynam., 9, 1025–1043, https://doi.org/10.5194/esd-9-1025-2018, 2018.

Yan, Y., Bender, M. L., Brook, E. J., Clifford, H. M., Kemeny, P. C., Kurbatov, A. V., Mackay, S., Mayewski, P. A., Ng, J., Severinghaus, J. P., and Higgins, J. A.: Two-million-year-old snapshots of atmospheric gases from Antarctic ice, Nature, 574, 663–666, https://doi.org/10.1038/s41586-019-1692-3, 2019.

In the article, we have used a conceptual model with few tunable parameters to represent the ice volume evolution over the Quaternary. The glaciation threshold I_0, as well as the different time constants (τ_i, τ_d,τ_g) are kept fixed and the deglaciation threshold V_0 is the only parameter being varied in our study. We used different summer insolation, at 65°N, as input : the summer solstice insolation, the caloric season and the integrated summer insolation above two different thresholds : 300 and 400 $W \cdot m^{-2}$. We have shown that our model is able to represent the main features of the Quaternary ice volume record. We are able to represent the evolution from 41 kyr cycles before the MPT to longer cycles afterwards by raising the deglaciation threshold V_0 over time, while the other model parameters are kept fixed. This is valid for each of the four insolation types studied. The 100 kyr cycles observed over the last million year are more easily reproduced with the summer solstice insolation, that has a stronger precession component, while the 41 kyr cycles found prior to the MPT are better reproduced with insolations having a stronger obliquity component, such as the caloric season. For three out of the four summer insolation used (all except the summer solstice insolation), it is not possible to represent the last million year with the same deglaciation threshold V_0. This threshold needs to increase over the last cycle to correctly represent the longer last cycle.

2.3 . What can be said about ice volume evolution over the next million years in a natural case with a conceptual model

In this part, we use the model developed previously and run it over the next million years. This represents the case of a natural scenario and we do not take into account the influence of anthropogenic CO_2 emissions.

In the article, we have shown that it is possible to find values of the deglaciation threshold V_0 allowing to reproduce the ice volume evolution over the Quaternary for the four insolation types considered. For three out of the four summer insolation types used, the deglaciation threshold needs to increase again over the last glacial cycle in order to fit the data. Therefore, we present here 4 scenarios, one for each insolation type studied, with an increased deglaciation threshold over the last cycle. The simulation started at 1 Myr BP. For each insolation, the deglaciation threshold that best reproduces the data over the last million year is used until 100 kyr BP. It varies between 4.0 and 5.0 depending on the insolation type. After 100 kyr BP, the deglaciation threshold is raised at 5.5 for each insolation type, and this value is kept constant for the whole interval [100 kyr BP, 1 Myr AP]. The results are presented on Figure 2.4. They correspond to the dashed lines of Figure 5 of Leloup and Paillard [2022], extended over the next million years.

The model results with the four different insolation share a similar feature until around 350 kyr AP. After this time, the timing of the deglaciation differs depending on the input forcing used. This experiment shows that only by changing the

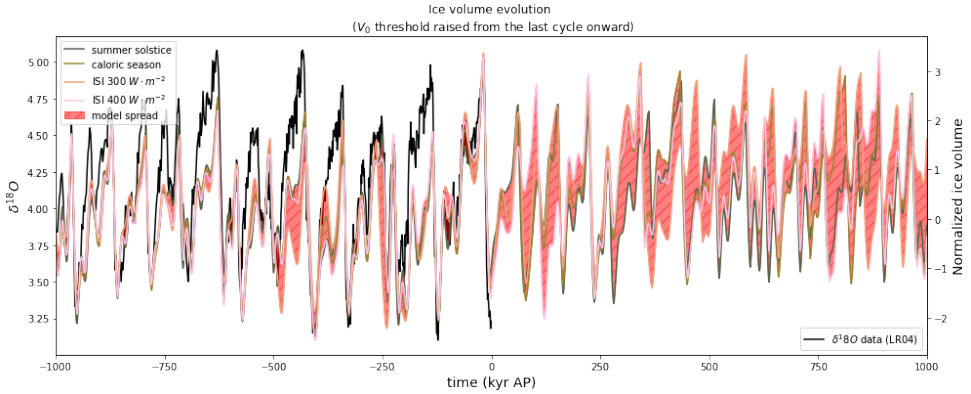

Figure 2.4: Ice volume evolution computed with our model from 1 Myr BP to 1 Myr AP, with the four different insolation types. The deglaciation threshold V_0 is raised from 100 kyr BP from (the last glacial cycle) onward. Model results with the summer solstice insolation, caloric season, ISI above 300 W^{-2} and ISI above 400 W^{-2} are respectively in green, brown, orange and pink. The $\delta^{18}O$ data (Lisiecki and Raymo [2005] curve) is in black.

definition of the summer solstice insolation, very different results can be obtained after 400 kyr AP. This shows one of the limits of this kind of conceptual model, with threshold behaviour. It is sensitive to the insolation forcing used : at a specific time the threshold might be crossed or not for a slight change in the definition of the insolation forcing, leading to very different behaviour.

In the previous experiments, we have kept all parameters fixed to the value used in Leloup and Paillard [2022]. In Leloup and Paillard [2022], the glaciation threshold, the insolation threshold for which the model enters the glaciation state, was fixed to a constant value of $I_0 = 0$. We have not considered other I_0 threshold values, nor the possibility of a trend in the I_0 threshold. This choice was made in order to focus rather on the deglaciation threshold V_0. Here, as an example, we focus on the case of the summer solstice insolation forcing in order to study the influence on the model results of the use of another glaciation threshold I_0. The model is run on the last and next million years for the summer solstice insolation forcing with two different glaciation threshold : $I_0 = 0$ like in the article, and a lower insolation threshold, I_0 = -0.8. In these runs, the deglaciation threshold is set to 4.5 before 100 kyr BP and raised to 5 after. The results are displayed in Figure 2.5.

For the two glaciation thresholds, the model behaviour is very similar over the past million year. However, results on the next million years differ, especially in the next 50 kyr, and around 400 kyr and 800 kyr AP, corresponding to periods of eccentricity minima. In the next 50 kyr, the model either simulates a glaciation for $I_0 = 0$ or a long interglacial for $I_0 = -0.8$. This very different behaviour

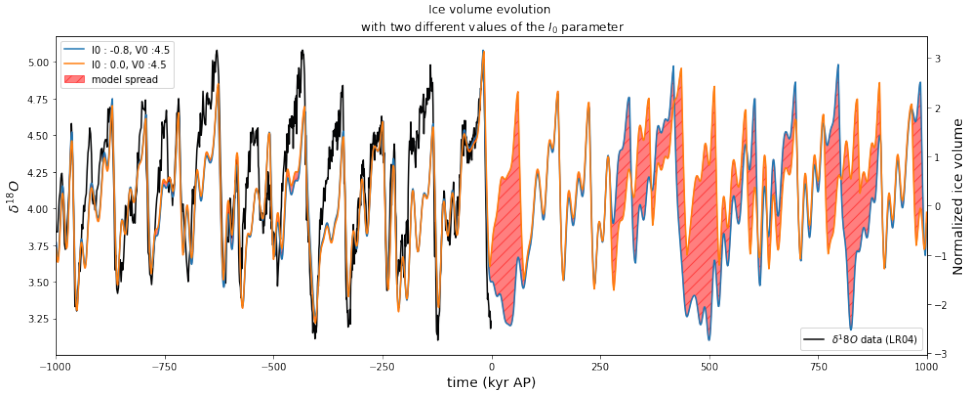

Figure 2.5: Ice volume evolution for two different glaciation thresholds (I_0 = 0 in orange and I_0 = -0.8 in blue) over the last Myr, and extended over the next Myr, with the summer solstice insolation as input. The red shading represents the spread between the model results for the different glaciation thresholds.

between these two glaciation thresholds in the next 100 kyr is not surprising and is due to the low eccentricity of the Earth, and the corresponding low variation of summer insolation, especially in the case of the summer solstice insolation. If the insolation threshold is "missed" at present, then it takes a long time before reaching again a value of insolation that is low enough to start a glaciation state. These widely different behaviour of the ice volume evolution over the next 100 kyr, depending on the glaciation threshold, is in accordance with the work of previous authors For instance, Paillard [2001] used a similar conceptual model for the ice age evolution (the Paillard [1998] model). He also obtained two widely different behaviours over the next glacial cycle, depending on the glaciation threshold used. Similarly to our result, a glaciation at present is obtained in the case of a higher glaciation threshold, while a lower glaciation threshold leads to a particularly long interglacial. In this case also, the use of different glaciation thresholds does not change the results obtained over the past million year, with almost identical ice volume evolution in both cases.

Additionally, it is most likely that the I_0 threshold is not constant over time. Indeed, the insolation needed to reach a glacial inception varies with other factors, such as the CO_2 [Ganopolski et al., 2016]. The insolation threshold decreases with increased CO_2 levels : if the CO_2 levels are higher, then the insolation must be even lower to reach the conditions for a glaciation, which corresponds to a lower insolation threshold value. This possibility is not accounted for in our model, where the I_0 threshold was set to a constant value. However, other studies have investigated this effect with ice sheets models and climate models of intermediate complexity. For instance, Berger and Loutre [2002] have used the LLN 2-D model, a sectorially averaged latitude-latitude model including northern hemisphere ice

sheets over the next hundred thousand years. The model was forced with different CO_2 levels and a "natural" CO_2 scenario (obtained from the CO_2 evolution in the past, shifted to correspond to current CO_2 levels). The results obtained on the next 100 kyr differ widely depending on the CO_2 level, with either a glaciation start at present for CO_2 levels around 250 ppm and no glacial inception at all in the next 130 kyr in the case of levels around 290 ppm. For the case of a natural CO_2 scenario, the current interglacial is exceptionally long. Very similar results have been obtained by Cochelin et al. [2006]. They used the green MPM EMIC, containing interactive vegetation and ice sheet with different CO_2 levels, over the next thousand hundred years. They have shown that the next glacial inception depends on the CO_2 concentration, with an imminent glaciation at present in the case of low CO_2 (lower than 270 ppm) or an inception in 50 kyr in the case of CO_2 levels around 280-290 ppm. No glacial inception is obtained over the next 100 kyr in the case of CO_2 levels higher than 300 ppm. Ganopolski et al. [2016] used the CLIMBER-2 model, including the SICOPOLIS ice sheet model to obtain four different versions of the model, being coherent with paleodata. The model was forced with insolation and CO_2 data and the versions producing a glaciation at MIS 19 and 11, and no glaciation at the Holocene were selected. With these model versions, it was shown that if the CO_2 levels of the Holocene had been lower (240 ppm instead of 280 ppm), this would have led to a glaciation at present. However, as the threshold for glaciation has been narrowly missed at present, the next glaciation is only expected to occur at the next favorable orbital configuration, in 50 kyr AP. Therefore, with the current orbital configuration, a relatively small change in the CO_2 level can have a strong impact, as it will correspond to crossing or not the threshold.

In this section, we have developed a conceptual model that is able to correctly reproduce ice volume evolution over the past. However, simulations on the next million years highlight the model sensitivity to several parameters. More specifically, the choice of the summer insolation definition used as input to the model leads to different results over the next million years. The results are also sensitive to the glaciation and deglaciation thresholds. Conceptual models are very computer efficient and are very useful to investigate past changes. Due to their computing efficiency, this kind of conceptual models are currently widely used in studies on timecales of the next million years such as in the BIOCLIM project and more recently in Lord et al. [2019], Williams et al. [2022]. However, due to their sensitivity to model parameters, several experiments should be carried out, and one cannot rely on a single model realization. Another downside of the use of conceptual model on the future is the underlying assumption that the governing processes on the next million years remain the same as in the past. However, anthropogenic forcing will likely modify these processes. For instance, the Greenland ice sheet exhibits hysteresis behaviour [Robinson et al., 2012] and its complete melting that is expected under moderate to high emissions scenarios or warming [Van Breedam

et al., 2020, Clark et al., 2016, Gregory et al., 2020] could impact the sequence of glacial interglacial cycles. But most importantly, conceptual models of ice volume evolution based on the Northern Hemisphere ice volume evolution (such as used in BIOCLIM, Archer and Ganopolski [2005], Lord et al. [2019], Talento and Ganopolski [2021], Williams et al. [2022]) are structurally not designed to model melting of the Antarctic ice sheet. However, modelling studies have shown that a substantial loss of the Antarctic ice sheet can be expected on a multi millenial timescales if emissions continue unabated [Winkelmann et al., 2015, Van Breedam et al., 2020]. In the following, we therefore focus on the possibility of a melting of the Antarctic ice sheet, and its reversibility by investigating the ice sheets behaviour under different CO_2 levels, when starting from a configuration where ice is present and a configuration where no ice is present. The methodology is described in the next chapter, Chapter 3, and the results are described in Chapter 4.

3 - Setup of the coupled iLOVECLIM-GRISLI model

Chapter aims:

1. Present the models used in this study : the climate model of intermediate complexity iLOVECLIM, and the ice sheet model GRISLI (used for Antarctica).
2. Develop a reference configuration, for which the Antarctic ice sheet obtained with the coupled iLOVECLIM-GRISLI model is in equilibrium at pre-industrial CO_2 levels ans insolation, and close to the observations.

Highlights:

↪ The low computation time of the iLOVECLIM and GRISLI model allows to perform several coupled simulations to calibrate the coupled iLOVECLIM-GRISLI model.

↪ The reference ice sheet obtained for pre-industrial CO_2 levels and insolation, with the coupled iLOVECLIM-GRISLI Antarctica setting is in equilibrium. It has a satisfactory geometry and velocity pattern.

In this study, we would like to investigate the behaviour of the Antarctic ice sheet under different CO_2 levels, while taking into account the different feedbacks between ice sheet and climate. To do so, the climate response to different CO_2 levels is modelled using the climate model of intermediate complexity iLOVECLIM, that represents the ocean, atmosphere, and vegetation. The Antarctic ice sheet is modelled with the GRISLI ice sheet model. The interactions between ice sheet and climate are taken into account by coupling the two models : climate changes impact ice sheet geometry, and in turn ice sheet geometry changes impact climate. This chapter presents the two models used, iLOVECLIM and GRISLI and details the coupling setup between the two models. The results will be presented in the next chapter, Chapter 4. It is the first time that the iLOVECLIM model and the Antarctic component of the GRISLI model are coupled. Therefore, calibrations were needed in order to obtain a satisfactory reference ice sheet with the coupled iLOVECLIM-GRISLI setting under pre-industrial CO_2 levels, ie an ice sheet that resembles the observations and is in equilibrium. The modifications performed and the reference ice sheet obtained are detailed in this Chapter.

3.1 . The climate model of intermediate complexity iLOVECLIM

General description

The iLOVECLIM model is a three dimensional Earth system Model of Intermediate Complexity (EMIC). Although there is a wide variety of EMICs [Claussen et al., 2002], a common feature of EMICs compared to General Circulation Model (GCM) is their coarser spatial resolution, and the parametrization of some processes that are explicitely modelled in GCMs. This results in a much lower computational time than GCMs, and therefore permits the integration of additional components of the Earth System into the model, and / or the achievement of longer simulations. EMICs are particularly useful tools for studying feedbacks between different components of the Earth System on long timescales. On the contrary, EMICs are not suitable for the study of small scale processes requiring high spatial resolution [Claussen et al., 2002]. In this study, EMIC is the designated tool as multi-millenial simulations are needed, in order to reach the equilibrium with the ice sheet.

The iLOVECLIM model originates from the LOVECLIM model, described in Goosse et al. [2010]. The LOVECLIM model is composed of an atmospheric component (ECBILT), a ocean and sea ice component (CLIO), a vegetation component (VECODE), a carbon and biogeochemical cycles component (LOCH) and an ice sheet component (AGISM). Compared to the LOVECLIM model, several modifications have been performed in the iLOVECLIM model, notably by the implementation of water isotopes in the model [Roche, 2013, Roche and Caley, 2013], a new ocean carbon cycle model [Bouttes et al., 2015], a permafrost module [Kitover et al., 2019], an iceberg module [Bügelmayer et al., 2015], the addition of optional more complex vegetation module (CARAIB), that can optionally replace VECODE [Extier, 2019]. However, the atmospheric (ECBILT), ocean and sea ice (CLIO), and vegetation component (VECODE) that we will use here remain similar to the version described in Goosse et al. [2010]. In this study, the carbon cycle was not activated. Indeed, we have chosen to focus on the evolution of the climate system (and notably, ice sheet evolution) in the case of different, prescribed CO_2 levels. In our simulations, we impose a constant CO_2 concentration throughout the simulation, and do not look at its influence on the carbon distribution between the different reservoirs. Our focus being mainly the interactions with the atmosphere, ocean and ice sheet, we have kept the simplest version of the vegetation module, VECODE.

A major difference between the LOVECLIM and iLOVECLIM model relevant to our study is the difference in the ice sheet component. Whereas in LOVECLIM, AGISM is included for the ice sheet component, it is the GRISLI ice sheet model [Quiquet et al., 2018a] in iLOVECLIM [Roche et al., 2014, Quiquet et al., 2021]. The GRISLI ice sheet model will be further detailed in Section 3.2. As the typical resolution of the ice sheet model is much smaller than the resolution of the at-

mospheric grid, dynamical downscaling of the temperature and precipitation fields has been implemented into iLOVECLIM to produce higher resolution fields to feed the climate model [Quiquet et al., 2018b]. The coupling between the atmospheric, oceanic and ice sheet components will be further detailed in Section 3.3. Ice sheets are part of the climate system and GRISLI can be seen as a component of the iLOVECLIM Earth System Model. However, for simplicity we refer in the following by "iLOVECLIM" to the atmospheric oceanic and vegetation components. The ice sheet model GRISLI is here seen as an external component, coupled to the iLOVECLIM model. iLOVECLIM "offline" simulations refer to simulations with ECBILT-CLIO-VECODE, where the ice sheet model GRISLI is not included and the Greenland and Antarctic ice sheets are imposed to their current geometries. GRISLI "offline" simulations refer to simulations of the GRISLI model only, not coupled to the iLOVECLIM model. iLOVECLIM-GRISLI coupled simulations refer in this work to simulations where the iLOVECLIM model and the GRISLI Antarctic ice sheet module are coupled. Until very recently the inclusion of the ice sheet component in iLOVECLIM was limited to the Northern Hemisphere [Roche et al., 2014, Quiquet et al., 2021]. No studies have been published yet on the Antarctic. As a result of the current code structure, it is not yet possible to have at the same time Antarctic and Northern Hemisphere ice sheets included in iLOVECLIM. Therefore, in this study, the Northern Hemisphere ice sheet is fixed to its current geometry (Greenland ice sheet). At the beginning of my PhD, the code of the coupling of the iLOVECLIM model and GRISLI for the southern Hemisphere was implemented, but remained to be tested and tuned. The ice sheet obtained under pre-industrial condition was very far from the observations. This led to coupling modifications, as well as a retuning of the dynamical parameters of the GRISLI model, that will be further discussed in 3.3.3.

In this section, a short description of the atmospheric, oceanic and vegetation components of iLOVECLIM is provided.

The atmospheric component : ECBILT

In the iLOVECLIM model, the most important simplifications compared to GCMs are in the atmospheric component, as it is usually a very computationally expensive component in GCMs [Goosse et al., 2010]. ECBILT is a three dimensional atmospheric component. Its vertical extent consists of three levels and its horizontal resolution is T21; corresponding to $\sim$5.6° in latitude and longitude, and a grid size of $\sim$625km at the equator. It is based on the quasi-geostrophic approximation.

The longwave radiation scheme is based on anomalies from a reference state. The longwave flux is computed as the sum of a reference value (for a specific temperature profile, humidity content, and greenhouse gases concentration) and anomaly terms, relative to the difference of temperature profile, greenhouse gases concentration and humidity compared to the reference. Longwave fluxes are com-

puted following this method for both clear-sky and covered conditions. The longwave flux is then obtained by a weighted average of these "clear-sky " and "covered" longwave fluxes, depending on the cloud cover. In iLOVECLIM, the clouds are not computed explicitly and the cloud cover is fixed and prescribed to an observational dataset. The prescribed cloud cover depends on the location and season. Therefore, the impact of cloud modifications in response to different CO_2 levels cannot be investigated with the iLOVECLIM model. In a similar manner, the transmissivity of the atmosphere is not computed directly, but varies with the season and location. The surface albedo is computed relatively to the different fraction of the cell covered by ocean, sea ice and vegetation (trees, gras and desert) and their corresponding albedo.

The oceanic component : CLIO

The CLIO component [Goosse et al., 1997, Goosse and Fichefet, 1999] comes from the coupling of a comprehensive sea ice model [Fichefet and Morales Maqueda, 1997] and an ocean general circulation model [Campin and Goosse, 1999]. The ocean flow is described by the Navier Stokes equations, with classical approximations. The horizontal discretization, is 3° x3°. There are 20 levels along the vertical. The sea ice component is a thermodynamic-dynamic sea ice model. The surface albedo of sea ice is parametrized and takes into account the state of the surface (frozen or melting) and the thickness of the snow and ice covers.

The continental biosphere component : VECODE

The VECODE terrestrial biosphere component [Brovkin et al., 2002] simulates changes in vegetation structure and terrestrial carbon pools. Here, we focus only on the vegetation structure, as the carbon cycle is not activated in our study. VECODE possesses two plant functional types (PFTs): grass, and trees. The rest is desert. For a given climate (atmospheric fields), there is a unique stable composition of PFTs. As the climate evolves, the vegetation changes according to the changes in the atmospheric fields. The albedo is computed following the albedo of tree, grass and desert, and their relative proportion into a T21 grid cell.

3.2 . Modelling the Antarctic ice sheet with the GRISLI Antarctic Ice sheet model

To model the Antarctic ice sheet, we use the GRISLI ice sheet model. The GRISLI ice sheet model has been extensively described in Ritz et al. [2001] and Quiquet et al. [2018a]. Some of the main features are summarized here. In particular, the parameters that will be tuned in the next section are introduced.

3.2.1 . The GRISLI ice sheet model

Mass conservation equation

In GRISLI, the ice sheet is considered as composed of pure ice only and its density is taken homogeneous and constant (ρ_i= 918 $kg{\cdot}m^{-3}$). The ice is therefore considered as an incompressible fluid, and the mass conservation equation reads :

$$\overrightarrow{\nabla} \cdot \overrightarrow{u} = \frac{\partial u_x}{\partial x} + \frac{\partial u_y}{\partial y} + \frac{\partial u_z}{\partial z} = 0 \tag{3.1}$$

where (u_x, u_y, u_z) are the components of the ice velocity vector $\overrightarrow{u}$ in a Cartesian frame. Integrating the mass conservation equation, Eq. 3.1 over the vertical between the base of the ice sheet (z = b(x,y,t)) and the surface (z = h(x,y,t)) gives :

$$\frac{\partial H}{\partial t} = -\frac{\partial HU_x}{\partial x} - \frac{\partial HU_y}{\partial y} + SMB - B_{melt} \tag{3.2}$$

where H is the ice thickness, H = h - b. U_x and U_y are the vertically integrated velocities, $U_x = \int_{z=b}^{z=h} u_x dz$ and $U_y = \int_{z=b}^{z=h} u_y dz$. SMB is the Surface Mass Balance, and B_{melt} the basal melt.

Momentum conservation equation

For ice sheets, the Reynolds number is very low, and inertial terms of the momentum equation are therefore neglected. When considering an infinitesimal cube of ice, the gravity force is the single force acting on it. Therefore, the equation reads :

$$\begin{cases} \frac{\partial \sigma_x}{\partial x} + \frac{\partial \tau_{xy}}{\partial y} + \frac{\partial \tau_{xz}}{\partial z} = 0 \\ \frac{\partial \tau_{xy}}{\partial x} + \frac{\partial \sigma_y}{\partial y} + \frac{\partial \tau_{yz}}{\partial z} = 0 \\ \frac{\partial \tau_{xz}}{\partial x} + \frac{\partial \tau_{yz}}{\partial y} + \frac{\partial \sigma_z}{\partial z} = \rho_i g \end{cases} \tag{3.3}$$

with $\tau_{ij,i\neq j}$ the shearing stress tensor terms and σ_i the longitudinal stress tensor terms ($\tau_{ii} = \sigma_i$). The deviatoric stress tensor is defined as $s_{ij} = \tau_{ij} + \delta_{ij} P$ with $P = -\frac{1}{3}(\sigma_x + \sigma_y + \sigma_z) = -\frac{1}{3} tr(\tau)$. Isotropy is assumed, thus the deviatoric stress tensor and the deformation rate $\dot{\varepsilon}_{ij}$ are related by :

$$\dot{\varepsilon}_{ij} = \frac{1}{\eta} s_{ij} \tag{3.4}$$

with η being the ice viscosity. The ice is considered as a non-Newtonian fluid, therefore the ice viscosity varries with the stress applied. The viscosity variation with the stress applied are computed following a Glen flow law (empirical formulation).

$$\frac{1}{\eta} = B_{AT}\tau^{n-1} \tag{3.5}$$

The B_{AT} term represents the viscosity variations of the ice with the temperature. The ice viscosity increases with decreasing temperatures, following an exponential Arrhenius law.

$$B_{AT} = S_f B_{BAT0} exp(\frac{E_a}{R}(\frac{1}{T_m} - \frac{1}{T})) \tag{3.6}$$

S_f is a flow enhancement factor, B_{BAT0} a flow law coefficient, E_a the activation energy, R the gas constant and T the local temperature. In GRISLI, both a Glen viscosity with n = 3 and a linear Newtonian viscosity (n =1) are used, with added contributions : $\dot{\varepsilon}_{ij} = (B_{AT1} + \tau^2 B_{AT3})s_{ij}$. The S_f parameter will be calibrated in Section 3.3.3.

Heat equation

The temperature calculation is performed by resolving the heat equation. The temperature field is determined by heat conduction, heat convection and heat production due to ice deformation. In the ice sheet, the horizontal diffusion is assumed to be negligible relative to the vertical diffusion.

The temperature at the ice sheet surface is taken equal to the near surface annual air temperature. A geothermal heat flux is applied at 3km below the bedrock, and is used to compute (by solving the heat equation in the bedrock) the heat flux at the ice bedrock interface.

Modelling accurately the temperature profile in the ice sheet is of particular importance, as the viscosity, and thus the deformation depends on temperature. Moreover, the boundary conditions at the base of the ice sheet for basal drag and basal velocity differ for cold-based ice or temperate based-ice.

Shallow ice and Shallow Shelf Approximation

Ice sheets are considered as an incompressible fluid and their motion can be described by the Navier-Stokes equations. Therefore, it is possible to resolve explicitly the motion equations, without the use of approximation. This kind of model, that resolve explicitly all the terms in the stress tensor are called full Stokes models [Seddik et al., 2012, Larour et al., 2012]. Their application at the ice sheet scale is however limited to a few decades, due to a strong computational cost. For paleo applications as well as long future simulations, less computationally expensive models are needed. And to do so, approximations have to be made. This is the case of the GRISLI ice sheet model [Ritz et al., 2001, Quiquet et al., 2018a], used in this study. The GRISLI ice sheet model is a hybrid Shallow Ice Approximation (SIA) and Shallow Shelf Approximation (SSA) model. These approximation use

the small aspect ratio of ice sheet : the vertical scales are much shorter than the horizontal ones, as the mean Antarctic ice thickness is around 2200m and the horizontal scale is 3000km.

- The Shallow Ice Approximation (SIA) is well suited for regions where the ice flows slowly, dominated by vertical shear stress (gravity driven flow).

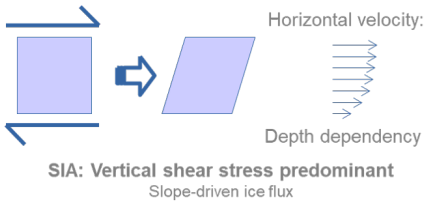

Figure 3.1: Schematic representation of the Shallow Ice Approximation. Figure from Aurélien Quiquet.

- The Shallow Shelf Approximation (SSA) is used in fast flowing regions, where the vertical stresses are much smaller than the longitudinal shear stresses, and are therefore neglected. This approximation is valid in case of floating ice shelves, where the basal drag is negligible. Within this approximation, the horizontal velocities are uniform along the vertical dimension.

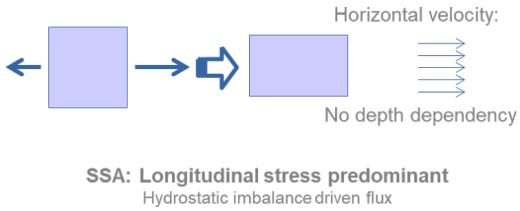

Figure 3.2: Schematic representation of the Shallow Shelf Approximation. Figure from Aurélien Quiquet.

The velocity in GRISLI is computed on the whole domain as a superposition of the SIA and SSA components : $u = u_{SIA} + u_{SSA}$. This allows a smooth transition from frozen regions, where there is no basal sliding to non frozen regions where basal sliding occurs.

The ice anisotropy tends to facilitate deformation due to vertical shear and reduce deformation due to longitudinal stress. The anisotropy is not directly modelled into GRISLI. However, in order to take into account its effect, different proportionality factors are used in the Arrhenius law linking viscosity variations of the ice with the temperature in the case of the computation of the SIA component or the SSA component. The proportionality coefficient in the Arrhenius law for the

SIA, driven by vertical shear, is the enhancement factor, S_f (equation 3.6). The proportionality coefficient in the Arrhenius law for the SSA, driven by longitudinal stress is set to $\frac{S_f}{8}$. For similar conditions, this smaller proportionality coefficient in the Arrhenius law for the SSA compared to the SIA results in a lower B_{AT} value, and thus in a higher viscosity (following Eq. 3.5) and thus a smaller deformation rate for a similar stress applied (following Eq. 3.4).

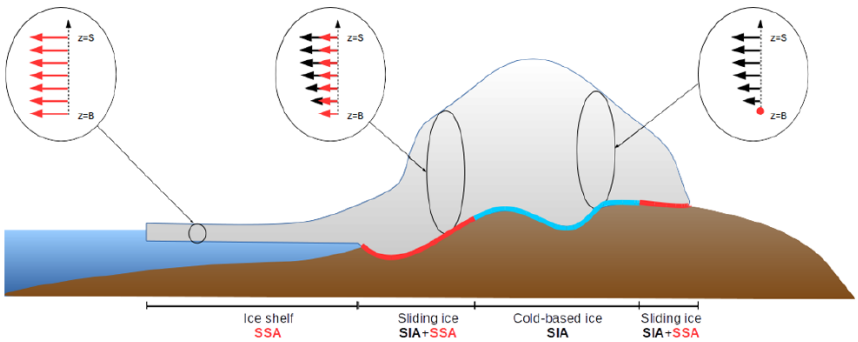

Figure 3.3: Schematic representation of the different types of flows in GRISLI and their associated velocity profiles. The red arrows stand for the sliding velocity, which is non-zero for temperate-based grounded regions. Figure and legend from Quiquet et al. [2018a].

Basal drag

For cold-based grounded ice (depicted in blue in Fig. 3.3), the basal velocity u_b is equal to zero. A very high basal drag (of order $\tau_b = 10^5$Pa) is imposed to ensure no-slip conditions at the interface with the bedrock.

For floating ice shelves, the basal drag τ_b is negligible.

For temperate-based grounded ice (depicted in red in Fig. 3.3), the basal drag and basal velocity ($\overrightarrow{u_b}$) are related by a sliding law. Several sliding laws have been proposed. However, the parameters of these laws remain weakly constrained, as we have limited knowledge of the ice-sediment interface. In addition, these parameter can even change at the scale of a grid cell (40 km). It is often assumed that sliding depends on the effective water pressure at the base of the ice sheet. In GRISLI, we use a Weertman sliding law [Weertman, 1957] :

$$|\tau_b|^{m-1}\,\overrightarrow{\tau_b} = -\beta\overrightarrow{u_b} \tag{3.7}$$

β, the basal drag coefficient, is positive. The law is viscous (linear) for m = 1, and plastic for $m > 1$. In this study, we have assumed that the deformation is viscous. This corresponds to m = 1 and leads to a linear relation between the basal drag and basal velocity :

$$\overrightarrow{\tau_b} = -\beta\overrightarrow{u_b} \tag{3.8}$$

In our study, the β coefficient is taken proportional to the effective water pressure ie the pressure difference between the pressure exerted by the ice to the ground, and the pressure exerted by the water :

$$\beta = C_f N \tag{3.9}$$

with C_f a parameter that needs to be calibrated. And N defined by :

$$N = \rho_i g H - \rho_w g h_w \tag{3.10}$$

with ρ_i and ρ_w respectively the ice and water densities, H the ice thickness, h_w the water height, computed within the GRISLI basal hydrology module.

Studies suggest that the ice sheet grounding line is more dynamic in the case of a non linear, more plastic law [Pattyn, 2017, Brondex et al., 2019, Sun et al., 2020], and that it could better represent the ice sheet behaviour [Gillet-Chaulet et al., 2016]. Non linear sliding law has recently been implemented into the GRISLI ice sheet model, following the methodology of Pattyn [2017]. However, due to lack of time, simulations were performed with the linear law only, and no sensitivity test to the use of a more plastic sliding law were performed.

Another possibility to compute the basal drag coefficient β are inverse methods. In this case, the basal drag coefficient is computed in order to match the observed ice sheet geometry and / or velocity. By construction, the ice sheet obtained is very close to the observations, and this method is widely used for short term sea level projections, like in the first phase of the Ice Sheet Modelling Intercomparison project [Nowicki et al., 2016, Quiquet and Dumas, 2021]. However, the basal drag coefficient computed with the present day geometry becomes inappropriate when the ice margin moves from its present day position. As we want to carry simulations leading to the complete deglaciation of the Antarctic ice sheet, we have not used an inverse method in this study, and have chosen to compute the basal drag coefficient from the effective water pressure.

Basal hydrology

The GRISLI model has a basal hydrology module. The water obtained by melting at the base of the ice sheet is routed outside, following a Darcy law, that describes the flow of fluid through a porous medium. The water flux is proportional to the hydraulic conductivity of the till K_0. The evolution of the water height h_w is computed with a diffusivity equation.

Isostasy

Under the load of an ice sheet, the bedrock is deformed. The bedrock sinks for a rising ice thickness and rises for a decreasing ice thickness, modifying the ice sheet elevation (altitude of the ice sheet surface). It is important to take this process into account, as some points of the ice sheet previously above sea-level

could become below it (and conversely). All other things being equal, this also changes the surface temperature seen by the ice sheet, as the surface altitude changes. In GRISLI, an elastic lithosphere - relaxed asthenosphere model as in Le Meur and Huybrechts [1996] is used.

Iceberg calving

In GRISLI, iceberg calving is not modelled explicitly. Instead, a constant homogeneous thickness criterion is used. At a point in an ice shelf, if the ice flow is not able to sustain a ice thickness higher than 250m, then the corresponding point is considered to be deglaciated, and represents the iceberg calving.

Flux at the grounding line

The grounding line is the separation between the grounded ice sheet and the floating ice shelves, and its representation is therefore of crucial importance for the ice sheet dynamics. To represent it correctly, a very high resolution, lower than 5 km, is needed [Durand et al., 2009]. Due to the computational cost, this is not suited for paleo or long term applications. In GRISLI, to accurately represent the grounding line migration, the ice flux at the grounding line is computed using the analytical formulation of either Schoof [2007] or Tsai et al. [2015]. In this study, we use the analytical formulation of Tsai et al. [2015].

3.2.2 . GRISLI Antarctic reference ice sheet

Reference parameters and offline Antarctic ice sheet

Different parameters have been identified as important over the years for the GRISLI ice sheet model. These parameters are the enhancement factor S_f (all other things being equal, a higher enhancement factor leads to lower viscosities, as visible in Equations 3.5 and 3.6, and thus faster flow), the basal drag coefficient C_f (proportionality factor between basal drag and effective pressure in equation 3.9), the till conductivity K_0 that changes the efficiency of basal water routing (the greater K_0, the faster the basal water is routed outside glaciated areas), as well as a proportionality coefficient for basal melting rates. Quiquet et al. [2018a] have realized a calibration of these parameters. The GRISLI ice sheet model was forced with the annual mean temperature and SMB of the regional climate model RACMO2.3 [Van Wessem et al., 2014] and the basal melting rates were prescribed according to the ISMIP-Antarctica project [Nowicki et al., 2016]. The parameter space was sampled using a Latin Hypercube Sampling Method, and simulations corresponding to the sampled parameter sets were carried out. The simulated ice thickness of the different simulation where then compared to the ice thickness observation (data from Fretwell et al. [2013]). Parameters of simulations with the lowest Root Mean Square Error between the modelled and observed ice thickness

were kept as reference parameter.
Since the Quiquet et al. [2018a] paper, code modifications were performed to the GRISLI model that notably affect the friction of the points at the grounding line. This changes the behaviour of the ice sheet. When using the GRISLI model offline, the previously calibrated parameters do not give a satisfactory present day ice sheet with the new code version. Additionally, when using the GRISLI model coupled to iLOVECLIM, some parameters adjustments have to be made. Indeed, in the coupled setting, the GRISLI model is not forced anymore with the surface mass balance from RACMO and prescribed basal melting rates, but by the outputs from the atmospheric and oceanic component of the iLOVECLIM model. This changes the surface and basal melt balance, and parameters have to be adjusted in order to keep a satisfactory present day ice sheet geometry. Instead of performing a new calibration of the GRISLI parameters for the offline version, and then performing changes for the iLOVECLIM-GRISLI coupled version, I have directly focused on calibrating the GRISLI ice sheet model, when coupled to the iLOVECLIM climate model. This will be explained in the next section.

3.3 . Coupling between the iLOVECLIM and GRISLI models

The first version of the coupling between the iLOVECLIM and the GRISLI model has been performed by Roche et al. [2014]. The coupling procedure has been modified, with an improved computation of the surface and sub-shelf mass balance. These modifications are described in Quiquet et al. [2021]. However, previous published work only focused on the Northern Hemisphere Ice sheet. Therefore, calibration and coupling modifications were needed for Antarctica.

The objective of this chapter is to obtain a reference configuration, from which to start further simulations with different CO_2 levels. We cannot know if the pre-industrial Antarctic ice sheet was at equilibrium or would have gained or lost mass if CO_2 levels and insolation had remained identical to pre-industrial. In order to study the influence of CO_2 levels on the Antarctic ice sheet, we have no choice but to make the assumption that it was equilibrated (ice sheet not gaining or losing mass) under pre-industrial CO_2 levels and insolation. Therefore, we want to obtain a reference configuration for which the Antarctic ice sheet obtained with the coupled iLOVECLIM-GRISLI model is in equilibrium at pre-industrial CO_2 levels and insolation, and close to the observations.

First, the default coupling procedure between the iLOVECLIM and GRISLI Antarctica models is presented in section 3.3.1. In order to obtain the reference configuration, I have first run an equilibrium simulation with the default version of the coupling between iLOVECLIM and GRISLI Antarctica, with pre-industrial CO_2 levels and insolation. The results of this simulation are presented in section 3.3.2 and highlight the fact that with the default coupling version, the obtained ice sheet under PI CO_2 levels and insolation does not resemble the current Antarctic ice sheet. Thus, calibrations are needed in order to obtain the reference configuration. This is presented in section 3.3.3. I have computed the atmospheric and oceanic temperature and precipitation biases of the iLOVECLIM model, and modified the coupling code in order to correct these biases, when atmospheric or oceanic fields are given as input to the GRISLI model. Also, I have performed several simulations with the iLOVECLIM-GRISLI coupled model in order to calibrate some of the model parameters : the enhancement factor S_f of the GRISLI model (defined in section 3.2.1), and the proportionality coefficient K_T for the basal melt rates (defined in 3.3.1).

3.3.1 . Standard version of the coupling

As discussed in Section 1.2.2, ice sheets interact with the atmosphere, ocean, and solid Earth. The interactions of the ice sheet with the solid Earth are not part of the coupling detailed here. The bedrock response to the ice sheet load is directly included in the GRISLI ice sheet model. Varying sea level is not taken into account in our simulations and the eustatic sea level seen by the ice sheet is fixed to the pre-industrial level. Therefore, only the interactions of the ice sheet with the

atmosphere and ocean are described in the following. For clarity, "climate" refers here to the atmospheric and oceanic fields. First, the way in which atmospheric and oceanic variations affect the ice sheet evolution in the coupled model are described. Then, the way in which ice sheet variations affect the modelled climate are described.

Influence of the climate on the ice sheet

Climate influences ice sheet evolution. Indeed, the ice sheet is forced by the surface mass balance, the atmospheric surface air temperature and the oceanic basal melting rates (represented in Figure 3.4). The surface mass balance depends on atmospheric conditions and the oceanic basal melting rates on oceanic conditions.

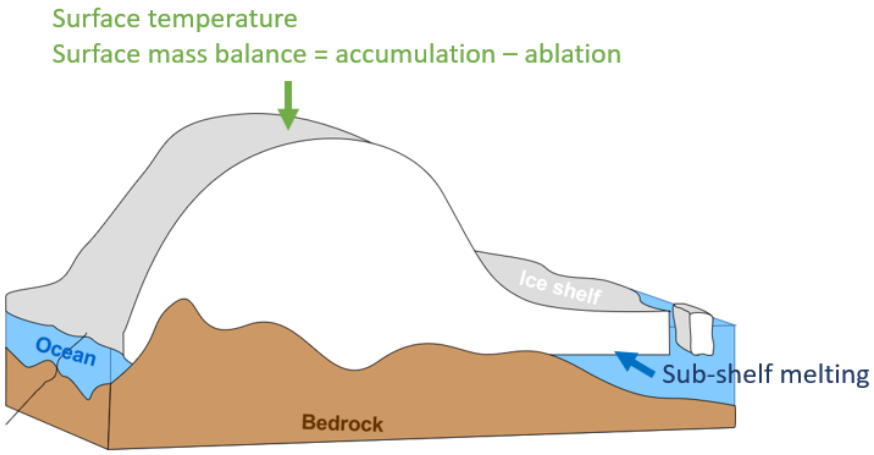

Figure 3.4: Schematic representations of the interactions of the atmosphere and ocean to the ice sheet. Figure adapted from Aurélien Quiquet.

The atmospheric part of iLOVECLIM, ECBILT, has a resolution of T21. This is a coarse resolution, with cells of ∼250km width around 80°S. The GRISLI ice sheet model has a much higher resolution, with grid cells of 40km x40km. To force the ice sheet model with the atmospheric fields (temperature and precipitation), they need to be interpolated on a higher resolution grid. This is done using a downscaling procedure, described in Quiquet et al. [2018b]. Based on the surface topography (at the higher resolution), the temperature and precipitation fields are interpolated from the coarser grid to the higher resolution grid.

GRISLI does not include a snow module. Therefore, the surface mass balance is calculated directly from the atmospheric fields and is used to force the ice sheet model. The surface mass balance is composed of an accumulation (Acc) and a melting term (M_s). In this study, we have neglected the possibility of refreezing. The surface mass balance (SMB) therefore reads :

$$SMB = Acc - M_s \tag{3.11}$$

The accumulation (Acc) is taken equal to the snow precipitation of iLOVECLIM. We therefore make the assumption that all the snow that falls on the ice sheet contributes to ice sheet mass gain.

The melting term M_s is computed following the ITM methodology [Pollard, 1980, van den Berg et al., 2008], using the downscaled fields. The amount of melt M_s over one timestep Δt is computed by :

$$M_s = max(0, \frac{\Delta t}{\rho_w L_m}((1-\alpha)SW_s + c_{rad} + \lambda T_s)) \tag{3.12}$$

T_s is the near surface air temperature (in °C), SW_s is the shortwave radiation at the surface, α is the surface albedo, ρ_w is the density of water (liquid), L_m is the specific latent heat of fusion. The $\lambda T + c_{rad}$ term is a parametrisation for longwave radiation and turbulent exchange. λ and c_{rad} are empirical parameters that need to be calibrated. The albedo α on the downscaled grid is obtained by interpolating the albedo from the coarser T21 grid. Then, a linear correction with the altitude is performed, that leads to lower albedo values at lower altitude. Additionally, it is imposed that the albedo in the downscaled cell is always higher than 0.5 when there is ice underneath.

Most studies [Pollard, 1980, van den Berg et al., 2008, Robinson et al., 2010] have set $\lambda = 10 W m^{-2} K^{-1}$. This is also the case in Quiquet et al. [2021], which describes the iLOVECLIM- GRISLI coupling for the Northern Hemisphere ice sheets. The value of $\lambda = 10 W m^{-2} K^{-1}$ was therefore kept for this study.

The c_{rad} parameter depends on the domain considered [van den Berg et al., 2008] as well as on the parametrisation used for the albedo [Robinson et al., 2010]. Contrary to the λ parameter, the c_{rad} parameter value used differs broadly in the literature and following the area considered. For instance, for the Northern Hemisphere ice sheets value vary from $c_{rad} = -88$ Wm^{-2} in Bintanja et al. [2002] to values up to $c_{rad} = -32$Wm^{-2} in de Boer [2014]. For the Antarctic Ice Sheet, values of -30 and -5 $W m^{-2}$ were used in for the East Antarctic Ice sheet and the West Antarctic Ice sheet respectively in Stap et al. [2014]. In Stap et al. [2022], a value of -5.2 $W m^{-2}$ was used on the whole Antarctic ice sheet. In this study, I have kept the value used in Quiquet et al. [2021] for the Northern Hemisphere ice sheet and set c_{rad} = -40 Wm^{-2}.

The SMB is calculated at each time step of the atmospheric model (4h), and is summed over the year. The SMB summed over the year is then used as input for the ice sheet model.

The sub-shelf melt rates depend on the oceanic conditions in the cavities under the ice shelves. However, most climate models do not resolve the ocean in the cavities. To solve this problem, various parametrization linking basal melt under the ice shelves and the properties of the open ocean (temperature and salinity)

have been developed over the years. The simplest of these parametrisation are linear [Beckmann and Goosse, 2003] or quadratic [Holland et al., 2008, DeConto and Pollard, 2016, Favier et al., 2019] : the melt rate increases linearly or in a quadratic way with the thermal forcing at the edge of the ice shelf and at the corresponding depth. More recently, models have been developped that try to mimic the ocean behaviour under the cavities, with for instance box models [Olbers, 2010, Reese et al., 2018] that simulates the overturning transport of heat and salt from the far field to the grounding line, and then along the ice-ocean interface up to the front; plume parametrisations [Jenkins, 1991, Lazeroms et al., 2018, 2019, Jourdain et al., 2020] that describes the evolution of a 2-dimensional buoyant plume, starting at the grounding line with zero thickness, or a combination of box model and plume parametrisation [Pelle et al., 2019].

Currently, it is only possible to parametrize the basal melt in a linear or quadratic manner in the iLOVECLIM-GRISLI model, as none of the more complex model is yet implemented. In Quiquet et al. [2021], a linear parametrization to the thermal forcing was used. Favier et al. [2019] assessed various melting parametrizations ranging from simple linear and quadratic parametrizations to more complex box and plume models. They show that for simple scalings, a quadratic as opposed to linear dependency on thermal forcing is required. Therefore, we have used a quadratic parametrization instead of linear in this study :

$$bmelt(z) = \frac{K_T \rho_w c_w}{\rho_i L_f} |T_0 - T_f| (T_0 - T_f) \tag{3.13}$$

$bmelt$ is the basal melting rate in m yr^{-1} that depends on the horizontal location (longitude and latitude) as well as the depth z. T_0 is the ocean temperature of the nearest point, at the same depth in the CLIO model. T_f is the local freezing point temperature at the ice base. ρ_w and ρ_i are the density of liquid water and ice, c_w the specific heat capacity of sea water, L_f the enthalpy of fusion, and K_T a parameter that needs calibration. In the model, the basal melt is computed each day and summed over the year.

As in DeConto and Pollard [2016], we apply a sector dependant calibration of the K_T parameter. This will be further detailed in Section 3.3.3.

The freezing point temperature depends on the depth z and the salinity S. We compute the temperature of the freezing point (in °C) following the formulation of Beckmann and Goosse [2003] :

$$T_f = 0.0939 - 0.057S + 7.64 \cdot 10^{-4} z \tag{3.14}$$

Influence of ice sheets on the rest of the climate system

The presence of ice sheets and their geometry influences the climate system. The ice sheet geometry influences the atmospheric circulation. Therefore, the topography seen in the climate model is updated each year, based on the ice sheet

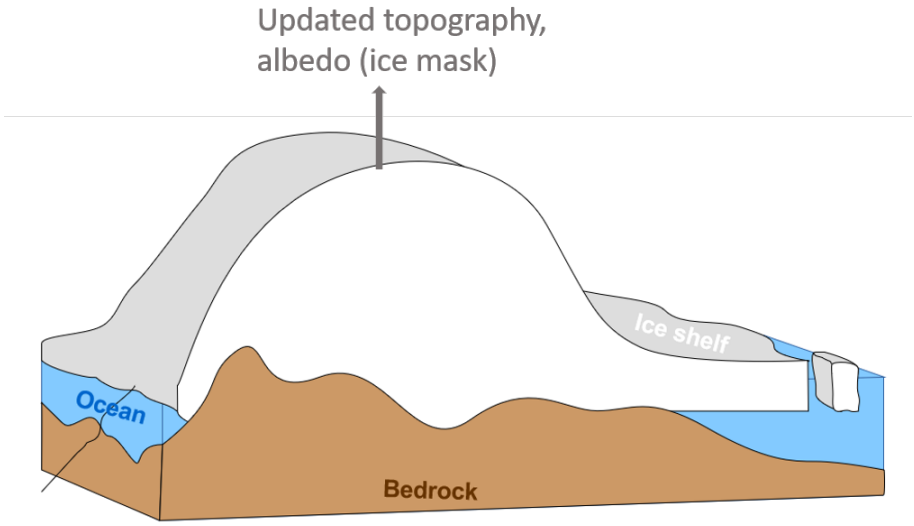

Figure 3.5: Schematic representations of the interactions of the ice sheet to the atmosphere. Figure adapted from Aurélien Quiquet.

evolution. Ice sheet have a strong albedo and their presence or not at a grid point affects the albedo seen by the climate model. In the model, the atmospheric grid cells (coarse resolution) are either glaciated or not. Atmospheric grid cells are considered glaciated if more than 30% of the sub-grid cells have an ice thickness greater than 1m. Glaciated cells have a fixed albedo of 0.85. The albedo of unglaciated cells is calculated according to the vegetation, as explained in Sect. 3.1.

Basal and surface melt, as well as iceberg calving can influence the oceanic circulation. However, this effect is not taken into account in our study : the freshwater released by ice melting is not transferred to the ocean.

The updated topography and ice mask seen by the climate model as the ice sheet evolves in our setup allows to take into account several feedbacks that cannot be taken into account by ice sheet model forced with climatic fields. These feedbacks are the elevation / SMB feedback, ice-sheet topography / precipitation feedback and the albedo / melt feedback (see Section 1.2.2).

Coupling ratio

In the default version of the coupling between GRISLI and iLOVECLIM, exchanges between the climate and ice sheet take place every year. Most of the computation time arises from the iLOVECLIM model. In this study, we want to perform equilibrium simulations for the ice sheet, which can take several thousand years. In order to save computational time, we use a "coupling ratio". The climate model is not run after every year of ice sheet simulation, but after every 100 years. Therefore, one year of climate is used to force 100 years of ice sheet

evolution. This allows us to reduce the computational time, while keeping most of the coupling mechanisms. As ice sheets evolve slowly, it is not necessary to update the topography and ice mask and compute the corresponding climate every year. However, a downside of this methodology is that a particularly cold or warm year due to natural variability is then used to force the ice sheet during 100 years. Also, we emphasize that with this setup, the number of years performed by the ice sheet model does not correspond to a "real" transient time as our model is asynchronously coupled. Specifically, if we apply a CO_2 perturbation in an uncoupled climate model, atmospheric temperature equilibrium will be reached after $\sim$1000 years. In our case, as we run one year of climate model every 100 year of ice sheet model, the ice sheet model will have already run $\sim$100 000 years when atmospheric temperature reach equilibrium. In addition, the insolation is kept fixed to the pre-industrial values over the simulation length in all the simulations (to the exception of sensitivity experiments, where the insolation is also kept fixed, but to other values than pre-industrial). In the following, we therefore mostly focus on the equilibrium of the simulations, not the transient part, or only to discuss qualitative features, not in terms of timing. Climatic years refer to years run by the climate model and ice sheet years to year run by the ice sheet model (100 times more). When it is not specified, the time refers to the years run by the ice sheet model.

3.3.2 . Simulation with the default coupling configuration

A first simulation was carried out with the default version of the coupled iLOVECLIM-GRISLI model under pre-industrial CO_2 levels. This simulation starts from an uncoupled iLOVECLIM simulation, equilibrated with the (offline) GRISLI reference ice sheet. From this, the coupling of the iLOVECLIM and GRISLI model and the climate evolution starts to affect the ice sheet evolution and conversely. The simulation is run for 100 climatic years, with a coupling ratio of 100. This corresponds to 10 000 years of simulation for the ice sheet.

The total ice mass evolution over the simulation is displayed in Figure 3.6. Over the simulation, the ice sheet is quickly gaining mass. After 10 000 ice sheet years, the ice sheet has gained $\sim$ 20% mass, and is much bigger than the offline GRISLI reference ice sheet, from which it started.

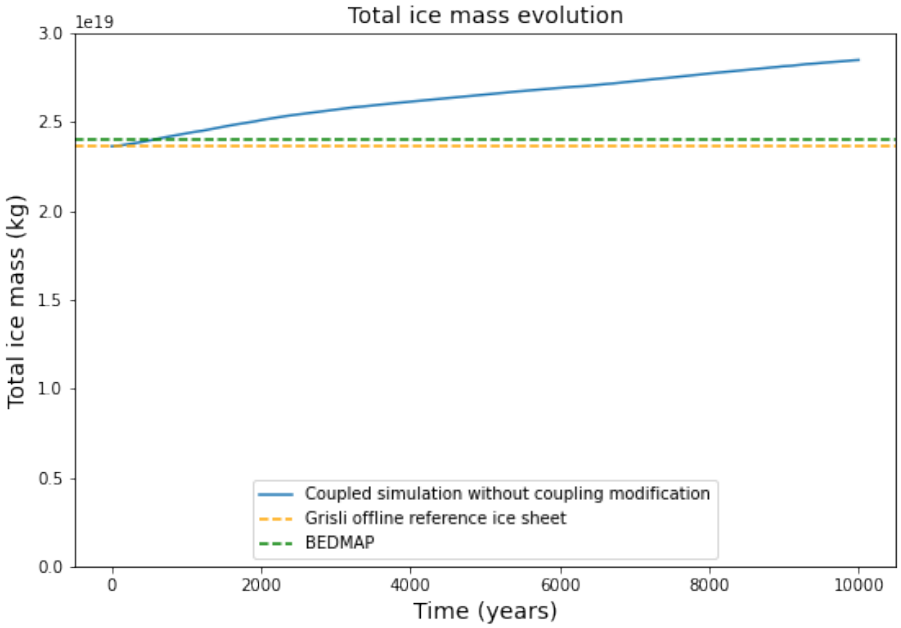

Figure 3.6: Total ice mass evolution.

The ice sheet obtained at the end of the 10 000 years of simulation as well as the observations (BEDMAP) and the GRISLI reference ice sheet are displayed in Figure 3.7.

Figure 3.8 represents the ice thickness difference between BEDMAP and the reference offline GRISLI ice sheet (panel a), the ice thickness difference between BEDMAP and the ice sheet simulated after 10 000 years (panel b) and the ice thickness difference between the GRISLI reference ice sheet and the ice sheet simulated after 10 000 years (panel c).

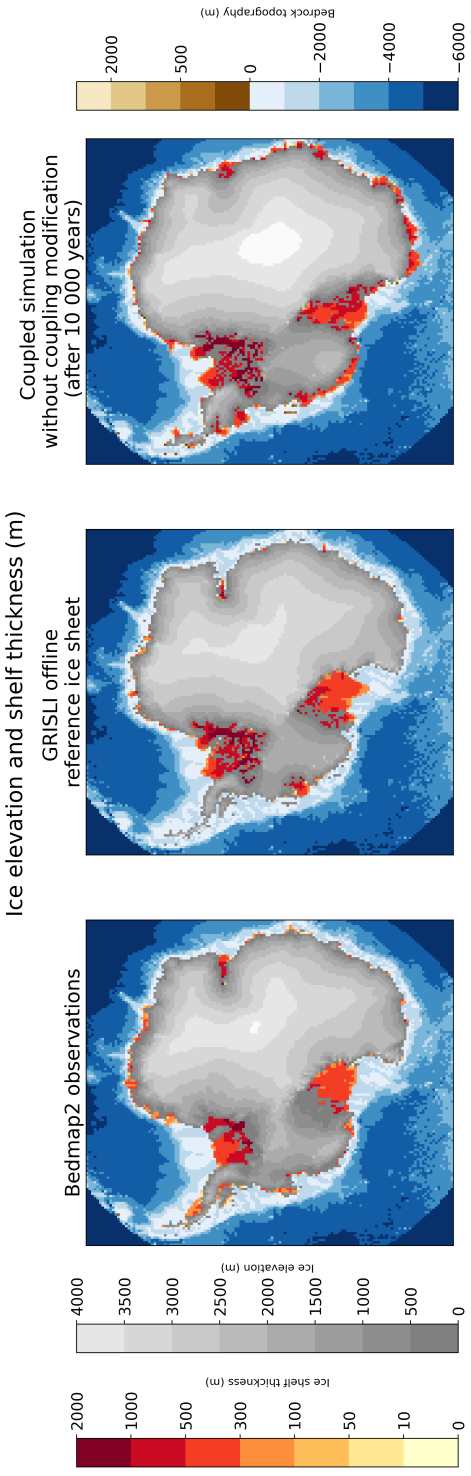

Figure 3.7: Ice elevation (in grey), ice shelves (in red / orange) and bedrock topography (in blue below sea level, brown above) for : BEDMAP, the GRISLI offline reference ice sheet and the ice sheet obtained after 10 000 years of simulation (no modifications of the coupling).

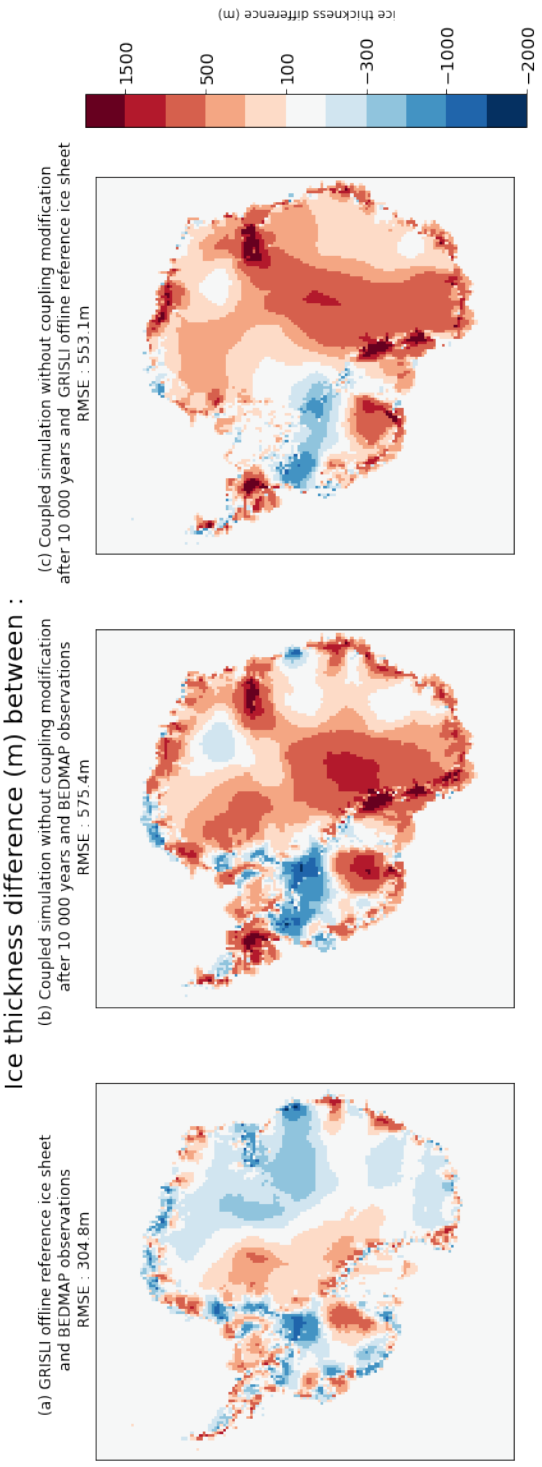

Figure 3.8: Ice thickness difference between : (a) the current Antarctic ice sheet (Bedmap observations) and the GRISLI offline reference ice sheet, (b) the current Antarctic ice sheet and the coupled simulation after 10 000 years (no coupling modifications), (c) the GRISLI offline reference ice sheet and the coupled simulation after 10 000 years

At the end of the simulation, the ice sheet simulated is much thicker in the Eastern part than the BEDMAP observations. The ice sheet has also expanded over the oceans and the shelves are more developed than in the observations. With the default version of the coupling (no coupling modification), the simulated ice sheet is not in equilibrium after 10 000 ice sheet years and differs from the GRISLI reference ice sheeet and the observations (BEDMAP). This is not surprising for several reasons. First, since the calibration of the dynamical parameters of the GRISLI model, the code has changed (see Section 3.2.2). Second, the reference offline ice sheet was obtained by forcing the SMB by the RACMO SMB [Van Wessem et al., 2014] and imposing basal melt rates. In the coupled version, the SMB comes from the atmospheric outputs of iLOVECLIM and the basal melt is calculated from the oceanic temperature and salinity of iLOVECLIM. This leads to different SMB and basal melt rates, and the ice sheet evolves from its initial state.

The goal of our study is to look at the effect of different CO_2 levels on the Antarctic ice sheet. We cannot know if the pre-industrial Antarctic ice sheet was at equilibrium or would have gained or lost mass if CO_2 levels and insolation had remained identical to pre-industrial. In order to study the influence of CO_2 levels on the Antarctic ice sheet, we have no choice but to make the assumption that it was equilibrated (ice sheet not gaining or losing mass) under pre-industrial CO_2 levels and insolation. Then, we can examine if higher CO_2 levels lead to mass loss or gain and how much. Therefore, we would like to obtain a coupled ice-sheet climate reference configuration, where the ice sheet is equilibrated with the pre-industrial climate and resembles the observations. From this configuration, different CO_2 levels could then be applied. In order to obtain this reference pre-industrial ice sheet, I have carried out modifications of the coupling, as well as re calibrated one of the dynamical parameters of the GRISLI model, that are explained in the next section.

3.3.3 . Coupling modification and reference coupled ice sheet

The modifications performed on the coupling can be divided into two categories. First, a correction of the biases of the iLOVECLIM model and second, a calibration of several model parameters : the enhancement factor S_f of the GRISLI model (defined in section 3.2.1), and the proportionality coefficient K_T for the basal melt rates (defined in 3.3.1).

Bias correction

Biases in the computation of air temperature, snow precipitation and oceanic temperature in the iLOVECLIM model affect the SMB and basal melt rates provided to the ice sheet model. To obtain a modelled ice sheet that is in equilibrium for a PI climate and resembles the observations, we could have chosen to calibrate the modelling parameters based on these (biased) climatic fields. Instead we have preferred to correct the biases in the climatic field before calibrating the parameters.

The fields are not directly corrected into the iLOVECLIM model, but corrected in a simple way before being given as input to the GRISLI ice sheet model.

A 2000 years simulation under PI CO_2 levels was carried out with the iLOVECLIM model offline (not coupled to the GRISLI ice sheet model). This reference simulation for PI climate was then compared to the temperature modelled by RACMO [Van Wessem et al., 2014], over the historical period. In doing so, we make the hypothesis that the differences arising between the PI and historical climate are much smaller than the model biases, and that differences between the PI simlation and the historical observations provide a good estimate of the iLOVECLIM model biases.

Records of the temperature and surface accumulation covering the whole Antarctica and over time do not exist. Due to the scarcity of observations on the ice sheet, regional climate models (RCMs) outputs are often used as an alternative to observed fields [Agosta et al., 2019]. Therefore, we have chosen to compare the results of iLOVECLIM with the output of regional climate models, such as the regional climate model RACMO [Van Wessem et al., 2014] or MAR [Agosta et al., 2019]. As the surface temperature and surface mass balance of RACMO averaged over the 1979 - 2006 period was used to calibrate the GRISLI ice sheet model [Quiquet et al., 2018a], we use it again here as a reference surface mass balance over Antarctica. For atmospheric temperature, the temperature modelled by iLOVECLIM on the downscaled grid (40km x 40 km) was compared to the RACMO temperature.

Compared to the RACMO model, the iLOVECLIM model is too warm in the center of the Antarctic ice sheet, but too cold on the sides and the Western part. This temperature bias (displayed in Figure 3.9) can affect the surface melt. Therefore, as in Quiquet et al. [2021], we used a local modification of the melt parameter c_{rad}. For positive temperature biases (when the iLOVECLIM model is warmer than RACMO), the c_{rad} parameter is decreased, reducing the surface melt computed. This is done using a linear correction to the temperature bias. In this study, I have used a different value for the correction factor, and a positive 10°C bias leads to c_{rad} = -52 $W \cdot m^{-2}$, instead of the reference value c_{rad} = -40 $W \cdot m^{-2}$. For simulations with different CO_2 levels than the pre-industrial one, we make the assumption that the temperature bias remains constant locally.

The modelled PI surface melt for the iLOVECLIM model is displayed in Figure 3.10 and compared to the snowmelt modelled by RACMO. In the pre-industrial configuration, iLOVECLIM overestimates the melt a little on the side of the East Antarctic, and underestimates it on the Antarctic peninsula. Under present-day conditions, the surface melt on the Antarctic ice sheet is small, and limited to the Antarctic peninsula and some parts of the ice sheet edges. Therefore, it would be very difficult to "tune" our model to the present-day "observed" melt. We have therefore retained the parameter values presented here as they give a relatively satisfactory melt pattern and magnitude for pre-industrial conditions.

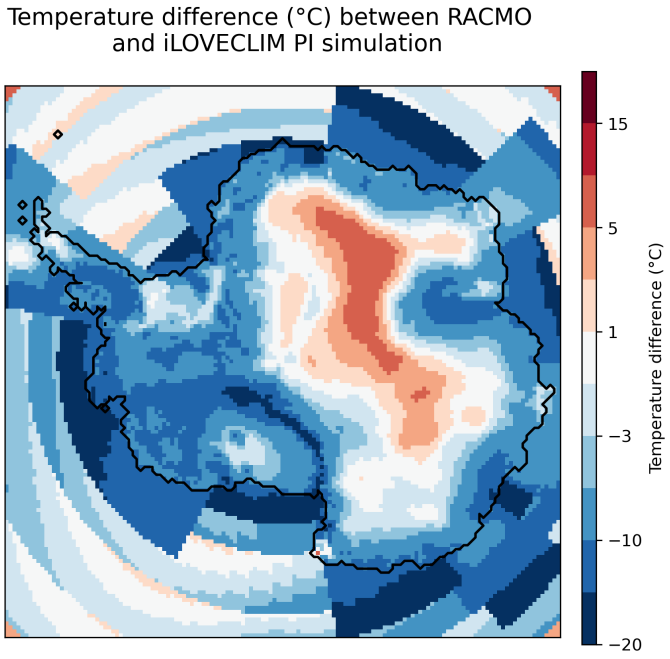

Figure 3.9: Temperature difference at 2m between the iLOVECLIM and RACMO models. The Antarctic ice contour is shown in black.

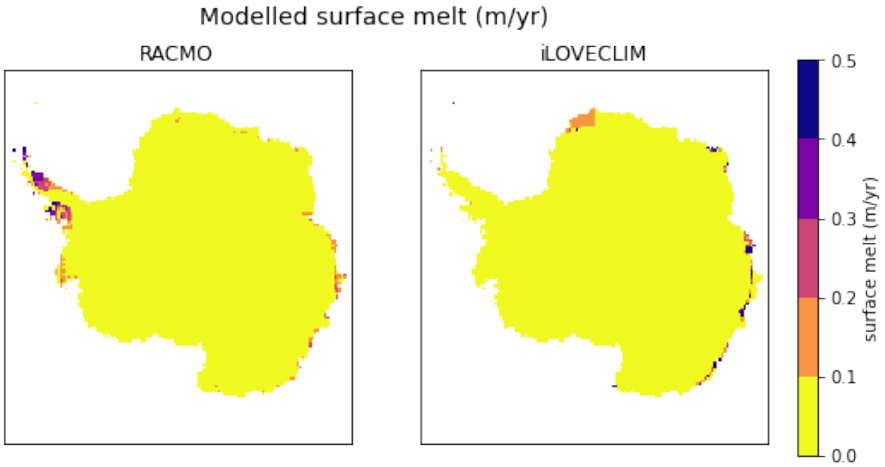

Figure 3.10: Modelled surface melt by the RACMO model [Van Wessem et al., 2014] and the iLOVECLIM model.

The iLOVECLIM snow precipitations were compared to the Accumulation in RACMO. Figure 3.11 represents the SMB of the regional climate model RACMO2.3 [Van Wessem et al., 2014] averaged over the period 1979 - 2006, and interplated into the GRISLI grid. As the SMB was only available on the ice sheet, the data were completed with the SMB of MAR outside the ice sheet. The snow accumu-

lation (averaged over 100 years) for a pre-industrial simulation obtained with the iLOVECLIM model, on the downscaled grid is also displayed. As the snowmelt is very low under present-day conditions, the SMB is a good approximation of the accumulation.

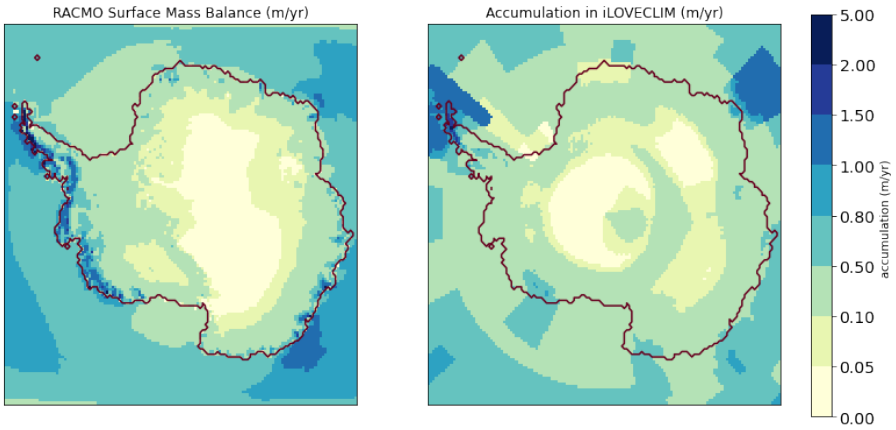

Figure 3.11: RACMO surface mass balance [Van Wessem et al., 2014] compared to the iLOVECLIM Accumulation. The ice contour (Bedmap2 observations [Fretwell et al., 2013]) is displayed in brown.

Figure 3.12 displays the ratio between the RACMO SMB (averaged over the 1979 - 2016 period) and the Accumulation in the iLOVECLIM model (pre industrial simulation, averaged over the simulation length). The ratio was then smoothed by averaging with neighbouring cells, and bounded by 0.2 and 5.

iLOVECLIM does not produce enough snow precipitation over the Western part of Antarctica (ratio higher than one) and produces too much snow precipitation over the Eastern part of Antarctica (ratio lower than one). This bias in accumulation is partly responsible for the large mass gain in the center of the East Antarctic ice sheet compared to the GRISLI offline reference ice sheet, and mass loss in over West Antarctica visible in Figure 3.8.

We have decided to correct this bias in the simplest manner possible, and modify the accumulation given as input to GRISLI by multiplying by this spatially varying ratio.

$$Acc(new) = Acc(ilc) \cdot ratio \tag{3.15}$$

where $Acc(ilc)$ is the snow accumulation computed by iLOVECLIM and $Acc(new)$ is the accumulation given as input to the GRISLI model. We therefore make the assumption that the precipitation biases remain constant in time. For example, we suppose that regions where the iLOVECLIM model simulated two times less precipitation compared to the observation for PI CO_2 levels will also produce two times less precipitations under different CO_2 levels. We know that this is not entirely valid. Indeed, the high precipitations over West Antarctica seen in the observations

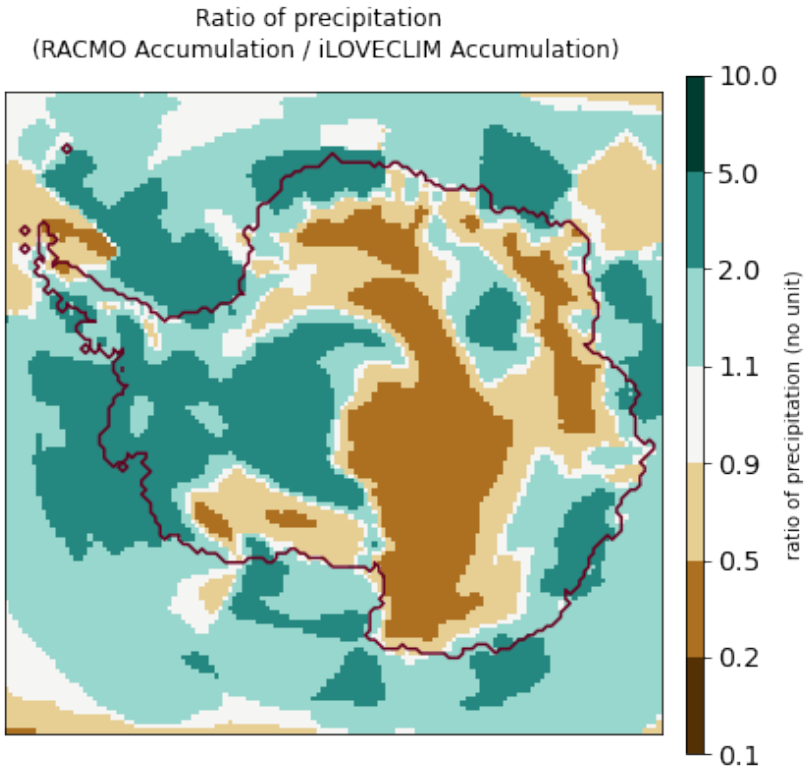

Figure 3.12: Ratio of Accumulation between RACMO (averaged over the 1979 - 2016 period) and the iLOVECLIM model (pre industrial simulation, averaged over the simulation length). The ratio was then smoothed by averaging with neighbouring cells, and bounded by 0.2 and 5.

are orographic precipitations. These orographic precipitation patterns will evolve in coupled simulations, as the ice sheet evolve. However, having no practical other alternatives, we kept this methodology for correcting the precipitation bias. The ratio is bounded by 0.2 and 5 to avoid to multiply or divide the initially computed snow by too large amounts.

iLOVECLIM also has oceanic temperature biases. To estimate the oceanic temperature biases of iLOVECLIM, we used the present-day oceanic temperature dataset constructed by Jourdain et al. [2020]. This dataset was made by combining data from two standard ocean climatologies (data from the World Ocean Atlas [Locarnini et al., 2018] and the Met Office EN4 subsurface ocean profiles [Good et al., 2013]) as well as data from the Marine Mammals Exploring Oceans from Pole to Pole (MEOP) community [Treasure et al., 2017]. The observations were compared to the temperature of a pre-industrial simulation with iLOVECLIM (averaged over 100 years after 2000 years of simulation) and the oceanic temperature bias around Antarctica at different depths is displayed in Figure 3.13.

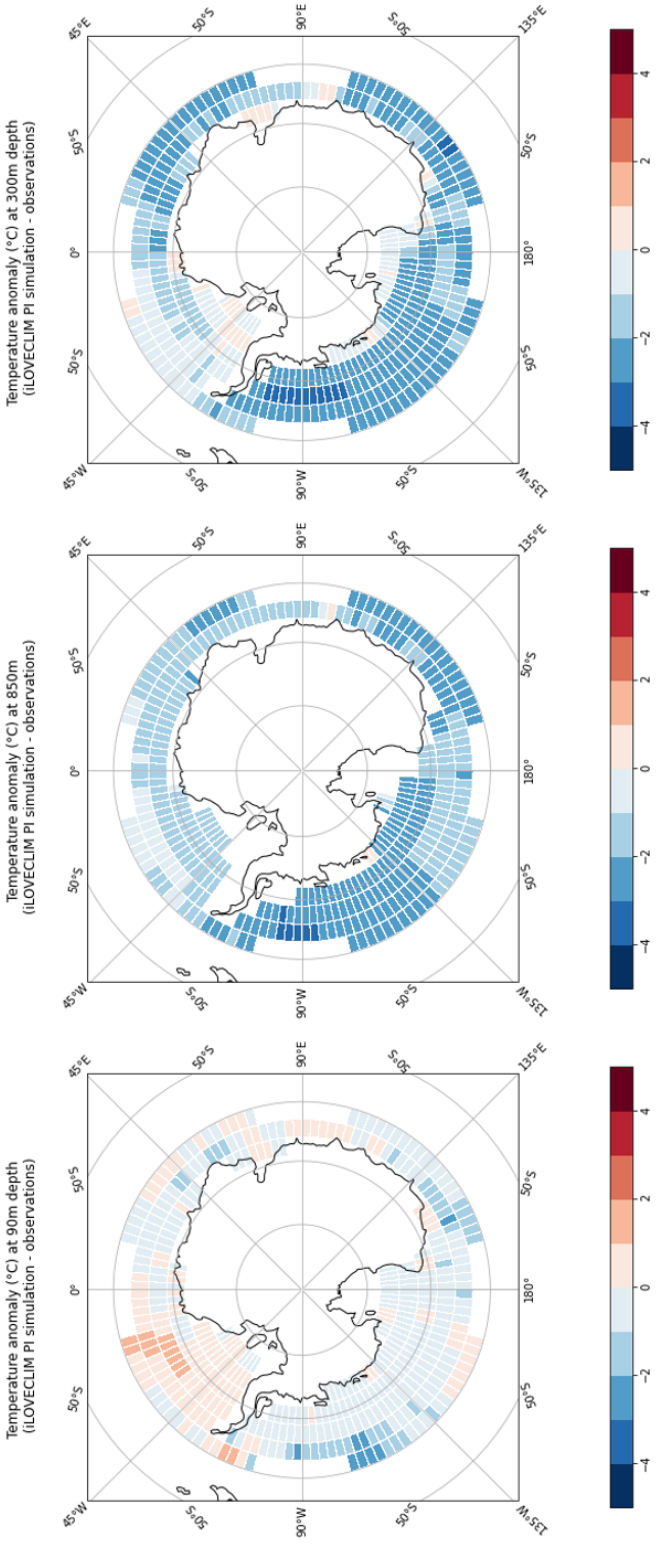

Figure 3.13: Temperature anomaly (iLOVECLIM pre-industrial simulation - observations)

As explained previously, we have decided to use a quadratic parametrisation for the oceanic basal melting rates (see equation 3.13).

with T_0 the oceanic temperature computed by the iLOVECLIM model and T_f the temperature of the freezing point. T_0 and T_f both depend on the location and depth. To account for the oceanic temperature biases, we replace this formula by :

$$bmelt = \frac{K_T \rho_w c_w}{\rho_i L_f} |T_0 - T_{bias} - T_f| (T_0 - T_{bias} - T_f) \tag{3.16}$$

with T_{bias} the oceanic temperature bias (at the corresponding location and depth).

As in DeConto and Pollard [2016], we use a sector dependant calibration of the K_T parameter. To do so, we took the ISMIP sectors [Jourdain et al., 2020]. The reference value of the K_T parameter was taken to K_T = 47.5 $m \cdot yr^{-1} K^{-1}$. This reference value for K_T is very close to the value used in Choudhury et al. [2020], K_T = 47.3 $m \cdot yr^{-1} K^{-1}$, and is of the same order of magnitude as the value used in Pollard and DeConto [2012], DeConto and Pollard [2016], where the reference K_T of 15.77 $m \cdot yr^{-1} K^{-1}$ is modulated by a sector dependant factor of order one.

Parameter calibration

Having accounted for temperature and precipitation biases, several parameters remain to be calibrated. The K_T parameter, proportionality constant for the basal melt rates (see equation 3.16), needs a calibration over the different Antarctic sectors, and the dynamical parameters of the GRISLI ice sheet model also need to be recalibrated.

To do so, I started by calibrating the dynamical parameters of the GRISLI ice sheet model. I have performed several simulations with the GRISLI model coupled only to the the atmospheric component of the iLOVECLIM model, under pre-industrial CO_2 levels. These simulations are called "atmosphere only" in the following. In this setting, the GRISLI ice sheet SMB is computed from the iLOVECLIM fields, but the oceanic basal melt rates are imposed, and do not depend on the modelled oceanic temperature and salinities. They are taken equal to the values used for the GRISLI reference ice sheet.

As explained in section 3.2.2, different parameters of the GRISLI ice sheet model concerning the ice dynamics have been identified as particularly important on the ice sheet behaviour. These parameters are the enhancement factor S_f (see equations 3.5 and 3.6)), the basal drag coefficient C_f (see equation 3.9), and the till conductivity K_0. However, these parameters are weakly constrained and need to be calibrated. As the GRISLI code has changed since the calibration made by Quiquet et al. [2018a], a new calibration is needed. This new calibration is performed directly on the coupled iLOVECLIM-GRISLI setting. A calibration using a Latin Hypercube Sampling of the parameters as in Quiquet et al. [2018a] could

be performed. However, this requires a large amount of simulations. Previous sensitivity studies with the GRISLI model offline (not shown here) had shown that the S_f parameter has a large influence on ice sheet dynamics, while being weakly constrained. Therefore, I have chosen to re-calibrate the S_f parameter only. No calibration of the other dynamical parameters such as the till conductivity K_0 and the basal drag coefficient C_f was performed.

The S_f parameter can usually take values between 1 and 5 [Quiquet et al., 2018a]. I have performed "atmosphere only" simulations with different values of the S_f parameter and selected a S_f parameter that minimize the RMSE between the modelled ice sheet and the current ice sheet (BEDMAP).

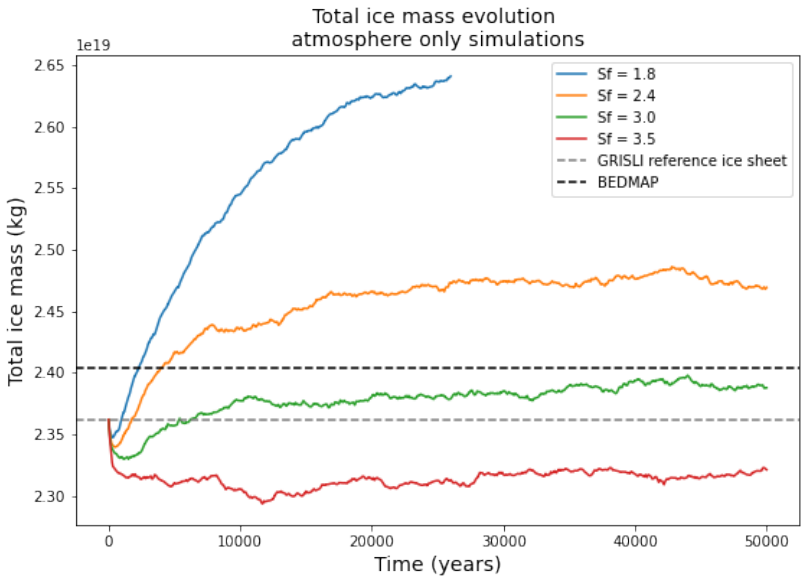

Figure 3.14: Total ice mass evolution for different S_f parameter values, for "atmosphere only" simulations. The grey and black dotted lines represent respectively the total ice mass of the GRISLI offline reference ice sheet and of the observations (BEDMAP). Please note that the y-axis does not start at zero.

Simulations with $S_f = 1.8$, $S_f = 2.4$, $S_f = 3.0$, $S_f = 3.5$ were performed. The total ice mass evolution of the "atmosphere only" simulations with the different S_f parameters for 50000 years of simulation (500 years of climate with a coupling ratio of 100) are displayed in Figure 3.14. The ice thickness differences with BEDMAP of the corresponding modelled ice sheets at the end of the simulations are displayed in Figure 3.15. The simulation with $S_f = 3.5$ minimizes the RMSE between the modelled ice thickness at the end of the simulation and the observation. The simulation with $S_f = 3.0$ gives similar results in terms of RMSE globally, and the ice thickness is not as underestimated in the Antarctic Peninsula as with $S_f = 3.5$.

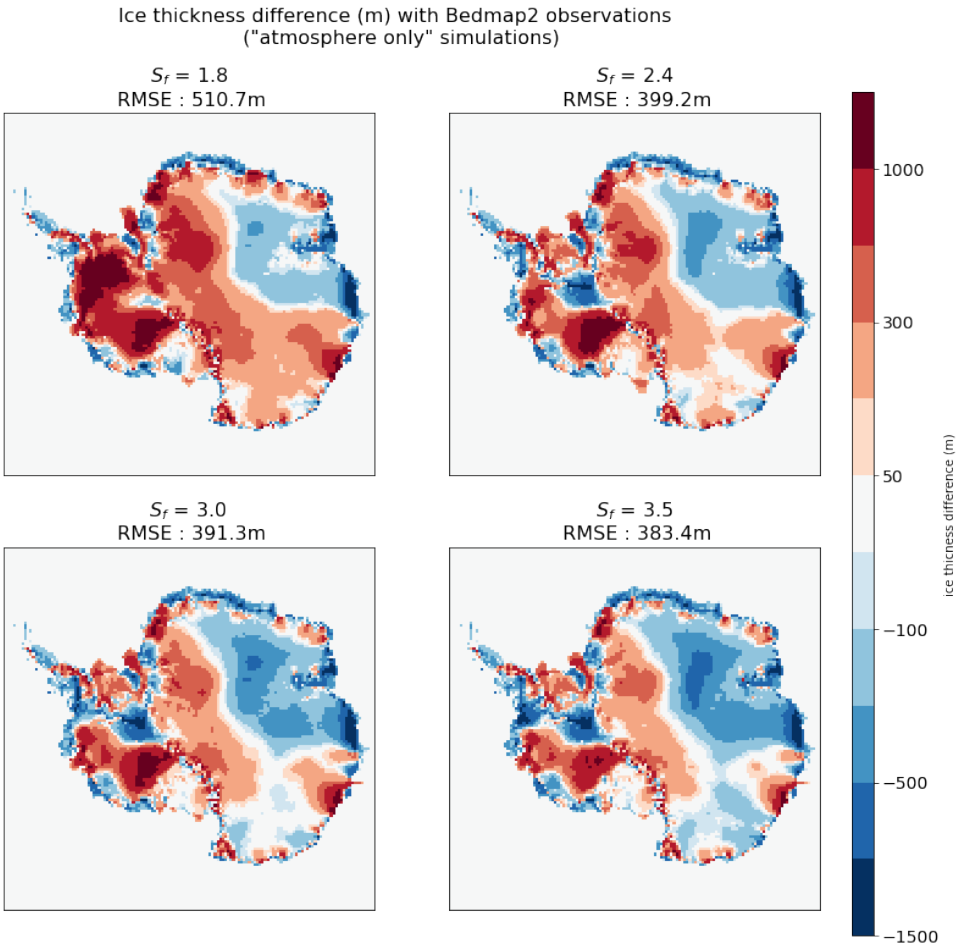

Figure 3.15: Ice thickness difference to BEDMAP for the "atmosphere only" simulations, with different values of the S_f parameter.

As a compromise, the value of $S_f = 3.0$ was chosen and is used in the following.

In a second step, I have performed simulations with the iLOVECLIM and GRISLI model fully coupled. This means that the GRISLI SMB is given by the atmospheric fields of iLOVECLIM and the basal melt rates are computed depending on the iLOVECLIM oceanic temperature and salinity. The K_T parameter remains to be calibrated and can vary depending on the sector.

First, the homogeneous value of $K_T = 47.5$ was applied in each sector. The corresponding total ice mass evolution, ice thickness difference to BEDMAP and ice thickness are represented in Figures 3.16, 3.18 and 3.17.

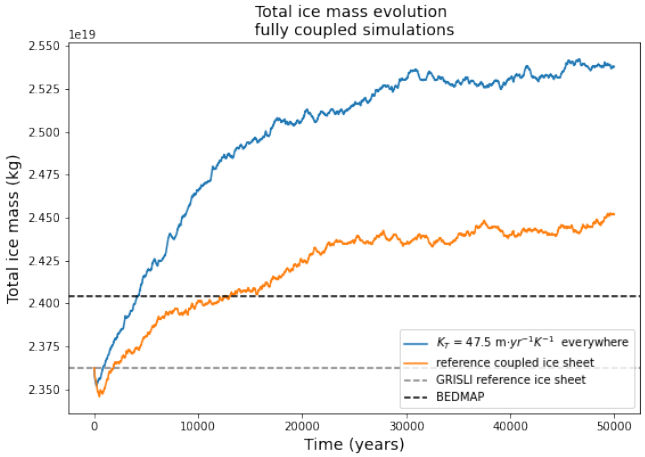

Figure 3.16: Total ice mass evolution for fully coupled simulations. With an homogeneous K_T parameter in blue, and the configuration chosen as reference (varying K_T per sector) in orange. Please note that the y-axis does not start at zero.

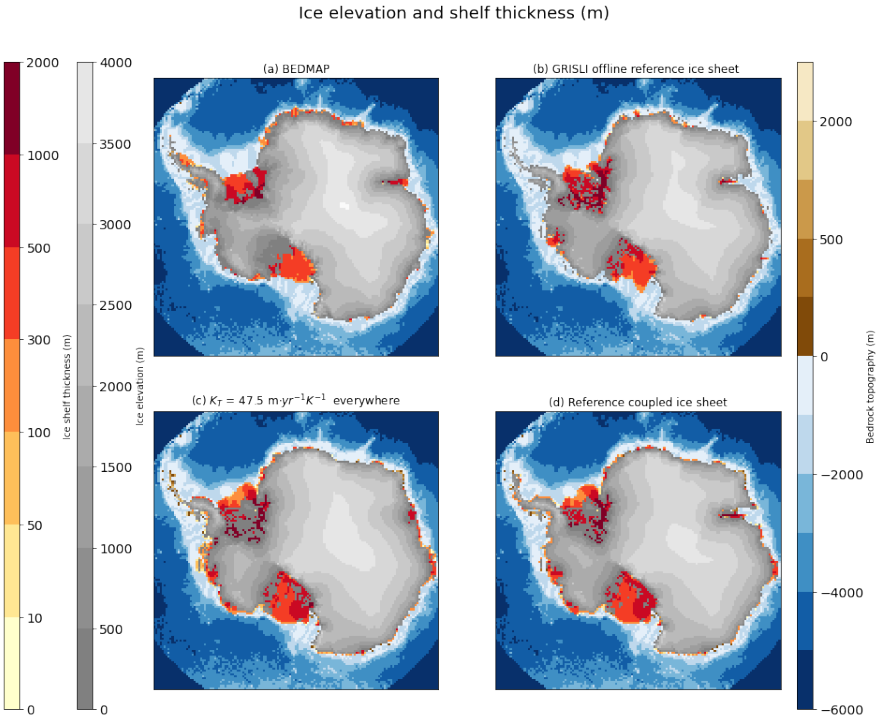

Figure 3.17: Ice elevation and shelf thickness for (a) observations (BEDMAP), (b) the GRISLI offline reference ice sheet, (c) the simulation with homogeneous K_T (end of the simulation, after 50 000 years), (d) the reference simulation (end of the simulation, after 50 000 years)

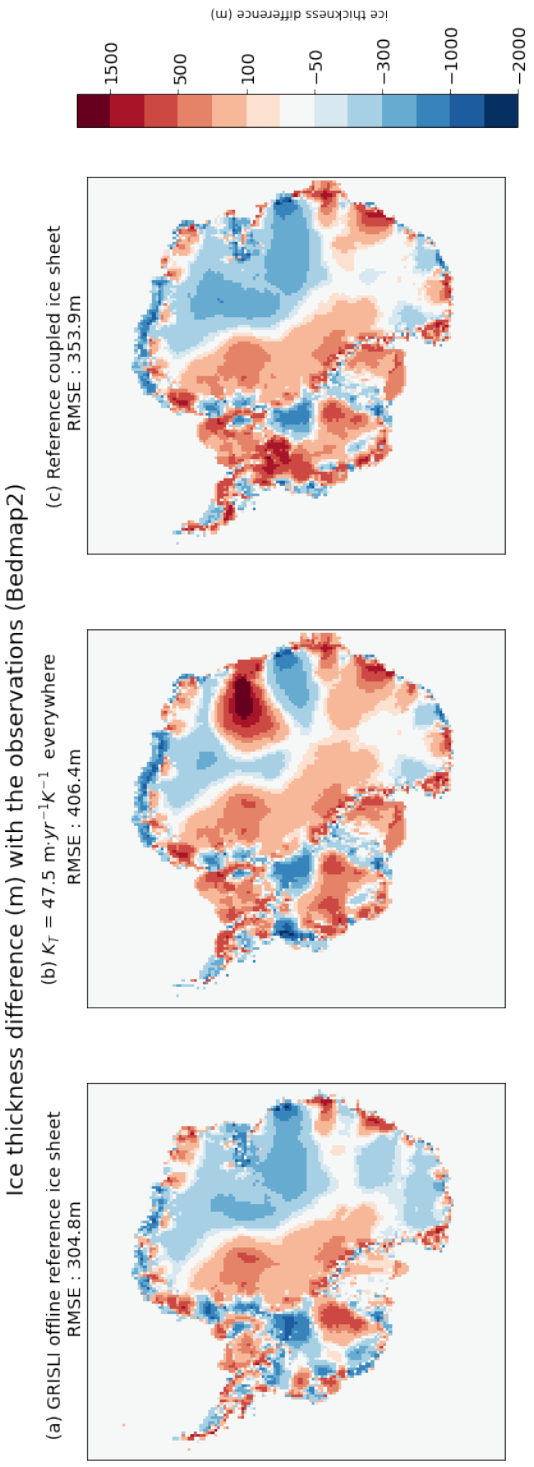

Figure 3.18: Ice thickness difference to observations (BEDMAP) for : (a) the GRISLI offline reference ice sheet, (b) the simulation with homogeneous K_T (end of the simulation, after 50 000 years), (c) the reference simulation (end of the simulation, after 50 000 years)

There are several differences between the simulated ice sheet with an homogeneous K_T and the observations. Based on the difference between the observations and the simulation with a homogeneous K_T, the K_T value was adjusted in some sectors : it was increased when the ice thickness was too high, and conversely. Compared to the observations, the simulation with an homogeneous K_T has too much ice in the Amery sector. The ice sheet even become grounded there, while it is an ice shelf at present. Therefore, it was decided to increase the value of K_T in the Amery sector, in order to increase the basal melt in this sector. The Antarctic peninsula is smaller in the simulation than in the observations, and the K_T value was reduced in this sector. The ice shelves around Dronning Maud Land are not well represented in the simulation, and are almost absent in the simulation. The K_T value was therefore reduced in the corresponding sector. There are too thick and developed shelves in the Pine Island sector, so the K_T value was raised in this sector. The choice of the new values was done with a "trial and error" method, and only the chosen ice sheet is displayed here.

The ice sheet obtained at the end of the 50 000 ice sheet years simulation with the varying K_T is called "reference coupled ice sheet". It is displayed in panel (d) of Figure 3.17. It is compared with the observations (BEDMAP2, panel (a)), the GRISLI offline reference ice sheet (ie the reference GRISLI ice sheet when there is no coupling with the iLOVECLIM model, panel (b)) and the modelled ice sheet with an homogeneous K_T (panel (d)). Its ice thickness difference to the BEDMAP2 observations is shown in panel (c) of Figure 3.18. It is compared to the ice thickness difference between the modelled ice sheet with an homogeneous K_T and the observations (panel (b)), and the ice thickness difference between the GRISLI offline reference ice sheet and the observations (panel (c)). The velocity at the end of the reference coupled simulation is displayed in panel (b) of Figure 3.20. This velocity is compared with the observations (panel (a)) and the modelled velocity of the GRISLI offline reference ice sheet (panel (c)).

The configuration obtained with a spatially varying K_T has a global RMSE of ice thickness of 353m with respect to the observations. In comparison, the GRISLI offline (not coupled to iLOVECLIM) reference ice sheet, obtained at the same resolution of 40km and with the same methodology for the basal friction computation, through a calibration with a Latin Hypercube Sampling has a RMSE of 305m. We therefore cannot expect to obtain much lower RMSE values with our simpler procedure. Lower RMSE can be obtained with the GRISLI ice sheet model, by using a higher spatial resolution and an inverse method to compute the basal drag coefficient. For instance the RMSE is of 120 m in Quiquet and Dumas [2021] with a resolution of 16 km and the use of an inverse method to compute the basal drag coefficient. However, using a spatial resolution of 16 km would largely increase the computational time and the use of inverse methods to compute the basal drag coefficient is not suited when the ice margins move away from their present day condition. Also, the value of 353m is in the range of model

value used in the ISMIP Antarctica project [Seroussi et al., 2020], where RMSE of ice thickness range from 100 to 400m depending on models. As the focus of this thesis is on long term future, it is not crucial to have an ice sheet that perfectly matches the observations for pre-industrial CO_2 levels. Therefore, the RMSE of 353m was considered satisfactory for our purpose and we did not try to improve further the agreement with the observations.

Modelled velocity

The modelled velocity pattern is coherent with the observations, with very low velocities at the center of the ice sheet, and the presence of ice streams, with much larger velocity. The ice velocity is much higher on the ice shelves than on grounded ice, as in the observations. The modelled velocity pattern is smoother than the observations. This is due to the model resolution, that cannot represent all small scale features. The modelled velocity (for the coupled and uncoupled ice sheets) against observed velocity are plotted in Figure 3.19.

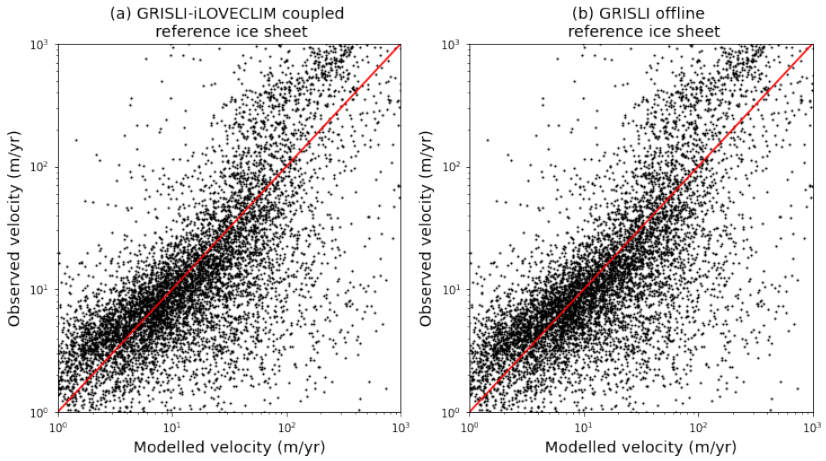

Figure 3.19: Observed ice velocity (data from Mouginot et al. [2017]) against modelled ice velocity. Panel (a) : the modelled velocity is the velocity at the end of the 5000 years coupled iLOVECLIM-GRISLI PI simulation. Panel (b) : the modelled velocity is the velocity of the GRISLI offline reference ice sheet.

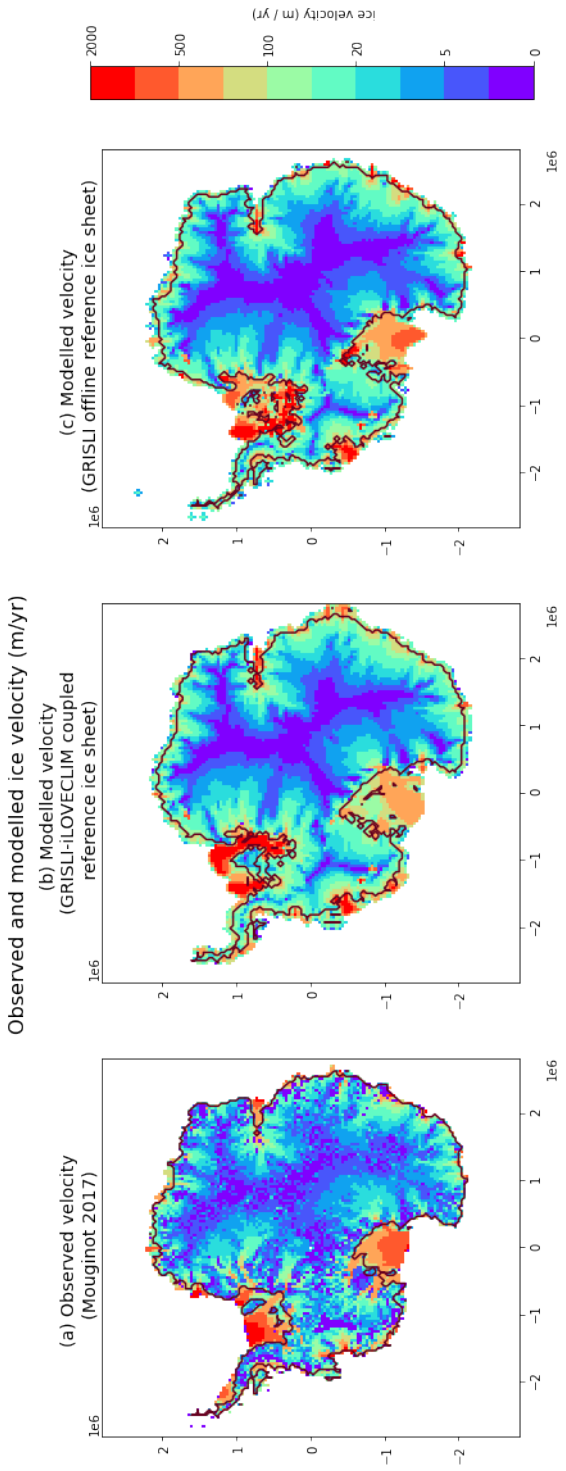

Figure 3.20: Ice velocity. Panel (a) observations (data from Mouginot et al. [2017]) Panel (b) : modelled velocity at the end of the 5000 years coupled iLOVECLIM-GRISLI PI simulation. Panel (c) : modelled velocity of the GRISLI offline reference ice sheet. The grounding line is displayed in brown countour.

Pre-industrial simulation from the reference configuration

The configuration obtained at the end of the 50 000 ice sheet years simulation with the modified S_f value and the spatially varying K_T parameter has a satisfactory geometry (not too far from BEDMAP2 observations) and velocity pattern. It was defined as the reference pre-industrial configuration, from which further simulations will be started.

Starting from the reference pre-industrial configuration, the simulation was extended for 200 kyr (2000 years of climate with a coupling ratio of 100, with the same parameter values and CO_2 content). The total ice mass evolution over the extended simulation is displayed in Figure 3.21. This extended PI simulation from the reference configuration shows that the ice sheet obtained at the end of the reference configuration simulation is in equilibrium with the simulated climate, as the ice sheet mass does not vary much (<1%) over the extended simulation.

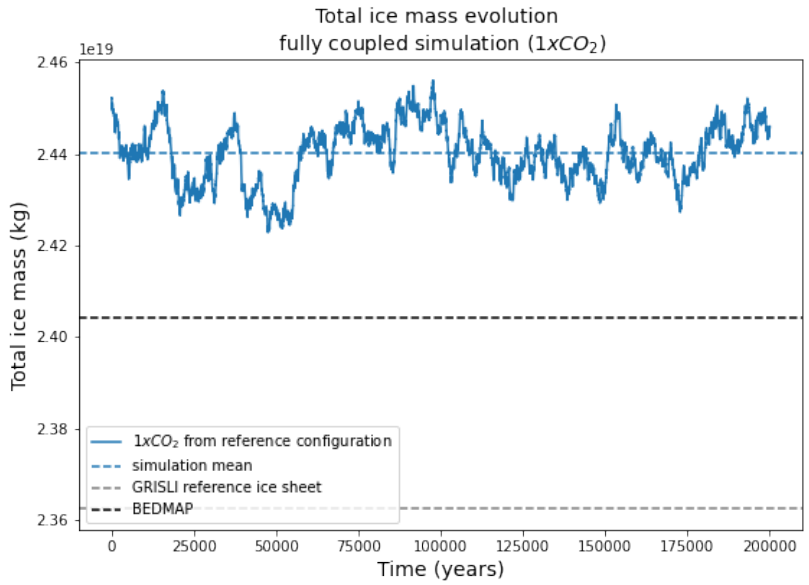

Figure 3.21: Total ice mass evolution for a PI iLOVECLIM-GRISLI coupled simulation under PI CO_2 levels, starting from the reference configuration. Please note that the y-axis does not start at zero.

The different mass loss fluxes were estimated during this simulation. The mass fluxes are divided according to their cause : surface melt or accumulation (grouped in surface mass balance), basal melt or calving. Due to the structure of the code, these fluxes are only computed on the "ice mask", where the ice sheet is present. Ice advected outside the existing ice sheet (outside the ice mask) that is lost due to either surface or basal melt is grouped in a single term ("mass loss outside ice mask"). As a consequence, the contribution of the different processes to the mass

loss outside the ice mask usually cannot be differentiated. However, in the case of this pre-industrial simulation, there is very limited surface melt (see Figure 3.10), so we assume that in this simulation, all mass lost outside the ice mask corresponds to basal melt.

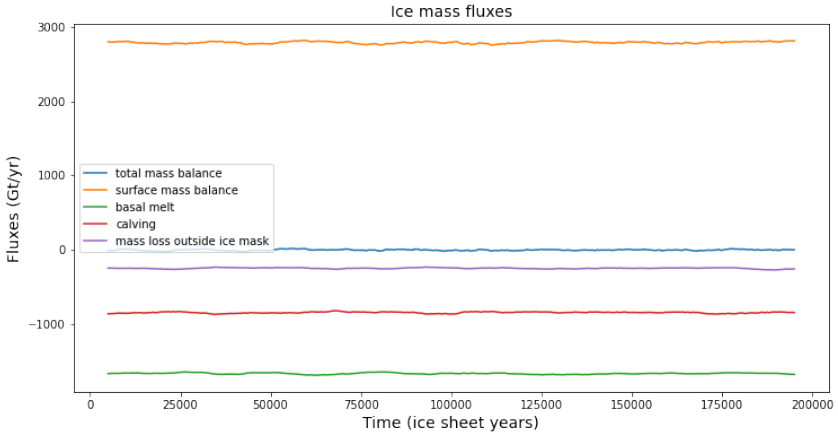

Figure 3.22: Antarctic ice mass fluxes (Gt/yr) for the reference PI simulation (200 000 ice sheet years). The fluxes are averaged over 10 000 ice sheet years. Negative values contribute to mass loss and positive values correspond to mass gain. The total mass balance is in blue, surface mass balance in orange, basal melt fluxes in green, calving fluxes in red. The purple curve corresponds to the ice mass that is lost on grid cells that are not part of the ice sheet at the previous timestep (ice mask). This can be due to surface melt or basal melt.

The average of the different fluxes over the simulation (200 000 ice sheet years) is :

- Surface Mass Balance : $\sim$2775.1 Gt yr^{-1}
- Calving : $\sim$-855.1 Gt yr^{-1}
- Basal melt : $\sim$-1919.8 Gt yr^{-1} (from which 245Gt yr^{-1} is lost outside the ice mask)
- Total mass balance : $\sim$0.2 Gt yr^{-1}

Mottram et al. [2021] performed an intercomparison of five different regional climate models, forced by ERA-Interim reanalysis, in simulating the near-surface climate and surface mass balance (SMB) of Antarctica. They found an ensemble mean annual SMB over the Antarctic ice sheet including ice shelves of 2329 $\pm$ 94 Gt/yr over the 1987–2015 period and 2483 Gt/yr over the 1980 to 2010 period,

with individual estimates varying from 1961 $\pm$ 70 to 2519 $\pm$ 118 Gt / yr. We make the assumption that the Surface Mass Balance over the pre-industrial period is not too far away from the surface mass balance over the 1980 - 2010 period. With a model value of $\sim$2775 Gt/yr, we are slightly overestimating the surface mass balance over the Antarctic Ice sheet.

Rignot et al. [2013] and Depoorter et al. [2013] estimated Antarctic calving fluxes to be 1089 $\pm$ 139 Gt yr^{-1} and 1321$\pm$144 Gt yr^{-1} respectively, and the basal melt fluxes being 1325 $\pm$ 235 Gt yr^{-1} and 1454 $\pm$174 Gt yr^{-1}. Adusumilli et al. [2020] estimated basal melt flux from ice shelves to be 1100 $\pm$ 60 Gt yr^{-1} in steady state, 1090 $\pm$ 150 Gt yr^{-1} in 1994, 1570 $\pm$ 140 Gt yr^{-1} in 2009, 1160 $\pm$ 150 Gt yr^{-1} in 2018. With averaged model values of $\sim$855 Gt/ year for calving and $\sim$1920 Gt/yr for basal melt, we are slightly underestimating calving fluxes. On the contrary, we are overestimating basal melt.

The mean total mass balance over the simulation (200 000 ice sheet years) is 0.2 Gt yr^{-1}: starting from the reference PI configuration, the PI simulation performed give an ice sheet that is in equilibrium (very small imbalance value).

The PI ice sheet we obtain is in equilibrium and only slightly overestimates the ice sheet mass compared to the BEDMAP observations (see Figure 3.21). The surface mass balance is slighlty over estimated and the the calving flux slightly underestimated, but this is partly compensated by an overestimated basal melt.

To sum up, in this Chapter, I have presented the model of intermediate complexity iLOVECLIM and the ice sheet model GRISLI used in this study. I have developed the reference configuration for the coupled iLOVECLIM-GRISLI Antarctica setting, which had never been done before. This implied to correct biases in the iLOVECLIM output fields as well as recalibrating parameters (the internal parameter of the GRISLI model, S_f and the basal melt proportionality coefficient, K_T). The ice sheet chosen as reference pre-industrial configuration has a satisfactory geometry and velocity pattern. In addition, it is equilibrated with the pre-industrial climate. Compared to the observations, the basal melt and surface mass balance are overestimated, but are of the same order of magnitude than the observations. It is therefore considered that the obtained reference coupled ice sheet is satisfactory for our purpose : studying long term Antarctic changes. In the next chapter, we apply different CO_2 levels, starting from this configuration and study the ice sheet's response.

4 - Investigating the Antarctic ice sheet behaviour under different atmospheric CO_2 levels with the coupled ice sheet - climate model iLOVECLIM-GRISLI

Chapter aims:

1. Investigate the Antarctic ice sheet response to different CO_2 levels, when starting from a present-day like ice sheet or a configuration with no ice.
2. Investigate the role of the orbital configuration on the results.
3. Investigate the role played by the albedo-melt feedback.

Highlights:

↪ The Antartic ice sheet exhibits a strong hysteresis behaviour in our coupled setting, with the equilibrium Antarctic ice sheet for a same CO_2 level being either a widely developed ice sheet or no ice sheet at all, depending on the starting configuration.

↪ The transitions between an ice free and glaciated Antarctica and conversely are more brutal than in studies not including the albedo-melt feedback. In our setup, when increasing the CO_2 level, there is no intermediate configuration between a widely developed ice sheet in East Antarctica and an ice free Antarctica. In a similar manner, when decreasing the CO_2 level, there is no intermediate configuration between an almost ice free Antarctica and a widely developed ice sheet.

↪ A different orbital configuration leads to different CO_2 threshold for Antarctica glaciation or complete deglaciation. In our equilibrium simulations with fixed CO_2 levels and insolation, at CO_2 levels around three times the pre-industrial value, both states (ice being present on Antarctica or not) can be stable, depending on the insolation.

In this chapter, we use the previously developed iLOVECLIM-GRISLI coupled setting to carry out simulations under different atmospheric CO_2 levels. First, starting from the reference configuration, that resembles the current Antarctic ice sheet, we apply increasing CO_2 levels. In a second time, we start from a

configuration where there is no Antarctic ice sheet anymore, and apply decreasing CO_2 levels. This was motivated by the fact that previous studies have highlighted that the Antarctic ice sheet exhibits hysteresis behaviour [Pollard and DeConto, 2005, Garbe et al., 2020]. For instance, Garbe et al. [2020] used an ice sheet model forced by temperature increase until the Antarctic ice sheet melts completely (for $\sim$10°C increase in Global Mean Temperature compared to the pre-industrial period) and then forced by temperature decrease, until the ice sheet grows back. They showed that for each anomaly of temperature compared to pre-industrial, the ice sheet is bigger in the melt phase than in the growth phase. Here, we perform the same kind of study, but instead of forcing an ice sheet model with global mean temperature increase or decrease, we use the coupled iLOVECLIM-GRISLI setting and look at increasing and decreasing CO_2 levels. We also study the influence on our modelling results of two important processes : the inclusion of the albedo feedback, and the insolation. Lastly, we discuss our results and propose some perspectives.

4.1 . Simulations under different atmospheric CO_2 levels starting from both the current Antarctic configuration and a configuration without ice sheet.

4.1.1 . Simulations starting from the reference configuration : the melt branch

Starting from the reference configuration (pre-industrial simulation with equilibrated climate and Antarctic ice sheet, presented in Chapter 3), simulations with different atmospheric CO_2 levels are performed : two, four, six, eight, ten and twelve times the pre-industrial CO_2 level (280 ppm). The simulations are noted 2xCO_2, 4xCO_2, 6xCO_2, 8xCO_2, 10xCO_2, 12xCO_2 in the following. We apply a constant CO_2 concentration over the simulation length. As explained in section 3.3.1, our model is asynchronously coupled with a coupling ratio of 100 in order to reduce the computational time needed to reach equilibrium. The climate model is run for a year and then the ice sheet model is run for 100 years with this climate. The ice sheet obtained is used to calculate the climate during a year, and so on. Consequently, in the following, the different times are either expressed as "climate years" when referring to the number of climate years run by the model and "ice sheet years" when referring to the number of ice sheet years run by the model. We emphasize that the number of years performed by the ice sheet model does not correspond to a classical transient time as our model is asynchronously coupled. Therefore, we mostly focus on the ice sheet equilibrium. For most simulations, the model is run for 3000 climatic years, corresponding to 300 000 ice sheet year, in order to reach equilibrium for both the climate and ice sheet. As we apply a positive CO_2 perturbation at the start of the simulation, the atmospheric and

oceanic temperatures increase over time as a result of equilibrium to both the CO_2 perturbation and the ice sheet changes over time.

The ice mass evolution of the Antarctic ice sheet over the simulations is displayed in Figure 4.1. Additional simulations with CO_2 levels of 6.7xCO_2 and 7.4xCO_2 were performed, in order to refine between the 6xCO_2 and 8xCO_2 simulation. These simulations were started from the end of the 6xCO_2 simulation, and run for another 3000 climatic year (300 000 ice sheet years). The 8xCO_2 simulation was not equilibrated after 300 000 ice sheet years and was therefore carried out for 100 000 additional ice sheet years (400 000 years in total). The 1xCO_2 simulation is run for 200 000 ice sheet years (the simulation is already equilibrated, as no CO_2 perturbation from the reference configuration is applied).

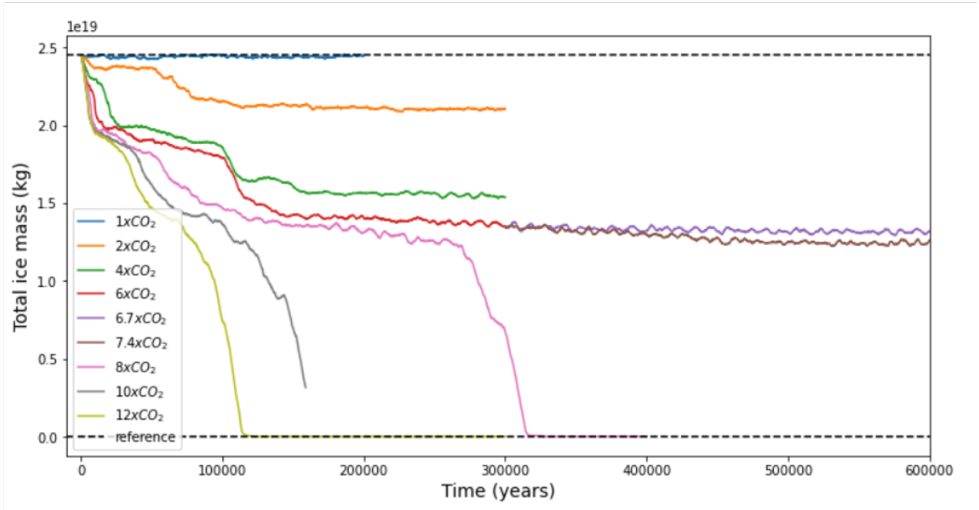

Figure 4.1: Total ice mass evolution over time for the different simulations carried out. The upper black dotted line represent the total ice mass of the reference configuration, from which the simulations start. The lower black doted line denotes zero. The time axis is the ice sheet time : simulations are run for 3000 climatic years with a coupling ratio of 100, leading to 300 000 ice sheet years.

Figure 4.1 shows that in all simulations carried out for CO_2 levels higher than pre-industrial, the Antarctic ice sheet melts at least partly and is losing mass over time. Therefore, in the following, the simulations starting from the reference configuration to which higher CO_2 levels are applied are called the "melt simulations". The higher the CO_2 level applied, the lower is the ice mass at the end of the simulation. The mass loss occurs sooner in the case of higher CO_2 levels, as atmospheric and oceanic conditions are sooner favourable to ice sheet mass loss in the simulations. The ice sheet state at the end of the 2xCO_2, 4xCO_2, 6xCO_2 and 8xCO_2 simulation are displayed in Figure 4.2. These are compared to the

current Antarctic ice sheet (Bedmap2 observations [Fretwell et al., 2013]) and the ice sheet at the end of the 200 000 years 1xCO_2 simulation.

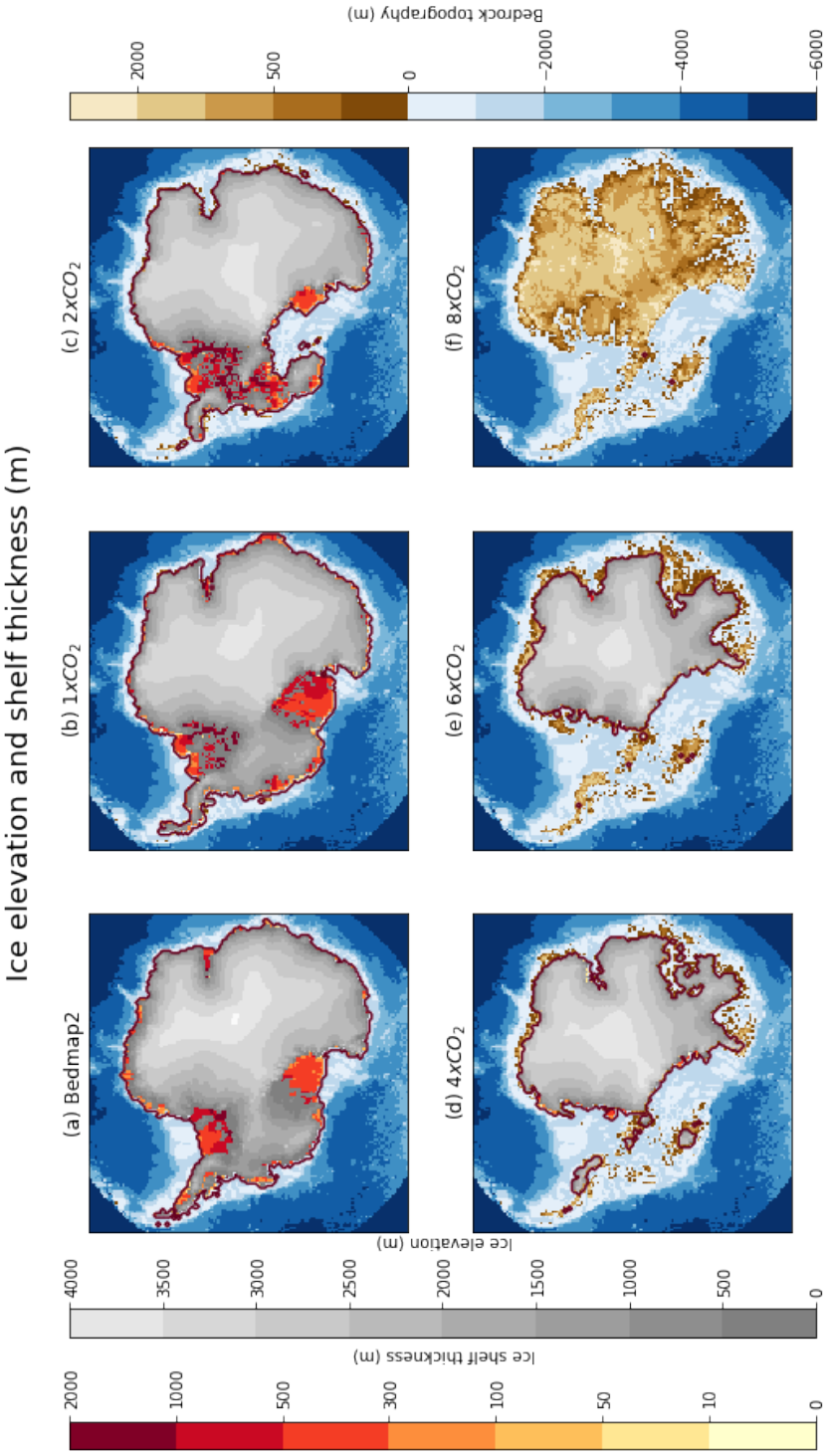

Figure 4.2: Panel (a) : present-day Antarctic ice sheet (observations : Bedmap2 [Fretwell et al., 2013]). Panel (b) : ice sheet at the end of the 1xCO_2 simulation, similar to the reference ice sheet. Panels (c), (d), (e), (f) : ice sheet at the end of the 2xCO_2, 4xCO_2, 6xCO_2 and 8xCO_2 simulations.

At the end of the 2xCO_2 simulation, a part of the West Antarctic ice sheet has disappeared. Notably, the sector of Pine Island is not grounded anymore and there are instead ice shelves in this sector, and the Ross ice shelf has disappeared. There are no shelves anymore around the East Antarctic ice sheet, which becomes only grounded. At 4xCO_2, all the ice shelves have disappeared, even in West Antarctica. Ice remains on West Antarctica only on the parts where the bedrock lies above sea level, such as the Antarctic Peninsula. In the Eastern part, the ice sheet has retreated in the sectors of Wilkes and Aurora, mostly where the bedrock lies below sea level. However, a large ice cap remains in East Antarctica mostly where the bedrock lies above sea level. The marine parts of the ice sheet are thus susceptible to lower levels of warming than the parts resting on bedrock above sea level. The fact that marine ice sheets are more sensible to warming is coherent with the litterature [Weertman, 1974, Mercer, 1978, Winkelmann et al., 2015, Golledge et al., 2015, Garbe et al., 2020]. Warmer water melts the ice shelves at the base, and in case of retrograde slopes, Marine Ice Sheet instability can be triggered (see section 1.2.1). At 6xCO_2, all ice caps have disappeared in West Antarctica, even on parts whose bedrock lie above sea level. The ice sheet has further retreated on the margins in the East. However, there remains a large Antarctic ice cap in the East. A striking feature is the huge difference between the end of the 6xCO_2 and 8xCO_2 simulation. While there is still more than half of the initial total ice mass at the end of the simulation 6xCO_2 simulation, the Antarctic ice sheet has completely disappeared at the end of the 8xCO_2 simulation.

Therefore, simulations were carried out at intermediate CO_2 levels between 6 and 8xCO_2 : 6.7xCO_2 and 7.4xCO_2, starting from the end of the 6xCO_2 simulation. The state of the Antarctic ice sheet at the end of the 6, 6.7, 7.4 and 8xCO_2 simulations are displayed in Figure 4.3.

Compared to the 6.7xCO_2 simulation, the ice sheet has further retreated in the Wilkes basin, and around Coats land in the 7.4xCO_2 simulation. However, differences between the 6.7 and 7.4xCO_2 simulations remain limited and in both cases a large grounded East Antarctic ice sheet remains. The remaining ice sheet at 7.4xCO_2 is mostly terrestrial, although some small parts remain in contact with the ocean, such as in the Amery sector and Coats land sector. These additional simulations between 6xCO_2 and 8xCO_2 show that there is no intermediate state of the ice sheet possible in our coupled model between a large terrestrial East Antarctic ice sheet and an Antarctic ice sheet that has completely disappeared. There seems to be a critical threshold around 8xCO_2 levels, that leads to the complete disintegration of the Antarctic ice sheet.

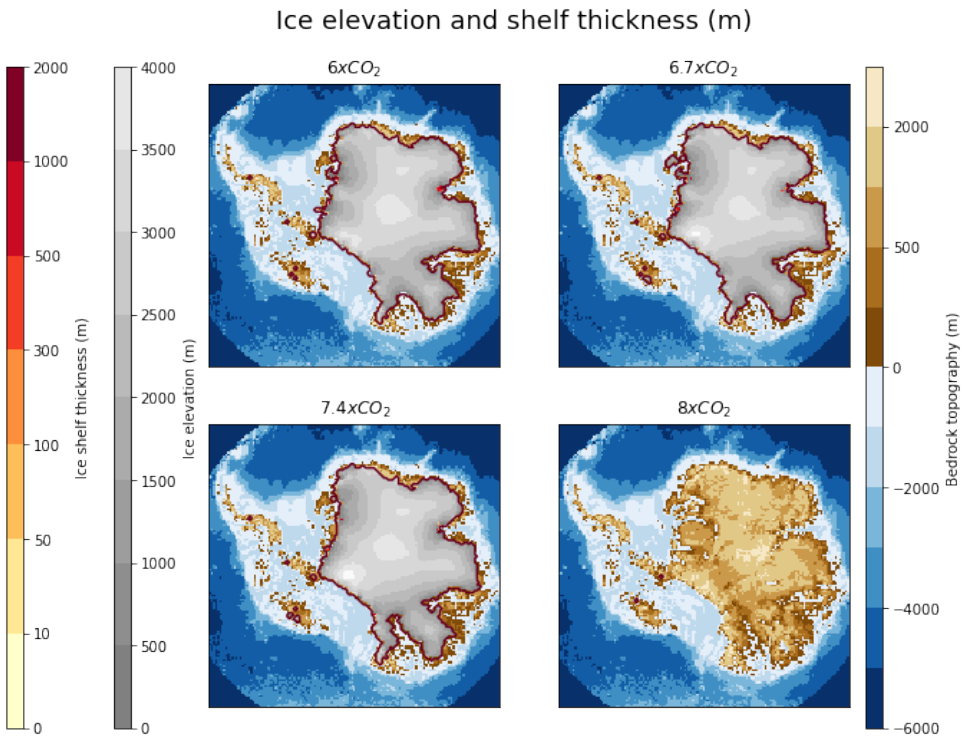

Figure 4.3: Ice sheet at the end of 6xCO_2 6.7xCO_2, 7.4xCO_2 and 8xCO_2 simulations.

In the following, we focus on the 8xCO_2 simulation and the different stages of the ice sheet melt. The maps of the Antarctic ice sheet at different model timesteps of the 8xCO_2 simulation is displayed in Figure 4.4, and the Antarctic temperature and ice volume evolution in Fig. 4.6.

Even if the times do not correspond to a real transient evolution, this allows us to see which parts of the ice sheet are more vulnerable, and lost before others. First (state (A) of Figure 4.4), the Ross ice shelf disappears. The Pine Island sector is not grounded anymore. The ice sheet has retreated in the Wilkes basin. Then (state (B) of Figure 4.4), the ice shelves in the Pine Island sector have completely disappeared. The ice sheet has further retreated in the Wilkes sector and the Aurora sector. However, the Ronne Filchner ice shelf remains. Then (state (C) of Figure 4.4), almost all ice has disappeared on the Western part, even on parts where the bedrock lies above sea level. In the East, the ice sheet has retreated further in the Wilkes and Aurora basin. At some point (state (F) of Figure 4.4), the ice sheet is not in contact with the ocean anymore, at the exception of limited location in Coats Land and the Amery sector. In state (H), the ice sheet is fully terrestrial and its extent is largely reduced to above half of its extent of state (F). At the end of the simulation (not shown on Figure 4.4 but visible on Fig. 4.2), the ice sheet has completely disappeared. During the simulation, marine parts of the ice sheet

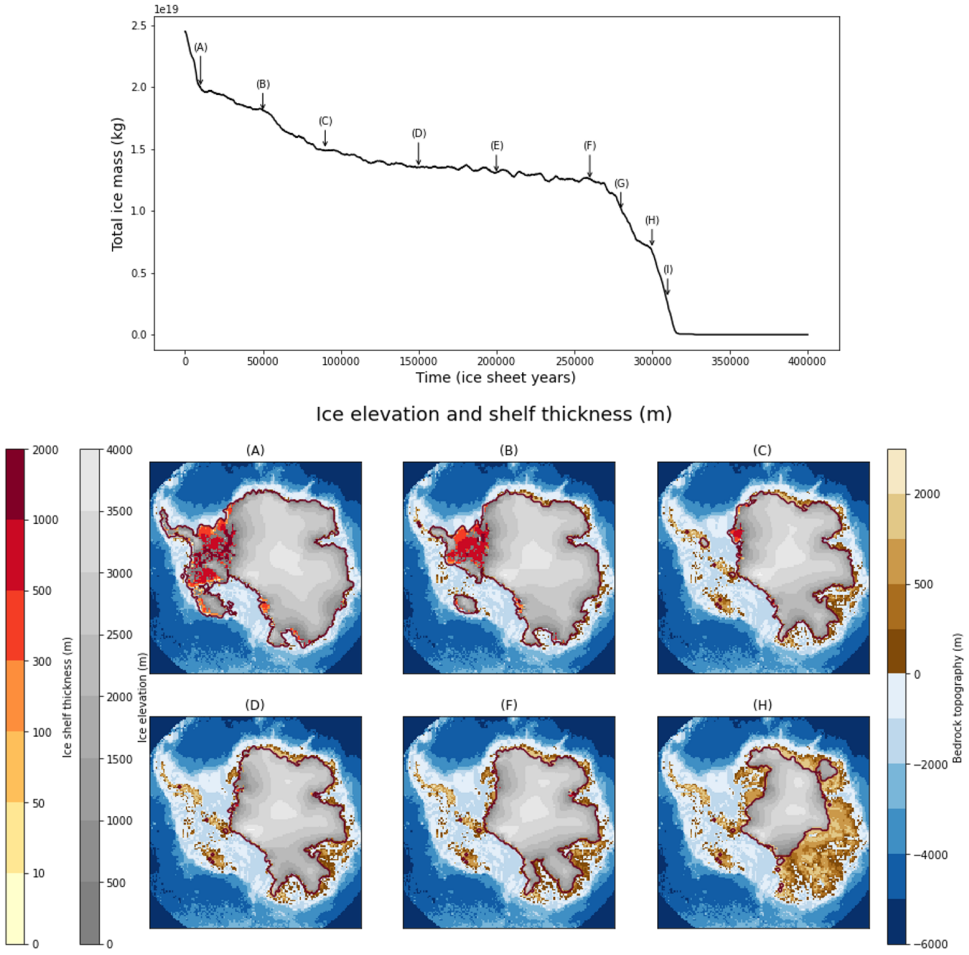

Figure 4.4: Total ice mass evolution and ice sheet state at different steps of the 8xCO_2 melt simulation.

are the first to disappear. This is coherent with previous work, and with the results obtained from the equilibrated ice sheets under different CO_2 levels. Indeed, as the CO_2 perturbation is applied at the start of the simulation, and the climate updated only every 100 ice sheet years, the temperature increases throughout the simulations, as a result of both the radiative adjustment to higher CO_2 levels, and adjustment to ice sheet loss. Marine parts, affected by oceanic warming, are lost at lower global mean temperatures changes compared to grounded parts : therefore, sooner in the course of the 8xCO_2 simulation, and in general for lower CO_2 levels when looking at the equilibrium.

The difference in atmosphere and ocean driven processes is further indicated by the different ice mass fluxes over the 8xCO_2 melt simulation, displayed in Figure 4.5. Positive mass fluxes correspond to mass gain and conversely. The

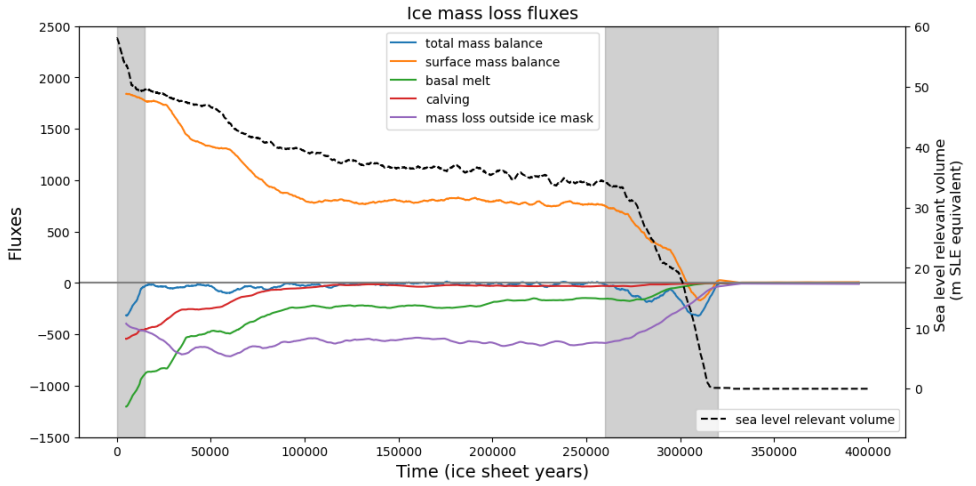

Figure 4.5: Left axis : Antarctic ice mass fluxes (Gt/yr). Negative values contribute to mass loss and positive values correspond to mass gain. The total mass balance is in blue, surface mass balance in orange, basal melt fluxes in green, calving fluxes in red. The purple curve corresponds to the ice mass that is lost on grid cells that are not part of the ice sheet at the previous timestep (ice mask). This can be due to surface melt or basal melt. Right axis : ice-sheet volume (in m SLE).

mass fluxes are divided according to their cause : surface melt or accumulation (grouped in surface mass balance), basal melt or calving. Due to the structure of the code, these fluxes are only computed on the "ice mask", where the ice sheet is present. Ice advected outside the existing ice sheet (outside the ice mask) that is lost due to either surface or basal melt is grouped in a single term ("mass loss outside ice mask"). As a consequence, the contribution of the different processes to the mass loss outside the ice mask cannot be differentiated. At the start of the simulation, there are strong calving and basal melt fluxes. Due to these strong negative contribution, the total mass balance is strongly negative and the ice sheet looses mass quickly, due to oceanic processes. The basal melt and calving fluxes diminish over time as there is less and less ice in contact with the ocean. Between the state (C) and (F), the positive surface mass balance and the negative fluxes almost balance each other and the total mass balance is only slightly negative. The ice sheet looses mass less rapidly than at the start. However, starting around state (F) of Figure 4.4, when the ice sheet that remains is mostly grounded in East Antarctica, the surface mass balance flux decreases, and the total mass balance becomes more negative. The ice sheet is losing mass quickly via atmospheric processes due to the albedo and elevation feedbacks.

As our model is asynchronously coupled, the direct adjustment to the CO_2 perturbation that would usually take 1000 - 2000 years in an ocean-atmosphere

model takes 100 000 - 200 000 simulation year in our setting, as the climate is only run every 100 ice sheet years. To this direct adjustment to the CO_2 forcing, feedbacks come into play as a result of a coupling to the ice sheet model. Indeed, as the ice sheet melts, the albedo and surface elevation decrease, resulting both in a temperature increase. Therefore, during the simulation, the Antarctic temperature increases as a result of both the adjustment to the 8xCO_2 perturbation applied (and the internal climatic feedbacks, excluding the ice sheet) and the feedbacks due to the ice sheet.

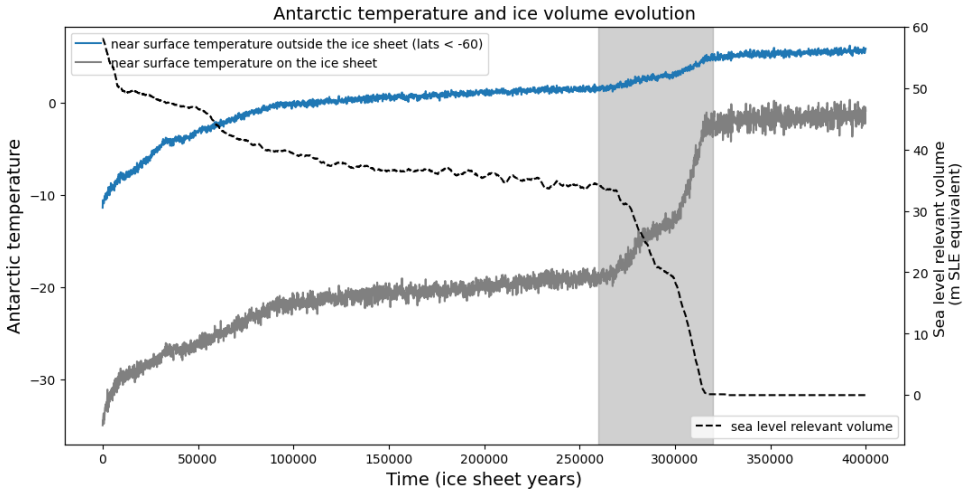

Figure 4.6: Left axis : Antarctic near surface temperature. Two definitions of the Antarctic temperature are shown : one on the ice sheet (in grey), the other outside (in blue). Right axis : the black dotted line represents ice-sheet volume (in m SLE).

Figure 4.6 represents the Antarctic temperature in parallel with the ice volume evolution. Two different Antarctic temperature are computed. First, the temperature is averaged on grid points that belong to the ice sheet at the start of the simulation (ice mask of the reference coupled ice sheet). This is displayed in grey in Figure 4.6. This corresponds to the average near surface temperature change on the initial Antarctic ice sheet and is due to the adjustment to the CO_2 perturbation, the change in albedo due to the ice sheet retreat (a lower albedo increases near surface temperature) as well as changes in surface elevation as the ice sheet melts (near surface temperature are higher for lower surface elevations). Second, the temperature is averaged on grid points of latitudes lower than 60° south, that are outside the ice sheet at the start of the simulation (ie outside the ice mask of the reference coupled ice sheet). These point remain outside the ice sheet for the whole simulation, as the ice sheet melts and does not grow outside the initial ice mask. This corresponds to oceanic points of latitudes lower than 60° and this temperature is therefore not directly influenced by the surface elevation

changes. It is visible on both Antarctic temperature that there is a slope change in the temperature evolution at the time where the East Antarctic part of the ice sheet starts to melt (starting around state (F), depicted with grey shading in Figure 4.6). This slope increase is due to the temperature feedback resulting from the ice sheet melt. In the case of the temperature outside the ice sheet, this is due to the albedo feedback, and in the case of the temperature on the ice sheet, this is due to both albedo and surface elevation changes. Within the initial ice sheet mask, the 8xCO_2 perturbation leads to an average +35°C temperature change as a result of adjustement to the CO_2 perturbation and the height and albedo feedback resulting from the ice sheet change. Outside the ice sheet, the temperature increase is around +17°C.

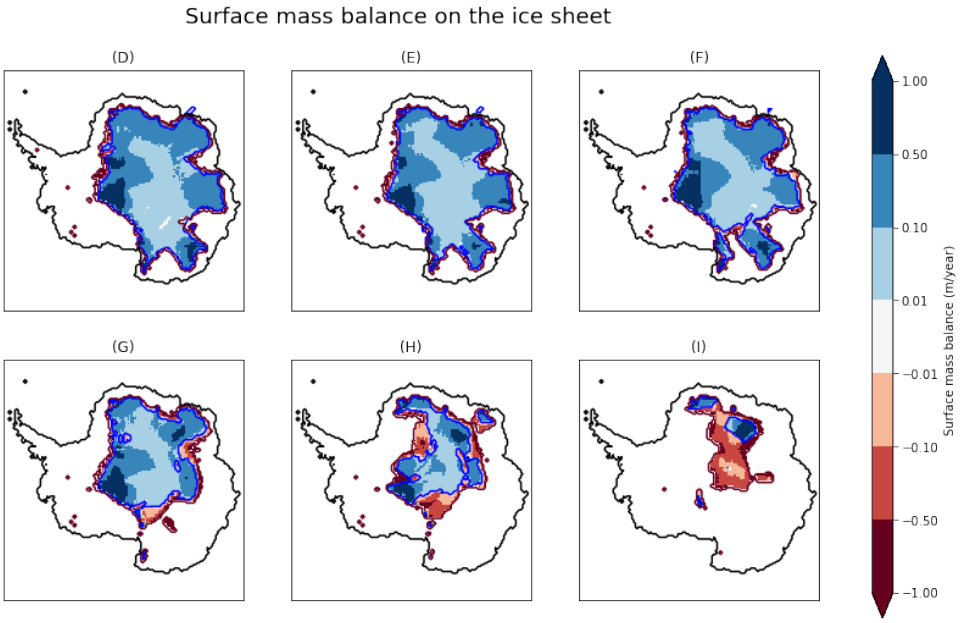

Figure 4.7: Surface mass balance over the ice sheet at different timesteps (8xCO_2 simulation). The contour of the ice sheet is represented in red and the boundary between positive and negative mass balance is represented in blue countour. Positive surface mass balance (accumulation) is displayed in blue while negative surface mass balance (melt) is displayed in red. The black contour represents the Antarctic ice contour at present day.

Figure 4.7 represents the surface mass balance over the ice sheet for the 8xCO_2 simulation. At state (D) and (E), the surface mass balance is mostly positive inside the ice sheet. The surface mass balance is slightly negative on the edges of the ice sheet. This leads to ice sheet melt on the sides of the ice sheet. This melt is however limited and the total ice mass remains mostly stable. As the ice sheet melts and its elevation decreases, the temperature becomes higher at the ice sheet

surface. Additionally, as the ice sheet contour evolves, the albedo is reduced outside the ice sheet, leading to higher temperatures locally and allowing further melt on the ice sheet edges. Around state (F), the melt increases largely, decreasing the surface mass balance and the ice sheet volume. At state (H), when the ice sheet has already retreated to about half of its initial extent in East Antarctica, the surface mass balance is not only negative on the edges of the ice sheet, but also on large parts inside, leading to faster mass loss.

4.1.2 . Simulations starting in a configuration without Antarctic ice sheet : growth branch

After having looked at the melt behaviour of the Antarctic ice sheet when higher CO_2 levels are applied, we have looked at the growth behaviour. To do so, a new initial condition is needed. We want to start in a configuration without Antarctic ice sheet, and look at its behaviour when lower CO_2 levels are applied. To do so, the growth simulations were started from the end of the 8xCO_2 melt simulation, and lower CO_2 levels were applied. At the end of the 8xCO_2 melt simulation, the atmospheric temperature is equilibrated. The oceanic temperature around Antarctica has not yet fully equilibrated at the end of the simulation and is increasing, as it is still adjusting to the ice sheet mass loss and the local temperature change it triggered. However, this is not problematic, as lower CO_2 levels are applied starting from this configuration, leading to lower temperatures. As the ice sheet model has run for more than 80 kyrs after the complete loss of the Antartic ice sheet in the 8xCO_2 melt simulation (from ice sheet years around 320 000 to the end of the simulation - 400 000), the bedrock has completely bounced back. In the following, the end of the 8xCO_2 melt simulation is called the "reference no Antarctic" configuration.

Starting from the reference no Antarctic configuration, simulations of 300 000 ice sheet years (3000 climate years with a coupling ratio of 100) with a lower CO_2 levels were performed in order to obtain equilibrated ice sheets and climate. The CO_2 levels applied at the start of the simulation are multiples of the pre-industrial CO_2 level (280 ppm): 6xCO_2, 4xCO_2, 2xCO_2, 1xCO_2, 0.8xCO_2 and 0.5xCO_2. Additional simulations between 2xCO_2 and 1xCO_2 levels were performed, starting from the end of the 2xCO_2 simulation : 1.75xCO_2, 1.5xCO_2 and 1.25xCO_2. The ice sheet state at the end of the 0.5xCO_2, 0.8xCO_2, 1xCO_2, 1.25xCO_2, 1.5xCO_2, 2xCO_2 growth simulations are displayed in Figure 4.8.

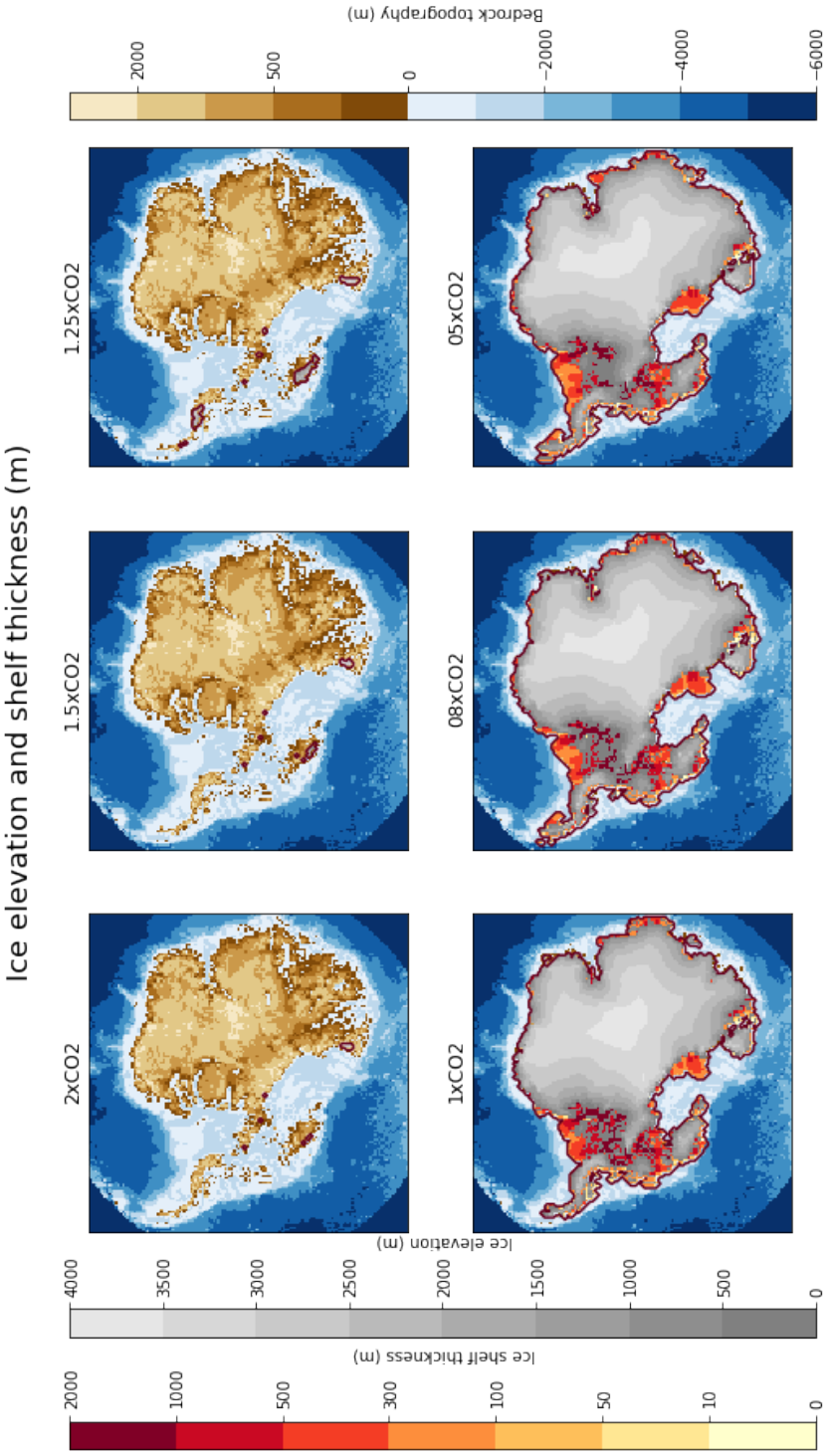

Figure 4.8: Ice sheet at the end of 0.5xCO_2, 0.8xCO_2, 1xCO_2, 1.25xCO_2, 1.5xCO_2, 2xCO_2 growth simulations.

At the end of the 2xCO_2, 1.5xCO_2 and 1.25xCO_2, the Antarctic ice sheet has not regrown at all. This was also the case at the end of the 6xCO_2 and 4xCO_2 simulations (not shown here). At the end of the 1.25xCO_2 simulation, there are limited ice caps, in the West and one in the East near Wilkes basin. However, the rest of the bedrock remains bare, and no marine ice sheet develop. However, at 1xCO_2, the final state of the ice sheet differs widely : the ice sheet has developed over all East Antarctica, although the ice sheet is less developed than in the reference pre-industrial configuration. There is ice on all parts of the West Antarctic ice sheet where the bedrock lies above sea level, and the Ronne Filchner ice shelf has recovered. However, the Ross ice shelf has not recovered. The sector of Pine Island is composed of ice shelves and is not grounded as it was in the reference PI configuration. The ice thickness difference between the regrown ice sheet (1xCO_2,0.8xCO_2 and 0.5xCO_2 growth simulations in panels (a), (b), (c)) and the reference ice sheet are plotted in Figure 4.9. The blue shading represents parts where the regrown ice sheet has more ice than the reference ice sheet, and conversely for red shadings. The yellow area represent parts where the regrown ice sheet is ice free, while there was ice in the reference ice sheet.

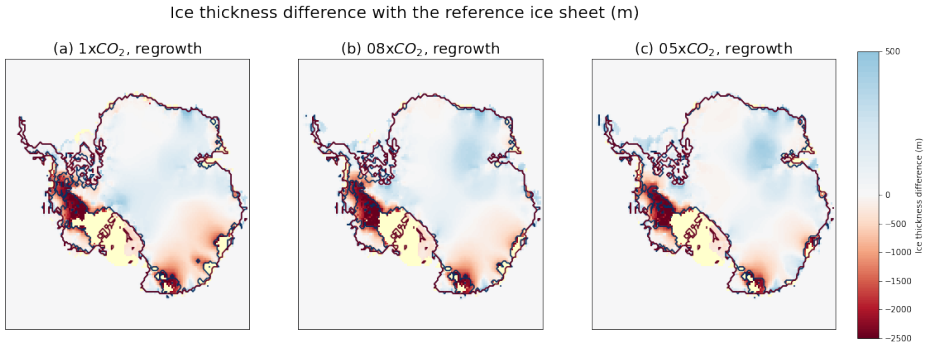

Figure 4.9: Ice thickness difference with the reference ice sheet for (a) the 1xCO_2 growth simulation, (b) the 08xCO_2 growth simulation, (c) the 05xCO_2 growth simulation. The grounding line of the reference ice sheet is depicted with red contour. The grounding line of the ice sheet at the end of the 1xCO_2, 0.8xCO_2, 0.5xCO_2, growth simulation is depicted in blue contour. The yellow shading represents parts where ice was present in the reference configuration and which are ice free for the regrown ice sheet.

It is striking that the final state of the 0.5xCO_2, 0.8xCO_2 and 1xCO_2 growth simulations are very similar. For the three simulations, the ice sheet grows back in East Antarctica, but the Ross shelf remains ice free and the Pine Island sector is not grounded. There are some differences in the Aurora sector, where the 0.8xCO_2 and 0.5xCO_2 simulated ice sheets are thicker than the 1xCO_2 : there are less ice free area (in yellow in Figure 4.9) and the ice thickness difference with the reference

ice sheet becomes lower.

In our model, there is no intermediate state between an absent Antarctic ice sheet (very limited ice caps at CO_2 levels higher or equal to 1.25xCO_2) and a widely developed Antarctic ice sheet (for CO_2 levels lower or equal to 1xCO_2). However, even for lower levels than PI (such as the 0.5xCO_2 and 0.8xCO_2 simulations), the ice sheet does not regrow to its full pre-industrial extent. This will be discussed in section 4.3.2.

In the following, we focus on the 1xCO_2 growth simulation. The ice mass evolution over the simulation as well as the ice sheet state at different timesteps are shown in Figure 4.10. Once again, due to our asynchronous coupling setup, these time do not correspond to transient times and we therefore refer to different ice sheet steps. The ice volume evolution as well as the Antarctic temperature evolution during the simulation are represented in Figure 4.11.

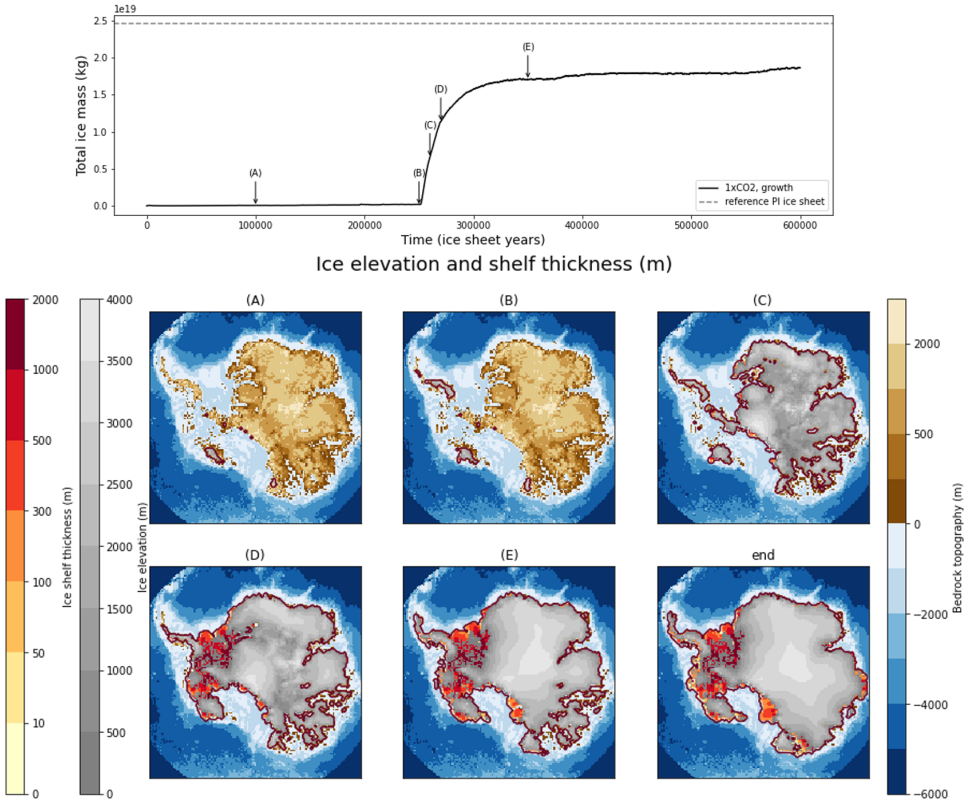

Figure 4.10: Total ice mass evolution and ice sheet state at different steps of the 1xCO_2 growth simulation.

At the start of the 1xCO_2 growth simulation (start of the simulation, state (A) to state (B) in Figure 4.10), only limited ice caps form. These ice caps are in parts of West Antarctica where the bedrock lies above sea level. From the start of the simulation to state (B), there is a decreasing temperature trend, due to the

adjustement to the CO_2 level, as the simulation is started from a configuration where 8xCO_2 was applied, and 1xCO_2 levels are applied at the beginning of the simulation. At that time, there are almost no feedbacks due to ice sheet changes (albedo changes or elevation changes), as the ice caps are very limited, and the decreasing temperature trend can therefore be attributed to the adjustment to CO_2 levels. From state (B), the ice sheet starts to grow, and the total ice mass increases quickly : from $2 \cdot 10^{17}$ kg at state (B) to $1.14 \cdot 10^{19}$ kg at state (D), which represents a change from less than 1% to 46% of the reference PI ice sheet mass. In our setting, this happens in 20 000 ice sheet year (200 climate year with a coupling ratio of 100). At the same time, starting from state (B), their is a marked slope change in the temperature curve : it decreases faster than before. This is due to the growth of the ice sheet that feedbacks on the climate system. As the ice sheet forms, this raises the albedo and decreases the temperature around. Also, as the surface elevation increases, the near surface temperature decreases.

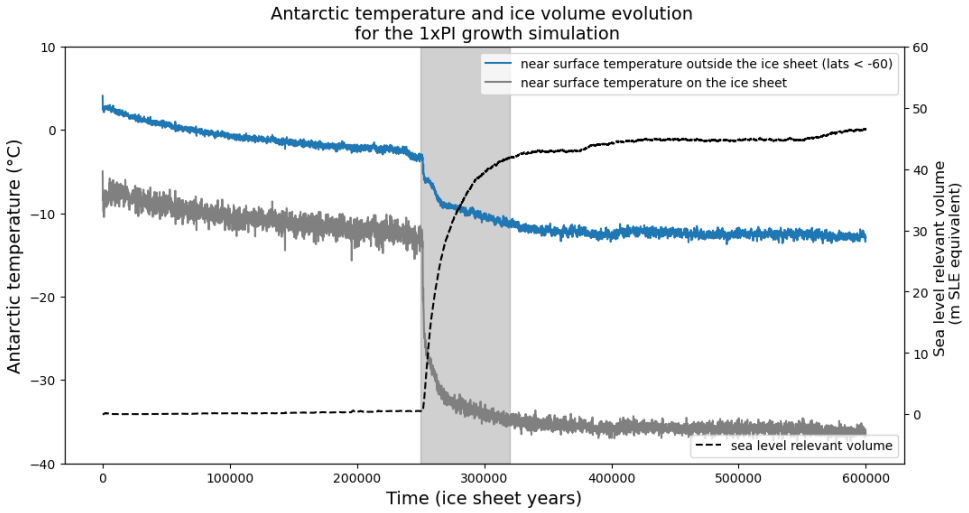

Figure 4.11: Left axis : Antarctic near surface temperature for the 1xCO_2 growth simulation. Two definitions of the Antarctic temperature are shown : one on the ice sheet (in grey), the other outside (in blue). Right axis : the black dotted line represents ice-sheet volume evolution (in m SLE) for the 1xCO_2 growth simulation.

Figure 4.11 shows two different Antarctic temperature, as in Figure 4.6. The near surface temperature outside the ice mask of the reference coupled ice sheet (in blue in Figure 4.11) decreases sharply after state (B), due to the albedo feedback. The near surface temperature inside the ice mask of the reference coupled ice sheet (in grey in Figure 4.11) is affected by both the albedo feedback and the height feedback.

A striking feature visible in Fig. 4.10 is that the ice sheet rapidly covers the whole continent : at state (B) there is limited ice, while at state (C), the ice sheet

covers the whole continent. Additional timesteps between state (B) and state (C) are shown in Figure 4.12. It takes around 2000 simulation years in our setting (20 climate years with a coupling ratio of 100, 2000 ice sheet years) for the ice sheet to extend to almost all the East Antarctic continent. Once the ice sheet has initiated, the albedo feedback and the consequent temperature drop it triggers, favors the ice sheet extension over the whole continent.

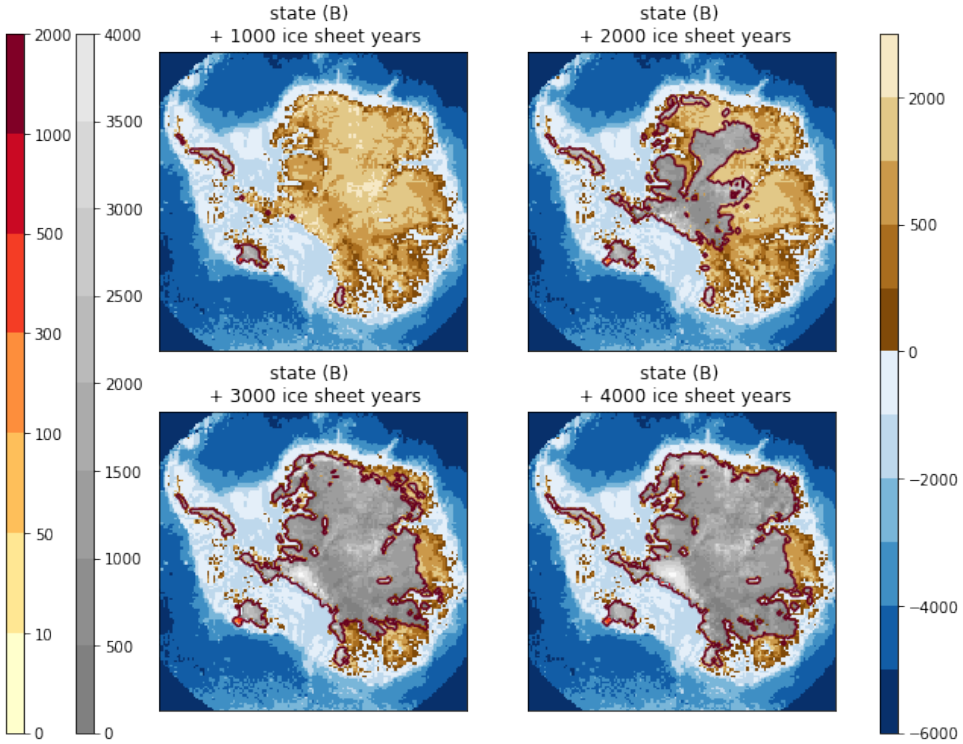

Figure 4.12: Total ice mass evolution and ice sheet state at different times of the 1xCO_2 growth simulation. The different timesteps are taken at state (B) + 1000, 2000, 3000 and 4000 ice sheet years (10, 20, 30, 40 climatic years with a coupling ratio of 100)

In the 1xCO_2 simulation, the ice sheet starts to grow when the temperature has decreased enough to allow for perennial snow to stay all year long in some locations. This highly increases the albedo at these locations, leading to lower temperatures that enable the formation of the ice sheet.

The coupled climate ice - sheet system exhibits a strong hysteresis behaviour : equilibrium ice sheet volume are very different for the same CO_2 levels if the simulation starts from the PI Antarctic ice sheet or without Antarctic ice sheet. Equilibrium ice sheet volumes for the melt and growth branch as a function of the CO_2 levels applied are displayed in Figure 4.13. Equilibrium ice sheet volumes for the melt and growth branch as a function of the global temperature change at the end of the simulation (relative to the reference pre-industrial configuration) are displayed in Figure 4.14. In our simulations, the hysteresis loop does not close, as the ice sheet does not regrow to its full extent, even for lower CO_2 values than PI. Possible explanations are discussed in section 4.3.2.

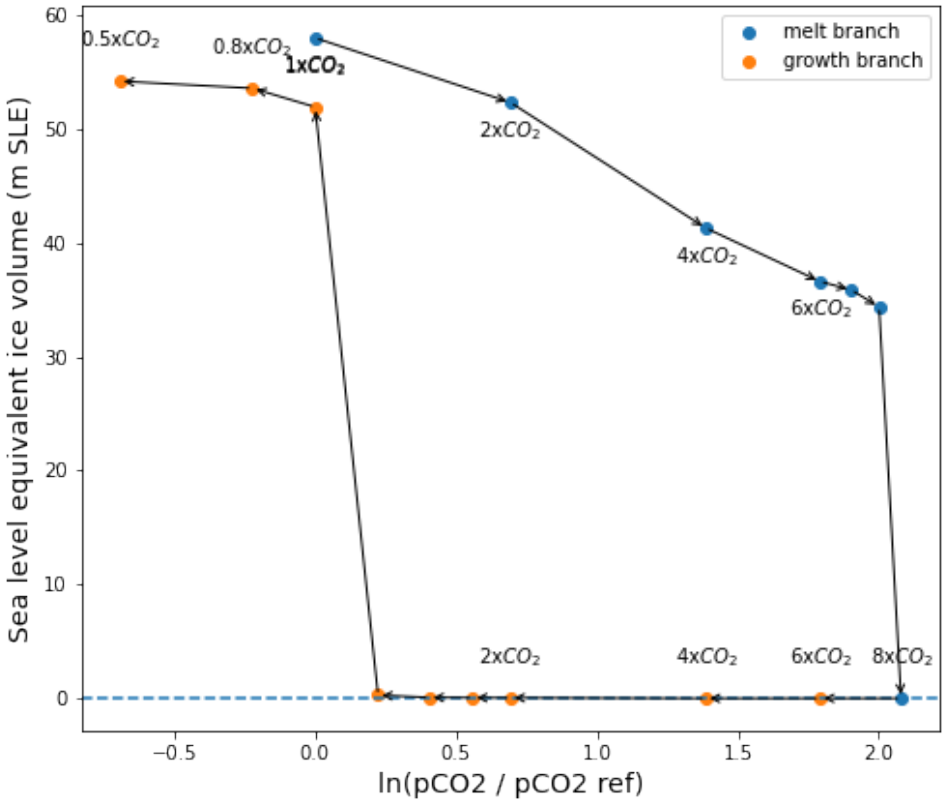

Figure 4.13: Sea level equivalent ice volume (m SLE) at the end of the different melt and growth simulations, as a function of the CO_2 level applied.

We emphasize the fact that the global mean temperature change at the end of the simulation does not correspond to a "threshold temperature" that leads to the obtained equilibrium, as it is influenced by the ice sheet feedbacks. In the case of the 8xCO_2 melt simulation, as the ice sheet melts entirely, this changes the albedo over the whole Antarctic continent and thus further increases the Global

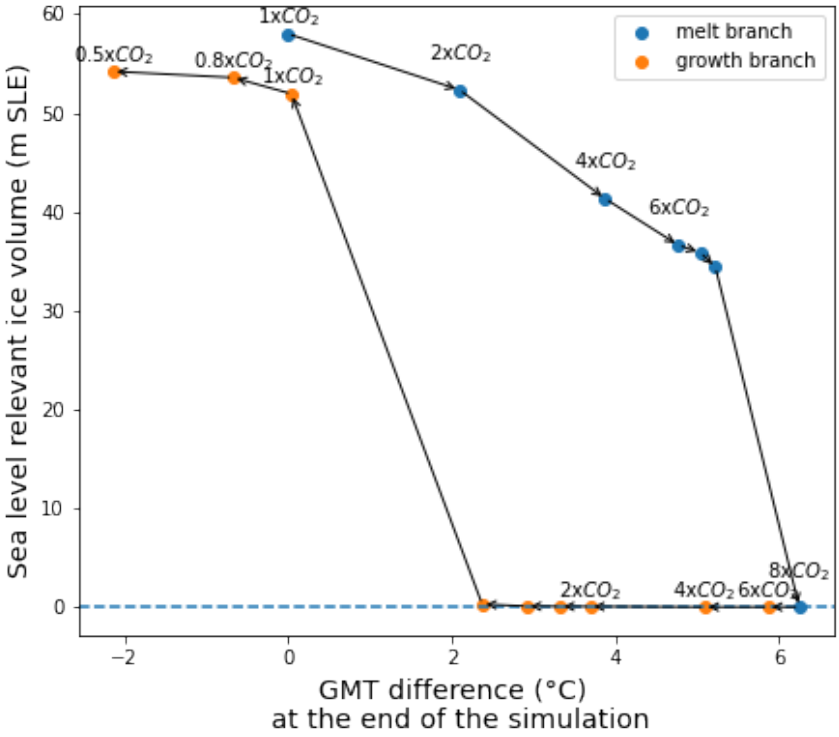

Figure 4.14: Sea level relevant ice volume (m SLE) at the end of the different melt and growth simulations, as a function of the global mean temperature change at the end of the simulation (relative to the reference PI configuration).

Mean Temperature. The Global Mean Temperature change leading to the complete disintegration of the ice sheet is thus lower than the Global Mean Temperature at the end of the simulation. Conversely, for the 0.5xCO_2, 0.8xCO_2 and 1xCO_2 growth simulations, the ice sheet grows back to a large extent of the pre-industrial configuration, and the consequent albedo changes over the Antarctic continent leads to a Global Mean Temperature decrease. The Global Mean Temperature at the end of the simulation is thus lower than the Global Mean Temperature limit, allowing the ice sheet to grow.

4.2 . Additional study : the role of insolation and of the albedo feedback

In this part, sensitivity studies to two important processes are carried out. First, a sensibility study to the insolation used in our simulations is performed. Indeed, the orbital parameters were kept fixed to their present-day values in our previous simulations. However, on the timescale of millenia, orbital parameters evolve and can impact the thresholds obtained previously. Second, the role of the albedo feedback is studied. A particularity of our coupled setting compared to studies that force ice sheet model with climatic fields (such as in Winkelmann et al. [2015], Garbe et al. [2020]) is that the albedo feedback can be taken into account. We therefore look at its influence on our results.

4.2.1 . Influence of the insolation

In the simulations carried out previously, the orbital parameters (eccentricity, precession and obliquity), were kept to their present day values. Although the mean energy received by the Earth only slightly varies with the eccentricity, orbital parameter variations have a strong influence on the energy quantity received on a specific latitude at a specific season. For a given eccentricity and precession, a higher obliquity corresponds to more energy received at the poles annually. For a given obliquity, the energy received at the summer solstice in the Southern hemisphere increases with the precession parameter, defined as esin(ω).
In the following, I have decided to focus on two idealized case in order to study the influence of the orbital parameters on the results and the thresholds of the hysteresis. I have considered the maximum and minimum December solstice insolation at 80°S on the next million years. The minimum december solstice insolation at 80°S is reached at 631 kyr AP, and the maximum at 642 AP (shown in Figure 4.15). The corresponding orbital parameters are summed up in Table 4.1. I carried out simulations in the melt branch with the maximum insolation, to see how the CO_2 threshold for complete Antarctic deglaciation (see section 4.1.1) varies with insolation. I also carried out simulations in the growth branch to see how the CO_2 threshold for Antarctic glaciation (see section 4.1.2) varies with insolation.

	PI	min inso	max inso
eccentricity	0.0167	0.0539	0.0480
precession angle (°)	102.4	263.16	88.12
obliquity (°)	23.45	22.79	23.62
december solstice insolation at 80°S (Wm^{-2})	553	469	594

Table 4.1: Values of eccentricity, precession angle and obliquity used in the different simulations. The corresponding december solstice insolation value at 80°S is also shown.

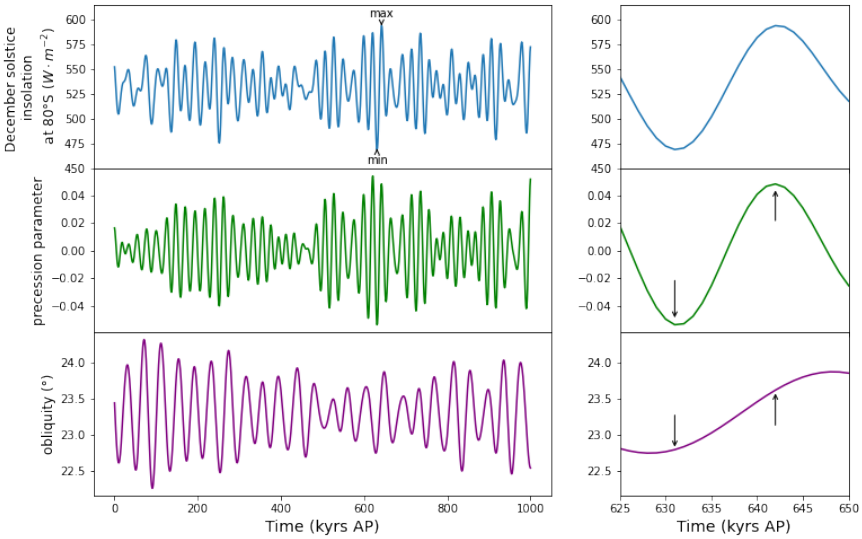

Figure 4.15: (top) December solstice insolation at 80°S over the next million year, (middle) precession parameter on the next million year, (bottom) obliquity over the next million year.

Influence of the insolation on the melt branch

First, I carried out simulations at 2xCO_2, 4xCO_2, and 6xCO_2 levels with the "max inso" configuration (starting from the 2xCO_2, 4xCO_2, and 6xCO_2 simulations with present-day insolation respectively). The ice sheet at the end of the 2xCO_2, 4xCO_2, and 6xCO_2 "max inso" melt simulations are shown in panels (d), (e), (f) of Figure 4.16, and compared with the ice sheet at the end of the 2xCO_2, 4xCO_2, and 6xCO_2 with present-day insolation simulations (panels (a), (b), (c)). The two equilibrium ice sheet at the end of the 2xCO_2 simulations look very similar, independently from the insolation applied. At 2xCO_2 levels, a higher insolation than the present-day does not impact much the ice sheet obtained. In the case of the 4xCO_2 and 6xCO_2 levels, the situation is very different than with 2xCO_2 levels. With the present day insolation, a large ice sheet in East Antarctica remains for 4xCO_2 and 6xCO_2 levels, with also grounded ice in parts of West Antarctica whose bedrock lie above sea level for the 4xCO_2 simulation. With the maximum insolation, there is almost no ice at all in Antarctica at the end of the 4xCO_2 simulation, with only a small ice cap remaining, close to the Dronning Maud land sector, where the bedrock topography is high. For the 6xCO_2 maximum insolation simulation, there is no ice at all at the end of the simulation. These simulations highlight the fact that the orbital configuration can largely impact the CO_2 threshold for Antarctic deglaciation. As explained earlier, there is a

critical threshold in our simulation for which the Antarctic ice sheet switches from a developped East Antarctic ice sheet to no ice sheet at all. This threshold depends on both CO_2, and insolation. A stronger Southern Hemisphere summer insolation will decrease the CO_2 level at which the Antarctic ice sheet disappears. With the present-day insolation, the CO_2 threshold is between and 7.4 and 8xCO_2, whereas it is between 2 and 4xCO_2 in the case with the maximum insolation.

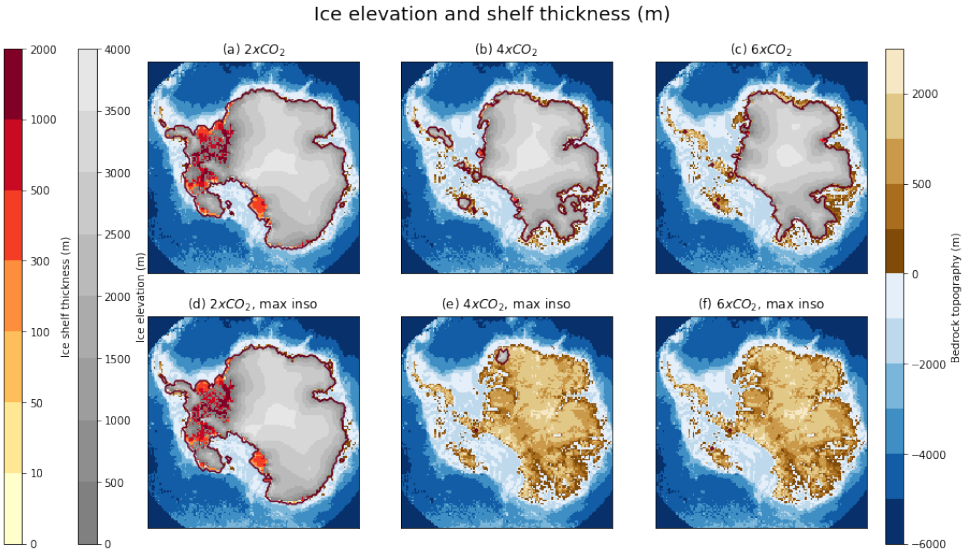

Figure 4.16: Ice sheet at the end of the simulation. Panels (a) -(f) : 2xCO_2, 4xCO_2 and 6xCO_2 simulations, with present-day or maximum insolation.

Influence of the insolation on the growth branch

In the growth simulations with the present-day orbital configuration, the ice sheet did not regrow at 2xCO_2. And the threshold leading to glaciation was found between 1.25xCO_2 (limited ice caps in West Anatrctica) and 1xCO_2 (widely developped ice sheet). Here, a growth simulation with 2xCO_2 levels and the "min inso" orbital parameters was performed, in order to determine if insolation changes can change the previously obtained threshold for Antarctic glaciation.

The ice sheet obtained at the end of the 2xCO_2 "min inso" growth simulation is shown in panel (b) of Figure 4.17, and compared with the ice sheets obtained at the end of the 2xCO_2 and 1xCO_2 growth simulation with present-day insolation (panels (a) and (c) of Figure 4.17).

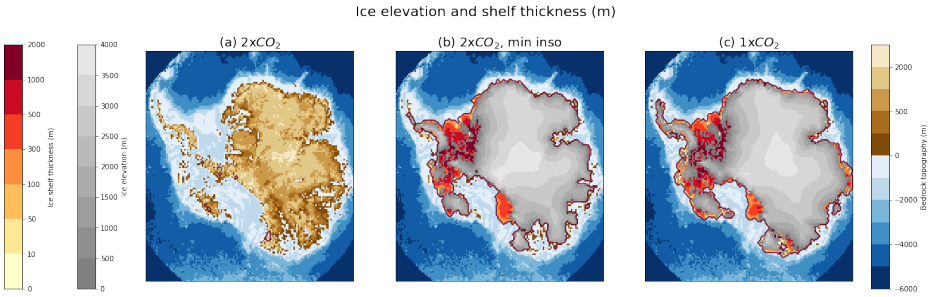

Figure 4.17: Ice sheet at the end of the simulation. Panel (a) : 2xPI simulation, with present-day insolation. Panel (b) : 2xPI simulation, with the minimum insolation. Panel (c) : 1xPI simulation, with present-day insolation.

With the minimum insolation, the ice sheet grows at 2xCO_2 levels, which was not the case with the present-day insolation. Changing the insolation changes the CO_2 threshold for Antarctic glaciation. The ice sheet obtained at 2xCO_2 with the minimum insolation is widely developed over East Antarctica and resembles the ice sheet obtained at 1xCO_2 with the present day insolation. There are however difference between the 2xCO_2 min inso and 1xCO_2 equilibrium ice sheet, notably in the marine parts of the East Antarctic Ice Sheet. At 2xCO_2 with the minimum insolation, the ice sheet has not regrown to its pre-industrial extent in the Wilkes and Aurora sectors. This is also visible in Figure 4.18, that displays the differences of the equilibrium 2xCO_2 min inso and 1xCO_2 regrowth ice sheets with the pre-industrial reference ice sheet. Additionnaly, a growth simulation with the "min inso" orbital parameters and CO_2 levels of 4xCO_2 was also carried out. In this case, no ice sheet forms on Antarctica.

In our simulations, the threshold for Antarctic glaciation with present day insolation is between 1 and 1.25xCO_2 levels. With the minimum insolation, this threshold is crossed for CO_2 levels between 2xCO_2 and 4xCO_2.

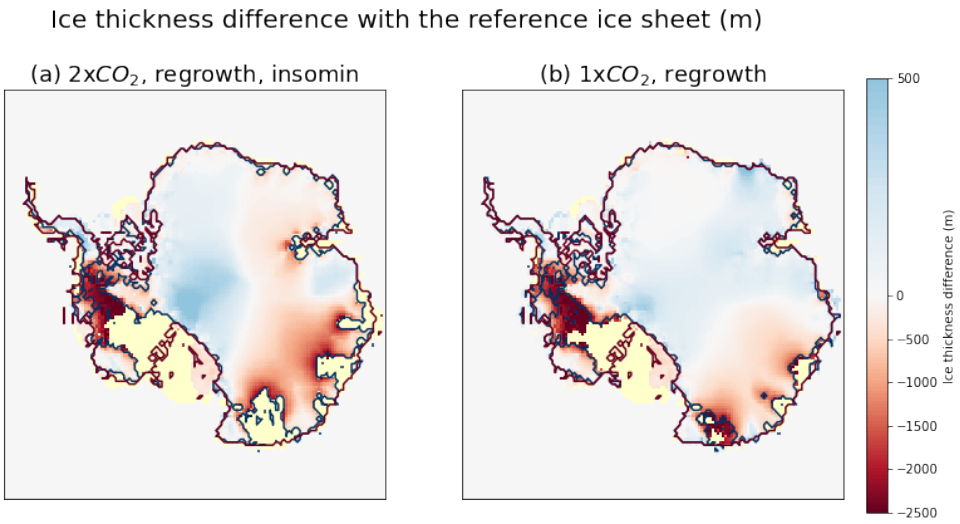

Figure 4.18: Ice thickness difference with the reference ice sheet for : (a) the 2xCO_2 min insolation growth simulation, (b) the 1xCO_2 growth simulation. The grounding line of the reference ice sheet is depicted with red contour. The grounding line of the ice sheet at the end of the simulation is depicted in blue contour. The yellow shading represents parts where ice was present in the reference configuration and which are ice free for the regrown ice sheet.

The equilibrium ice volume of the simulations carried out with the present day insolation, as well as with a different insolation than present-day (2xCO_2, 4xCO_2 with a maximum insolation for the melt branch and 2xCO_2, and 1.25xCO_2 with a minimum insolation for the growth branch) are depicted in Figure 4.19.

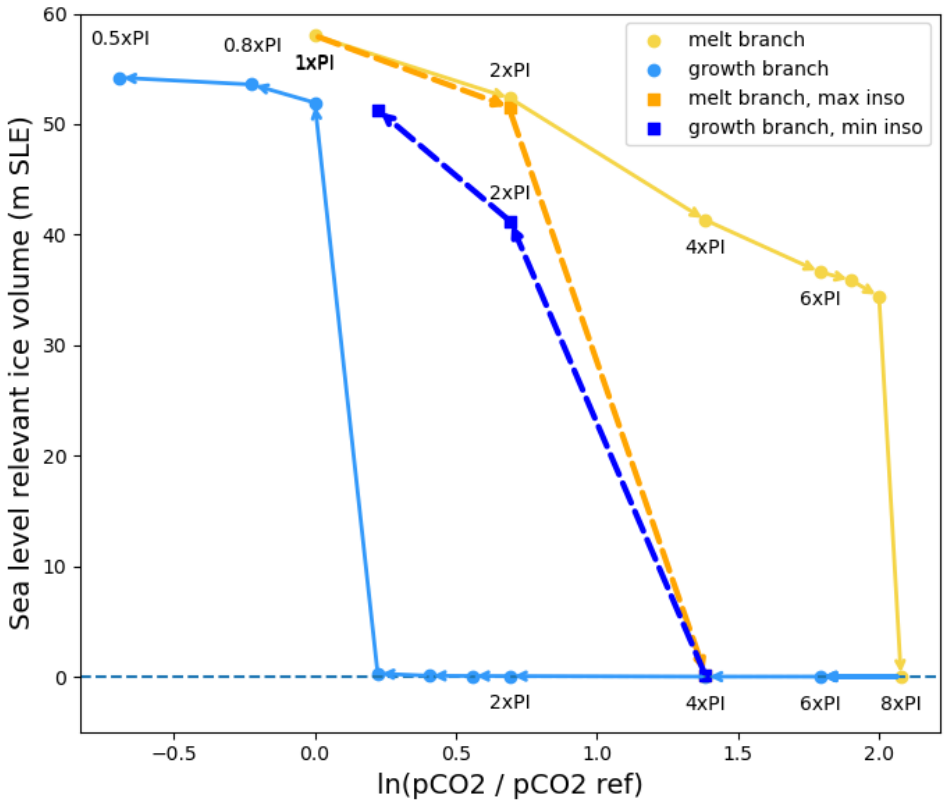

Figure 4.19: Sea level equivalent ice volume (m SLE) at the end of the different melt and growth simulations, as a function of the CO_2 level applied. The simulations with present-day insolation are marked with circles. The simulations with maximum insolation for the melt branch are depicted in orange squares(2xCO_2, 4xCO_2). The simulations with minimum insolation for the growth branch are depicted in blue squares (4xCO_2, 2xCO_2, and 1.25xCO_2).

These simulations with a higher or lower summer insolation in the South than at present-day highlight the fact that the orbital configuration can impact the CO_2 threshold for Antarctic glaciation and deglaciation. With the "optimal" insolation, the threshold for Antarctic glaciation and deglaciation are closer to another : the deglaciation threshold is between 2 and 4xCO_2 with the highest insolation and the glaciation threshold is also between 2 and 4xCO_2 with the minimum insolation.

In our simulations, at CO_2 levels around three times the pre-industrial value, both states (ice being present on Antarctica or not) can be stable, depending on the insolation. This suggests a possibility to obtain oscillations of the Antarctic ice sheet at CO_2 levels around 3xCO_2, due to the varying insolation. However, the simulations performed here remain idealized as the orbital parameters remain fixed throughout the simulations, and transient simulations would be needed to investigate this possibility.

4.2.2 . Influence of the albedo feedback

In this part, we focus on the albedo feedback and its influence on our simulations. The objective is double. First, to determine the role played by the albedo feedback and second, being able to compare our work to studies that do not take this feedback into account. To do so, I have performed simulations with the coupled setting used in 4.1, with the notable exception that the albedo on the Antarctic continent is kept fixed and does not varry when the ice sheet melts. This conceptually corresponds to painting the Antarctic continent in white. These simulations are called "melt simulations without albedo feedback" in the following. Starting from the reference PI configuration, different CO_2 levels were applied : 2xCO_2, 4xCO_2, 6xCO_2, 8xCO_2 and 16xCO_2. The simulations were run for 300 000 ice sheet years (3000 climate years with a coupling ratio of 100). The state of the ice sheet at the end of the simulations is displayed in Figure 4.20 and compared to the state of the ice sheet at the end of the simulations including the albedo feedback for the same CO_2 levels. The fact that the albedo is kept constant impacts two components of our model. First, the albedo is used to compute the melt with the insolation temperature melt (ITM) method (see section 3.3.1 and Equation 3.12), and in this setup albedo changes are not taken into account in the ITM computation. Second, albedo changes lead to local temperature changes, which also affects the melt (see equation 3.12).

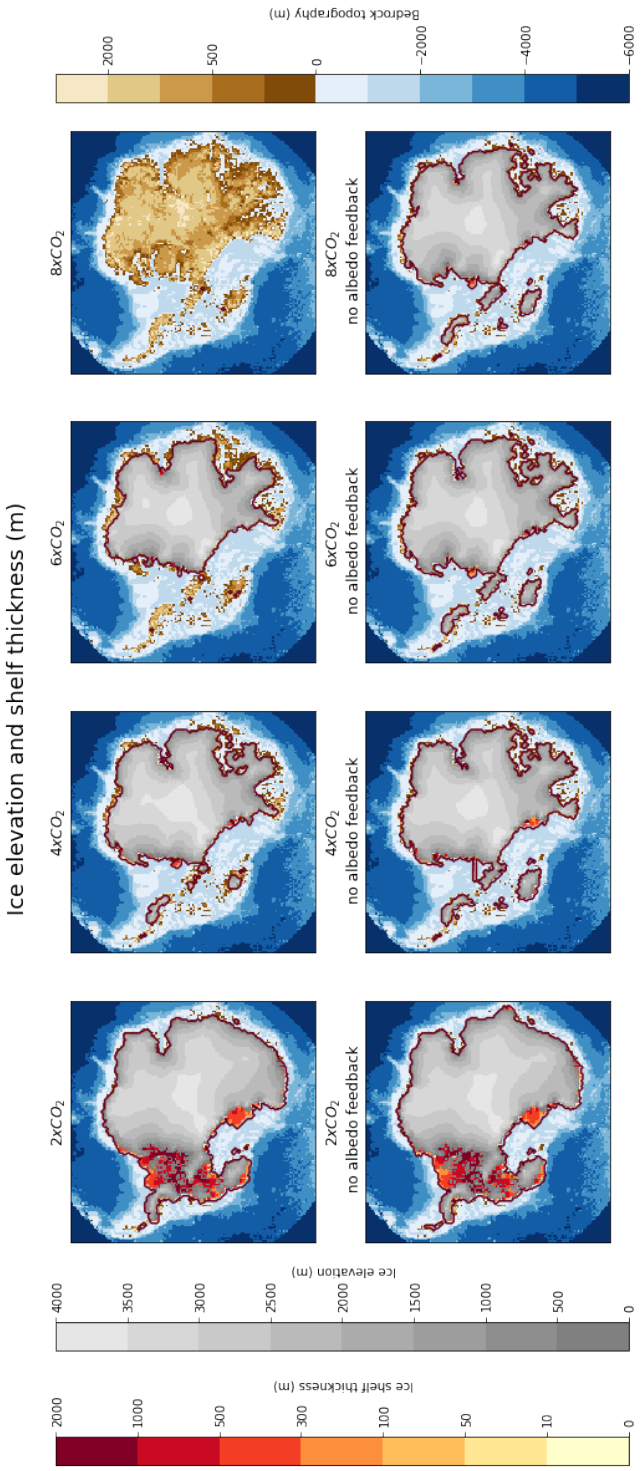

Figure 4.20: Antarctic ice sheet state at the end of the 2xCO_2, 4xCO_2, 6xCO_2, 8xCO_2 melt simulations with and without the albedo feedback.

For the 2xCO_2 melt simulations, taking into account or not the albedo feedback does not change significantly the equilibrium ice sheet. At 4xCO_2, some difference appear between the simulations with and without albedo feedback. Without the albedo feedback, the ice caps remaining in West Antarctica are more extended, and the ice sheet does not retreat as much in the Wilkes basin. For the 6xCO_2, the differences become stronger between the two simulations : there are still ice caps in West Antarctica when the albedo feedback is not taken into account while they have disappeared when the albedo feedback is taken into account. On the edges of the Eastern part, the ice sheet retreats less without albedo feedback. However, the most striking difference appears at 8xCO_2. While in the simulation with albedo feedback, surface melt has led to the disappearance of the whole ice sheet, there remains a large East Antarctic ice sheet when the albedo feedback is not taken into account. As could have been expected, taking into account or not the albedo feedback does not change anything to the loss of marine ice sheet parts, that are lost due to basal melting. However, taking into account the albedo feedback leads to strong differences in the parts that are lost due to surface melt. When the albedo does not change, the melt of ice sheet edges do not raise the temperature locally at the new ice sheet edges, and this does not lead to additional melt, contrary to the case with albedo feedback. Additionally, in the reference setting (with albedo feedback), the albedo on the downscaled grid, that is used to compute the melt with the ITM is first interpolated from the coarser T21 grid. Then, a linear correction with the altitude is performed, that leads to lower albedo values at lower altitude (see Section 3.3.1). In the case without albedo feedback, the albedo is always fixed to the ice sheet value, and thus there are no lower values at the ice sheet edges, that could facilitate ice sheet melt.

After having seen that the albedo feedback plays a key role in ice sheet loss due to surface melt, I choose to investigate its impact on the hysteresis behaviour of the ice sheet. A possibility is to perform simulations without albedo feedback with higher CO_2 levels, where the ice sheet melts completely and then lower the CO_2 level and let the ice sheet regrow. However, without enabling the albedo feedback (albedo on the Antarctic continent remains fixed at the ice sheet albedo value, whether ice is being present or not), it was not possible to melt entirely the Antarctic ice sheet. Indeed, a large East Antarctic ice sheet remained up to 16xCO_2 levels. As its radiative code is based on the linearization of the radiative code of a GCM, the iLOVECLIM model is not suited for very high CO_2 levels. To circumvent this problem, simulations without the albedo feedback but with artificially "enhanced melt" were performed. More specifically, we modified the surface melt (equation 3.12). The λT_s term is replaced by $\lambda T_{PI} + \lambda\beta(T_s - T_{PI})$ where T_{PI} is a temperature obtained with a reference pre-industrial simulation. The temperature depends on the location and the time of the year, $T_{PI}(lat, lon, day)$. For values of β higher than one, this corresponds to artificially increasing the temperature difference to PI seen by the ice sheet. Thus, taking $\beta > 1$ produces

an enhanced melt compared to our default simulations and $\beta < 1$ a reduced melt. Here, we have taken $\beta = 1.5$. This allows us to have a stronger melt given as input to the GRISLI ice sheet model, without modifying the climate computed by the iLOVECLIM model. In the following, these simulations are called "enhanced melt simulation".

Simulations of 300 000 ice sheet years (3000 climatic years with a coupling ratio of 100), starting from the reference pre-indutrial configuration were performed for different CO_2 levels : 2xCO_2, 4xCO_2, 6xCO_2, 8xCO_2, 10xCO_2 and 16xCO_2 (melt branch). In the 16xCO_2 enhanced melt simulation, only ice caps remain in high altitude regions such as the Transantarctic mountains and Dronning Maud Land. From the end of the 16xCO_2 enhanced melt simulation, simulation with lower CO_2 levels were carried out : 10xCO_2, 8xCO_2, 6xCO_2, 4xCO_2, 2xCO_2 and 1xCO_2 (melt branch). The corresponding ice sheet state is shown in Figure 4.21. The corresponding hysteresis curve is shown in Figure 4.22. We emphasize that these results cannot be compared with the results of section 4.1 according to the CO_2 level, as we have artificially increased the temperature in the melt equation. However, the "enhanced melt" simulation can still give us insights into the system behaviour when no albedo feedback due to ice sheet retreat or regrowth is taken into account.

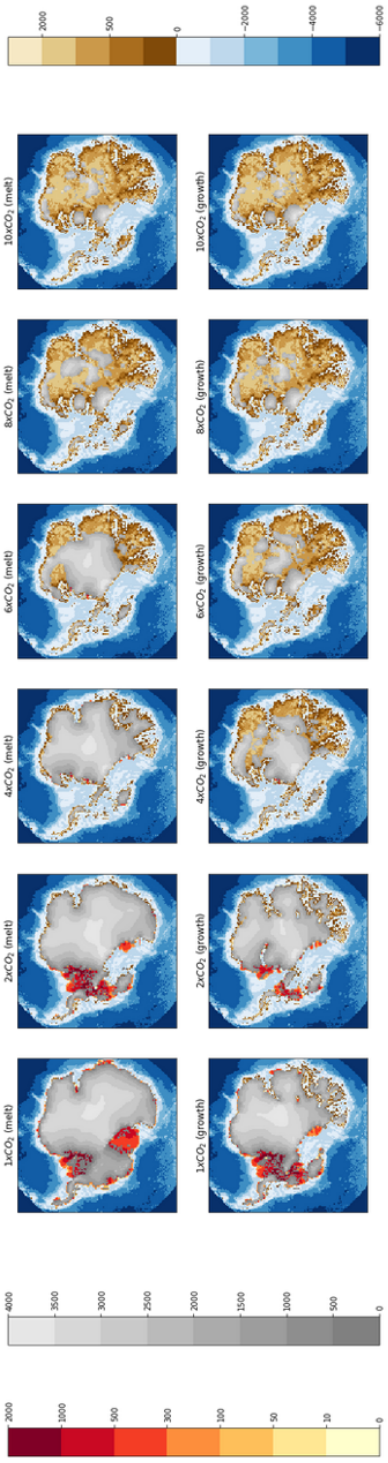

Figure 4.21: Antarctic ice sheet state at the end of the 2xCO_2, 4xCO_2, 6xCO_2, 8xCO_2 and 16xCO_2 enhanced melt simulations (not taking into account the albedo feedback). Both branches (melt and growth) are shown.

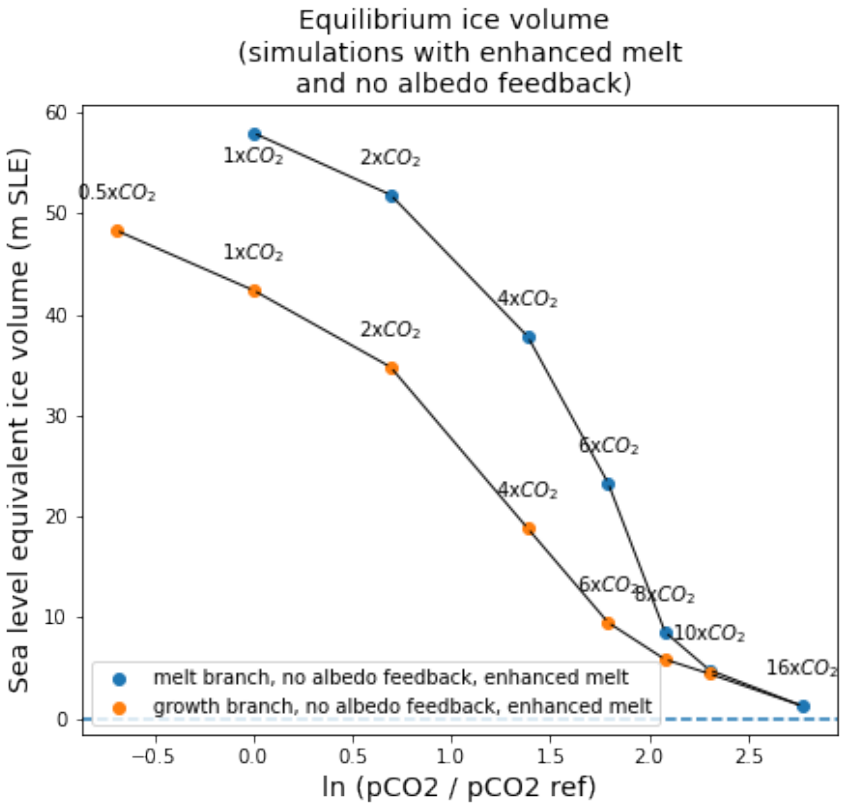

Figure 4.22: Sea level equivalent ice volume (m SLE) at the end of the "enhanced melt, no albedo feedback" simulations, as a function of the CO_2 level applied. We emphasize that these results cannot be compared with the results of section 4.1 according to the CO_2 level, as we have artificially increased the temperature in the melt equation.

There is a major difference between the simulations with and without albedo feedback in the growth and melt behaviour. In the simulations with albedo feedback, there are critical thresholds : once a CO_2 threshold is crossed, the ice sheet state is very different from before this threshold. This is the case in both the melt and growth branch. In our melt simulations with albedo feedback, the ice sheet final state switches from an extended East Antarctic ice sheet at 7.4xCO_2 (34m SLE) to no ice sheet at all at 8xCO_2. In our growth simulations with albedo feedback, the ice sheet final state switches from reduced ice caps in a very limited amount of regions (amounting to only 0.3 m SLE) to a fully developed ice sheet (at the exception of some parts in West Antarctica) for CO_2 values around 1xCO_2 (47 m SLE). However, these critical thresholds do not exist anymore in the simulations without albedo feedback. There are intermediate states in the Antarctic ice sheet. For instance, at 6xCO_2 in the melt branch, there is a stable ice sheet in part of East Antarctica (23m SLE), with a reduced extent compared to the 4xCO_2

simulation. At 4xCO_2 in the growth simulation, a large ice sheet has developed (19 m SLE), but it does not extend to the whole Antarctic continent. For the simulations without albedo feedback, the hysteresis is less pronounced than with albedo feedback. Even without the albedo feedback, there is still a pronounced hysteresis behaviour, especially around 4xCO_2 CO_2 levels where the sea level relevant volume difference between the melt and regrowth phase amounts 19m. For large CO_2 values (larger than 8xCO_2) the difference between the melt and growth branch diminishes, and ice caps only exist in high altitude regions in both cases. As for the simulation with albedo feedback, the ice sheet does not regrow to its initial extent.

These additional simulations show that inclusion of the albedo feedback gives rise to critical thresholds, that lead to the complete loss of the Antartic ice sheet or its almost complete regrowth, that are not obtained in simulations without albedo feedback (there are intermediate ice sheet states). Therefore, we suggest that studies on the future long term Antarctic ice sheet evolution not taking into account the albedo feedback might underestimate the thresholds for Antarctic melt, and that more sudden ice sheet mass loss once a threshold is crossed could be expected.

4.3 . Discussion

4.3.1 . Comparison with the litterature

The fact that the Antarctic ice sheet exhibits hysteresis is consistent with other studies [Pollard and DeConto, 2005, Garbe et al., 2020, Stap et al., 2022]. In the following, we compare our results with studies having performed hysteresis curves for the Antarctic ice sheet, and to studies focusing on the Antarctic glaciation at the Eocene-Oligocene transition.

The Eocene-Oligocene transition represents an important shift in the Earth's climate, marking the transition from the Eocene "Warmhouse" to the Oligocene "Coolhouse" [Westerhold et al., 2020]. A long term decline in global temperatures and atmospheric CO_2 concentration [Anagnostou et al., 2020, Rae et al., 2021] culminated in the rapid expansion of the Antarctic ice sheet [DeConto and Pollard, 2003a, Westerhold et al., 2020]. The suggested cause for the Antarctic expansion are oceanic circulation (and associated ocean heat transport) changes, due to the opening of Southern Ocean gateways [Kennett, 1977, Bijl et al., 2013], a decrease in atmospheric CO_2 [DeConto and Pollard, 2003a] and favorable insolation [Coxall et al., 2005].

Several modeling studies have investigated the CO_2 threshold for Antarctic glaciation. DeConto and Pollard [2003a] have estimated that the Antarctic ice sheet could reach a continental scale when atmospheric CO_2 levels were around 2.5-3xCO_2 (700-840 ppm). Ladant et al. [2014] estimated this threshold to be rather around 900 ppm (3.2xCO_2). Gasson et al. [2014] forced an ice sheet model with different GCMs, and found that the threshold was between 560 and 920 ppm (between 2xCO_2 and 3.3xCO_2), except for one model (HadCM3L) that did not produce Antarctic glaciation, even for pre-industrial CO_2 levels (280 ppm). The values around 700-900 ppm are in the range of published CO_2 values for this period with marine proxies [Pagani et al., 2011, Pearson et al., 2009, Rae et al., 2021]. For instance, Rae et al. [2021] suggests that CO_2 levels have fallen from $\sim$ 1000 ppm (3.6xCO_2) in the late Eocene Warmhouse to below $\sim$ 800 ppm (2.9xCO_2) at the Eocene Oligocene boundary. However, Steinthorsdottir et al. [2016] pointed out that reconstructed CO_2 values with terrestrial proxies such as fossil plant stomata are significantly lower than when using marine CO_2 proxies, with CO_2 levels estimated around $\sim$410 ppm (1.5xCO_2) at the Eocene-Oligocene boundary. Thus, CO_2 reconstructions differ widely among proxies used. Even when using the same proxy there remains a large spread in this period (as visible for instance with the alkenone and boron CO_2 proxy on Figure 1.4 of section 1.1.2), and it cannot be excluded that CO_2 varied on orbital timescale in addition to the decreasing trend from the Eocene to the Oligocene.

At the Eocene, the paleogeography and the Antarctic bedrock topography were different than at present. The bedrock topography can influence the CO_2 threshold for Antarctic glaciation. For instance, Van Breedam et al. [2022] found

that the threshold could vary between CO_2 levels lower than 620 ppm to 880 ppm (from less than 2xCO_2 to 3.1xCO_2), depending on the bedrock topography, with a lower bedrock topography leading to a lower threshold. Paleotopographic reconstructions for West Antarctica and the East Antarctic marine basins 34 Ma ago [Paxman et al., 2019, Wilson et al., 2012] show that they were largely above sea level at that time. Thus Antarctica could hold more terrestrial ice than today, even with a warmer climate, as the cooling threshold necessary to allow a high elevation terrestrial-based ice sheet to develop is lower than that of a marine-based ice sheet, that are highly sensitive to oceanic heat fluxes [Wilson et al., 2013, Galeotti et al., 2022].

In our simulations, the threshold for Antarctic glaciation varies with insolation. It is between 1 and 1.25xCO_2 in a case with present day insolation and between 2xCO_2 and 4xCO_2 in a case with minimal insolation. This is coherent with previous studies. Pollard and DeConto [2005] carried out experiments with decreasing CO_2 levels until the Antarctic ice sheet grows, and then increasing CO_2 levels until the ice sheet melts. They performed different experiments : in a case they include orbital variability, while the insolation was kept fixed in another case. They showed that varying insolation allowed to reach earlier the thresholds than when there is no orbital forcing (a higher CO_2 threshold is obtained for glaciation when insolation is decreased, and a lower CO_2 threshold is obtained for deglaciation when insolation is increased). Van Breedam et al. [2022] also found that there was a range of CO_2 threshold to glaciation for a given bedrock topography depending on the orbital forcing.

Due to the dependency of the CO_2 threshold for Antarctic glaciation to paleogeography, bedrock topography and insolation, it is not straightforward to compare the CO_2 threshold we obtain to modeling studies specifically performed on the Eocene-Oligocene transition. Additionally our simulations are equilibrium simulation with fixed CO_2 levels and orbital configuration, while most of the studies had varying orbital parameters through the course of the simulation.

In our study, once the glaciation threshold is crossed, the ice sheet extends to a large area of the continent rapidly. This differs from other studies such as DeConto and Pollard [2003a,b], Pollard and DeConto [2005], Ladant et al. [2014], where there are several thick ice caps that form on higher elevation areas and then join to form the Antarctic ice sheet. This difference might be due to the different methodologies used. These studies ([DeConto and Pollard, 2003a,b, Pollard and DeConto, 2005, Ladant et al., 2014]), used a climate matrix method to interpolate climate between different CO_2 levels and ice sheet sizes (see section 1.2.2). This method allows them to take into account feedbacks between ice sheet and climate, but the albedo feedback might be underestimated. For instance Pollard and DeConto [2005] state that with their methodology (being the same as in DeConto and Pollard [2003a,b]) "[...] the albedo feedback of ice sheet extent on the climate is only roughly captured, and not at all for sudden transitions".

Therefore, we suggest that the Antarctic glaciation could be more brutal than suggested by previous modelling studies, due to the albedo feedback, with an ice sheet rapidly extending in area. However, the albedo effect might be overestimated in our simulations, as will be explained in Section 4.3.2.

Our results with and without the albedo feedback show that the inclusion of the albedo feedback gives rise to sharper transitions, between a glaciated East Antarctic ice sheet and an ice free Antarctic, or between an ice free Antarctic and a widely developed ice sheet. In the work of Garbe et al. [2020] or Pollard and DeConto [2005] that do not include the albedo feedback, there are more intermediate steps possible in the melt and growth branch.

For the melt of the Antarctic ice sheet, the most comparable study to our results is the one of Garbe et al. [2020]. Garbe et al. [2020] performed simulations of the Antarctic ice sheet starting from both the current Antarctic configuration towards an ice free Antarctica and a configuration without ice towards a glaciated Antarctica (melt and growth branch). However, our simulations cannot be compared in terms of CO_2 levels as they applied temperature anomalies and not CO_2 level. In their study, global mean temperature anomalies are scaled to regional atmospheric Antarctic temperature changes and oceanic Antarctic temperature changes, using constant proportionality factors : a constant scaling factor of 1.8 for atmospheric temperature variation for latitudes lower than 66°S (Antarctic near surface temperature) compared to global mean temperature difference, and a constant ratio of 0.7 for oceanic temperatures compared to the global mean temperature difference. The changes in oceanic temperature are used to compute basal melt rates using the PICO model [Reese et al., 2018]. The changes in Antarctic near surface temperature are used to compute the surface mass balance, through a Positive Degree Days (PDD) scheme [Reeh, 1991]. In this approach the elevation / surface mass balance feedback (see section 1.2.2) is taken into account via the use of an atmospheric lapse rate. However, their approach does not take into account the albedo feedback, as the PDD formulation does not depend on albedo and near surface Antarctic temperature changes are always scaled with the same scaling factor (1.8) to global mean temperature increase, which conceptually corresponds to a constant polar amplification. This does not take into account the fact that a lower albedo as the ice sheet retreats will increase temperatures locally, and thus polar amplification. Figure 4.23 displays the results of the equilibrium simulations carried out by Garbe et al. [2020] for every degree of global mean temperature anomaly with the pre-industrial climate. Results of the equilibrium simulations of Garbe et al. [2020] are compared with the results we obtained in Section 4.1. For our results, the global mean temperature difference is taken at the end of the simulation. However we emphasize the fact that while global mean temperature difference is solely a forcing in the study of Garbe et al. [2020], it is not with our coupled climate-ice sheet setting, as the global mean temperature increase is influenced by both the CO_2 forcing, and the feedbacks due to the (partial or complete)

ice sheet retreat. In other words, the global mean temperature at the end of the melt simulations is higher than the global mean temperature needed to trigger the obtained ice sheet retreat. As previously noted, the presence of brutal transitions

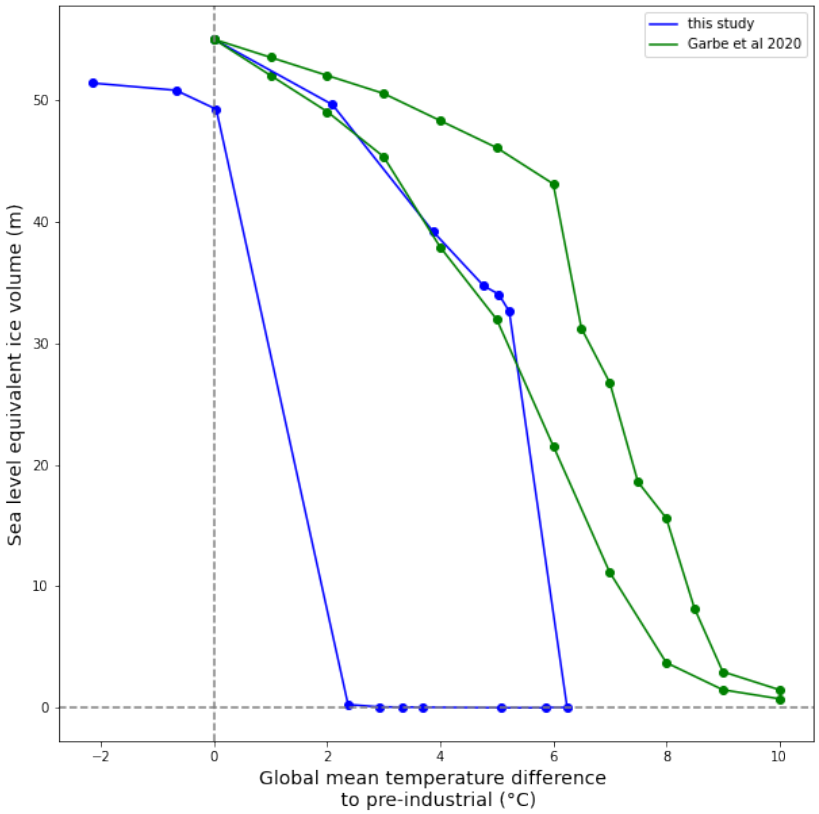

Figure 4.23: Equilibrium ice sheet volume as a function of global mean temperature difference to pre-industrial, for the study of Garbe et al. [2020] and this study.

in both the melt and growth branch found in our results differs from the Garbe et al. [2020] study, which might be explained by the fact that their setting does not allow to take into account the albedo feedback.

In our simulations, the threshold for complete Antarctic deglaciation is reached around 6°C of global mean temperature difference with the pre-industrial : there is still a large East Antarctic ice sheet at +5.2°C, and there is no ice sheet anymore at +6.2°C. In the study of Garbe et al. [2020], there remains less than 10% of the initial ice sheet (in SLE) at 8°C of warming, and around 1% at 10°C. One of the main reasons for the different values obtained for the Global Mean Temperature

increase leading to an ice free Antarctica in the Garbe et al. [2020] study and ours is that the polar amplification of the iLOVECLIM model is stronger than the one used in the Garbe et al. [2020] study. Simulations for different CO_2 levels with the iLOVECLIM model not coupled to the GRISLI ice sheet model (not shown here) have shown that the polar amplification (defined here as the ratio of temperature change for latitudes lower than 66°S to global mean temperature difference, to be coherent with Garbe et al. [2020]) is ∼2.6. This polar amplification of 2.6 is almost constant for different CO_2 levels in iLOVECLIM, when not coupled to an ice sheet model. Garbe et al. [2020] used a value of 1.8 for the polar amplification, based on the results of a long-term simulation with the climate model ECHAM5/MPIOM. Therefore, for a same global mean temperature increase, the Antarctic temperature increase is stronger in our case than in the case of Garbe et al. [2020].

Therefore, a more suitable metric to compare our results is in terms of Antarctic surface temperature change. However, as previously discussed and visible in Figure 4.6 and 4.11, the temperature in and around Antarctica is widely influenced by the growth and the decay of ice sheets in our simulations. For instance, in the 8xCO_2 melt simulation where the Antarctic ice sheet disappears entirely the Antarctic near surface temperature at the end of the simulation is much higher than the temperature that initially led to retreat, due to the albedo and elevation feedbacks. Conversely, in the 1xCO_2 growth simulation, the temperature at the end of the simulation is much lower than the temperature that initially allowed the ice sheet to initiate. In order to be able to compare our results for the melt branch, we have considered that the Antarctic temperature difference to pre-industrial leading to the obtained ice sheet could be approximated by the global mean temperature increase multiplied by the polar amplification of the iLOVECLIM model, when not coupled to an ice sheet model (2.6 in our case). However, this methodology is not applicable for the regrowth branch. On Figure 4.24 the equilibrated ice sheet volume for the melt branch is plotted as a function of Antarctic near surface temperature difference to pre-industrial (1.8 times the global mean temperature difference to pre-industrial for Garbe et al. [2020], 2.6 times the global mean temperature difference to pre-industrial in our case). Our settings are different, with melt computed with a PDD approach in Garbe et al. [2020] and no albedo feedback. However, we find similar order of magnitude for Antarctic temperature increase from pre-industrial leading to a virtually ice-free Antarctic ice sheet : around +15-18°C compared to pre-industrial.

Our results show a strong hysteresis with a stable Antarctic ice sheet once it is formed, and conversely, a stable ice free-Antarctica once the ice sheet has melted. However, there are also suggested evidence for ephemeral glaciations before the Eocene-Oligocene transition [Gulick et al., 2017, Scher et al., 2014]. These findings contradict the view of a very stable Antarctic ice sheet once established. Van Breedam et al. [2022] modelled ephemeral glaciation prior to the Eocene. In their setup, they use a varying insolation, as well as a varying CO_2 curve based on several

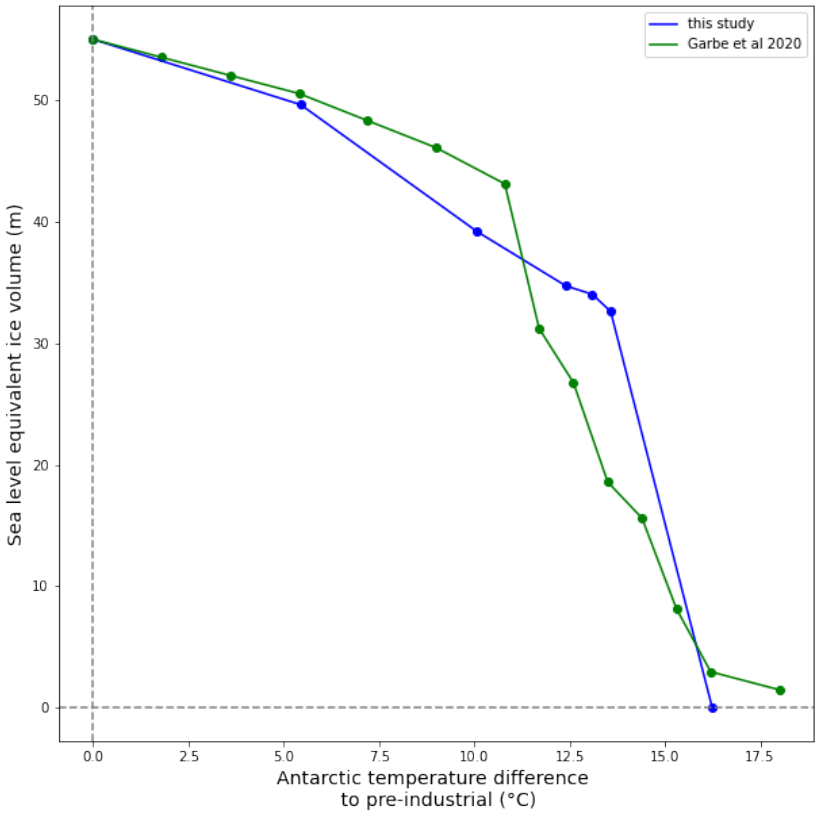

Figure 4.24: Equilibrium ice sheet volume as a function of Antarctic near surface temperature difference to pre-industrial, for the study of Garbe et al. [2020] and this study. For this study, the Antarctic temperature difference was computed as the product of the polar amplification (2.6) and global mean temperature difference at the end of the simulation.

reconstructions. In addition to the overall declining trend in CO_2 throughout the late Eocene, their CO_2 curve displays a large temporal variability. With this temporally variable CO_2, the ice sheet can grow to a continental scale and decline when CO_2 values exceed a threshold.

Our simulations with different orbital configurations have shown that the CO_2 threshold for Antarctic glaciation and deglaciation are dependant of orbital parameters. In our setting with a present day insolation, if the Antarctic becomes glaciated (around $\sim$1xCO_2 levels) the CO_2 needs to largely increase in order to permit the ice sheet to disappear (around $\sim$8xCO_2 levels). However, when considering the most favourable insolation for melt (max inso) and growth (min inso), the dif-

ference between the CO_2 threshold for glaciation and deglaciation is much lower, with both an Antarctic glaciation and a complete melt being possible at CO_2 levels between 2 and 4xCO_2, depending on the orbital configuration. Thus at CO_2 levels around 2-4xCO_2, varying CO_2 and insolation could lead to an Antarctic glaciation and deglaciation. While at CO_2 levels around pre-industrial, the Antarctic ice sheet will not retreat significantly, even for large insolation changes.

4.3.2 . Study limitations and perspectives

In this section, we discuss the limitations of our study and possible perspectives.

Our simulations were carried out with fixed insolation until equilibrium. The threshold for glaciation and deglaciation would probably be different in a transient case (where the orbital parameters do not stay to the most favorable configuration for melt or growth during the whole simulation). In our simulations, once the ice sheet starts to grow it extends to a widely developed and stable ice sheet, with no intermediate configuration. However, in a setting with variable insolation, if an ice sheet started to grow for a favorable orbital configuration, it might not be stable enough when the next insolation maxima is reached ($\sim$10 kyr afterwards, due to the $\sim$20 kyr periodicity of precession), leading to an ice sheet retreat, before the ice sheet has reached its maximum regrowth size. Therefore, it would be insightful to carry out transient simulations with varying insolation. Additionally, simulations with varying CO_2 levels and insolation could also be carried out. For instance, when looking at the Antarctic ice sheet response to anthropogenic CO_2 levels, transient simulations with varying CO_2 and insolation would be needed. In our simulations, the Antarctic ice sheet disappears entirely for fixed CO_2 levels around 8xCO_2 (2240 ppm) and a present day insolation. In the extended SSP5-8.5 scenario (high fossil fuel development), peak CO_2 levels are around 2200 ppm, but are expected to decrease afterwards [Meinshausen et al., 2020]. With a varying insolation and CO_2 level, the behaviour of the Antarctic ice sheet will probably differ than from the one modelled here with a fixed insolation and CO_2. Also, we have kept concentrations of other greenhouse gas such as methane (CH_4) and nitrous oxide (N_2O) constant to their pre-industrial values. After CO_2, CH_4 is the major contributor to additional radiative forcing. Although it has a higher radiative impact, its atmospheric lifetime is short ($\sim$ 10 years), as it is then oxidized into CO_2. For transient simulations, other greenhouse gas should also be consider, as a higher concentration of other greenhouse gas than CO_2 will decrease the amount of CO_2 needed in order to obtain the same radiative forcing. For instance, for the Pliocene, other greenhouse gas than CO_2 could represent $\sim$40% of the CO_2 radiative forcing [Hopcroft et al., 2020].

Most of the time, the results were discussed depending on the CO_2 applied. However, the results obtained are dependant of the climate model used, and its sensitivity to CO_2. iLOVECLIM has a low climate sensitivity compared to other models. Indeed, its climate sensitivity (obtained when not coupled to an ice sheet model) is of 2°C while the IPCC AR6 best estimate is 3°C with a likely range of 2.5° to 4°C (high confidence) [IPCC, 2021]. On the other hand, the polar amplification of iLOVECLIM is quite strong (ratio of 2.6 between Antarctic temperature difference and global mean temperature difference, when not coupled to an ice sheet model). The value of the CO_2 threshold for a given insolation could be different if using an other climate model with the same ice sheet model. The influence of the value of polar amplification on the results could be investigated by

using different factors β, that was used previously for the "enhanced melt" simulations (see Section 4.2.2). Taking β<1 corresponds to a "reduced melt" setting, that reduces the temperature seen by the ice sheet model for computing the melt. This conceptually corresponds to lowering the polar amplification. However, this approach would be incomplete, as the temperature difference is reduced in the melt seen by the ice sheet model, but remains unchanged in the rest of the climate model. Additionally, the uncertainty in the projection made due to the parameters of the iLOVECLIM model could be assessed by using different parameter sets. For instance, Van Breedam et al. [2020] used the LOVECLIM climate model coupled to the AGISM ice sheet model and performed sensitivity tests with different parameter sets of the LOVECLIM climate model, leading to different climate sensitivities. This results in wide differences in the modelled Antarctic ice sheet after 10 000 years. In the case of a high emission scenario, a large East Antarctic ice sheet remains after 10 000 years (the sea level rise due to Antarctica is $\sim$27m) with their default parameter set (climate sensitivity $\sim$2K). However, with a higher climate sensitivity parameter set (climate sensitivity $\sim$3K), the whole Antarctic ice sheet is lost after 10 000 years. More generally, more coupled ice sheet - climate studies are needed in order to compare our results.

A number of limitations arise from the fact that in order to do several coupled equilibrium climate-ice sheet simulations, the model used should not be too computationally expensive, and one should make concessions. For instance in our case, our coupling is not synchronous (coupling ratio of 100), the iLOVECLIM model cells are coarse, and the surface mass balance and basal melt are parametrized.

We have carried out simulations with a coupling ratio of 100. This can bias our results as a single climate year is used to force 100 ice sheet years. For example, in the case of initiation of ice sheet growth, a single cold year allowing for perennial snow to maintain over year is used to force 100 ice sheet model years. In the meantime, an ice sheet can start to develop, and its high albedo can lead to further ice sheet development on the sides. Similarly, a particularly warm year can provide a surface mass balance with melt on ice sheet edges, that is then used to force the ice sheet model during 100 years, leading to ice loss on the edges and potentially triggering a melt-albedo feedback. Therefore, the influence of the coupling ratio should be investigated in further studies. Due to computational limitations, it would not be possible to carry out all the simulations performed here with a coupling ratio of 1. But the coupling ratio could be reduced at specific critical times of the simulation. An other alternative that would not change the computation time could be to force 1000 ice sheet model years with the mean climate obtained on 10 climatic years. Changing the coupling ratio might change the threshold at which the ice sheet completely melts, or the threshold at which it regrows.

Our simulations exhibit strongly different behaviour when the albedo feedback is or not taken into account. Taking into account the albedo feedback is expected

to raise non linearity, as it triggers a positive feedback. However, this effect might be partly overestimated in our setup. Indeed, the iLOVECLIM model has a coarse resolution, and the albedo changes are seen at the level of the coarse T21 cells, not the downscaled one (40km x 40km). If at least 30% of the subgrid cells are glaciated, the corresponding T21 cell is considered glaciated, and its albedo is set to the value of the ice sheet albedo (0.85 in our study). If less than 30% of the subgrid cells are glaciated, the cell albedo is calculated following the albedo of the vegetation (see section 3.1), with values usually around 0.4-0.5. Thus, brutal albedo changes take place on the whole T21 cell when the threshold of 30% of subgrid glaciated cells is crossed. In the case of a melting ice sheet, this can potentially lead to higher temperature in zones that are still glaciated, thus favouring their melt. Conversely, in the case of a growing ice sheet, this can lead to lower temperatures in areas that are not yet glaciated, favouring ice sheet initiation in these areas. Therefore, our modelling results likely depend on the threshold of subgrid glaciated cell to switch the T21 cell albedo to glaciated (30% in our study). Furthermore, the albedo value of the ice sheet in our model is very high, and this probably enhances the impact of the albedo feedback (differences would be lower if the ice albedo was around 0.7, for example). Thus, the sensitivity of our model results to both the 30% threshold of subgrid glaciated cells and the ice sheet albedo value should be tested in further studies. Instead of using a threshold on the amount of glaciated subgrid scale, an alternative way could be to parametrize the albedo of the coarse T21 grid cells relatively to the fraction of glaciated subgrid cells. This would allow for a smoother transition between vegetation albedo values around 0.4-0.5 and the 0.85 ice sheet value when ice grows, and conversely for ice sheet melt. Allowing for a smoother transition might dampen the effect of the melt albedo feedback seen in our model. However, other aspects of our modelling setup potentially artificially reduce the albedo feedback. Indeed, in our study, the albedo / melt feedback is only partly taken into account. Warmer snow (with higher liquid content) has a lower albedo than cold snow. Furthermore, when snow melts, underlying snow that has a lower albedo is exposed. This is not taken into account in our study, where the albedo only changes when the ice sheet has retreated. Taking into account this effect by a parametrization of an albedo decrease for warmer snow or previously unexposed snow, could lead to faster Antarctic ice sheet retreat.

The use of a snow model could be an option to better represent the albedo, at a subgrid scale. In our setting, the surface mass balance is computed through the semi-empirical Insolation Temperature Melt formulation (equation 3.12 in section 3.3). An alternative way could be to use the BESSI model [Born et al., 2019]. The BESSI model is a surface energy and mass balance model that is relatively computationally efficient. Based on precipitation, shortwave radiation at the bottom of the atmosphere and surface air temperature fields, the BESSI model simulates the snow and firn on 15 layers. Work is currently ongoing to implement the BESSI

model in the coupled iLOVECLIM-GRISLI model.

In our simulations, the ice sheet does not regrow to its full extent, even for lower CO_2 values than PI. The major differences between the reference configuration and the regrown ice sheet at 05xCO_2 appear in West Antarctica. The Ross shelf does not regrow, and the Pine Island sector does not return to grounded, though the basal melt rates in the 05xCO_2 regrowth simulation are comparable to the basal melt rates in the reference PI configuration. This might be due to the fact that there is not enough ice flow from the grounded ice sheet to this sector. Basal melt rates need to be probably much lower to allow the ice sheet to ground, compared to the pre-industrial configuration, where the ice sheet is grounded in this sector and ice flux to this sector is higher. In a similar manner, the Ross ice shelf probably does not regrow due to a lack on ice inflow from the Pine Island sector, that is grounded at present-day and feeds the Ross ice shelf. Additionally, we might be applying too large melt rates for the regrowth phase in our setup, for instance in the Pine Island sector. In our setup, the oceanic circulation in cavities is not represented. Melt rates at a given depth and location are computed depending on the temperature and salinity of the closest oceanic grid point in the CLIO model, and at the same depth (see section 3.3). The grid of the CLIO ocean model is fixed, and does not evolve as ice sheet retreats. Thus, while in the pre-industrial configuration, the grounding line is relatively close to the closest oceanic point in the CLIO oceanic grid (except for the Ross and Ronne-Filchner ice shelves), temperatures are extrapolated from further away in the regrowth branch, as the grounding line is further away from the closest oceanic grid point. Ideally, one could use fully coupled ocean-ice sheet model, where the oceanic circulation is resolved under the shelves and the oceanic cavities evolve as the ice sheet retreats or advances. Such models do exist ([Goldberg et al., 2012, Seroussi et al., 2017]) but they are still limited to short timescales (decades- centuries) due to their computational cost. An alternative way that could be suitable for our application (long term simulations) is to use the PICO model [Reese et al., 2018], which simulates the vertical overturning circulation in ice-shelf cavities. It is based on an ocean box model that coarsely resolves ice shelf cavities and its computational time thus remains relatively low. In PICO, the cavity is divided into n boxes along the ice-shelf base. Ocean water from the ice shelf front (first box) enters the ice-shelf cavity at the depth of the sea floor and is advected to the grounding line (second box). Freshwater influx resulting from melting at the ice-shelf base makes the water buoyant, causing it to rise along the shelf, where further melt can occur. Work is currently ongoing to implement the PICO model in the iLOVECLIM-GRISLI coupled model, and it would be particularly interesting to study how the use of a different parametrization of basal melting influences the retreat and regrowth of the ice sheet.

Model parameters such as dynamical parameters of the GRISLI model and coefficients in the surface melt and basal melt equations have been chosen in order to obtain a pre-industrial ice sheet equilibrated with the climate. A better

approach would be to calibrate these parameters over the past glacial interglacial cycles. However, this is not an easy task as climate models have biases. Therefore, we have chosen to calibrate our model parameters on the pre-industrial in our study. However, a sensitivity to model parameters should be carried out in a further study in order to assess the dependence of our modelling results to these parameter choice. Parameters that seems of particular influence are parameters involved in the basal sliding law. Indeed, the mechanics of basal friction remain largely unkwnown [Pattyn and Morlighem, 2020], and the basal sliding law has a strong influence on grounding line retreat and glacier acceleration in response to perturbations, and varies spatially [Sun et al., 2020].

In our setting, the Greenland ice sheet is fixed to its present day configuration. For the range of CO_2 levels considered here, the Greenland ice sheet is expected to melt entirely. This would slightly raise the global mean temperature due to the albedo change, but could also lead to circulation changes that are not taken into account in this study. However, circulation changes are often not modelled correctly by climate models.

Finally, it should be noted that some feedbacks are not taken into account into our setting. We have focused on feedbacks that are expected to be the most important, such as the albedo and elevation feedbacks. However, other feedbacks could dampen or amplify the ice sheet response to CO_2 changes. For instance, gravity feedbacks are expected to dampen the ice sheet melt. Ice volume changes lead to local gravity change that affect the sea level locally. Ice loss leads to a locally lower sea level, potentially reducing marine ice sheet instability [Fyke et al., 2018]. In addition, the solid Earth's response to ice sheet loading or unloading is spatially homogeneous in GRISLI. However, several studies have shown that the rheological properties under the AIS vary strongly spatially, with a with a thin lithosphere and a low-viscosity upper mantle beneath West Antarctica and a thick lithosphere and a more viscous upper mantle beneath East Antarctica [Chen et al., 2018, Lloyd et al., 2020, van der Wal et al., 2015]. The structure observed under the WAIS will produce a faster and more localized viscoelastic response of the solid Earth to ice-load changes accentuating the local relative sea-level fall, facilitating stabilizing feedbacks and promoting the stability of the West Antarctic ice sheet (WAIS) [Gomez et al., 2015, Konrad et al., 2016, Coulon et al., 2021]. On the other hand, other positive feedbacks not taken into account could be of importance, such as the fact that surface melt can enhance hydrofracturing and thus, ice shelves collapse [Scambos et al., 2009].

5 - A broader view of the long term carbon cycle ?

Chapter aims:

1. Develop a new conceptual model for the geological carbon cycle, that is able to reproduce past $\delta^{13}C$ variations.
2. Discuss the future CO_2 evolution on the next million years, based on idealized scenarios.

Highlights:

↪ The geological carbon cycle model developed here is able to reproduce multi-million years cycles observed in past $\delta^{13}C$ records, that were not modelled by previous studies, as a response to astronomical forcing of organic matter burial.

↪ The modelling of multi-million years cycles in $\delta^{13}C$ as a response to eccentricity forcing is possible due to the presence of multiple equilibria in the geological carbon cycle in our model.

↪ The potential presence of multiple equilibria in the geological carbon cycle could have important implications for the CO_2 evolution on long timescales.

In this chapter, we explore other possible theories for the long term fate of atmospheric CO_2. As was explained in Chapter 1, current existing modelling studies on long term removal of atmospheric CO_2 make the assumption that CO_2 is ultimately removed by silicate weathering only. However, in these studies, no changes of the organic matter fluxes are considered, and this does not allow to explain the $\delta^{13}C$ variations that are recorded over the Cenozoic. Due to the large fractionation factor of organic matter, changes in its fluxes to and from the geological sinks is the most likely candidate to explain $\delta^{13}C$ variations. In this chapter, we first describe the $\delta^{13}C$ oscillations seen over the Cenozoic and current modelling studies aiming at reproducing these oscillations. In these studies, some oscillations seen in the $\delta^{13}C$ are reproduced, such as oscillations at 400 kyr and 2.4 Myr. However, these studies do not model longer term oscillations, such as the 8-9 Myr oscillations observed in the record. Therefore, we propose a new conceptual model for the geological carbon cycle. Contrary to previous carbon cycle models, this one is not linear, and has multiple equilibria. This allows us to produce oscillations of 8-9

Myr in the $\delta^{13}C$, that are visible in the data but were not represented by previous models. This study was submitted to the journal Earth System Dynamics and is currently under review. The model is shortly described in the main text, and the manuscript submitted to the journal Earth System Dynamics containing the whole study is included. Finally, we look at idealized scenarios for the carbon cycle over the next million years.

5.1 . Records of $\delta^{13}C$ oscillations over the Cenozoic and current modelling studies

During the whole Cenozoic, $\delta^{13}C$ exhibit oscillations with a period of 400 kyr : during the Paleocene [Westerhold et al., 2011], the Eocene [Lauretano et al., 2015], the Oligocene [Pälike et al., 2006], Miocene [Billups et al., 2004] and during more recent time periods [Wang et al., 2010]. The 400 kyr frequency corresponds to one of the frequencies of eccentricity, and this is the most stable astronomical periodicity through geological times [Laskar et al., 2004]. The $\delta^{13}C$ oscillations are correlated to the eccentricity oscillations. This is for instance visible in Figure 1 of Pälike et al. [2006] (panels C and D) : filtered eccentricity and (inverted) $\delta^{13}C$ curve exhibit the same pattern.

In addition to 400 kyr oscillations, 2.4 Myr oscillations are also observed over the Cenozoic in $\delta^{13}C$ records : over the Oligocene [Boulila et al., 2012] and Miocene [Liebrand et al., 2016]. The 2.4 Myr periodicity is at the same time a true eccentricity cycle and present in the Amplitude Modulation (AM) of the 100 kyr and 400 kyr cycles [Laskar et al., 2011, Boulila et al., 2012]. The 2.4 Myr oscillations are for instance visible in Figure 2 of Boulila et al. [2012] (panel a) : there is a good correlation between $\delta^{13}C$ record and AM eccentricity.

Much longer and dominant cycles of approximately 9 Myr have been found in $\delta^{13}C$ records, over the Cenozoic [Boulila et al., 2012] and the Mesozoic [Martinez and Dera, 2015]. Cycles of around 8 Myr have been seen in $\delta^{13}C$ in the late Cretaceous [Sprovieri et al., 2013]. This periodicity is very stable over time and the robust presence of $\sim$9 Myr cycles over various time periods, hints at an astronomical origin. The $\sim$9Myr cycles over the Cenozoic and Mesozoic are visible in Figure 1 of Boulila et al. [2012] (panels 4 and 5) and Figure 3 of Martinez and Dera [2015] (panels C, D, E, H).

Cycles of $\sim$4.5 Myr have also been observed in $\delta^{13}C$ in the late Creataceous [Sprovieri et al., 2013] as well as the latest Ordovician and Silurian [Sproson, 2020]. In the case of 4.5 and 9 Myr cycles, the link to the astronomical forcing is less clear than in the case of the 400 kyr and 2.4 Myr oscillations, as these frequencies are not easily seen in the eccentricity spectra. A $\sim$4.5 Myr periodicity is visible in the eccentricity solution, although with a very low amplitude. The AM envelopes of the 100 kyr and 400 kyr eccentricity also show a $\sim$4.5 Myr cyclicity, but again with low amplitude. The $\sim$9 Myr frequency is not directly visible in the eccentricity spectra.

Although it has been suggested that the AM envelope of the ∼2.4 Myr filtered eccentricity has a ∼9 Myr cyclicity [Boulila et al., 2012], this remains uncertain or with a very low amplitude. Therefore, the way in which the astronomy could pace these multi-million year cycles remains mysterious.

5.2 . Modelling the observed $\delta^{13}C$ oscillations

Modelling studies [Paillard, 2017, Kocken et al., 2019] were able to reproduce the higher frequency cycles in $\delta^{13}C$: 400 kyr and 2.4 Myr cycles. This was performed by forcing astronomically the organic carbon burial. For instance, in Kocken et al. [2019], marine organic carbon burial decreases with eccentricity values. Periods of low eccentricity favour low seasonal contrast and annual wet conditions and thus favour clay formation. As the majority of organic carbon is buried in association with clay particles [Hedges and Keil, 1995], eccentricity minima could lead to higher organic carbon burial in the ocean, and thus increase $\delta^{13}C$. Others explanation have been proposed for a link between organic matter burial and astronomical forcing and are detailed in the manuscript submitted to Earth System Dynamics. However, these studies [Paillard, 2017, Kocken et al., 2019] were not able to reproduce the ∼4.5 Myr and ∼8-9 Myr cycles observed in the data. In both studies, the carbon cycle model used were linear.

In our study, we introduce a new conceptual model for the carbon cycle, that possesses multiple equilibria, and look at the modelled $\delta^{13}C$ evolution when the organic matter burial is forced with the eccentricity. We base our work on the previous conceptual model of Paillard [2017].

As in Paillard [2017], the conceptual model represents the evolution of the Earth's surface carbon content C, that includes carbon stored in the atmosphere, ocean and biosphere. This is opposed to carbon stored in deep soils, rocks, or sediments (geological reservoir). In our model, exchanges between surface and geological carbon reservoirs take place by either : carbon release to the surface reservoir through volcanism, that is supposed constant (V_0); carbon loss from the surface reservoir through the oceanic carbonate deposition flux (D) that is associated with silicate weathering; net organic matter burial flux (B), that is composed of organic matter burial (B^+) and organic matter oxidation (B^-) : $B = B^+ - B^-$. The model is schematized in Figure 5.1.

The surface carbon content C evolution is represented by the equation :

$$\frac{dC}{dt}(t) = V_0 - B(t) - D(t) \tag{5.1}$$

As in the Paillard [2017] model, organic matter burial is forced astronomically. The forcing term differs slightly in both models.

The main difference to the Paillard [2017] model, is that the net organic matter burial does not only depend on the astronomical forcing. Additionally, the organic matter burial varies with climate. At first order, climate is influenced by the

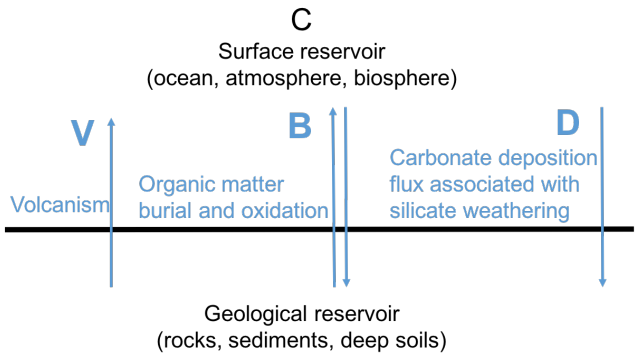

Figure 5.1: Schematic representation of the modelled geological carbon cycle.

CO_2 quantity in the atmosphere and thus the surface carbon content C. Organic matter burial (B) depends on surface carbon content (C) through the climate dependency of organic matter burial, and reciprocally C depends on B since the carbon content evolution depends on organic matter burial, as visible in Equation 5.1. In addition, the organic matter burial varies with oxygen contents. We have considered a global oxygen content (O) representing both the atmospheric O_2 and dissolved O_2 in oceans. Organic matter burial is facilitated in locally lower oxygen concentrations. All other things being equal, a higher oxygen content globally in the atmosphere will lead to higher oxygen contents locally in the ocean. Therefore, organic matter burial decreases for higher oxygen concentrations and inversely. The oxygen contents also vary with organic matter burial, as organic matter oxidation reduces the oxygen quantity, while burial of organic matter adds oxygen to the surface system. Thus, B depends on O and O depends on B. The surface carbon content C and oxygen content O are thus coupled via the organic matter burial term B. This is schematically represented in Figure 5.2.

Figure 5.2: Schematic representation of the coupling between the carbon content C and oxygen content O through the net organic matter burial B.

The organic matter burial variations can be expressed as :

$$B(C(t), O(t), F(t)) = B_0(C(t), O(t)) - a_f F(t)$$

with $F(t)$ being the astronomical forcing, $F(t)$ = (e(t) -mean(e(t))) / max(e(t)) where e(t) is the eccentricity at time t, mean and max represent respectively the mean and maximum of eccentricity over the time period considered. a_f is a coefficient that represents the strength of the astronomical forcing. $B_0(t)$ represents the organic matter burial value without astronomical forcing.

If B_0 is a non linear function of climate C, it is possible to obtain multiple equilibria in the coupled (C,O) system, and internal oscillations. The system can oscillate between different (C,O) values even when the organic matter burial is not forced astronomically. This is further discussed in the manuscript submitted to Earth System Dynamics. These multiple equilibria and internal oscillations allow to obtain a different behaviour in the model when the organic matter burial is additionally forced astronomically (B = B(C(t), O(t), F(t))), than in a case where the organic matter burial depends of the astronomical forcing only.

https://doi.org/10.5194/esd-2022-46
Preprint. Discussion started: 10 October 2022

Earth System Dynamics Discussions

Multi-million year cycles in modelled $\delta^{13}C$ as a response to astronomical forcing of organic matter fluxes.

Gaëlle Leloup[1,2] and Didier Paillard[2]

[1]Agence Nationale pour la gestion des déchets radioactifs (ANDRA), 1 Rue Jean Monnet, 92290 Châtenay-Malabry, France
[2]Laboratoire des Sciences du Climat et de l'Environnement, LSCE/IPSL, CEA-CNRS-UVSQ-Université Paris-Saclay, 91198 Gif-sur-Yvette, France

Correspondence: Gaëlle Leloup (gaelle.leloup@lsce.ipsl.fr)

Abstract.

Along with 400 kyr periodicities, multi-million year cycles have been found in $\delta^{13}C$ records over different time periods. A ∼8-9 Myr periodicity is found throughout the Cenozoic, and part of the Mesozoic. The robust presence of this periodicity in $\delta^{13}C$ records suggests an astronomical origin. However, this periodicity is barely visible in the astronomical forcing. Due to the large fractionation factor of organic matter, its burial or oxidation produces large $\delta^{13}C$ variations for moderate carbon variations. Therefore, astronomical forcing of organic matter fluxes is a plausible candidate to explain the oscillations observed in the $\delta^{13}C$ records. So far, modelling studies forcing astronomically the organic matter burial have been able to produce 400 kyr and 2.4 Myr cycles in $\delta^{13}C$, but were not able to produce longer cycles, such as 8-9 Myr cycles. Here, we propose a mechanism that could explain the presence of multi-million year cycles in the $\delta^{13}C$ records, and their stability over time, as a result of preferential periodicity locking to multiples of astronomical forcing periods. With a simple non linear conceptual model for the carbon cycle that has multiple equilibria, we are able to extract longer periods than with a simple linear model, and more specifically, multi-million year periods.

1 Introduction

Astronomical frequencies are imprinted into the carbon cycle. A 400 kyr oscillation has been seen in many $\delta^{13}C$ records covering the Cenozoic : during the Paleocene (Westerhold et al., 2011), the Eocene (Lauretano et al., 2015), the Oligocene (Pälike et al., 2006), Miocene (Billups et al., 2004) and during more recent time periods (Wang et al., 2010). The 400 kyr frequency corresponds to one of the frequencies of eccentricity, and this is the most stable astronomical periodicity through geological times (Laskar, J. et al., 2004).

Longer cycles of 2.4 Myr have also been found in $\delta^{13}C$ records over the Cenozoic : over the Oligocene (Pälike et al., 2006; Boulila et al., 2012), and Miocene (Liebrand et al., 2016). The 2.4 Myr periodicity is at the same time a true eccentricity cycle and present in the amplitude modulation (AM) of the 100 kyr and 400 kyr cycles (Laskar, J. et al., 2011; Boulila et al., 2012). ∼4.5 Myr cycles have also been observed in $\delta^{13}C$ in the late Creataceous (Sprovieri et al., 2013) as well as the latest Ordovician and Silurian (Sproson, 2020).

Much longer and dominant cycles of approximately 9 Myr have been found in $\delta^{13}C$ records, over the Cenozoic (Boulila et al.,

https://doi.org/10.5194/esd-2022-46
Preprint. Discussion started: 10 October 2022


Earth System Dynamics Discussions
Open Access
EGU

2012) and the Mesozoic (Martinez and Dera, 2015). Cycles of around 8 Myr have been seen in $\delta^{13}C$ in the late Creataceous (Sprovieri et al., 2013). This periodicity therefore seems very stable over time. The robust presence of ∼9 Myr cycles over various time periods, hints at an astronomical origin. However, in the case of 4.5 Myr and 9 Myr cycles, the link to the astronomical forcing is less clear, as these frequencies are not easily seen in the eccentricity spectra. A ∼4.5 Myr periodicity is visible in the eccentricity solution, although with a very low amplitude. The AM envelopes of the 100 kyr and 400 kyr eccentricity also show a ∼4.5 Myr cyclicity, but again with low amplitude. The ∼9 Myr frequency is not directly visible in the eccentricity spectra. Although it has been suggested that the AM envelope of the ∼2.4 Myr filtered eccentricity has a ∼9 Myr cyclicity (Boulila et al., 2012), this remains with a very low amplitude. Therefore, the way in which the astronomy could pace these multi-million year cycles remains mysterious.

It has been suggested (Paillard, 2017; Kocken et al., 2019) that an astronomical forcing of organic carbon fluxes could explain the observed $\delta^{13}C$ cyclicities at 400 kyr and 2.4 Myr. Indeed, organic, ^{12}C enriched, matter burial or oxidation can lead to relatively large δ^{13}C variation for a moderate carbon variation, which is not possible with silicate weathering (Paillard, 2017; Russon et al., 2010). It is usually assumed that long term carbon cycle is mainly controlled by silicate weathering. But it is a negative feedback, that does not allow for oscillatory behaviour as observed in the data. Additionally, recent studies have highlighted the importance played by organic carbon fluxes in the long term carbon budget, acting as either a source if petrogenic organic carbon is eroded and oxidized, or a sink if terrestrial organic carbon is exported and buried into sediments (Hilton and West, 2020). Organic carbon contributions are of the same order of magnitude than silicate weathering (Hilton and West, 2020). Therefore, astronomical forcing of the organic matter burial is a plausible candidate to explain the observed cyclic $\delta^{13}C$ variations.

Kocken et al. (2019) suggested that the link between $\delta^{13}C$ and the astronomical forcing could be explained by enhanced marine organic carbon burial for lower eccentricity values. Periods of low eccentricity and therefore low seasonal contrast could favor annual wet conditions, and consequently clay formation. The majority of organic carbon burial is buried in association with clay particles (Hedges and Keil, 1995). If transport is not limiting, lower eccentricity would lead to higher marine organic carbon burial and increase $\delta^{13}C$. Paillard (2017) suggested a link between monsoons and organic carbon burial. Monsoon favor soil erosion and sediment transports. Recent soil as well as petrogenic organic carbon can be eroded and carried to the oceans via rivers. The net effect on organic carbon burial depends on the geomorphological dynamics. For aggradational situations, that favour burial, the net result is organic matter burial. In that case, $\delta^{13}C$ increases with increased eccentricity and monsoon strength. However, for progradational situations, oxidation of petrogenic organic carbon is favoured, leading to a $\delta^{13}C$ decrease with eccentricity increase. Martinez and Dera (2015) suggested that low eccentricity values and the associated stable and humid conditions could favor constant freshwater and nutrient inputs, thus favoring water mass stratification, productivity levels, leading to persistent anoxia and therefore higher organic carbon burial rates. On the contrary, high eccentricity values are associated with a recovery of oxic conditions during the cool season, limiting organic carbon burial. It has also been suggested that terrestrial organic carbon burial could increase with eccentricity minima, as this would favor annual soil anoxia (Kurtz et al., 2003). Laurin et al. (2015) suggested that $\delta^{13}C$ variations in the Late Cretaceous could be explained by a transient storage of organic matter or methane in quasi-stable reservoirs such as wetlands, soils, marginal zones of marine euxinic strata,

https://doi.org/10.5194/esd-2022-46
Preprint. Discussion started: 10 October 2022


Earth System Dynamics Discussions
Open Access
EGU

and permafrost. These quasi-stable reservoirs could respond non linearly to changes in obliquity and the consequent high latitude insolation changes or changes in meriodional insolation gradients. Other mechanisms have been proposed to explain $\delta^{13}C$ variation as a consequence from astronomical variations. de Boer et al. (2014) suggested that ice sheet dynamics and linked changes in carbon cycle dynamics could explain the 400 kyr cycles in $\delta^{13}C$. However, this mechanism does not permit to explain the presence of such cycles for periods without ice sheet (Kocken et al., 2019).

Modelling studies forcing the net organic matter burial through eccentricity have been able to produce 400 kyr and 2.4 Myr cycles in the $\delta^{13}C$ (Paillard, 2017; Kocken et al., 2019). However, these studies did not find longer cycles, such as the $\sim$4.5 and $\sim$9 Myr cycles observed in geological records. The model used were linear, and non linear mechanisms might be necessary in order to produce multi-million year cycles that have a very low amplitude in the input forcing.

Here, we develop a new conceptual model of the carbon cycle, that includes a net organic matter burial term and force it astronomically with the eccentricity, similarly to the study of Paillard (2017). However, contrary to this study, the organic matter fluxes depend also on the surface carbon content, through its influence on climate, and on atmospheric oxygen content. Our model therefore couples the carbon and oxygen cycle, and is non linear, with the possibility of multiple equilibria. With this model, it is possible to obtain multi-million year frequencies in the $\delta^{13}C$. Depending on the strength of the astronomical forcing, periodicities of 2.4 Myr, $\sim$4.8 Myr $\sim$7 Myr, and $\sim$9 Myr are produced preferentially, presumably as a result of periodicity doubling of the 2.4 Myr eccentricity frequency.

2 Methods

2.1 Model description

Here, we develop a simple, yet non linear conceptual model, coupling the carbon and oxygen cycle. When forced by the eccentricity signal as input, the model is able to produce multi-million year frequencies as output, and multiples of the 2.4 Myr frequency of eccentricity : 2.4 Myr cycles, $\sim$4.5 Myr cycles, $\sim$7 Myr cycles and $\sim$9 Myr cycles.

Our model is based on the conceptual model of Paillard (2017). This model represents the evolution of the surface Earth carbon content, including the atmosphere, the ocean and the biosphere. This is opposed to carbon stored in deep soils, rocks or sediments. In our model, we have added a crude representation of the surface oxygen evolution. In the following, the features common to the Paillard (2017) model and ours are summarized and the differences are described.

In our model, the modeling of the surface carbon evolution is identical to the Paillard (2017) model. The surface carbon evolution is determined by the volcanic input V, the oceanic carbonate deposition flux D that is associated with silicate weathering, and the organic carbon burial B.

$$\frac{dC}{dt} = V - B - D \tag{1}$$

The organic matter burial B is meant as a net burial, and represents all organic carbon fluxes. $B = B^+ - B^-$ where B^+ represents organic carbon burial and B^- represents organic matter oxidation.

https://doi.org/10.5194/esd-2022-46
Preprint. Discussion started: 10 October 2022


Earth System Dynamics Discussions
Open Access
EGU

As in Paillard (2017), we assume that the oceanic calcium concentration does not vary significantly over time and that carbonate compensation restores the oceanic carbonate content. With the use of an alkalinity balance (see Paillard (2017) for details), we obtain the following equation for the carbon evolution :

$$\frac{dC}{dt} = 2(V - B) - W \tag{2}$$

where W is the alkalinity flux to the ocean associated with silicate weathering. As in Paillard (2017), we assume silicate weathering to be the main stabilizer of the carbon system, with a fixed relaxation time τ_c : W = C/τ_c. The volcanic input is considered as constant, $V = V_0$. The $\delta^{13}C$ evolution is described by :

$$\frac{d\delta^{13}C}{dt} = \frac{1}{C}(V(\delta^{13}V - \delta^{13}C) - B(\delta^{13}B - \delta^{13}C)) \tag{3}$$

We have assumed a constant -5‰ volcanic source ($\delta^{13}V$ = -5‰) and a constant -25‰ organic matter fractionnation ($\delta^{13}B - \delta^{13}C$ = -25‰). This slightly differs from the equation used in Paillard (2017), however the results remain very similar (for a detailed discussion, see the interactive discussion of the Paillard (2017) paper).

Compared to the previous model, we have added a crude representation of the oxygen cycle. Indeed, the oxygen interacts closely with organic matter burial and oxidation. On one side, the burial of organic matter is facilitated in low oxygen zones. On the other side, organic matter oxidation reduces the oxygen quantity, while burial of organic matter adds oxygen to the surface system. We consider a global oxygen content O, representing both the atmospheric O_2 and dissolved O_2 in oceans. On geological timescales, the atmospheric O_2 is driven by the net organic matter burial, the net burial of pyrite ($F_{pb} - F_{po}$ with F_{pb} and F_{po} the pyrite burial and oxidation), oxidation of volcanic gases (F_v) and oxidative weathering of sedimentary rocks, not already accounted in the net organic matter and pyrite burial, such as ferrous iron (F_w) (Berner, 2001; Canfield, 2005).

$$\frac{dO}{dt} = (B^+ - B^-) + (F_{pb} - F_{po}) - F_v - F_w \tag{4}$$

The oxidation of other elements than organic carbon is grouped in a single term, Ox, leading to :

$$\frac{dO}{dt} = B - Ox \tag{5}$$

We make the assumption that the oxidation of other elements than organic carbon increases linearly with oxygen contents : $Ox = a_{ox} \cdot O + b_{ox}$, with a_{ox} and b_{ox} two constants.

Although organic carbon perturbations are expected to have a weak impact on atmospheric O_2 concentrations, as atmospheric O_2 is relatively high in the Phanerozoic (Bergman et al., 2004; Berner and Canfield, 1989), perturbations to atmospheric O_2 of a few permill have been seen in Pleistocene ice cores (Stolper et al., 2016).

As in the Paillard model, the organic matter burial is forced astronomically, while the forcing term differs slightly in both models. Here, we choose to express the organic matter burial variations as :

$$B = B_0 - a_f F(t)$$

with F(t) = (e(t) -mean(e(t))) / max(e(t)) where e(t) is the eccentricity at time t, mean and max represent respectively the mean and maximum of eccentricity over the time period considered. B_0 represents the organic matter burial value without

https://doi.org/10.5194/esd-2022-46
Preprint. Discussion started: 10 October 2022


Earth System Dynamics Discussions
Open Access
EGU

astronomical forcing. The Analyseries software (Paillard et al., 1996) provides the La04 orbital parameters (Laskar, J. et al., 2004).

Several mechanisms have been proposed to be responsible of the link between organic matter burial and astronomical forcing. Here, we do not intend to focus on a specific mechanism. We rather focus on the output signal that can be obtained from a simple astronomical forcing. Therefore, we have chosen the easiest possible relationship : a linear variation of the organic matter burial with the astronomical forcing. The negative sign was chosen in order to match the data, where eccentricity minima correspond to $\delta^{13}C$ minima, and thus organic matter burial maxima.

In the Paillard model, the B_0 term was constant and the organic matter burial therefore only varried with the astronomical forcing. However, in our model, the organic matter burial depends not only on the astronomical forcing but also on the surface carbon content and the oxygen content, meaning $B_0 = B_0(C,O)$, as explained below.

Organic matter burial is facilitated in locally lower oxygen concentrations. All other things being equal, a higher oxygen content globally in the atmosphere will lead to higher oxygen contents locally in the ocean. Therefore, organic matter burial decreases for higher oxygen concentrations and inversely. Here, we have assumed an inverse linear dependency between the organic matter burial and the oxygen content O. If O_1 and O_2 are two oxygen contents, then the difference in organic matter burial (for the same carbon content C) is :

$$B_0(C,O_1) = B_0(C,O_2) - \delta(O_1 - O_2) \tag{6}$$

δ is a positive constant. For a similar carbon content C, the organic matter burial is higher in the case of lower oxygen quantities.

Here, we also suggest that net organic carbon burial depends on the surface carbon quantity C. Indeed, climate can influence the organic matter burial, and as a first approximation, larger carbon values C in the surface system correspond to warmer, wetter climates. Net organic matter burial contribution to the surface carbon evolution is composed of two opposite contributions : biospheric organic carbon erosion leading to CO_2 drawdown (CO_2 sink) and therefore surface carbon decrease, and oxidation of petrogenic organic carbon, leading to CO_2 rise (CO_2 source), and therefore surface carbon increase. Eroded terrestrial organic matter from plants is delivered to rivers (Meybeck, 1982; Ludwig et al., 1996). If a part of this biospheric organic carbon is buried into sediments without being degraded, this corresponds to a decrease of the surface carbon content. It has been estimated that the current burial flux of organic carbon eroded from land into oceanic sediments is around 40-80 MtC/yr (Hilton and West, 2020). On the other hand, exhumation of sedimentary rocks can lead to the oxidation of petrogenic organic carbon and therefore to CO_2 release (Hilton et al., 2014). The carbon flux released to the atmosphere through petrogenic organic carbon oxidation has been estimated to be between 40 and 100 MtC/yr (Hilton and West, 2020). Climate can act on these processes on several ways. When the surface carbon content increases, this globally results in a warmer and wetter climate. Warmer temperatures and stronger runoff increase erosion and transfer of biospheric organic carbon (Hilton, 2017; Smith et al., 2013). In addition, warmer temperatures increase ocean stratification and decrease the solubility of oxygen in surface waters (Bopp et al., 2002), leading to expansion of oxygen minimum zones (Stramma et al., 2008, 2010). This decreases organic matter oxidation and favours its burial into oceanic sediments (Jessen et al., 2017). Other climatic related factors, have been

https://doi.org/10.5194/esd-2022-46
Preprint. Discussion started: 10 October 2022

Earth System Dynamics Discussions
Open Access
EGU

suggested to limit dissolved oxygen in the ocean, such as increased phosphorus inputs (Baroni et al., 2020; Niemeyer et al., 2017). These inputs are expected to increase for warmer and wetter climate, that increases weathering, leading to regional deoxygenation and organic carbon burial (Baroni et al., 2020).

It has also been suggested that the oxidation of petrogenic organic carbon could be linked to climate as petrogenic organic carbon oxidation could be locally limited by temperature, O_2 contents, and microbial activity (Chang and Berner, 1999; Bolton et al., 2006; Hemingway et al., 2018; Petsch et al., 2005). Higher temperature could lead to stronger petrogenic carbon oxidation. We have made the assumption that for intermediate carbon value, and thus intermediate temperatures, this mechanism is dominant, whereas the increase in export of biospheric carbon and increased burial dominates for warmer temperatures (larger C values). We have supposed that there is no dependency to climate for lower carbon values. This results in a non monotonic dependency of B to C. For low carbon values (C $<C_1$) and thus colder climates, the organic carbon burial B does not depend on C. Then, for intermediate carbon values (C_1 < C < C_2), the organic carbon burial decreases with increasing temperatures, and thus increasing carbon C. Finally, for higher carbon values (C > C_2) the organic carbon burial increases with increasing temperature (and thus, carbon C). For the sake of simplicity, we have made the assumption of linear variations. The resulting shape of the evolution of organic carbon burial fluxes as function of the carbon content C is represented in Figure 1.

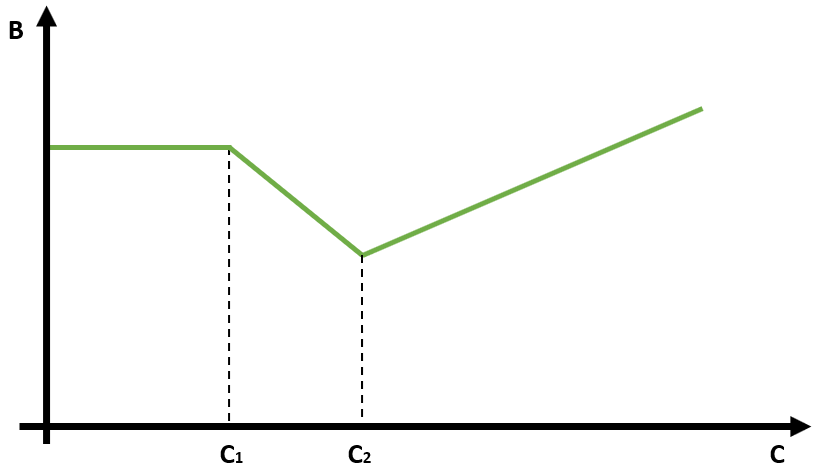

Figure 1. Schematic representation of the organic carbon burial B evolution with carbon content C

These assumptions on the dependency of the organic matter burial flux to the surface carbon content C are strong. It is not an easy task to quantify at present day the net magnitude of carbon burial, as some regions are known to be carbon sinks and others known to be carbon sources. It is an even more complicated task to have an estimation of this budget for different climates, and therefore different carbon contents. However, the results discussed below do not depend on the specific shape choosen for the dependency of the organic matter burial B to the carbon content C. Similar results could be obtained with an other dependency, as long as it is non monotonic with the carbon content C and we place ourselves here in one of the simplest case possible. The shape of the organic burial evolution is certainly different and more complex than the one presented here. However, as many

https://doi.org/10.5194/esd-2022-46
Preprint. Discussion started: 10 October 2022


Earth System Dynamics Discussions
Open Access
EGU

process act on the net organic matter burial, some favoring organic matter burial, and some favoring organic matter oxidation, we are confident in the fact that the relationship between organic matter burial and surface carbon content is non monotonic. In our model, carbon and oxygen evolution depend on the organic matter burial term, that conversely depends on both, carbon and oxygen quantities. Therefore, in our model the carbon and oxygen cycle are coupled via the organic matter burial term. This is the main difference with the model of Paillard 2017, as this results in a non linear model, where it is possible to have multiple equilibria in the carbon and oxygen system, and thus oscillations even without astronomical forcing.

2.2 Parameter values

We first consider the case where the organic matter burial is not forced astronomically (a_f = 0). For simplicity, we have chosen B_0 to be piecewise constant when considering the variations due to carbon. It is decreasing linearly with oxygen. Therefore, we can write B_0 as :

$$B_0(C,O) = B_0(C,O_{ref}) - \delta(O - O_{ref}) \tag{7}$$

with

$$B_0(C,O_{ref}) = \begin{cases} \alpha & \text{for C} < C_1 \\ \alpha - \beta(C - C_1) & \text{for } C_1 < \text{C} < C_2 \\ \alpha - \beta(C_2 - C_1) + \gamma(C_2 - C_1) & \text{for C} > C_2 \end{cases} \tag{8}$$

Where δ (δ >0) is the coefficient representing the strength of the organic matter burial evolution with oxygen. The higher δ, the stronger is the organic matter burial decrease with oxygen content. α represents the constant value of organic matter burial for low carbon values ($C < C_1$). -β ($-\beta$ < 0) represents the slope of the carbon burial evolution for intermediate carbon values ($C_1 < C < C_2$), for which the organic matter burial decreases with increasing carbon content. γ ($\gamma > 0$) represents the slope of the carbon burial evolution for high carbon values ($C > C_2$), for which the organic matter burial increases with increasing carbon content. We choose to place ourselves in the case where there are two stable equilibria for the carbon cycle for the current oxygen value (see section 3.1). This corresponds to panel (a) of Figure 2. These equilibria are called C_{eq1ref} and C_{eq2ref}.

Our unforced model therefore contains 13 parameters : the value of carbon emissions associated with volcanism V_0, the time constant associated with silicate weathering τ_c, the current oxygen content O_{ref}, the two values of the equilibria for $O = O_{ref}$, C_{eq1ref} and C_{eq2ref}, parameters linked to the shape of the evolution of organic carbon burial with carbon (C_1, C_2, β, γ, α), one parameter linked to the evolution of organic matter burial with oxygen (δ), and two parameters linked to the evolution of oxidation of other elements than carbon with oxygen (a_{ox} and b_{ox}). When the organic carbon burial is forced astronomically, there is one additional parameter, representing the strength of the astronomical forcing : a_f.

O_{ref} is the current oxygen level and is equal to O_{ref} = $1.19 \cdot 10^6$ Pg. C_{eq1ref} and C_{eq2ref} are the stable equilibria for $O = O_{ref}$. We have choosen C_{eq1ref} to be equal to the pre industrial carbon content of Earth's surface reservoirs (atmosphere, oceans and biosphere). It is estimated to be around 43 000 PgC (Ciais et al., 2013). We have chosen the second equilibria to be

https://doi.org/10.5194/esd-2022-46
Preprint. Discussion started: 10 October 2022


Earth System Dynamics Discussions
Open Access
EGU

at higher carbon values, C_{eq2ref} = 47000 PgC. The τ_c constant is set to 200 kyr (Archer et al., 1997). The V_0 value was chosen in order to have $\delta^{13}C$ values around zero for medium carbon values, $V_0 = (5/8)\cdot(1/2)(C_{eq1ref}+C_{eq2ref})/\tau_c$ = 140 TgCyr^{-1}. This is a value slightly higher than in Paillard (2017). However, it remains in the range of possible values for carbon emissions from volcanism, estimated between 40 and 175 TgC/yr (Burton et al., 2013). That C_{eq1ref} and C_{eq2ref} are equilibria for $O = O_{ref}$ in the unforced case gives constraints on the α and γ parameters. Several values of β remain possible, with the constraint that we should have $\beta > 1/2\tau_c$. C_1 and C_2 should be contained between C_{eq1ref} and C_{eq2ref} : $C_{eq1ref} < C_1 < C_2 < C_{eq2ref}$. In the following, we have taken $\beta = 2.4 \cdot 1/2\tau_c$, $C_1 = C_{eq1ref} + (1/3)(C_{eq2ref} - C_{eq1ref})$, $C_2 = C_{eq1ref} + (2/3)(C_{eq2ref} - C_{eq1ref})$. Changing these parameters would change slighlty the form of the unforced oscillations. The δ parameter influences the size of the free oscillations for the oxygen. We have set δ in order to have free oscillations of the size of a few percent of the reference oxygen value. This corresponds to $\delta \sim 2 \cdot 10^{-7}$. Different values of the parameters a_{ox} and b_{ox} are studied in the following, corresponding to the four possible different cases outlined by the four panels of Figure 3 (see Section 3.1).

3 Results and discussion

Here we study the results for three different cases to examine the importance of the different processes.

- In a first step, we do not consider astronomical variations of the organic matter burial B. Therefore, organic matter burial only depends on the carbon and oxygen quantities, $B = B_0(C,O)$.
- In a second step, we consider a formulation similar to the model of Paillard (2017), where the organic matter burial depends on the astronomical forcing but does not depend on the carbon and oxygen quantities : $B = B_{0cst} - a_f F(t)$ with B_{0cst} being a constant.
- In a last step, we consider that the organic matter burial depends on both the astronomical forcing and the carbon and oxygen contents (complete form) : $B = B_0(C,O) - a_f F(t)$

3.1 Results without astronomical forcing of the organic matter burial

First, we look at our model results in the case where the organic matter burial is not forced astronomically, corresponding to $a_f = 0 : B = B_0(C(t),O(t))$. This is done in order to better understand the dynamics of the coupled oxygen/ carbon system without astronomical forcing. We first consider the system from a theoretical point of view, by describing the different possible equilibria. Then, we compute the results numerically for different parameter values.

Equilibria for the carbon are defined as $\frac{dC}{dt}$ = 0. From equation 2, we get :

$$\frac{1}{2}\frac{dC}{dt} = (V - \frac{W}{2}) - B \tag{9}$$

Carbon equilibria are thus equivalent to $B = V - W/2$. As we have assumed $W = C/\tau_c$, and V to be constant, $V = V_0$, this corresponds to $B = V_0 - C/(2\tau_c)$. Figure 2 represents schematically the evolution the organic matter burial term and the V - W/2 term as a function of the carbon content C. Depending on the relative position of the B curve to the V - W/2 curve, this

https://doi.org/10.5194/esd-2022-46
Preprint. Discussion started: 10 October 2022

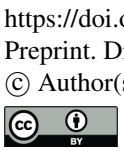

Earth System Dynamics Discussions
Open Access
EGU

leads to one or two stable equilibria. For clarity, in the following we will call the B curve (green in the Figures) the organic term, and the V - W/2 curve (red curve) the inorganic term.

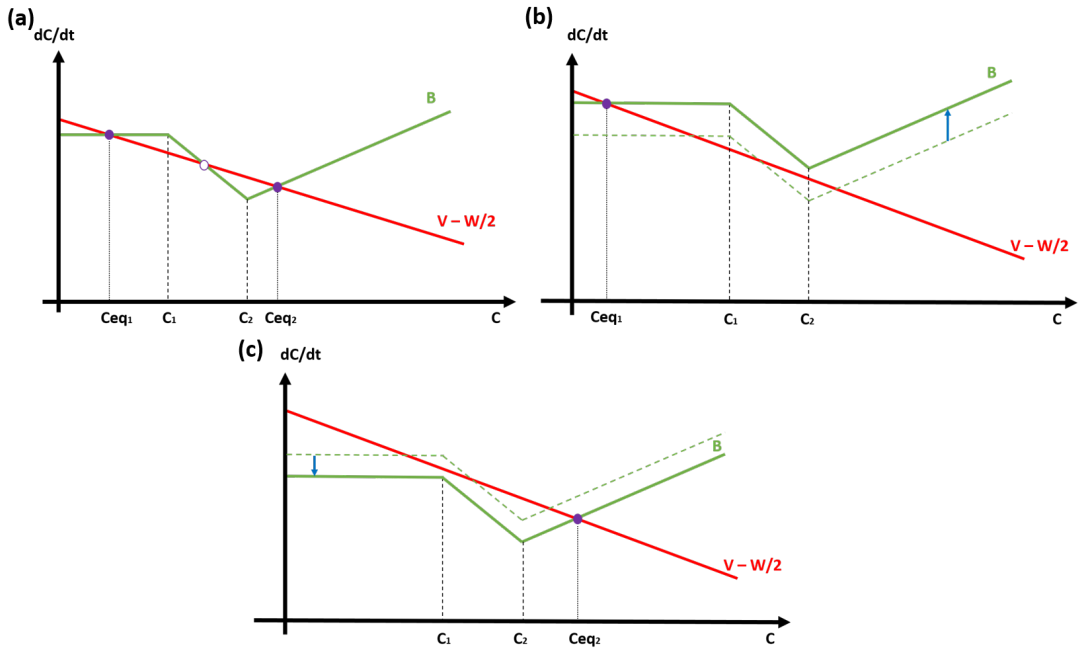

Figure 2. Schematic representation of the organic (green, B) and inorganic (red, $V_0 - C/(2\tau_c)$) terms as a function of the carbon content C. (a) Case of two equilibria in the carbon system (C_{eq1} and C_{eq2}). (b) Case of one equilibria in the carbon system, at low carbon value (C_{eq1}). (c) Case of one equilibria in the carbon system, at high carbon value C_{eq2}.

In the case represented by panel (a) of Figure 2, the organic and inorganic curves cross at three different locations, meaning that there are three different carbon values C for which an equilibrium is obtained (dC/dt = 0). However, only two of these equilibria are stable and are indicated by full purple circle, while the unstable equilibria is indicated by an empty purple circle. In the case of the empty circle, if we diverge a little from the equilibria value to higher carbon values, then V - W/2 > B (the red curve is above the green one) and thus dC/dt >0. This small divergence to higher carbon value, leads to even higher carbon values : the equilibrium is unstable. The same reasoning can be done if we diverge a little from the equilibrium towards lower carbon values. On the contrary, if we consider the first full purple point from panel (a) of Figure 2, it is a stable equilibrium. If we diverge a little from this equilibrium towards higher carbon values, then B > V - W/2 (the green curve is above the red) and thus dC/dt < 0. The system is brought back towards lower carbon values : the equilibrium is stable. Panel (a) of Figure 2 represents the case of two stable equilibria in the carbon system. However, it is possible to have only one stable equilibrium in the carbon system, if the value of B is higher or lower, as is shown in panels (b) and (c) of Figure 2. In the case of a higher organic matter burial, there is only one crossing between the green and red curves as represented in panel (b) of Figure 2 : there is only one equilibrium for the carbon cycle, C_{eq1}. A similar reasoning than previously shows that this

https://doi.org/10.5194/esd-2022-46
Preprint. Discussion started: 10 October 2022


Earth System Dynamics Discussions
Open Access
EGU

equilibrium is stable. In a similar manner, in the case of a lower organic matter burial, there is only one crossing between the green and red curves as represented in panel (c) of Figure 2 : there is only one equilibrium for the carbon cycle, C_{eq2}. This equilibrium is stable. These three configuration of the organic matter burial correspond to different oxygen values. Indeed, as $B(C,O) = B(C,O_{ref}) - \delta(O - O_{ref})$, higher oxygen values correspond to a shift of the organic matter (green) curve towards the bottom, and conversely. Therefore, it is possible to switch between the configurations, if the oxygen evolves.

Similarly to what has been done for the carbon cycle, we look at possible equilibria in the oxygen cycle. In our model, dO/dt = 0 corresponds to $B = Ox$, meaning that the organic matter burial is equal to the oxidation of other elements than carbon. These terms are represented in Figure 3. The four different configurations shown in panels (a) - (d) correspond to different values for the slope and intercept of the Ox curve. For these four configurations, the shape of the organic matter burial B (green) curve is similar. For low oxygen values ($O < O_{lim2}$), there is only one possible value of the organic matter burial B for each oxygen value. This corresponds to the case displayed in panel (b) of Figure 2, where there is only one possible equilibrium value for the carbon content C, and therefore only one possible value of B for a given oxygen value. For decreasing oxygen value, the organic burial increases. For high oxygen values, ($O > O_{lim1}$), there is also only one possible value of the organic matter burial B for each oxygen value. This corresponds to the case displayed in panel (c) of Figure 2. There is only one possible value for the carbon content C, and therefore only one possible value of B for a given oxygen value. These values of organic carbon burial B are lower than the one obtained with $O < O_{lim2}$. For intermediate oxygen values ($O_{lim2} < O < O_{lim1}$) there are two possible equilibrium values for the carbon content C, and therefore two possible equilibrium values for the organic matter burial B for a given oxygen value. This corresponds to the case displayed in panel (a) of Figure 2. The unstable equilibrium is displayed with dotted line.

Following our hypothesis, the Ox curve is simply a straight line. However, depending on the slope and intercept of the Ox curve, this leads to four different configurations, where the (blue) Ox curve either crosses the upper branch of B, the lower branch of B, none of them or both of them. These four different possibilities are schematized in Figure 3. When the Ox curve crosses the upper branch of B (Panel (b) of Figure 3), there is one possible equilibrium value for the oxygen (dO/dt = 0), represented by the full orange circle. It is a stable equilibrium : if we divert to lower oxygen values, then B > Ox (the green curve is above the blue line), meaning that dO/dt > O, and the oxygen value increases back towards equilibrium. Similarly, when the Ox curve crosses the lower branch of B (Panel (c) of Figure 3), there is one possible equilibrium value for the oxygen. This is also a stable equilibrium. When the Ox curve crosses both the upper and lower branches of B (Panel (d) of Figure 3), it crosses also the middle, unstable, branch. There are three possible equilibrium values for the oxygen, two of which are stable (the crossing with the upper and lower branch). For these three cases (panels (b), (c) and (d) of Figure 3), the system will converge towards an equilibrium value (C_{eq}, O_{eq}) and remain in this state as this are stable equilibria. When the equilibrium is reached the carbon and oxygen content will not evolve anymore. The organic matter burial and the $\delta^{13}C$ will therefore also not change.

However, the situation is different in the case where the Ox curve does not cross the lower or upper branch of B, but crosses the middle branch (dashed line), as represented in Panel (a) of Figure 3. This branch is not stable from the carbon point of view (it corresponds to the unstable equilibria of Figure 2). It is also not a stable equilibria for oxygen. In this case, no equilibrium is

https://doi.org/10.5194/esd-2022-46
Preprint. Discussion started: 10 October 2022

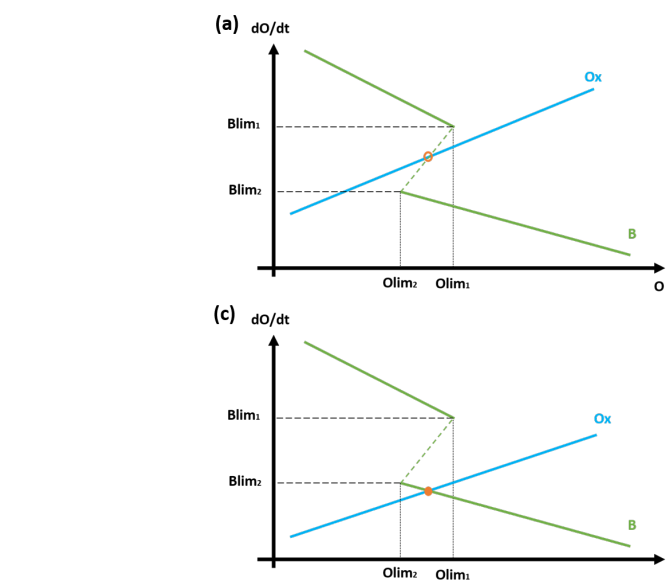

Figure 3. Schematic representation of the organic term (B, green curve) and the Ox term (blue curve) as a function of the oxygen content O. Four different cases are displayed, depending on the slope and intercept of the Ox curve : (a) one unstable equilibrium; (b) and (c) a stable equilibria; and (d) two stable equilibria

reached for the (C, O) system, and oscillations of the oxygen and carbon content can be obtained without astronomical forcing of the organic matter burial. The organic matter burial and the $\delta^{13}C$ therefore also oscillate.

To illustrate these cases, we run our model without astronomical forcing. For conciseness reasons, we consider only two out of the four possible cases described above. We will consider the two cases for which the Ox curve crosses the unstable middle branch, corresponding to panels (a) and (d) of Figure 3. We define the parameter a_{lim} as $a_{lim} = (B_{lim1} - B_{lim2})/(O_{lim1} - O_{lim2})$. If $a_{ox} > a_{lim}$, this corresponds to the case of panel (d) of Figure 3. If $a_{ox} < a_{lim}$, this corresponds to the case depicted in panel (a) of Figure 3.

3.1.1 $a_{ox} > a_{lim}$

The model is run for 100 Myr with $a_{ox} = 1.5 \cdot a_{lim}$, for one specific set of model parameters. The simulations start from different initial values for the carbon and oxygen. The Ox curve intercept parameter b_{ox}, is chosen in order to follow the configuration of panel (d) of Figure 3, where the Ox curve crosses 3 times the B curve. The carbon, oxygen, organic matter burial and $\delta^{13}C$ evolution over time are displayed in Figure 4. An equilibrium is reached in less than 10 Myr for all the simulations. The equilibrium value depends on the initial conditions. This is expected as there are two stable equilibria for the (C,O) system in this configuration. In the case of a different value of the parameter b_{ox}, leading to a single crossing with the B curve (case of panel (b) and (c) of Figure 3), an equilibrium would also be reached. The only difference is that the equilibrium would not depend on initial conditions, as there is only one possible equilibrium value.

https://doi.org/10.5194/esd-2022-46
Preprint. Discussion started: 10 October 2022

Earth System Dynamics
Discussions
Open Access
EGU

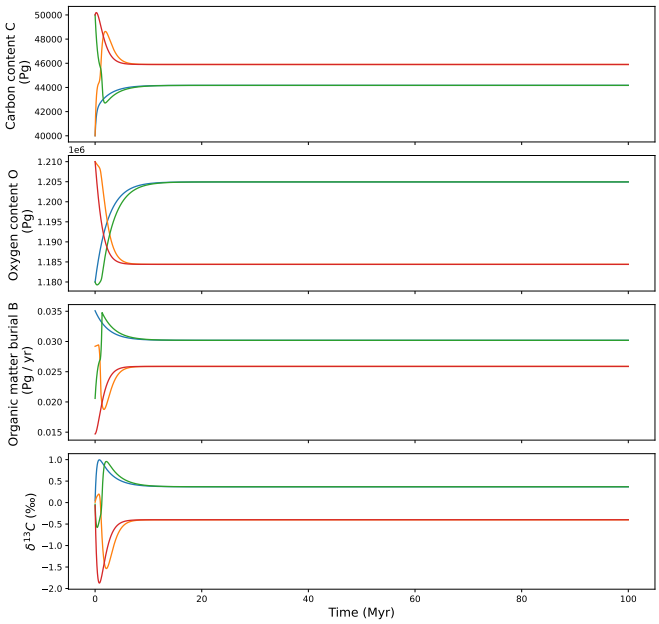

Figure 4. Modelled carbon content C, oxygen content O, organic matter burial B and $\delta^{13}C$ evolution in the case without astronomical forcing for different initial states. Case $a > a_{lim}$.

3.1.2 $a_{ox} < a_{lim}$

The model is run for 100 Myr with $a_{ox} = 0.5 \cdot a_{lim}$, for one specific set of model parameters, starting from different initial values for the carbon and oxygen. The parameter b_{ox}, is chosen in order to follow the configuration of panel (a) of Figure 3, where the Ox curve only crosses the unstable part of the B curve. The carbon, oxygen, organic matter burial and $\delta^{13}C$ evolution over time are displayed in Figure 5.

In this case, no equilibrium is reached and the system oscillates. The amplitude of the oscillations for the carbon is around 6000 PgC. The $\delta^{13}C$ oscillations have an amplitude around 2.5‰. The frequency of the oscillation is identical for the different initial conditions, and only the phase is different. The oscillations have a period of approximately 15 Myr with the parameter set used on this example. The frequency and shape of the oscillations depend on the model parameters. For example, for higher values of the δ parameter, the system would oscillate more quickly.

To sum up, we have detailed here a simple case, without astronomical forcing of the organic matter burial B. In that case, there are two possibilities for the evolution of the (C, O) system. If there is at least one stable equilibrium for the oxygen (case of panels (b), (c) and (d) of Figure 3), then the system will converge towards an equilibrium (C_{eq}, O_{eq}), and the modelled $\delta^{13}C$ will also converge towards an equilibrium. If there is no stable equilibrium for the oxygen (case of panel (a) of Figure 3), the

https://doi.org/10.5194/esd-2022-46
Preprint. Discussion started: 10 October 2022

Earth System Dynamics
Discussions
Open Access
EGU

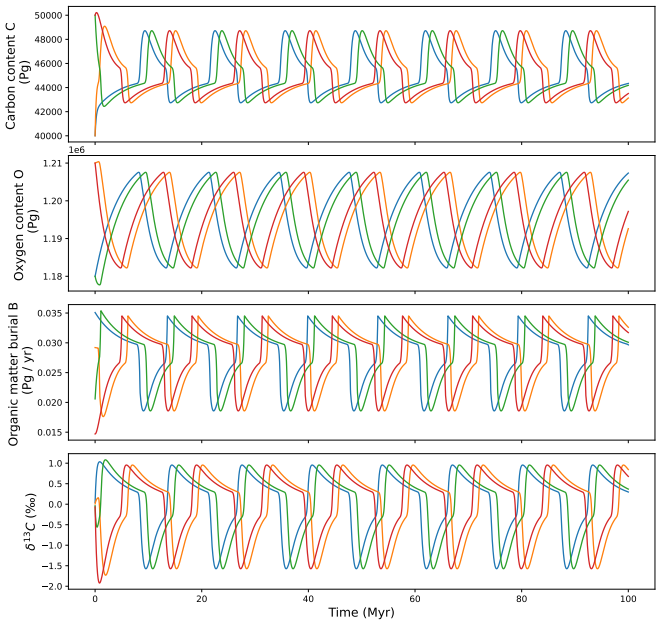

Figure 5. Modelled carbon content C, oxygen content O, organic matter burial B and $\delta^{13}C$ evolution in the case without astronomical forcing for different initial states. Case $a < a_{lim}$.

(C,O) system will oscillate freely, and the modelled $\delta^{13}C$ will also oscillate. However, in our model, the organic matter burial is also forced astronomically, through a dependency to eccentricity. This makes the situation more complex. When a stable equilibrium is reached in a case without astronomical forcing, the equilibrium can become unstable in the forced case, if the astronomical forcing is relatively strong (relatively high values of the a_f parameter). In this case, the astronomical forcing pushes the system away from its equilibrium towards another. This will be detailed in the third result section.

3.2 Results without oscillatory dynamics - organic matter burial not depending on surface oxygen.

In a second step, we study our model results in the case where the net organic matter burial does not depend on surface carbon and oxygen quantities, but is solely forced by the astronomical forcing : $B = B_{0cst} - a_f F(t)$, where B_{0cst} is a constant. This is close to the model of Paillard (2017). In this case we have no coupling anymore between the carbon and the oxygen cycle, and the system is linear, with an astronomical forcing.

$$\begin{cases} \frac{dC}{dt} = -\frac{1}{\tau_c} C + c_1 - 2a_f F(t) \\ \frac{dO}{dt} = -a_{ox} O + c_2 + a_f F(t) \end{cases} \tag{10}$$

https://doi.org/10.5194/esd-2022-46
Preprint. Discussion started: 10 October 2022

Earth System Dynamics
Discussions
Open Access
EGU

with c_1 and c_2 being constants, $c_1 = 2(V_0 - B_0)$, $c_2 = B_0 - b$. As $a_{ox} > 0$ and $\frac{1}{\tau_c} > 0$ the system is stable. Without the astronomical forcing, it would converge towards an equilibrium. The addition of the astronomical forcing yields oscillations around it.

In the following, we have run the model with the same parameters as previously, for different values of the a_f parameter. In Figure 6 the evolution of carbon, oxygen, organic carbon burial and $\delta^{13}C$ over time are displayed for a_f = 0.01 (green curves), a_f = 0.03 (orange curves) and a_f = 0.05 (blue curves). There are oscillations around an equilibrium value for the carbon and the $\delta^{13}C$. Changing the a_f value does not change the shape nor the frequency of the oscillations. It only changes their amplitude. For the $\delta^{13}C$, the oscillation amplitude varies from around 0.5‰ for the weakest astronomical forcing considered (a_f = 0.01) to 2‰ for the strongest astronomical forcing considered (a_f = 0.05). For the carbon, the oscillation amplitude varies from around 1000 PgC to 6000 PgC.

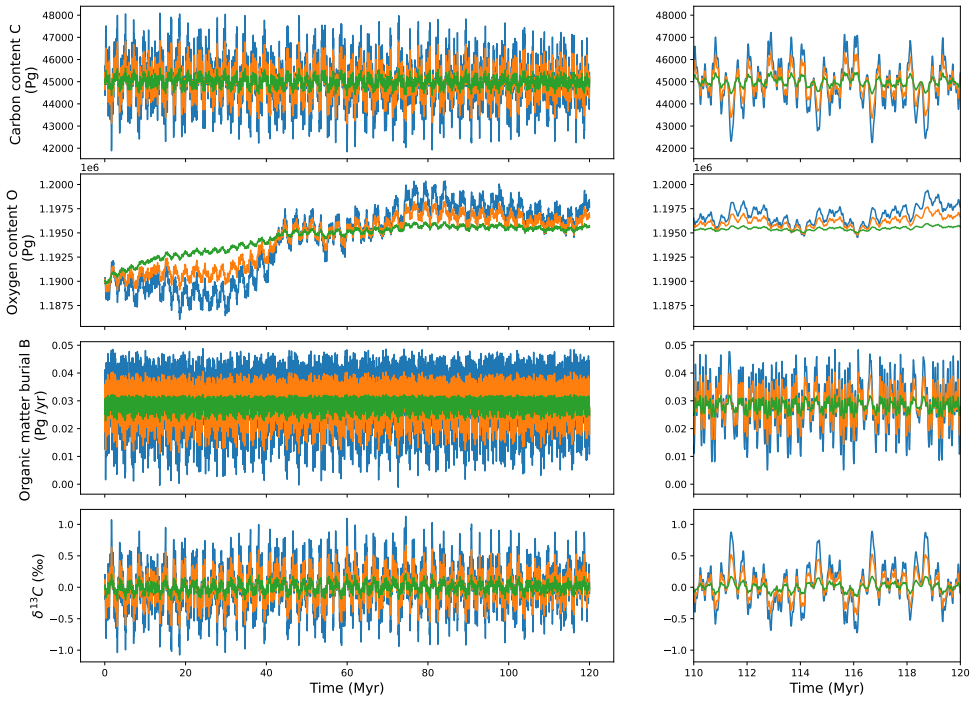

Figure 6. Modelled carbon content C, oxygen content O, organic matter burial B and $\delta^{13}C$ for different a_f values (a_f = 0.01 in green, a_f = 0.03 in orange and a_f = 0.05 in blue) when B_0 is a constant. The right panel is a zoom on the last 10 Myr of the simulation.

The spectral analysis of the $\delta^{13}C$ curve is shown in panel (a) of Figure 7. The dominant frequencies of the $\delta^{13}C$ oscillations are 400 kyr and 2.4 Myr. These frequencies are present in the input forcing (the eccentricity). The 400 kyr frequency is already

https://doi.org/10.5194/esd-2022-46
Preprint. Discussion started: 10 October 2022

Earth System Dynamics
Discussions
Open Access
EGU

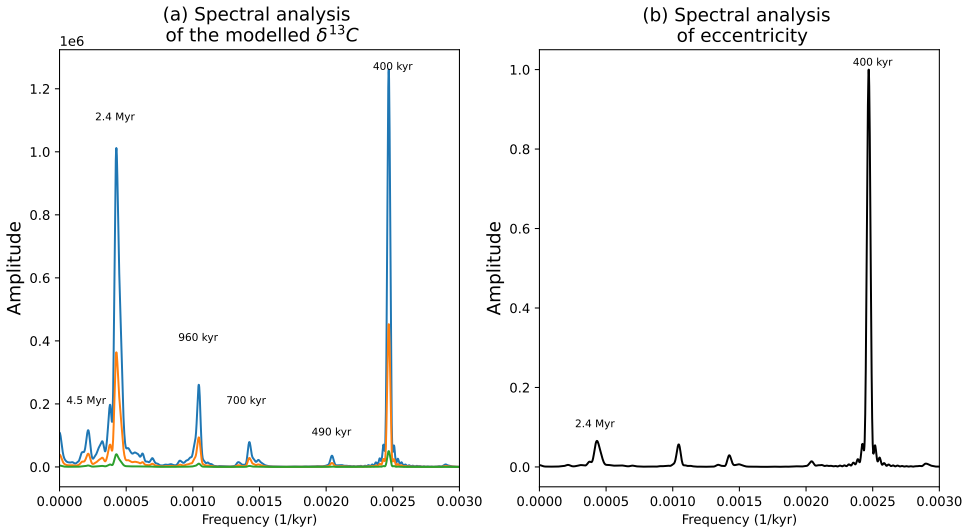

Figure 7. (a) Normalized spectral analysis of the resulting $\delta^{13}C$ for different a_f values (a_f = 0.01, 0.03 and 0.05 in green, orange and blue) when B_0 is a constant. (b) Spectral analysis of the eccentricity input forcing.

strong in the input forcing. However, the 2.4 Myr frequency is of low power in the eccentricity spectra, but strong in the modelled $\delta^{13}C$. The $\delta^{13}C$ spectral analysis also contains a weaker ∼4.5 Myr peak. This frequency is of very low amplitude in the input eccentricity forcing. As in the Paillard (2017) model, we are able to produce 400 kyr and 2.4 Myr cycles in $\delta^{13}C$ through the astronomical forcing of organic matter burial. However, as this model is linear, it is not possible to produce longer term cycles with a high amplitude, corresponding to frequencies with very low amplitude in the eccentricity spectra. A non linear model is needed to produce larger periods with a strong amplitude in $\delta^{13}C$ with a simple eccentricity forcing. This is the case with our model when we add the dependency of the organic matter burial to the carbon and oxygen contents. The results for specific parameter values are discussed in the next section.

3.3 Complete model : forcing of the organic matter burial.

Here, we use the complete form of the organic matter burial, as described in Section 2.1. The organic matter burial depends on the surface carbon quantity C, the surface oxygen quantity O and the astronomical forcing : $B = B_0(C(t), O(t)) - a_f F(t)$. We perform simulations for different a_f parameter values ranging from a_f = 0 to a_f = 0.05. This corresponds to different relative importance of the astronomical forcing on the organic matter burial. The simulations are run over 120 Myr. We perform these simulations in two different cases. The first [case A] corresponds to a situation where the system oscillates freely for a_f = 0. This corresponds to panel (a) of Figure 3. The second one [case B] corresponds to a situation where the system does not oscillate for a_f = 0 (presence of a stable equilibria). In our case, we have taken a situation corresponding to panel (b) of Figure 3. The evolution of $\delta^{13}C$ in these both cases is displayed in panels (a) of Figures 8 and 9. A zoom on the last 20 Myr of

https://doi.org/10.5194/esd-2022-46
Preprint. Discussion started: 10 October 2022

Earth System Dynamics
Discussions
Open Access
EGU

simulation is provided in panels (b). The spectral analysis of the modelled $\delta^{13}C$ is displayed in panels (c). The spectral analysis were carried out with the Blackman Tuckey method implemented in the Analyseries software (Paillard et al., 1996).

In case A, the $\delta^{13}C$ oscillates freely when the system is not forced astronomically ($a_f = 0$), with an amplitude around 2‰. For a relatively small influence of the astronomical forcing (a_f = 0.01) the shape of the large, free oscillations is still visible, and small oscillations of amplitude around 0.1‰ occur around it. However, the frequency of the free oscillations is affected by the astronomical forcing and differs from the unforced case. In case B, there are no oscillations for $a_f = 0$. For a_f = 0.1, oscillations similar to case A occur. In both cases, for higher values of a_f, the free oscillations are not visible anymore, and the signal is dominated by oscillations of lower period. The dominant, low period oscillations have an amplitude of around 2‰, and the smaller higher frequency oscillations have an amplitude of around 0.05‰. Oscillations of 400 kyr are present for all cases where the system is forced astronomically. However, their relatively low amplitude makes them hard to notice in the spectral analysis, especially for low a_f value. As the relative strength of the astronomical forcing increases (a_f increases), the power of the 400 kyr oscillations becomes stronger. The dominant period of the oscillations decreases with increasing a_f parameter.

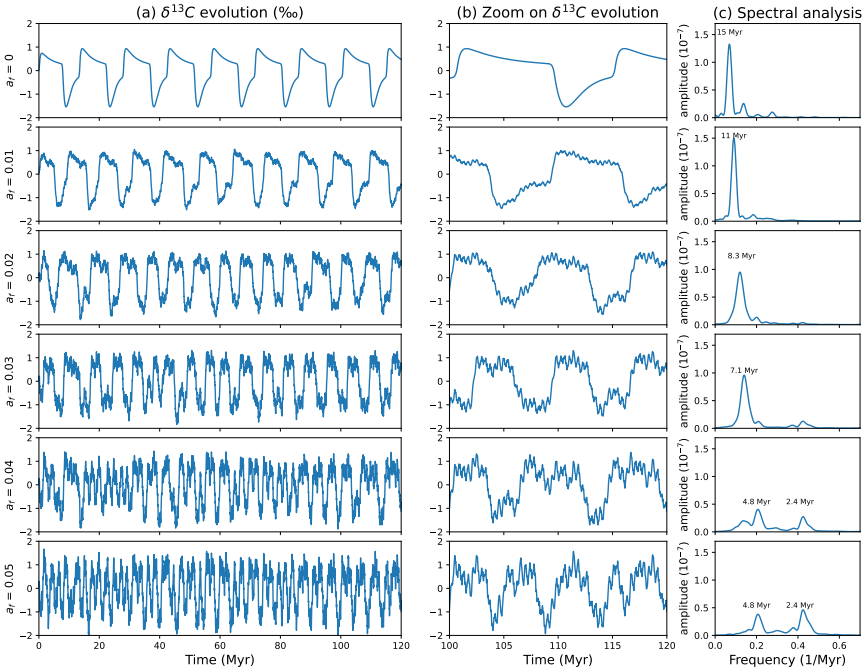

Figure 8. [case A] (a) Modelled $\delta^{13}C$ for different a_f values and $a = 0.5 \cdot a_{lim}$. (b) Zoom on the last 20 Myr of the simulation. (c) Spectral analysis of the modelled $\delta^{13}C$.

https://doi.org/10.5194/esd-2022-46
Preprint. Discussion started: 10 October 2022

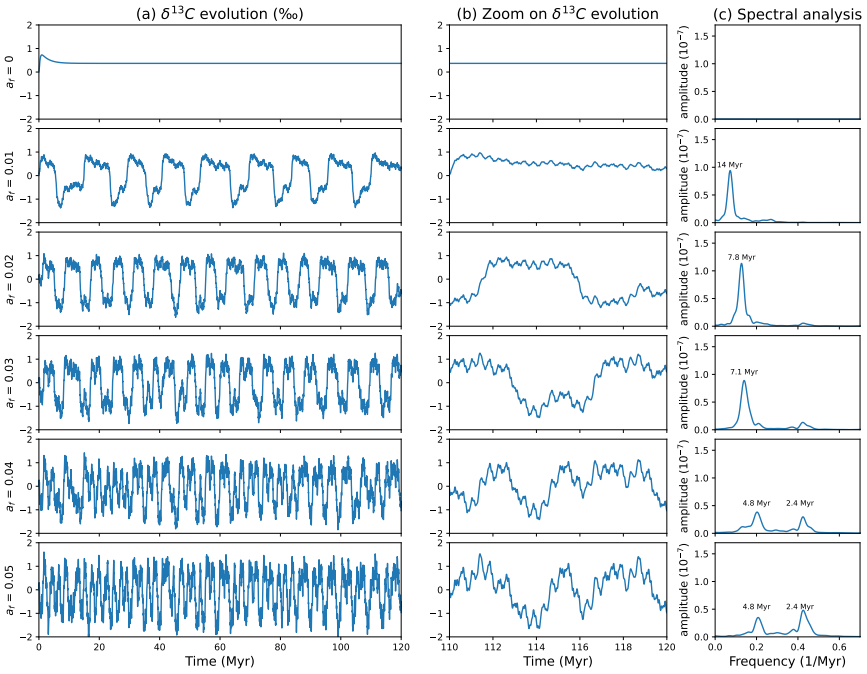

Figure 9. [case B] (a) Modelled $\delta^{13}C$ for different a_f values and $a = 1.5 \cdot a_{lim}$. (b) Zoom on the last 20 Myr of the simulation. (c) Spectral analysis of the modelled $\delta^{13}C$.

370 In both cases, the addition of the astronomical forcing changes the behaviour of the coupled system. The output signal has a dominant frequency that differs from the frequency of the unforced system. We are able to obtain oscillations on the $\delta^{13}C$ of several million years. However, one important feature to notice is that when the a_f parameter decreases, the output signal dominant period does not decrease continuously. Figure 10 represents the dominant period of the signal depending on the a_f parameter, for different parameter sets. The plot shows "steps" : there are preferential periods, meaning that for a range range 375 of a_f values, the output dominant period remains the same. The 2.4 Myr periodicity and its multiples are schematized with blue dotted lines.

For large a_f values (around 0.4 - 0.5), the dominant frequency is 2.4 Myr. Both 2.4 and 4.8 Myr periodicities are present in the spectral analysis. As the a_f parameter decreases slightly, the 4.8 Myr periodicity becomes dominant. It is particularly striking that for each parameter set, it is not possible to have a dominant frequency value between 2.4 and 4.8 Myr. The 4.8 380 Myr periodicity is the double of the 2.4 Myr periodicity of eccentricity. As the a_f parameter decreases, a period around 7 Myr becomes dominant. It is between 7.2 and 7.7 depending on the parameter set. This periodicity is not present in the eccentricity spectra. However, it corresponds to the triple of the 2.4 Myr periodicity. It is possible to obtain dominant frequencies between

https://doi.org/10.5194/esd-2022-46
Preprint. Discussion started: 10 October 2022

Earth System Dynamics
Discussions
Open Access
EGU

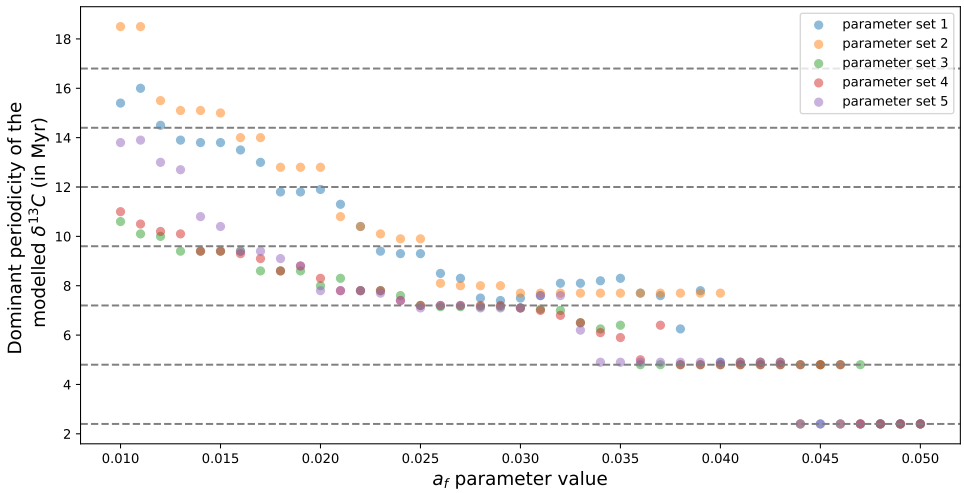

Figure 10. Dominant period of the modelled $\delta^{13}C$ as a function of the a_f value, for different parameter sets.

4.8 and 7 Myr. However, this is limited to very specific cases (specific a_f values for specific parameter values). On the contrary, the ∼7 Myr period is dominant for a wide range of a_f parameters, for all parameter sets (between a_f = 0.025 and a_f = 0.04 depending on the parameter set). Decreasing again the a_f parameter produces longer periods. The isolation of a preferential periodicity is not as clear as for the 2.4, 4.8 and ∼7 Myr frequencies, and the rise of the dominant frequency of the output signal with the a_f parameter decrease becomes more continuous. However, for each parameter set there is a small step around the fourth multiple of 2.4 Myr, ∼ 9.6 Myr (between 9 and 10 Myr, depending on the parameter set). The corresponding a_f interval is much smaller than in the case of the 4.8 and ∼7 Myr periods. As the a_f parameter decreases again, the evolution of the dominant frequencies seems to vary in a non continuous way, with preferred frequencies, but the behaviour is less clear. The presence of preferred period suggests a mechanism of frequency locking and periodicity doubling, which allows to obtain multiple of the 2.4 Myr eccentricity frequency.

As a response to a simple eccentricity forcing, our non linear model is able to produce multi-million year cycles of periods absent of the input forcing (or present with very low amplitude), most probably via a mechanism of period doubling.

However, the shape of the oscillations obtained is quite far away from the data. For each parameter set, there are values of the a_f parameter that produce ∼9 Myr cycles in the $\delta^{13}C$. One of them is displayed in Figure 11. For comparison, $\delta^{13}C$ from deep sea records (Zachos et al., 2001; Westerhold, 2020) are also shown. In the modelled $\delta^{13}C$, there are oscillations between high and low $\delta^{13}C$ value, and the shift between the low and high values is quite sudden. This is due to the fact that in our model the $\delta^{13}C$ has two equilibrium values, when the organic matter burial is not forced astronomically. When the astronomical forcing is added, oscillations occur around one equilibrium value, until the astronomical forcing becomes strong

https://doi.org/10.5194/esd-2022-46
Preprint. Discussion started: 10 October 2022

Earth System Dynamics Discussions
Open Access
EGU

	set 1	set 2	set 3	set 4	set 5
$\frac{a}{a_{lim}}$	0.5	1.5	0.2	0.5	1.5
δ	1.3e-7	1.3e-7	2e-7	2e-7	2e-7

Table 1. Value of the different parameter sets displayed in Figure 10.

enough to push the system towards the second equilibrium. 400 kyr cycles are also noticeable on top of the multi-million year oscillations. However, their strength is underestimated compared to the data.

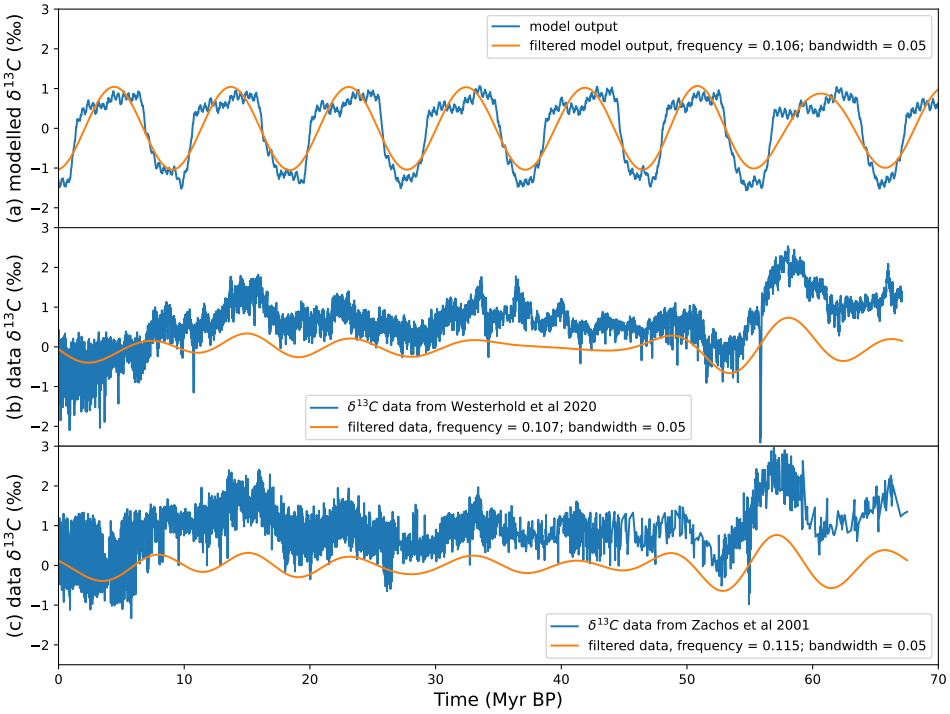

Figure 11. Comparison of (a) the modelled $\delta^{13}C$ and (b) deep sea record $\delta^{13}C$ (data are from Westerhold (2020)) in blue and filtered (frequency = 0.107; bandwidth = 0.05) in orange. The modelled $\delta^{13}C$ shown was taken among the model outputs that produces ∼9 Myr cyclicities.

At these timescale, many other processes not taken into account here, such as plate tectonics (Müller and Dutkiewicz, 2018), or other geochemical cycles could play a role and influence the carbon cycle. Our model is simple and excludes many processes that could be of importance, and other mechanisms can be considered to produce an internal oscillatory dynamics. In this model, we have linked the carbon and oxygen cycle through the organic matter burial term. The "real" dependency of

https://doi.org/10.5194/esd-2022-46
Preprint. Discussion started: 10 October 2022


Earth System Dynamics Discussions

the net organic carbon burial B to the surface carbon C and thus climate is probably much more complicated than the shape envisaged here. However, the results obtained are generic, and multiple equilibria and self-sustained oscillations (without any external forcing like eccentricity) could be obtained in the Earth system with a different shape of B corresponding to different mechanisms. One of the conditions to allow for multiple equilibria to exist is to have a non monotonic dependency of B(C). That B(C) has the same shape as the one assumed in this study is highly unlikely, but the fact that B varies in a non monotonic way with climate and thus the carbon content C is highly probable, due to the variety of processes involved, that might be favored for certain climate and thus lower or higher carbon values. One could also imagine to obtain more complex oscillations involving the sulfur cycle. Oxidation of sulfide minerals produces sulfuric acid, which can react with carbonate minerals and thus release CO_2 (Torres et al., 2014). And sulfide oxidation also affects the oxygen content. Here, we have based the oscillations on the (C,O) elements, but other mechanisms could certainly be considered.

4 Conclusions

Multi-million year oscillations are present in the $\delta^{13}C$ records throughout the Cenozoic and part of the Mesozoic. It has been suggested that these variations could be related to astronomical forcing of organic matter burial fluxes. However, no modelling study has been able to perform such long oscillations through astronomical forcing of organic matter fluxes. Here, we have proposed a mechanism that could explain the presence of multi-million year cycles in the $\delta^{13}C$ record, and their stability over time, as a result of preferential periodicity locking to multiples of astronomical forcing periods. A simple, linear astronomical forcing cannot alone produce multi-million year cycles longer than 2.4 Myr with a strong amplitude, but the presence of multiple equilibria in our model allows to extract longer periods. Our result show that astronomical forcing, superimposed to internal oscillations of the climate system (like here with carbon and oxygen) is a way to obtain very long term cycles on $\delta^{13}C$, with periodicities that are not directly present in the initial astronomical forcing.

Code and data availability. The model code as well as model outputs and figure code is available online : https://doi.org/10.5281/zenodo.7129166.

Author contributions. GL and DP designed the study. GL performed the simulations, and wrote the manuscript under the supervision of DP.

Competing interests. The authors declare that they have no conflict of interest.

Acknowledgements. We acknowledge the use of the LSCE storage and computing facilities and thank ANDRA for their financial support.

https://doi.org/10.5194/esd-2022-46
Preprint. Discussion started: 10 October 2022

Earth System Dynamics Discussions

References

Archer, D., Kheshgi, H., and Maier-Reimer, E.: Multiple timescales for neutralization of fossil fuel CO2, Geophysical Research Letters, 24, 405–408, https://doi.org/https://doi.org/10.1029/97GL00168, 1997.

Baroni, I. R., Palastanga, V., and Slomp, C. P.: Enhanced Organic Carbon Burial in Sediments of Oxygen Minimum Zones Upon Ocean Deoxygenation, Frontiers in Marine Science, 6, https://doi.org/10.3389/fmars.2019.00839, 2020.

Bergman, N. M., Lenton, T. M., and Watson, A. J.: COPSE: A new model of biogeochemical cycling over Phanerozoic time, American Journal of Science, 304, 397–437, https://doi.org/10.2475/ajs.304.5.397, 2004.

Berner, R.: Modeling atmospheric O2 over Phanerozoic time, Geochimica et Cosmochimica Acta, 65, 685–694, https://doi.org/https://doi.org/10.1016/S0016-7037(00)00572-X, 2001.

Berner, R. A. and Canfield, D. E.: A new model for atmospheric oxygen over Phanerozoic time, American Journal of Science, 289, 333–361, https://doi.org/10.2475/ajs.289.4.333, 1989.

Billups, K., Pälike, H., Channell, J., Zachos, J., and Shackleton, N.: Astronomic calibration of the late Oligocene through early Miocene geomagnetic polarity time scale, Earth and Planetary Science Letters, 224, 33–44, https://doi.org/https://doi.org/10.1016/j.epsl.2004.05.004, 2004.

Bolton, E. W., Berner, R. A., and Petsch, S. T.: The Weathering of Sedimentary Organic Matter as a Control on Atmospheric O2: II. Theoretical Modeling, American Journal of Science, 306, 575–615, https://doi.org/10.2475/08.2006.01, 2006.

Bopp, L., Le Quéré, C., Heimann, M., Manning, A. C., and Monfray, P.: Climate-induced oceanic oxygen fluxes: Implications for the contemporary carbon budget, Global Biogeochemical Cycles, 16, 6–1–6–13, https://doi.org/https://doi.org/10.1029/2001GB001445, 2002.

Boulila, S., Galbrun, B., Laskar, J., and Pälike, H.: A ∼9myr cycle in Cenozoic $\delta^{13}C$ record and long-term orbital eccentricity modulation: Is there a link?, Earth and Planetary Science Letters, 317-318, 273–281, https://doi.org/https://doi.org/10.1016/j.epsl.2011.11.017, 2012.

Burton, M. R., Sawyer, G. M., and Granieri, D.: Deep Carbon Emissions from Volcanoes, Reviews in Mineralogy and Geochemistry, 75, 323–354, https://doi.org/10.2138/rmg.2013.75.11, 2013.

Canfield, D.: THE EARLY HISTORY OF ATMOSPHERIC OXYGEN: Homage to Robert M. Garrels, Annual Review of Earth and Planetary Sciences, 33, 1–36, https://doi.org/10.1146/annurev.earth.33.092203.122711, 2005.

Chang, S. and Berner, R. A.: Coal weathering and the geochemical carbon cycle, Geochimica et Cosmochimica Acta, 63, 3301–3310, https://doi.org/https://doi.org/10.1016/S0016-7037(99)00252-5, 1999.

Ciais, P., Sabine, C., Bala, G., L. Bopp, V. B., Canadell, J., Chhabra, A., DeFries, R., Galloway, J., Heimann, M., Jones, C., Quéré, C. L., Myneni, R., Piao, S., and Thornton, P.: Carbon and Other Biogeochemical Cycles. In : Climate Change 2013: The Physical Science Basis. Contribution of Working Group I to the Fifth Assessment Report of the Intergovernmental Panel on Climate Change, Cambridge University Press, Cambridge, United Kingdom and New York, NY, USA, 2013.

de Boer, B., Lourens, L., and van de Wal, R.: Persistent 400,000-year variability of Antarctic ice volume and the carbon cycle is revealed throughout the Plio-Pleistocene., Nat Commun, 5, 299, https://doi.org/10.1038/ncomms3999, 2014.

Hedges, J. I. and Keil, R. G.: Sedimentary organic matter preservation: an assessment and speculative synthesis, Marine Chemistry, 49, 81–115, https://doi.org/https://doi.org/10.1016/0304-4203(95)00008-F, 1995.

Hemingway, J. D., Hilton, R. G., Hovius, N., Eglinton, T. I., Haghipour, N., Wacker, L., Chen, M.-C., and Galy, V. V.: Microbial oxidation of lithospheric organic carbon in rapidly eroding tropical mountain soils, Science, 360, 209–212, https://doi.org/10.1126/science.aao6463, 2018.

https://doi.org/10.5194/esd-2022-46
Preprint. Discussion started: 10 October 2022

Hilton, R. G.: Climate regulates the erosional carbon export from the terrestrial biosphere, Geomorphology, 277, 118–132, https://doi.org/https://doi.org/10.1016/j.geomorph.2016.03.028, connectivity in Geomorphology from Binghamton 2016, 2017.

Hilton, R. G. and West, A. J.: Mountains, erosion and the carbon cycle, Nature Reviews Earth Environment, 1, 284–299, https://doi.org/10.1038/s43017-020-0058-6, 2020.

Hilton, R. G., Gaillardet, J., Calmels, D., and Birck, J.-L.: Geological respiration of a mountain belt revealed by the trace element rhenium, Earth and Planetary Science Letters, 403, 27–36, https://doi.org/https://doi.org/10.1016/j.epsl.2014.06.021, 2014.

Jessen, G. L., Lichtschlag, A., Ramette, A., Pantoja, S., Rossel, P. E., Schubert, C. J., Struck, U., and Boetius, A.: Hypoxia causes preservation of labile organic matter and changes seafloor microbial community composition (Black Sea), Science Advances, 3, e1601 897, https://doi.org/10.1126/sciadv.1601897, 2017.

Kocken, I. J., Cramwinckel, M. J., Zeebe, R. E., Middelburg, J. J., and Sluijs, A.: The 405 kyr and 2.4 Myr eccentricity components in Cenozoic carbon isotope records, Climate of the Past, 15, 91–104, https://doi.org/10.5194/cp-15-91-2019, 2019.

Kurtz, A. C., Kump, L. R., Arthur, M. A., Zachos, J. C., and Paytan, A.: Early Cenozoic decoupling of the global carbon and sulfur cycles, Paleoceanography, 18, https://doi.org/https://doi.org/10.1029/2003PA000908, 2003.

Laskar, J., Robutel, P., Joutel, F., Gastineau, M., Correia, A. C. M., and Levrard, B.: A long-term numerical solution for the insolation quantities of the Earth, A&A, 428, 261–285, https://doi.org/10.1051/0004-6361:20041335, 2004.

Laskar, J., Fienga, A., Gastineau, M., and Manche, H.: La2010: a new orbital solution for the long-term motion of the Earth, A&A, 532, A89, https://doi.org/10.1051/0004-6361/201116836, 2011.

Lauretano, V., Littler, K., Polling, M., Zachos, J. C., and Lourens, L. J.: Frequency, magnitude and character of hyperthermal events at the onset of the Early Eocene Climatic Optimum, Climate of the Past, 11, 1313–1324, https://doi.org/10.5194/cp-11-1313-2015, 2015.

Laurin, J., Meyers, S. R., Uličný, D., Jarvis, I., and Sageman, B. B.: Axial obliquity control on the greenhouse carbon budget through middle- to high-latitude reservoirs, Paleoceanography, 30, 133–149, https://doi.org/https://doi.org/10.1002/2014PA002736, 2015.

Liebrand, D., Beddow, H. M., Lourens, L. J., Pälike, H., Raffi, I., Bohaty, S. M., Hilgen, F. J., Saes, M. J., Wilson, P. A., van Dijk, A. E., Hodell, D. A., Kroon, D., Huck, C. E., and Batenburg, S. J.: Cyclostratigraphy and eccentricity tuning of the early Oligocene through early Miocene (30.1–17.1 Ma): Cibicides mundulus stable oxygen and carbon isotope records from Walvis Ridge Site 1264, Earth and Planetary Science Letters, 450, 392–405, https://doi.org/https://doi.org/10.1016/j.epsl.2016.06.007, 2016.

Ludwig, W., Probst, J.-L., and Kempe, S.: Predicting the oceanic input of organic carbon by continental erosion, Global Biogeochemical Cycles, 10, 23–41, https://doi.org/https://doi.org/10.1029/95GB02925, 1996.

Martinez, M. and Dera, G.: Orbital pacing of carbon fluxes by a ˜9-My eccentricity cycle during the Mesozoic, Proceedings of the National Academy of Sciences, 112, 12 604–12 609, https://doi.org/10.1073/pnas.1419946112, 2015.

Meybeck, M.: Carbon, nitrogen, and phosphorus transport by world rivers, American Journal of Science, 282, 401–450, https://doi.org/10.2475/ajs.282.4.401, 1982.

Müller, R. D. and Dutkiewicz, A.: Oceanic crustal carbon cycle drives 26-million-year atmospheric carbon dioxide periodicities, Science Advances, 4, eaaq0500, https://doi.org/10.1126/sciadv.aaq0500, 2018.

Niemeyer, D., Kemena, T. P., Meissner, K. J., and Oschlies, A.: A model study of warming-induced phosphorus–oxygen feedbacks in open-ocean oxygen minimum zones on millennial timescales, Earth System Dynamics, 8, 357–367, https://doi.org/10.5194/esd-8-357-2017, 2017.

Paillard, D.: The Plio-Pleistocene climatic evolution as a consequence of orbital forcing on the carbon cycle, Climate of the Past, 13, 1259–1267, https://doi.org/10.5194/cp-13-1259-2017, 2017.

https://doi.org/10.5194/esd-2022-46
Preprint. Discussion started: 10 October 2022

Paillard, D., Labeyrie, L., and Yiou, P.: Macintosh Program performs time-series analysis, Eos, Transactions, AGU, 77, 379–379, https://doi.org/10.1029/96EO00259, 1996.

Petsch, S., Edwards, K., and Eglinton, T.: Microbial transformations of organic matter in black shales and implications for global biogeochemical cycles, Palaeogeography, Palaeoclimatology, Palaeoecology, 219, 157–170, https://doi.org/https://doi.org/10.1016/j.palaeo.2004.10.019, geobiology: Objectives, Concept, Perspectives, 2005.

Pälike, H., Norris, R. D., Herrle, J. O., Wilson, P. A., Coxall, H. K., Lear, C. H., Shackleton, N. J., Tripati, A. K., and Wade, B. S.: The Heartbeat of the Oligocene Climate System, Science, 314, 1894–1898, https://doi.org/10.1126/science.1133822, 2006.

Russon, T., Paillard, D., and Elliot, M.: Potential origins of 400–500 kyr periodicities in the ocean carbon cycle: A box model approach, Global Biogeochemical Cycles, 24, https://doi.org/https://doi.org/10.1029/2009GB003586, 2010.

Smith, J. C., Galy, A., Hovius, N., Tye, A. M., Turowski, J. M., and Schleppi, P.: Runoff-driven export of particulate organic carbon from soil in temperate forested uplands, Earth and Planetary Science Letters, 365, 198–208, https://doi.org/https://doi.org/10.1016/j.epsl.2013.01.027, 2013.

Sproson, A. D.: Pacing of the latest Ordovician and Silurian carbon cycle by a 4.5 Myr orbital cycle, Palaeogeography, Palaeoclimatology, Palaeoecology, 540, 109 543, https://doi.org/https://doi.org/10.1016/j.palaeo.2019.109543, 2020.

Sprovieri, M., Sabatino, N., Pelosi, N., Batenburg, S. J., Coccioni, R., Iavarone, M., and Mazzola, S.: Late Cretaceous orbitally-paced carbon isotope stratigraphy from the Bottaccione Gorge (Italy), Palaeogeography, Palaeoclimatology, Palaeoecology, 379-380, 81–94, https://doi.org/https://doi.org/10.1016/j.palaeo.2013.04.006, 2013.

Stolper, D. A., Bender, M. L., Dreyfus, G. B., Yan, Y., and Higgins, J. A.: A Pleistocene ice core record of atmospheric O_2 concentrations, Science, 353, 1427–1430, https://doi.org/10.1126/science.aaf5445, 2016.

Stramma, L., Johnson, G. C., Sprintall, J., and Mohrholz, V.: Expanding Oxygen-Minimum Zones in the Tropical Oceans, Science, 320, 655–658, https://doi.org/10.1126/science.1153847, 2008.

Stramma, L., Schmidtko, S., Levin, L. A., and Johnson, G. C.: Ocean oxygen minima expansions and their biological impacts, Deep Sea Research Part I: Oceanographic Research Papers, 57, 587–595, https://doi.org/https://doi.org/10.1016/j.dsr.2010.01.005, 2010.

Torres, M., West, A., and Li, G.: Sulphide oxidation and carbonate dissolution as a source of CO2 over geological timescales., Nature, 507, 346–349, https://doi.org/10.1038/nature03814, 2014.

Wang, P., Tian, J., and Lourens, L. J.: Obscuring of long eccentricity cyclicity in Pleistocene oceanic carbon isotope records, Earth and Planetary Science Letters, 290, 319–330, https://doi.org/https://doi.org/10.1016/j.epsl.2009.12.028, 2010.

Westerhold, T.: Cenozoic global reference benthic carbon and oxygen isotope dataset (CENOGRID), https://doi.org/10.1594/PANGAEA.917503, 2020.

Westerhold, T., Röhl, U., Donner, B., McCarren, H. K., and Zachos, J. C.: A complete high-resolution Paleocene benthic stable isotope record for the central Pacific (ODP Site 1209), Paleoceanography, 26, https://doi.org/https://doi.org/10.1029/2010PA002092, 2011.

Zachos, J., Pagani, M., Sloan, L., Thomas, E., and Billups, K.: Trends, Rhythms, and Aberrations in Global Climate 65 Ma to Present, Science, 292, 686–693, https://doi.org/10.1126/science.1059412, 2001.

In this study, we have proposed a new conceptual model for the geological carbon cycle. Contrary to previous studies [Paillard, 2017], the organic matter burial depends not only on astronomical forcing, but also on the surface carbon content C in a non linear way (through carbon content influence on climate, and climate influence on organic matter burial), and the oxygen content O. These assumed dependencies result in a non linear model with multiple equilibria. With this non linear model, it is possible to produce multi-million year oscillations as a response to eccentricity forcing. Multiples of the 2.4 Myr eccentricity frequency are preferred outputs of the model, suggesting a mechanism of periodicity locking. Our study shows that astronomical forcing, superimposed on internal oscillations of the climate system (in our case, obtained with the surface carbon and oxygen contents) is a way to obtain very long term cycles on $\delta^{13}C$, with periodicities that are not directly present in the initial astronomical forcing. We emphasize that the purpose of our model is not to be realistic. Net organic matter burial involves many different processes, already difficult to quantify at present, and impossible to evaluate for different climates, carbon contents, or oxygen contents. Additionally, several mechanisms not taken into account in our model could play a role on these timescales, such as plate tectonics [Müller and Dutkiewicz, 2018] or the release of atmospheric CO_2 through the oxidation of sulfide minerals that forms sulfuric acid and its reaction with carbonate rocks [Torres et al., 2014]. However, we emphasize the fact that linear models are not able to produce multi-million year oscillations in the $\delta^{13}C$ as a response to astronomical forcing, while it is possible with a non linear model based on multiple equilibria.

5.3 . Implications of multiple equilibria in the carbon cycle on future CO_2 projections

Current modelling studies on the long term fate of atmospheric CO_2 do not take into account organic matter burial and thus are not able to reproduce past $\delta^{13}C$ data. In addition, the formulation used is linear, either assumed [Archer et al., 1997, 1998, Archer, 2005] or modelled [Lord et al., 2016] : when the atmospheric CO_2 increases, CO_2 uptake by silicate weathering increases, allowing to return to the initial CO_2 values. The possibility of existence of multiple equilibria in the geological carbon cycle has never been considered before.

Here, we use the conceptual model we have developed in an idealized case. First in section 5.3.1 we look at the global surface carbon evolution over time, following a carbon release due to anthropogenic fossil fuel consumption. Our model represents the evolution of the surface carbon content C, of the ocean, atmosphere, and biosphere, opposed to the carbon stored in geological reservoirs. However, our model does not represent the exchanges and repartition between the different reservoirs that take place on shorter timescales and thus does not represent the CO_2 concentration for a given surface carbon content C. In a second

part, in section 5.3.2, we build illustrative scenarios of the CO_2 concentration over time, following anthropogenic emissions. On timescales up to 10 - 50 kyr, our scenarios are based on the existing litterature on these timescales. For timescales of a hundred thousand years, we suggest alternative possibilities to the currently existing litterature.

5.3.1 . Idealized scenarios for the surface carbon evolution, following a major carbon release

First, we look at the global surface carbon evolution in our model, following a carbon release. For past times, we use the conceptual model as described previously. At t=0, we add an anthropogenic contribution to the model. Indeed, the current anthropogenic use of fossil fuel corresponds to a release of carbon from the geological reservoir to the surface reservoir. More specifically, this corresponds to additional organic matter oxidation. This is schematized in Figure 5.3.

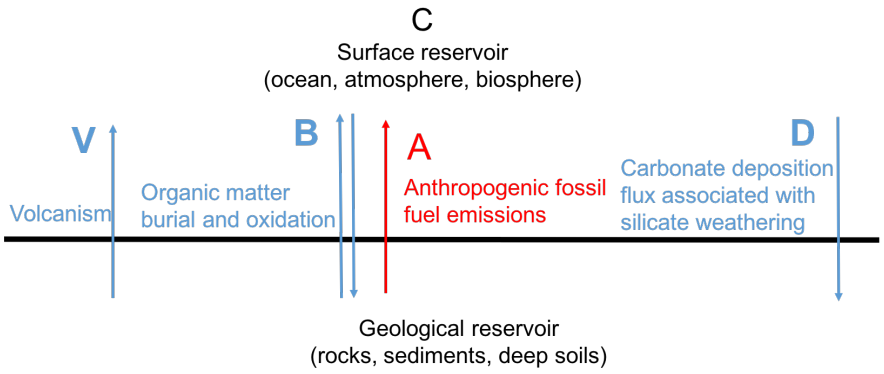

Figure 5.3: Schematic representation of the geological carbon cycle model, with anthropogenic contribution

The surface carbon content C evolution is then represented by the equation :

$$\frac{dC}{dt} = V - (B - A) - D \tag{5.2}$$

with A being the annual carbon release associated with anthropogenic fossil fuel consumption (anthropogenic organic matter oxidation). After a few decades, we consider that the anthropogenic fossil fuel emissions have stopped, and the anthropogenic contribution A is not included anymore in the model equations. We then compare the surface carbon content evolution in a case where an anthropogenic fossil fuel release took place for a few decades, and the case where no anthropogenic fossil fuel release took place.

It is estimated that fossil CO_2 emissions from coal, oil and natural gas from 1850 to 2020 represented 430 GtC [Friedlingstein et al., 2022]. Current yearly emissions (estimated on years 2019, 2020, 2021) are 9.5 - 10 GtC/yr [Friedlingstein et al., 2022]. In our case, we either apply an anthropogenic contribution of 5 or 10 GtC/yr during 100 year. This corresponds to a global anthropogenic contribution of 500 or 1 000 GtC. We do not seek to follow the temporal pattern of fossil fuel emissions following the already achieved emissions or the estimated future emissions (SSPs scenarios). Indeed, these simulations do not aim at being realistic, but rather illustrative and the temporal pattern of emission does not affect much the results. Furthermore, this model represents only the long term processes, on timescales larger than 10 kyr.

Here, three cases are shown, corresponding to different values of surface carbon at t=0, and different amount of anthropogenic carbon release. The first case is shown in Fig. 5.4, the second in Fig. 5.5 and the third in Fig. 5.6. In the first case (Figure 5.4), the surface carbon concentration is already quite high at t=0. The total anthropogenic carbon release is 1 000 GtC. In the second and third case (Figures 5.5 and 5.6), the surface carbon concentration is relatively low at t=0. The difference between the second and third case is the total carbon release : it is 500 GtC in the second case and 1 000 GtC in the third.

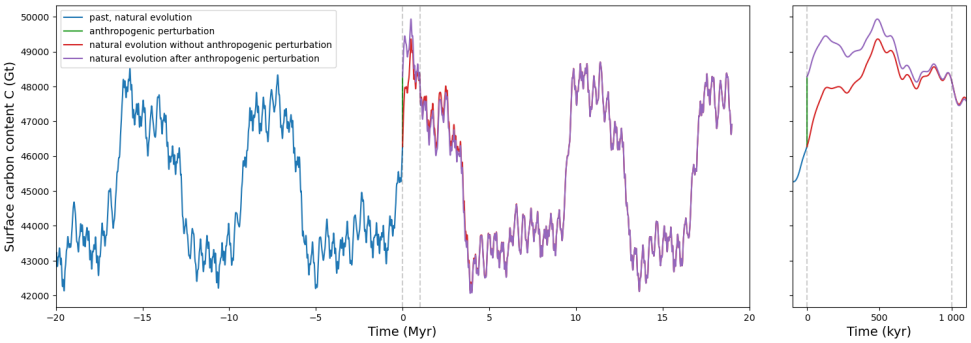

Figure 5.4: Surface carbon content evolution in case 1. In the left panel, the results are shown from 20 Myr BP to 20 Myr BP. In the right panel, a zoom on the period 0 - 1 Myr AP is performed. The evolution over past periods is shown in blue. The evolution between t=0 and t=1000 year is shown in green in the case where anthropogenic fossil fuel release takes place. The evolution after the fossil fuel perturbaton is shown in purple. The "natural" evolution (no fossil fuel perturbation) is shown in red.

In the first case (Figure 5.4), the anthropogenic perturbation, leads to a carbon increase after the year t = 0. Compared to the anthropogenic perturbation (1 000 GtC in our case), the raise in carbon quantity of the surface reservoir is twice as high (2 000 GtC in this case), due to the carbonate compensation. The decrease

in oceanic CO_3^{2-} concentration following an addition of carbon leads to seafloor $CaCO_3$ dissolution until the CO_3^{2-} concentration is restored, adding carbon to the surface system. This leads to a coefficient 2 in the equations, visible in Equation (2) of the preprint submitted to Earth System Dynamics. In the first case, the surface carbon content is affected $\sim$ 1 Myr after the perturbation. However, this does not affect the carbon cycle million years into the future, and the surface carbon content after the anthropogenic perturbation equals that of the case without anthropogenic perturbation after $\sim$1 Myr.

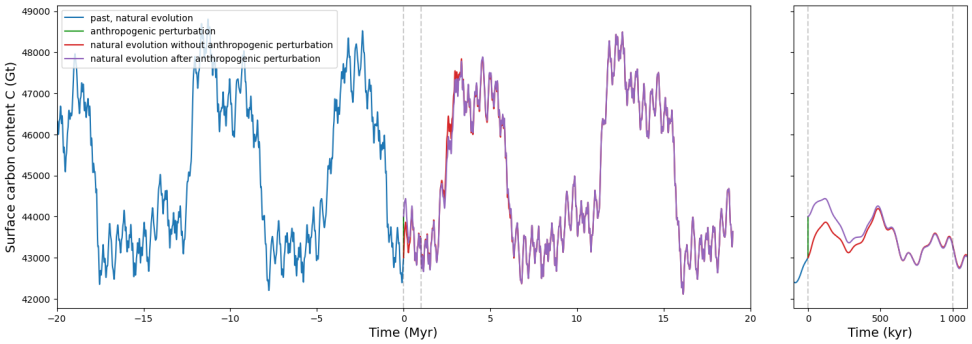

Figure 5.5: Surface carbon content evolution in case 2. In the left panel, the results are shown from 20 Myr BP to 20 Myr BP. In the right panel, a zoom on the period 0 - 1 Myr AP is performed. The evolution over past periods in shown in blue. The evolution between t=0 and t=1000 year is shown in green in the case where anthropogenic fossil fuel release takes place. The evolution after the fossil fuel perturbaton is shown in purple. The "natural" evolution (no fossil fuel perturbation) is shown in red.

In the second case (Figure 5.5), the anthropogenic perturbation, leads to a carbon increase after the year t = 0. As in the first case, the surface carbon content after the anthropogenic perturbation is similar to the one of the case without anthropogenic perturbation after $\sim$1 Myr.

However, the situation is completely different in the third case (Figure 5.6). In the third case, the anthropogenic perturbation does not only affect the surface carbon content over the next Myr, but over the following million years as well. This is due to the fact that our model is based on multiple equilibria in the carbon cycle (two equilibria in our case) and the anthropogenic perturbation has pushed the system from the lower equilibrium carbon value to the higher equilibrium carbon value. 1 Myr after the perturbation, the surface carbon content is still widely different from its value in a case without anthropogenic fossil fuel release. Due to the presence of multiple equilibria in the system, there is no return to the values of a case without anthropogenic perturbation on the next million years.

We emphasize that the simulations shown here are illustrative, and not predic-

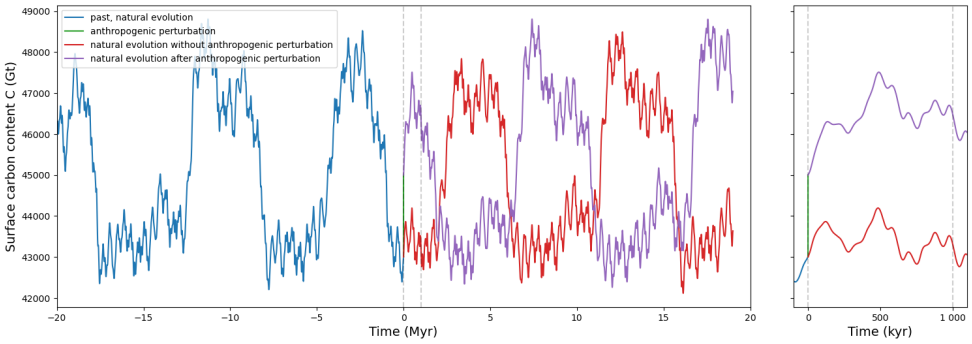

Figure 5.6: Surface carbon content evolution in case 3. In the left panel, the results are shown from 20 Myr BP to 20 Myr BP. In the right panel, a zoom on the period 0 - 1 Myr AP is performed. The evolution over past periods in shown in blue. The evolution between t=0 and t=1000 year is shown in green in the case where anthropogenic fossil fuel release takes place. The evolution after the fossil fuel perturbaton is shown in purple. The "natural" evolution (no fossil fuel perturbation) is shown in red.

tive. As explained previously, our conceptual model has a number of limitations. In particular, the numerical values of the possible equilibria are not well constrained and depend on the model parameters. As explained in section 2.2 of the manuscript submitted to Earth System Dynamics, in our case we have chosen to have a first equilibria for surface carbon values around 43 000 GtC, corresponding to pre-industrial carbon content, and a second equilibria around 47 000 GtC. However, these values could be changed. Despite these limitations, these three cases show that when taking into account the possibility of multiple equilibria in the carbon system, the response of the global surface carbon content C, to a sudden carbon addition is not necessarily to come back to values similar to those without perturbation. In our case, if the carbon perturbation is large enough, the system can be pushed towards a different equilibrium.

5.3.2 . Idealized scenarios for the surface atmospheric CO_2 evolution following a major carbon release

As explained previously, our model represents the sum of carbon contained in the surface reservoirs (the ocean, atmosphere, and biosphere). However, this does not represent the repartition between the different reservoirs and thus the CO_2 concentration for a given surface carbon content C. However, what is particularly relevant for the climate is the atmospheric CO_2 concentration, due to its greenhouse effect. In order to discuss climatic evolution over the next million years, scenarios for the evolution of the atmospheric CO_2 concentration are needed. In

the following, we develop four different idealized scenarios for the CO_2 concentration evolution.

Previous studies have represented the CO_2 concentration evolution over time after an emission pulse by a sum of decaying exponentials having different time constants [Archer et al., 1997, Solomon et al., 2009, Joos et al., 2013, Colbourn et al., 2015, Lord et al., 2016]. Therefore, here we assume that the CO_2 concentration evolution over time after an emission pulse can be represented by a sum of decaying exponentials having different time constants.

The CO_2 evolution over time can be described by :

$$CO_2(t) = CO_2^f + E \cdot \sum_{i=1}^{n} \alpha_i \cdot e^{-t/\tau_i} \tag{5.3}$$

with $CO_2(t = 0) = CO_2^p$, with CO_2^p the peak CO_2 concentration. E are the total carbon emissions (converted into ppm). τ_i are time constants and α_i are coefficients.

The number n of exponentials used to fit the decay of atmospheric CO_2 varries between studies. For instance, Archer et al. [1997] used n=4 exponentials, Lord et al. [2016] used n=5, and Colbourn et al. [2015] found that the optimal value was n = 6. The exponentials correspond to different processes or combinations of processes that act on different timescale to remove atmospheric CO_2. The timescales used also vary in the different studies. For instance in Archer et al. [1997] the timescales are 365 years, 5.5 kyr, 8.2 kyr and 200 kyr. In Lord et al. [2016], the different timescales are 1.2 yr, 36 yr, 730 yr, 11 kyr and 268 kyr. The shortest timescales are associated with ocean-atmosphere exchange, oceanic circulation ($\sim$ 1000 years), carbonate compensation ($\sim$ 10 kyr). In these studies, the largest timescales is associated with removal of remaining carbon via silicate weathering.

Here, we do not seek to fit the exponentials to one particular model result, but rather to provide scenarios that are representative of the literature. We choose to use 4 exponentials, and to account for the different timescales of the processes acting in CO_2 removal, we used timescales covering the range of existing studies : $\tau_1 \sim$ 100 years, $\tau_2 \sim$ 1 000 years, $\tau_3 \sim$ 10 000 years, $\tau_4 \sim$ 100 000 years.

However, while in existing studies, the longest timescale process (assumed to be silicate weathering) brings back CO_2 concentrations to pre-industrial CO_2 levels, here we make the assumption that the CO_2 concentration can equilibrate at a different value than the pre-industrial one, due to both the role of organic matter burial and oxidation, and silicate weathering. For two scenarios, the CO_2 concentration comes back to pre-industrial CO_2 levels (280 ppm). For the two others, the CO_2 concentration equilibrates at 700 ppm. We emphasize that the scenarios are only illustrative. The 700 ppm value is purely a modelling choice, in order to represent the possibility to reach a different equilibrium value than pre-industrial due to the geological processes and the precise number has no particular

justification.

To determine the value of the α_i coefficients, we based ourselves on existing modelling studies having examined the time evolution of the remaining atmospheric CO_2 fraction after an emission pulse (called airborne fraction) up to 10 000 years, with climate-carbon cycle models. These studies have usually examined the evolution of the CO_2 concentration after a pulse of emission of either 100, 1 000 or 5 000 GtC and many have found that the proportion taken by the ocean is a function of the size of emissions [Archer, 2005, Eby et al., 2009, Archer et al., 2009, Joos et al., 2013, Lord et al., 2016]. This is due to different carbon feedbacks : when the CO_2 emitted increases, so does temperature, which results in a lower solubility of gaseous CO_2 in sea water. Additionally, when CO_2 increases in the ocean, the buffering capacity of sea water decreases. Finally, feedbacks can occur due to modification of the oceanic circulation for higher CO_2 levels and thus temperature (decrease of the ocean overturning strength), leading to a less efficient CO_2 transport to depth [Lord et al., 2016]. Thus, the fraction of total emissions that remains after a certain time increases with total emissions.

In the following we focus on studies exploring the response to a 5 000 GtC pulse emission. Indeed, we want to focus on a high end scenario, and 5 000 GtC is close to the value of the high end scenario of the IPCC, SSP5-8.5. This scenario has been extended until 2500 [Meinshausen et al., 2020]. Under this scenario, cumulative emissions from 2015 to 2100 are 2 178 GtC, and 2 566 GtC from 2100 to 2250 (there are no emissions after 2250). With historical emissions from the pre-industrial period to 2015 being $\sim$600 GtC (assessed using data of Friedlingstein et al. [2022]) , this leads to a total of 5 344 GtC, close to the 5 000 GtC value. Another advantage of the 5 000 GtC release, is that several modelling experiments have been performed with this value.

Values of airborne fraction after 100, 1 000 and 10 000 years following a 5 000 GtC emission pulse from different studies are summed up in Table 5.1. The airborne fraction ranges from 50 - 85 % after 100 years, 14-60% after 1 000 years and 10-30% after 10 000 years. We consider total carbon emissions of 5 344 GtC corresponding to the sum of historical emissions up to 2015 and emissions under SSP5-8.5, and start from the peak CO_2 concentration of SSP5-8.5 (2210 ppm, reached around year 2250). We fitted the α_i coefficients of the exponentials in order to span the range of airborne fraction after 100, 1 000 and 10 000 years seen in the literature. For two scenarios, the airborne fraction after 100, 1 000 and 10 000 years is taken at the upper end of the literature and for the two other scenarios, it is taken at the lower end.

The four scenarios are displayed in Figure 5.7. The final CO_2 concentration is 280 ppm (pre-industrial value) for scenarios S1 and S3, while it is 700 ppm for scenarios S2 and S4. Scenarios S1 and S2 are at the upper end of modelled airborne fraction after 100, 1 000 and 10 000 years, while scenarios S3 and S4 are at the lower end. After 100 years, 73% of the total carbon emitted remains in the

atmosphere for scenarios S1 and S2 while it is 57% for scenarios S3 and S4. After 1 000 years, 58-59% of the total carbon emitted remains in the atmosphere for scenarios S1 and S2 and 30% for scenarios S3 and S4. After 10 000 years, 29-30% of the total carbon emitted remains in the atmosphere for scenarios S1 and S2 and 10-11% for scenarios S3 and S4.

	100 years	1 000 years	10 000 years
Archer [2005]	-	33%	15%
Lenton and Britton [2006]	-	14-16%	10-15 %
Ridgwell and Hargreaves [2007]	-	34%	12%
Tyrrell et al. [2007]	-	42%	21%
Archer and Brovkin [2008]	-	57%	26%
Eby et al. [2009]	-	60%	30%
Archer et al. [2009]	50 -80 %	22-60%	10-30%
Joos et al. [2013]	60 - 85%	30-60%	-
Lord et al. [2016]	70%	37%	13%

Table 5.1: Airborne fraction (ie remaining fraction of the total emissions) 100, 1 000, 10 000 years after a 5 000 GtC pulse emission. Archer et al. [2009] and Joos et al. [2013] are model intercomparison studies.

Scenarios in which the CO_2 concentration does not come back to its pre-industrial value on a million year timescale (scenarios S2 and S4) could lead to significant changes in the climate evolution over the next million year, compared to "conventional scenarios" where the CO_2 concentration comes back to its pre-industrial value (scenarios S1 and S3).

These scenario will help us to discuss possible climatic evolution over the next million years in the next section. However, we highlight that these scenarios are only illustrative. Several processes of the carbon cycle on different timescales require a better understanding. Particularly, while inorganic processes such as concentration equilibrium with the ocean, are taken into account in carbon cycle models, many carbon cycle model lack a representation of organic matter, and its subsequent burial or oxidation. In addition, the atmospheric CO_2 concentration has oscillated over the last million year with CO_2 values being lower during glacial periods and higher during interglacial periods [Lüthi et al., 2008, Bereiter et al., 2015]. The scenarios we have presented here do not consider the possibility of glacial-interglacial variations.

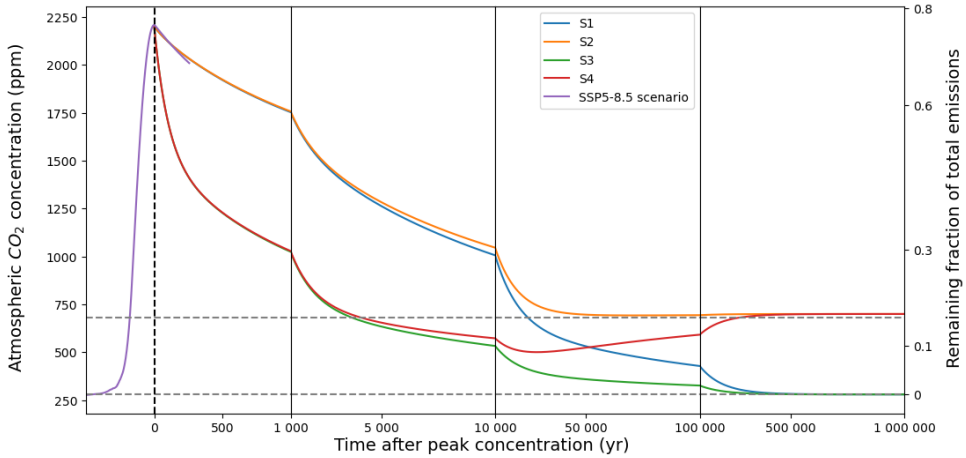

Figure 5.7: Illustrative CO_2 scenarios. The four different scenarios correspond to different assumptions : for S1 and S2, the airborne fraction after 100, 1 000 and 10 000 years is taken at the upper end of existing studies (73% after 100 years, $\sim$60% after 1 000 years and $\sim$30% after 10 000 years). for S3 and S4, the airborne fraction after 100, 1 000 and 10 000 years is taken at the lower end of existing studies (57% after 100 years, $\sim$30% after 1 000 years and $\sim$10% after 10 000 years). Evolution of the CO_2 concentration for scenarios S1, S2, S3, S4 are respectively in blue, orange, green and red. The SSP5-8.5 scenario is depicted in purple.

Discussion and conclusion

In this thesis we have focussed on two important components of the Earth System on long timescales : ice sheets and the carbon cycle.

First, we have used a conceptual model to represent the ice volume evolution over the Quaternary, and investigated possible scenarios for ice volume evolution in a case without anthropogenic influence. Then, using the iLOVECLIM - GRISLI coupled model, we have investigated the Antarctic ice sheet equilibrium behavior under different levels of atmospheric CO_2. In our equilibrium simulations with the present day orbital configuration, all marine parts of the West Antarctic ice sheet disappear for CO_2 levels between 2 and 4xPI. At 6xCO_2, only a grounded ice sheet remains in East Antarctica. This remaining ice sheet disappears abruptly for CO_2 levels between 7.4xCO_2 and 8xCO_2. With the present day orbital configuration, the ice sheet does not regrow until CO_2 levels have come back to the pre-industrial level. These thresholds for Antarctic deglaciation and glaciation depend on the orbital configuration, with a lower summer insolation in the Southern Hemisphere allowing to reach the threshold for glaciation at higher CO_2 levels, and conversely a higher summer insolation in the Southern Hemisphere allowing to reach the threshold for deglaciation at lower CO_2 levels. Finally, we have developed a conceptual model for the geological carbon cycle. This model is non linear and possesses multiple equilibria, that allow to produce multi-million year cycles in $\delta^{13}C$ in response to an astronomical forcing of organic matter fluxes. We have illustrated possible CO_2 evolution following anthropogenic emissions, in a case where the surface carbon equilibrates at a different value than before the perturbation.

In this last part, we discuss which insight our results can bring to the question : How will the anthropogenic fossil fuel emissions affect the climate, on a timescale up to a million years ?

There are of course many uncertainties on the climate of the next million years, and we do not aim at representing the climate evolution in a deterministic way over the next million years, but rather to explore possible scenarios.

One of the major uncertainties is the carbon content that will be released to the atmosphere due to anthropogenic emissions, with larger climatic changes expected for higher emissions. We have chosen to focus on high emission scenarios. Indeed, we want to have a comprehensive interval of possible future climate. In a case without anthropogenic emissions, glacial-interglacial cycles would have been expected to continue a million years into the future. Existing studies on the next million years such as Talento and Ganopolski [2021], Lord et al. [2019] or the BIOCLIM project have already focused on modeling the climate in a case where the global ice volume remains larger than at present. A novelty of this study is to consider the potential melt of the Antarctic ice sheet.

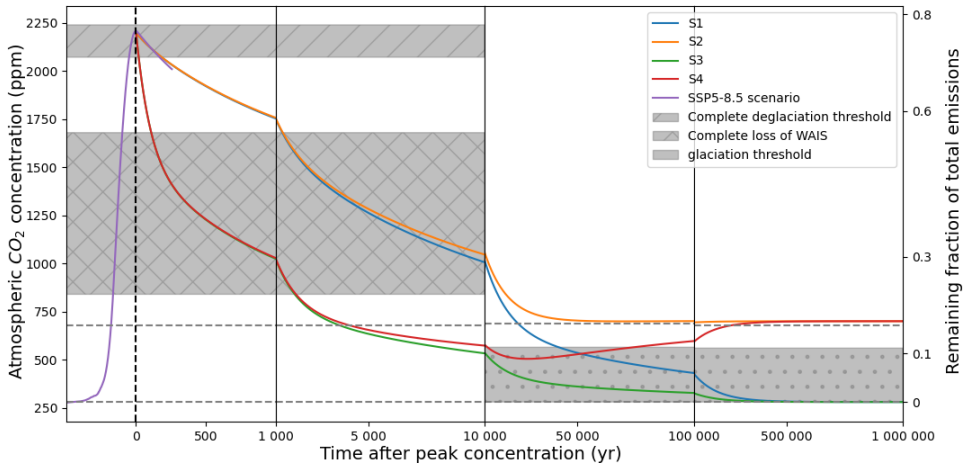

Figure 5.8: Illustrative CO_2 scenarios. The four different scenarios correspond to different assumptions : for S1 and S2, the airborne fraction after 100, 1 000 and 10 000 years is taken at the upper end of existing studies (73% after 100 years, ∼60% after 1 000 years and ∼30% after 10 000 years). for S3 and S4, the airborne fraction after 100, 1 000 and 10 000 years is taken at the lower end of existing studies (57% after 100 years, ∼30% after 1 000 years and ∼10% after 10 000 years). For scenarios S1 and S3, the CO_2 comes back to pre-industrial CO_2 levels after several hundreds of thousand years. For scenarios S2 and S4, the CO_2 concentration does not return to pre-industrial CO_2 levels. Evolution of the CO_2 concentration for scenarios S1, S2, S3, S4 are respectively in blue, orange, green and red. The SSP5-8.5 scenario is depicted in purple. The thresholds for the West Antarctic deglaciation, complete Antarctic deglaciation and Antarctic regrowth obtained with the iLOVECLIM-GRISLI model are depicted in grey.

Our results with the iLOVECLIM-GRISLI model have shown that the equilibrium of the Antarctic ice sheet depends on the CO_2 levels and the insolation. While the orbital parameters are known accurately for the next million years, large uncertainties remain in the carbon cycle, and the CO_2 evolution over time following fossil fuel release. In the last chapter, we have presented four idealized scenarios for the CO_2 evolution in the next million years, following a total carbon release of 5344 GtC, corresponding to the sum of emissions under scenario SSP5-8.5 of the IPCC, and historical emissions. The four CO_2 scenarios of Chapter 5 are displayed in Figure 5.8. The CO_2 threshold for deglaciation of the West Antarctic Ice sheet, of the complete Antarctic ice sheet as well as the threshold for glaciation are superimposed.

For the possible melt of the Antarctic ice sheet, we focus on the first ∼10

000 years following anthropogenic emissions, as it is a timescale relevant for ice sheet melt, and where the CO_2 levels are expected to be the highest. In our four scenarios, carbon dioxide concentrations are largest in the decades following anthropogenic emissions, then decreasing due to exchanges with the biosphere, the ocean and ultimately the geological reservoirs. According to different modeling studies, 10 to 30% of the emitted carbon could remain in the atmosphere after 10 000 years [Lenton and Britton, 2006, Archer and Brovkin, 2008, Archer et al., 2009, Lord et al., 2016]. In a sensitivity experiment with model parameters leading to a higher climate sensitivity ($\sim$3K) than their default parameter set (that leads to a climate sensitivity of $\sim$ 2K), and a high emission scenario ($\sim$ 5900 GtC emitted from the pre-industrial period), Van Breedam et al. [2020] has shown that the entire Antarctic ice sheet could melt in 10 000 years. With a very high emission scenario (10 000 GtC), Winkelmann et al. [2015] has also shown that the Antarctic ice sheet could melt almost entirely in 10 000 years.

The peak atmospheric CO_2 concentration (2210 ppm) reached under the SSP5-8.5 scenario is very close to the threshold leading to the deglaciation of the whole Antarctic ice sheet in our simulations with the present day insolation (between 2072 and 2240 ppm). Our simulations are equilibrium simulations with a fixed insolation and concentration of CO_2 and other greenhouse gas. The actual ice sheet evolution will depend on the transient evolution of insolation, CO_2 and other greenhouse gas. Over the next 10 000 years, summer insolation in the Southern Hemisphere will be lower than at present day. It will vary only slightly, due to the low value of eccentricity at present. For instance, over the next 10 millenia, the maximum December Solstice insolation at 80°S is 553 W m^{-2} (present-day) and its minimum value will be 505 W m^{-2}. The ice sheet evolution will largely depend on CO_2 evolution. If the CO_2 concentration decreases more rapidly as in scenarios S3 and S4 of Section 5.3, it is less likely that the entire Antarctic ice sheet would melt than in a case where the CO_2 decreases less rapidly. However, even if CO_2 decreases, this might not be sufficient to decrease the global temperature, due to the inertia of the climate system. For instance, Van Breedam et al. [2020] used CO_2 scenarios where CO_2 decreases after a peak : for the highest emission scenarios, there remains 25 - 33% of the total carbon emitted in the atmosphere after 10 000 years, but the global mean temperature anomaly has only slightly decreased compared to its peak, and remains high over the 10 000 years of simulation. Another question is the timing of the melting compared to the CO_2 and temperature evolution. In our simulations, a wide East Antarctic ice sheet is stable up to CO_2 levels between 2072 and 2240 ppm, where a strong albedo and height feedback initiate. Once the ice sheet has started to retreat, and these feedbacks have initiated, is a CO_2 and temperature decrease enough to counteract these feedbacks ? The answer to this question likely depends on the speed and magnitude of the CO_2 and temperature reduction, and cannot be assessed with the equilibrium simulations we have performed here. Furthermore, the CO_2

threshold for Antarctic complete deglaciation is very likely to be model dependent. As was mentioned in Section 4.3.2, the results obtained by Van Breedam et al. [2020] depend widely on the parameter set used for the LOVECLIM model and the corresponding climate sensitivity. It is expected that different climate and / or ice sheet models will lead to a different threshold. Another source of uncertainty is the quantity of carbon that will be emitted by societies in the future. The estimated resources and reserves vary largely in the literature. Resources correspond to the ultimate quantity of oil, gas, or coal that could be extracted, regardless of today's economical and technological conditions. Reserves represent a fraction of resources that are defined as recoverable under current economic conditions. The 5th report of the IPCC stated that reserves are between $\sim$1000 and $\sim$1940 GtC, while resources represent $\sim$ 8500 to $\sim$13650 GtC [Bruckner et al., 2014]. Additionally, future CO_2 concentrations will depend on potential carbon release to the atmosphere not due to anthropogenic fossil fuel consumption. For instance, large amounts of organic carbon are stored in Arctic permafrost (ground that remains frozen throughout the year) [Canadell et al., 2021]. With a warming climate due to an initial increase in greenhouse gas, areas of permafrost can thaw releasing some of carbon into the atmosphere in the form of carbon dioxide or methane, which results in additional warming. Existing projections from permafrost carbon models estimate the carbon release to be equivalent to 4-50 GtC released per 1°C of global warming.

The Antarctic ice sheet was formed $\sim$34 Myr ago, at the Eocene-Oligocene transition, and our results suggest that under high emission scenarios, a complete disappearance of the Antarctic ice sheet cannot be ruled out. Further studies including transient runs with varying insolation, CO_2 concentration and other greenhouse gas concentration should be carried out, in order to assess the evolution of the Antarctic ice sheet. Additionally, other climate and ice sheet models should be used in order to compare the results. As we have shown in Chapter 4, the inclusion of the albedo feedback largely influences the results, and it should ideally be taken into account in studies assessing the melt sensibility of the Antarctic ice sheet to anthropogenic emissions.

A follow-up question is, if the Antarctic ice sheet was to melt entirely following anthropogenic emissions, would it regrow ? Once again, there are large uncertainties associated with this question, as one of the primary drivers will be the evolution of the CO_2 concentration, that is highly uncertain. On the timescale of hundreds of thousand years to a million years, studies have assumed that silicate weathering brings back CO_2 concentration to their pre-industrial values [Archer et al., 1997, Archer, 2005, Colbourn et al., 2015, Lord et al., 2016]. However, if we consider the possibility for multiple equilibria in the carbon system, one can assume that CO_2 concentration can equilibrate to another value, which is schematically represented by our scenarios S2 and S4. In the case where CO_2 concentrations come back to their pre-industrial levels after a hundred of thousand years, it is likely that an ice

sheet will develop again on the Antarctic continent. Indeed, with our equilibrium simulations, the threshold for Antarctic regrowth after melting is around 280 - 350 ppm for the present day insolation, and can be at higher CO_2 levels ($>$ 560 ppm) in cases with a minimal insolation. However, if CO_2 levels were to remain at a higher level (700 ppm in our example, but that is solely illustrative), the Antarctic continent could remain ice free over the next million years. Here, we have deliberately focused on higher end scenarios, but substantial although not complete retreat of the Antarctic ice sheet could take place for intermediate scenarios.

There are several perspectives for this work.

The sensitivity of the results to the iLOVECLIM parameters could be assessed. The iLOVECLIM model has a relatively low climate sensitivity ($\sim$2K). The likely range of climate sensitivity estimated by the IPCC is 2.5° to 4°C, with a best estimate of 3°C [IPCC, 2021]. Using the LOVECLIM model, that shares the same code as the iLOVECLIM model for the atmosphere, ocean and vegetation components used in this study, Van Breedam et al. [2020] showed that using different parameter sets for the LOVECLIM model, with climate sensitivity of either $\sim$2K or $\sim$3K, the final ice sheet state could differ widely. Also, the sensitivity of the results to parameters of the GRISLI model or of the coupling should be assessed.

Additionally, transient simulations with varying insolation and greenhouse gases concentrations should be carried out, as we have only performed equilibrium simulations. For instance, one could carry out a 10 000 year transient simulation (without coupling frequency) with varying insolation and CO_2.

Furthermore, the behaviour of the Antarctic ice sheet under a given insolation and CO_2 concentration evolution is likely to be model dependent, and other coupled climate-ice sheet model should be used in order to compare the results.

All these perspectives require plausible scenarios of CO_2 on the future, which remains largely uncertain. On timescales up to 10 000 kyr, there is a relatively large spread between models on the proportion of the emitted carbon that has been removed from the atmosphere. For instance, it varies between 10 and 30% after 10 000 years [Archer et al., 2009]), most probably leading to different response of the Antarctic ice sheet in the two cases. In addition, it is not precisely known how the potential melt of the Greenland and Antarctic ice sheet could affect the oceanic circulation, and oceanic carbon sequestration. The uncertainty on CO_2 is even larger on geological timescales (a few hundred thousand years). While burial and oxidation of organic matter has been identified as potentially as important as silicate weathering to remove or add CO_2 on geological timescales [Hilton and West, 2020], it is currently not implemented in carbon cycle models used to predict the CO_2 evolution at the million year timescale. Before being able to implement these processes in carbon cycle models, a better quantification of these processes and their potential dependency to climate is needed. In addition, besides from the natural CO_2 evolution following emissions, the future evolution of technologies developed to capture carbon cannot be foreseen.

More generally, this thesis joins previous studies emphasizing that the current greenhouse gas release due to human activities, taking place on a few decades to centuries, will impact the Earth's climate on a timescale of hundreds of millenia [Archer and Ganopolski, 2005, Talento and Ganopolski, 2021], and can even lead to climatic states that have not been seen for millions of years.

Résumé en français

Quel sera l'impact de l'Homme sur le climat, à très long terme ? A quel point la consommation actuelle d'énergies fossiles, ayant lieu sur quelques décennies ou siècles peut-elle perturber l'évolution du climat terrestre ? Est-ce que cette perturbation correspond à un changement d'ère géologique ?

La question de l' "irreversibilité" à long terme des changements climatiques que nous sommes en train de produire se pose. Par ailleurs, ces questions ont également des implications très concrètes dans la gestion des déchets nucléaires, et plus particulièrement des déchets de haute activité (HA) et des déchets de moyenne activité à vie longue (MA-VL), qui restent dangereux pendant des centaines de milliers d'années. L'une des solutions envisagées pour gérer ces déchets est le stockage profond, et les impacts climatiques long terme sur la sécurité des sites de stockage doivent donc être étudiés.

Actuellement, peu d'études s'intéressent à la question de l'impact des émissions anthropiques de gaz à effet de serre sur l'évolution du climat à plus de quelques siècles. Pourtant, dû au long temps de résidence du CO_2 dans les enveloppes superficielles de la Terre, il est certain que les émissions anthropiques de gaz à effet de serre vont impacter le climat bien au delà du prochain siècle.

L'objectif de cette thèse est d'élargir le cadre des études actuelles sur le climat du prochain million d'années, en revisitant certaines des hypothèses classiquement faites. Pour cela, nous nous intéressons à deux composantes majeures du système climatique à long terme : les calottes de glace, et le cycle du carbone.

Dans un premier chapitre, nous posons le contexte et discutons des principales limitations des études existantes sur le climat du prochain million d'année. Concernant les calottes de glace, les études existantes considèrent rarement une fonte partielle ou totale de la calotte Antarctique. Concernant le cycle du carbone, les études existantes supposent que les concentrations atmosphériques de CO_2 reviennent à la valeur pré-industrielle au bout de centaines de milliers d'années, grâce à la rétroaction des silicates.

Dans cette thèse, nous revisitons ces hypothèses classiques. Nous commençons par étudier l'évolution des calottes de glace dans le futur, dans un cadre "naturel", c'est à dire sans influence anthropique. Puis, à l'aide du modèle couplé climat-calotte Antarctique iLOVECLIM - GRISLI nous étudions le comportement de la calotte Antarctique en réponse à différents niveaux de CO_2. Ensuite, nous développons un modèle conceptuel pour le cycle du carbone géologique qui contient des équilibres multiples et ayant pour objectif de reproduire les cycles de plusieurs millions d'années observés dans le $\delta^{13}C$. Nous étudions l'influence de ces potentiels équilibres multiples dans le cycle du carbone, sur l'évolution du CO_2 à long terme. Enfin, nous discutons de l'implication de nos résultats sur le climat du prochain million d'années.

Dans le chapitre 2, nous commençons par nous intéresser à l'évolution des calottes de glace dans le futur dans un cadre "naturel", c'est à dire sans influence anthropique. Le climat des derniers 2.6 millions d'années, le Quaternaire, est caractérisé par l'alternance de périodes dites froides, avec des calottes de glace très largement étendues dans l'Hémisphère Nord, et de périodes dites chaudes, avec des calottes de glace beaucoup moins étendues dans l'Hémisphère Nord. Ces alternances sont connues sous le nom de cycles glaciaires - interglaciaires. Tout d'abord, nous développons un modèle conceptuel permettant de représenter l'évolution du volume de glace au cours du Quaternaire. Dans ce modèle, le système climatique est représenté par des oscillations de relaxation entre deux états : glaciation et déglaciation. L'évolution du volume de glace est représentée par deux équations différentes : une pour l'état de glaciation et une autre pour l'état de déglaciation. Le seul forçage externe du modèle est l'insolation d'été à 65°N. Le passage de l'état de déglaciation à celui de glaciation se produit lorsque l'insolation devient suffisamment faible, inférieure au seuil de glaciation I_0. Le passage de l'état de glaciation à celui de déglaciation se produit lorsque la combinaison de l'insolation et du volume de glace devient suffisamment élevée, supérieure au seuil de déglaciation V_0. Afin d'étudier la robustesse du modèle, nous considérons différentes définitions de l'insolation d'été : l'insolation au solstice d'été, les saisons caloriques, ou bien l'insolation intégrée au dessus d'un certain seuil. Nous étudions également le rôle du paramètre de seuil de déglaciation, V_0. Cette étude à fait l'objet d'une publication dans le journal Climate of the Past ([Leloup and Paillard, 2022]). Notre modèle est capable de représenter les principales caractéristiques de l'évolution du volume de glace du Quaternaire, avec des cycles de 41 milliers d'années avant la transition Mid-Pleistocène et des cycles plus longs après, en augmentant le seuil de déglaciation V_0 au cours du temps. Ceci est valable pour les quatre types d'insolation étudiées. Ensuite, nous utilisons le modèle avec différents types d'insolation et différents seuils de glaciation I_0, afin de discuter des scénarios d'évolution du volume de glace dans le futur, dans un cadre naturel.

Les modèles conceptuels d'évolution du volume de glace calibrés sur le passé, et l'alternance de cycles glaciaires-interglaciaires dans l'Hémisphère Nord ne sont pas adaptés pour étudier l'évolution de l'Antarctique. Cependant, des études ont montrée qu'une fonte substantielle de l'Antarctique pouvait être attendue pour des scénarios de réchauffement importants [Van Breedam et al., 2020, Winkelmann et al., 2015].

Dans la suite, nous nous concentrons donc sur la possibilité d'une fonte de la calotte Antarctique et sur sa réversibilité en étudiant le comportement de la calotte sous différents niveaux de CO_2, en partant d'une configuration où la glace est présente et d'une configuration où il n'y a plus de glace. La méthodologie est décrite dans le chapitre 3, et les résultats dans le chapitre 4.

De nombreuses études de modélisation des climats passés et futurs sont réalisées en considérant que les calottes de glace n'évoluent pas [Kageyama et al.,

2017, Otto-Bliesner et al., 2017, Ivanovic et al., 2016]. A l'inverse, les simulations s'intéressant à l'évolution des calottes Groënlandaise et Antarctique au cours du prochain siècle utilisent des modèles de calotte de glace, forcés avec des champs climatiques (atmosphère, océan) qui sont calculés en amont [Nowicki et al., 2016, Seroussi et al., 2020, Nowicki et al., 2020]. Les champs climatiques ne sont alors pas affectés par l'évolution des calottes glaciaires.

Cependant, les calottes intéragissent avec les circulations atmosphériques et océaniques, ce qui peut donner lieu à de nombreuses rétroactions. Par exemple, lorsqu'une calotte recule, l'albédo diminue localement. Cette diminution de l'albédo va entrainer une hausse des températures, et potentiellement générer plus de fonte. C'est la rétroaction de l'albédo. Une autre rétroaction est due à la hauteur. Lorsque l'épaisseur de la calotte diminue suite à un réchauffement, cela augmente la température en haut de la calotte (car elle est plus basse en altitude), ce qui peut donner lieu à de la fonte additionnelle.

Les simulations climatiques avec des calottes fixées ou les simulations de calotte avec un climat pré-calculé ne permettent pas de prendre en compte ces interactions. Une des particularités de notre étude est de modéliser ces interactions, grâce au modèle couplé iLOVECLIM- GRISLI. Le modèle iLOVECLIM permet de représenter l'océan, la végétation et l'atmosphère. Il s'agit d'un modèle de complexité intermédiaire, ce qui le rend relativement rapide, et permet de réaliser plusieurs simulations. Le modèle GRISLI est un modèle de calotte de glace, que nous utilisons pour l'Antarctique. L'évolution de la calotte est prise en compte par le modèle de climat iLOVECLIM, ce qui modifie le climat. Inversement, les modifications du climat sont transmises au modèle GRISLI, ce qui modifie l'évolution de la calotte Antarctique.

Avant d'utiliser ce modèle couplé, différentes calibrations étaient nécessaires. En effet, lorsque l'on appliquait un niveau de CO_2 pré-industriel, la calotte Antarctique devenait très étendue, bien plus qu'à l'actuel. J'ai donc corrigé certains biais du modèle iLOVECLIM, ainsi que modifié des paramètres du modèle GRISLI, et des paramètres liés au couplage, afin d'avoir une calotte Antarctique qui soit à l'équilibre pour un niveaux de CO_2 pré-industriel, et qui soit proche des observations. Cette configuration (configuration de référence pré-industrielle) nous sert de base pour étudier le comportement de la calotte Antarctique pour différents niveaux de CO_2.

Dans le chapitre 4, nous réalisons différentes simulations d'équilibre à partir de la configuration de référence pré-industrielle, en appliquant des niveaux de CO_2 plus élevés que le pré-industriel : 2xCO_2, 4xCO_2, 6xCO_2, 6.7xCO_2, 7.4xCO_2, 8xCO_2. Ces simulations sont réalisées avec une insolation égale à l'actuelle, et sont appelées simulations de fonte. A 4xCO_2 (1120 ppm), la quasi-totalité de l'Antarctique de l'Ouest a disparu, avec de la glace restant uniquement dans les parties où le socle rocheux est au-dessus du niveau marin, comme la péninsule. En Antarctique de l'Est, la plus grande partie des bassins pour lesquels le socle

rocheux est en dessous du niveau marin (Wilkes, Aurora) ont disparu. A 6xCO_2 (1680 ppm), la totalité de l'Antarctique de l'Ouest et la quasi-totalité des parties marines de l'Antarctique ont disparues. En revanche, il reste une grosse calotte, posée sur le socle rocheux au dessus du niveau marin, en Antarctique de l'Est. La situation est très similaire pour des niveaux de CO_2 de 7.4xCO_2 (2070 ppm). En revanche, pour des niveaux de 8xCO_2 (2240 ppm), la situation est très différente : l'entièreté de la calotte restante a disparu. Il y a une transition brutale entre une large calotte en Antarctique de l'Est et le retrait complet de la calotte. Cela est dû à la mise en place de rétroactions, liées à l'albédo à la hauteur, qui amènent au retrait complet de la calotte.

Plusieurs études ont montré que la calotte Antarctique possède un comportement d'hystéresis [Pollard and DeConto, 2005, Garbe et al., 2020]. Le volume de glace d'équilibre pour une certaine variation de température ou de concentration de CO_2 n'est pas le même selon l'état initial de la calotte. Nous étudions l'hystéresis de la calotte Antarctique avec le modèle couplé GRISLI-iLOVECLIM. Pour cela, nous partons de la simulation 8xCO_2 où l'Antarctique a complétement disparu, et nous appliquons des niveaux de CO_2 décroissants jusqu'à ce que l'Antarctique se reforme. Dans ces simulations de croissance, l'insolation est également l'insolation actuelle. Pour des niveaux de CO_2 entre 8xCO_2 et $\sim$1.25xCO_2, la calotte ne se reforme pas. En revanche pour des niveaux inférieurs ou égaux à $\sim$1xCO_2, la calotte se reforme. Alors qu'il n'y avait que des glaciers très peu étendus à $\sim$1.25xCO_2, il y a une calotte très developpée à 1xCO_2, avec une large calotte sur l'Antarctique de l'Est, de la glace sur les parties de l'Antarctique de l'Ouest dont le socle rocheux est au dessus du niveau marin, et la plateforme de glace flottante de Ronne-Filchner s'est reformée. En revanche, les parties de l'Antarctique de l'Ouest où le socle rocheux est sous le niveau marin et la plateforme de glace flottante de Ross restent déglacés. Il y a donc une transition brutale entre un état quasiment entièrement déglacé, et un état largement englacé.

Ensuite, j'ai étudié l'influence de l'insolation sur ces simulations. J'ai réalisé des simulations de fonte, en partant de la configurtion de référence pré-industrielle, avec une insolation différente de l'actuelle. Plus précisément, j'ai modifié les paramètres orbitaux du modèle pour qu'ils correspondant au maximum d'insolation au solstice d'été de l'Hémisphère Sud (Décembre) sur le prochain million d'années. Avec une insolation plus forte en été dans l'hémisphère Sud, la calotte déglace entièrement pour un niveau de CO_2 plus faible qu'à l'actuel : elle disparait entièrement entre 2xCO_2 et 4xCO_2 avec l'insolation maximale, alors que cela se produisait entre 7.4xCO_2 et 8xCO_2 avec l'insolation actuelle. Similairement, j'ai réalisé des simulations de croissance de la calotte, en partant de la configuration sans glace, avec une insolation minimale, c'est à dire avec les paramètres orbitaux correspondent au minimum d'insolation au solstice d'été de l'Hémisphère Sud sur le prochain million d'années. Avec une insolation plus faible en été dans l'hémisphère Sud, la calotte Antarctique peut ré-englacer pour des niveaux de CO_2 plus élevés qu'avec

l'insolation actuelle. Avec l'insolation minimale, l'Antarctique peut ré-englacer pour des niveaux entre 2xCO_2 et 4xCO_2, alors que cela se produisait à des niveaux $\sim$1xCO_2 avec l'insolation actuelle.

J'ai également étudié l'influence de l'ajout de la rétroaction de l'albédo sur les résultats, car sa prise en compte est une spécificité de la configuration couplée, comparé aux études forçant des modèles de calotte avec des champs climatiques. Des simulations qui ne prennent pas en compte la rétroaction de l'albédo, c'est à dire où l'albédo reste fixé à la valeur élevée de la calotte même lorsque la calotte recule, ont été réalisées. Dans les simulations de fonte où la rétroaction de l'albédo est prise en compte, il n'y a pas d'états intermédiaires entre une configuration avec une large calotte restant en Antarctique de l'Est, et la disparition complète de la calotte. De façon similaire, dans les simulations de croissance, il n'y a pas d'états intermédiaires entre une configuration avec très peu de glace et une configuration où l'Antarctique est largement englacé. En revanche, dans les simulations sans rétroaction de l'albédo, il y a des états intermédiaires entre les configurations avec et sans glace, et le passage d'une configuration englacée à non englacée et inversement, se fait de façon plus continue. Ceci est comparable à d'autres études, notamment Garbe et al. [2020] où la rétroaction de l'albédo n'était pas prise en compte.

Dans le chapitre 5, nous nous intéressons à la modélisation du cycle du carbone géologique. Les enregistrements du $\delta^{13}C$ passé présentent des oscillations de 400 milliers d'années, mais également des oscillations à beaucoup plus long terme, de 2.4 millions d'années et 8-9 millions d'années. Ces oscillations de 8-9 millions d'années sont observées pendant tout le Cénozoique et une partie du Mésozoïque. La présence robuste de ces oscillations suggère une origine astronomique, mais cette périodicité n'est pas présente dans le forçage astronomique. En raison du grand facteur de fractionnement de la matière organique, son enfouissement ou son oxydation produit de grandes variations de $\delta^{13}C$ pour des variations modérées de carbone. Par conséquent, le forçage astronomique des flux de matière organique est un candidat plausible pour expliquer les oscillations observées dans les enregistrements de $\delta^{13}C$. Jusqu'à présent, les études de modélisation forçant astronomiquement l'enfouissement de la matière organique ont pu produire des cycles de 400 milliers d'années et 2.4 millions d'années dans le $\delta^{13}C$, mais n'ont pas été en mesure de produire des cycles plus longs, tels que des cycles de 8-9 millions d'années. Ici, nous proposons un mécanisme qui pourrait expliquer la présence de cycles de plusieurs millions d'années dans les enregistrements de $\delta^{13}C$, et leur stabilité dans le temps. Nous développons un modèle conceptuel non linéaire pour le cycle du carbone, qui possède des équilibres multiples, et permet donc d'obtenir des oscillations libres, sans forçage astronomique. Lorsque le modèle est également forcé astronomiquement, nous observons un accrochage de fréquence, et les oscillations modélisées sont préférentiellement d'une période multiple de 2.4 millions d'années (période contenue dans le forçage, l'excentricité). Cela nous permet de

produire des cycles de 8-9 millions d'années en réponse au forçage astronomique, ce qui n'était pas possible avec un modèle linéaire.

La potentielle présence d'équilibres multiples dans le cycle du carbone pourrait donner lieu à des évolutions du CO_2 atmosphérique à longue échelle de temps très différentes de celle des études actuelles. Afin de discuter de l'évolution du climat au cours du prochain million d'années, nous développons 4 scénarios idéalisées pour l'évolution de la concentration atmosphérique de CO_2 sur le prochain million d'année.

Enfin, dans une dernière partie, nous discutons de l'éclairage que nos résultats peuvent apporter à la question : Comment les émissions anthropiques de gaz à effet de serre affecteront-elles le climat, sur une échelle de temps allant jusqu'à un million d'années ?

Les scénarios d'émission élevées (comme le scénario SSP5-8.5 du dernier rapport du GIEC [IPCC, 2021]) sont associés à des concentrations de CO_2 du même ordre de grandeur que celles conduisant à la disparition complète de la calotte Antarctique dans nos simulations, et la possibilité d'une disparition complète de la calotte ne peut pas être exclue. Si l'Antarctique devait fondre entièrement, sa potentielle re-formation sur le prochain million d'années dépendra de l'évolution à long terme de la concentration de CO_2.

Plus généralement, cette thèse s'inscrit dans la lignée d'études antérieures soulignant que les rejets actuels de gaz à effet de serre dûs aux activités humaines, qui se déroulent sur quelques décennies à quelques siècles, auront un impact sur le climat de la Terre sur une échelle de temps de plusieurs centaines de millénaires [Archer and Ganopolski, 2005, Talento and Ganopolski, 2021]; voire conduiront à des états climatiques qui n'ont pas été observés depuis des millions d'années.

Bibliography

A. Abe-Ouchi, F. Saito, K. Kawamura, M. E. Raymo, J. Okuno, K. Takahashi, and H. Blatter. Insolation-driven 100,000-year glacial cycles and hysteresis of ice-sheet volume. *nature*, 500(7461):190–193, 2013.

S. Adusumilli, H. A. Fricker, B. Medley, L. Padman, and M. R. Siegfried. Interannual variations in meltwater input to the southern ocean from antarctic ice shelves. *Nature geoscience*, 13(9):616–620, 2020.

C. Agosta, C. Amory, C. Kittel, A. Orsi, V. Favier, H. Gallée, M. R. van den Broeke, J. T. M. Lenaerts, J. M. van Wessem, W. J. van de Berg, and X. Fettweis. Estimation of the antarctic surface mass balance using the regional climate model mar (1979–2015) and identification of dominant processes. *The Cryosphere*, 13(1):281–296, 2019. doi: 10.5194/tc-13-281-2019. URL https://tc.copernicus.org/articles/13/281/2019/.

S. Ahn, D. Khider, L. E. Lisiecki, and C. E. Lawrence. A probabilistic Pliocene–Pleistocene stack of benthic 18O using a profile hidden Markov model. *Dynamics and Statistics of the Climate System*, 2(1), 06 2017. ISSN 2059-6987. doi: 10.1093/climsys/dzx002. URL https://doi.org/10.1093/climsys/dzx002. dzx002.

E. Anagnostou, E. H. John, T. Babila, P. Sexton, A. Ridgwell, D. J. Lunt, P. N. Pearson, T. Chalk, R. D. Pancost, and G. Foster. Proxy evidence for state-dependence of climate sensitivity in the eocene greenhouse. *Nature communications*, 11(1):1–9, 2020.

J. D. Annan and J. C. Hargreaves. A new global reconstruction of temperature changes at the Last Glacial Maximum. *Clim. Past*, 9:367–376, 2013. doi: 10.5194/cp-9-367-2013.

J. D. Annan, J. C. Hargreaves, and T. Mauritsen. A new global surface temperature reconstruction for the last glacial maximum. *Climate of the Past*, 18(8):1883–1896, 2022. doi: 10.5194/cp-18-1883-2022. URL https://cp.copernicus.org/articles/18/1883/2022/.

D. Archer. Fate of fossil fuel co2 in geologic time. *Journal of Geophysical Research: Oceans*, 110(C9), 2005. doi: https://doi.org/10.1029/2004JC002625. URL https://agupubs.onlinelibrary.wiley.com/doi/abs/10.1029/2004JC002625.

D. Archer and V. Brovkin. The millennial atmospheric lifetime of anthropogenic co2. *Climatic Change*, 90(3):283–297, 2008.

D. Archer and A. Ganopolski. A movable trigger: Fossil fuel co2 and the onset of the next glaciation. *Geochemistry, Geophysics, Geosystems*, 6(5), 2005. doi: https://doi.org/10.1029/2004GC000891. URL https://agupubs.onlinelibrary.wiley.com/doi/abs/10.1029/2004GC000891.

D. Archer, H. Kheshgi, and E. Maier-Reimer. Multiple timescales for neutralization of fossil fuel co2. *Geophysical Research Letters*, 24(4):405–408, 1997.

D. Archer, H. Kheshgi, and E. Maier-Reimer. Dynamics of fossil fuel co2 neutralization by marine caco3. *Global Biogeochemical Cycles*, 12(2):259–276, 1998.

D. Archer, M. Eby, V. Brovkin, A. Ridgwell, L. Cao, U. Mikolajewicz, K. Caldeira, K. Matsumoto, G. Munhoven, A. Montenegro, et al. Atmospheric lifetime of fossil fuel carbon dioxide. *Annual review of earth and planetary sciences*, 37, 2009.

D. I. Armstrong McKay, A. Staal, J. F. Abrams, R. Winkelmann, B. Sakschewski, S. Loriani, I. Fetzer, S. E. Cornell, J. Rockström, and T. M. Lenton. Exceeding 1.5° c global warming could trigger multiple climate tipping points. *Science*, 377(6611):eabn7950, 2022.

J. L. Bamber, J. A. Griggs, R. T. W. L. Hurkmans, J. A. Dowdeswell, S. P. Gogineni, I. Howat, J. Mouginot, J. Paden, S. Palmer, E. Rignot, and D. Steinhage. A new bed elevation dataset for greenland. *The Cryosphere*, 7(2):499–510, 2013. doi: 10.5194/tc-7-499-2013. URL https://tc.copernicus.org/articles/7/499/2013/.

A. Beckmann and H. Goosse. A parameterization of ice shelf–ocean interaction for climate models. *Ocean Modelling*, 5(2):157–170, 2003. ISSN 1463-5003. doi: https://doi.org/10.1016/S1463-5003(02)00019-7. URL https://www.sciencedirect.com/science/article/pii/S1463500302000197.

D. J. Beerling and D. L. Royer. Convergent cenozoic co2 history. *Nature Geoscience*, 4 (7):418–420, 2011.

B. Bereiter, S. Eggleston, J. Schmitt, C. Nehrbass-Ahles, T. F. Stocker, H. Fischer, S. Kipfstuhl, and J. Chappellaz. Revision of the epica dome c co2 record from 800 to 600 kyr before present. *Geophysical Research Letters*, 42(2):542–549, 2015.

C. J. Berends, B. de Boer, and R. S. W. van de Wal. Application of hadcm3@bristolv1.0 simulations of paleoclimate as forcing for an ice-sheet model, anice2.1: set-up and benchmark experiments. *Geoscientific Model Development*, 11(11):4657–4675, 2018. doi: 10.5194/gmd-11-4657-2018. URL https://gmd.copernicus.org/articles/11/4657/2018/.

C. J. Berends, P. Köhler, L. J. Lourens, and R. S. W. van de Wal. On the cause of the mid-pleistocene transition. *Reviews of Geophysics*, 59(2):e2020RG000727, 2021. doi: https://doi.org/10.1029/2020RG000727. URL https://agupubs.onlinelibrary.wiley.com/doi/abs/10.1029/2020RG000727. e2020RG000727 2020RG000727.

A. Berger and M.-F. Loutre. An exceptionally long interglacial ahead? *Science*, 297 (5585):1287–1288, 2002.

A. Berger, X. Li, and M.-F. Loutre. Modelling northern hemisphere ice volume over the last 3 ma. *Quaternary Science Reviews*, 18(1):1–11, 1999.

A. A. Berhe, J. Harte, J. W. Harden, and M. S. Torn. The significance of the erosion-induced terrestrial carbon sink. *BioScience*, 57(4):337–346, 2007.

R. A. Berner. Geocarb ii: A revised model of atmospheric co [sub 2] over phanerozoic time. *American Journal of Science;(United States)*, 294(1), 1994.

P. K. Bijl, J. A. Bendle, S. M. Bohaty, J. Pross, S. Schouten, L. Tauxe, C. E. Stickley, R. M. McKay, U. Röhl, M. Olney, et al. Eocene cooling linked to early flow across the tasmanian gateway. *Proceedings of the National Academy of Sciences*, 110(24): 9645–9650, 2013.

K. Billups, H. Pälike, J. Channell, J. Zachos, and N. Shackleton. Astronomic calibration of the late oligocene through early miocene geomagnetic polarity time scale. *Earth and Planetary Science Letters*, 224(1):33–44, 2004. ISSN 0012-821X. doi: https://doi.org/10.1016/j.epsl.2004.05.004. URL https://www.sciencedirect.com/science/article/pii/S0012821X04003085.

R. Bindschadler, H. Choi, A. Wichlacz, R. Bingham, J. Bohlander, K. Brunt, H. Corr, R. Drews, H. Fricker, M. Hall, R. Hindmarsh, J. Kohler, L. Padman, W. Rack, G. Rotschky, S. Urbini, P. Vornberger, and N. Young. Getting around antarctica: new high-resolution mappings of the grounded and freely-floating boundaries of the antarctic ice sheet created for the international polar year. *The Cryosphere*, 5(3): 569–588, 2011. doi: 10.5194/tc-5-569-2011. URL https://tc.copernicus.org/articles/5/569/2011/.

R. Bintanja, R. van de Wal, and J. Oerlemans. Global ice volume variations through the last glacial cycle simulated by a 3-d ice-dynamical model. *Quaternary International*, 95-96:11–23, 2002. ISSN 1040-6182. doi: https://doi.org/10.1016/S1040-6182(02)00023-X. URL https://www.sciencedirect.com/science/article/pii/S104061820200023X. Inception: Mechanisms, patterns and timing of ice sheet inception.

L. Bopp, C. Le Quéré, M. Heimann, A. C. Manning, and P. Monfray. Climate-induced oceanic oxygen fluxes: Implications for the contemporary carbon budget. *Global Biogeochemical Cycles*, 16(2):6–1–6–13, 2002. doi: https://doi.org/10.1029/2001GB001445. URL https://agupubs.onlinelibrary.wiley.com/doi/abs/10.1029/2001GB001445.

A. Born, M. A. Imhof, and T. F. Stocker. An efficient surface energy–mass balance model for snow and ice. *The Cryosphere*, 13(5):1529–1546, 2019.

S. Boulila, B. Galbrun, J. Laskar, and H. Pälike. A ∼9myr cycle in cenozoic $\delta^{13}c$ record and long-term orbital eccentricity modulation: Is there a link? *Earth and Planetary Science Letters*, 317-318:273–281, 2012. ISSN 0012-821X. doi: https://doi.org/10.1016/j.epsl.2011.11.017. URL https://www.sciencedirect.com/science/article/pii/S0012821X11006741.

N. Bouttes, D. Paillard, D. M. Roche, V. Brovkin, and L. Bopp. Last Glacial Maximum CO_2 and $\delta^{13}C$ successfully reconciled. *Geophys. Res. Lett.*, 38, 2011. doi: 10.1029/2010GL044499.

N. Bouttes, D. M. Roche, V. Mariotti, and L. Bopp. Including an ocean carbon cycle model into iLOVECLIM (v1.0). *Geoscientific Model Development*, 8:1563–1576, 2015. doi: 10.5194/gmd-8-1563-2015.

P. V. Brady. The effect of silicate weathering on global temperature and atmospheric co2. *Journal of Geophysical Research: Solid Earth*, 96(B11):18101–18106, 1991.

R. D. Briggs, D. Pollard, and L. Tarasov. A data-constrained large ensemble analysis of antarctic evolution since the eemian. *Quaternary Science Reviews*, 103:91–115, 2014.

J. Brondex, F. Gillet-Chaulet, and O. Gagliardini. sensitivity of centennial mass loss projections of

the amundsen basin to the friction law. *The Cryosphere*, 13(1):177–195, 2019. doi: 10.5194/tc-13-177-2019. URL https://tc.copernicus.org/articles/13/177/2019/.

V. Brovkin, J. Bendtsen, M. Claussen, A. Ganopolski, C. Kubatzki, V. Petoukhov, and A. Andreev. Carbon cycle, vegetation, and climate dynamics in the Holocene: Experiments with the CLIMBER-2 model. *Global Biogeochem. Cy.*, 16, 2002. doi: 10.1029/2001GB001662.

T. Bruckner, I. A. Bashmakov, H. C. Y. Mulugetta, A. de la Vega Navarro, J. Edmonds, A. Faaij, B. Fungtammasan, E. H. A. Garg, D. Honnery, D. Infield, M. Kainuma, S. Khennas, S. Kim, H. B. Nimir, K. Riahi, N. Strachan, R. Wiser, and X. Zhang. *Energy Systems. in Climate Change 2014: Mitigation of Climate Change. Contribution of Working Group III to the Fifth Assessment Report of the Intergovernmental Panel on Climate Change*. Cambridge University Press, Cambridge University Press, Cambridge, United Kingdom and New York, NY, USA., 2014.

D. J. Burdige. Burial of terrestrial organic matter in marine sediments: A reassessment. *Global Biogeochemical Cycles*, 19(4), 2005. doi: https://doi.org/10.1029/2004GB002368. URL https://agupubs.onlinelibrary.wiley.com/doi/abs/10.1029/2004GB002368.

P. Burgess. *Future Climatic and Cryospheric Change on Millennial Timescales: An Assessment using Two-Dimensional Climate Modelling Studies*. PhD thesis, Climatic Research Unit, University of East Anglia, Norwich, UK., 1998.

A. Burke, T. M. Present, G. Paris, E. C. Rae, B. H. Sandilands, J. Gaillardet, B. Peucker-Ehrenbrink, W. W. Fischer, J. W. McClelland, R. G. Spencer, et al. Sulfur isotopes in rivers: Insights into global weathering budgets, pyrite oxidation, and the modern sulfur cycle. *Earth and Planetary Science Letters*, 496:168–177, 2018a.

K. D. Burke, J. W. Williams, M. A. Chandler, A. M. Haywood, D. J. Lunt, and B. L. Otto-Bliesner. Pliocene and eocene provide best analogs for near-future climates. *Proceedings of the National Academy of Sciences*, 115(52):13288–13293, 2018b.

M. R. Burton, G. M. Sawyer, and D. Granieri. Deep Carbon Emissions from Volcanoes. *Reviews in Mineralogy and Geochemistry*, 75(1):323–354, 01 2013. ISSN 1529-6466. doi: 10.2138/rmg.2013.75.11. URL https://doi.org/10.2138/rmg.2013.75.11.

M. Bügelmayer, D. M. Roche, and H. Renssen. Representing icebergs in the iLOVECLIM model (version 1.0) – a sensitivity study. *Geosci. Model Dev.*, 8:2139–2151, 2015. doi: 10.5194/gmd-8-2139-2015.

N. Calder. Arithmetic of ice ages. *Nature*, 252:216–218, 1974. doi: 10.1038/252216a0.

J.-M. Campin and H. Goosse. Parameterization of density-driven downsloping flow for a coarse-resolution ocean model in z-coordinate. *Tellus*, 51A:412–430, 1999. doi: 10.3402/tellusa.v51i3.13468.

J. Canadell, P. Monteiro, M. Costa, L. C. da Cunha, P. Cox, S. H. A.V. Eliseev, M. Ishii, S. Jaccard, C. Koven, A. Lohila, P. Patra, S. Piao, J. Rogelj, S. Syampungani, S. Zaehle, and K. Zickfeld. Global carbon and other biogeochemical cycles and feedbacks. In *Climate Change 2021: The Physical Science Basis. Contribution of Working Group I to*

the Sixth Assessment Report of the Intergovernmental Panel on Climate Change, page 673–816. Cambridge University Press, 2021. doi: doi:10.1017/9781009157896.007.

T. E. Cerling. Use of carbon isotopes in paleosols as an indicator of the p (co2) of the paleoatmosphere. *Global Biogeochemical Cycles*, 6(3):307–314, 1992.

C. Chambers, R. Greve, T. Obase, F. Saito, and A. Abe-Ouchi. Mass loss of the antarctic ice sheet until the year 3000 under a sustained late-21st-century climate. *Journal of Glaciology*, 68(269):605–617, 2022.

S. Charbit, C. Ritz, G. Philippon, V. Peyaud, and M. Kageyama. Numerical reconstructions of the northern hemisphere ice sheets through the last glacial-interglacial cycle. *Climate of the Past*, 3(1):15–37, 2007. doi: 10.5194/cp-3-15-2007. URL https://cp.copernicus.org/articles/3/15/2007/.

B. Chen, C. Haeger, M. K. Kaban, and A. G. Petrunin. Variations of the effective elastic thickness reveal tectonic fragmentation of the antarctic lithosphere. *Tectonophysics*, 746:412–424, 2018.

D. Choudhury, A. Timmermann, F. Schloesser, M. Heinemann, and D. Pollard. Simulating marine isotope stage 7 with a coupled climate–ice sheet model. *Climate of the Past*, 16(6):2183–2201, 2020.

P. Clark, D. Archer, D. Pollard, J. D. Blum, J. Rial, V. Brovkin, A. Mix, N. Pisias, and M. Roy. The middle pleistocene transition: characteristics, mechanisms, and implications for long-term changes in atmospheric pco2. *Quaternary Sci. Rev.*, 25:3150–3184, 2006. doi: 10.1016/j.quascirev.2006.07.008. URL https://www.sciencedirect.com/science/article/pii/S0277379106002332.

P. U. Clark, A. S. Dyke, J. D. Shakun, A. E. Carlson, J. Clark, B. Wohlfarth, J. X. Mitrovica, S. W. Hostetler, and A. M. McCabe. The last glacial maximum. *Science*, 325 (5941):710–714, 2009. doi: 10.1126/science.1172873. URL https://www.science.org/doi/abs/10.1126/science.1172873.

P. U. Clark, J. D. Shakun, S. A. Marcott, A. C. Mix, M. Eby, S. Kulp, A. Levermann, G. A. Milne, P. L. Pfister, B. D. Santer, et al. Consequences of twenty-first-century policy for multi-millennial climate and sea-level change. *Nature climate change*, 6(4): 360–369, 2016.

M. Claussen, L. A. Mysak, A. J. Weaver, M. Crucifix, T. Fichefet, M. F. Loutre, S. L. Weber, J. Alcamo, V. A. Alexeev, A. Berger, R. Calov, A. Ganopolski, H. Goosse, G. Lohman, F. Lunkeit, I. I. Mohkov, V. Petoukhov, P. Stone, , and Z. Wang. Earth System Models of Intermediate Complexity: closing the gap in the spectrum of climate system models. *Clim. Dynam.*, 18:579–586, 2002. doi: 10.1007/s00382-001-0200-1.

A.-S. B. Cochelin, L. A. Mysak, and Z. Wang. Simulation of long-term future climate changes with the green mcgill paleoclimate model: The next glacial inception. *Climatic Change*, 79(3):381–401, 2006.

G. Colbourn, A. Ridgwell, and T. M. Lenton. The time scale of the silicate weathering negative feedback on atmospheric co2. *Global Biogeochemical Cycles*, 29(5):583–596, 2015. doi: https://doi.org/10.1002/2014GB005054. URL https://agupubs.onlinelibrary.wiley.com/doi/abs/10.1002/2014GB005054.

E. community members. Eight glacial cycles from an antarctic ice core. *Nature*, 429 (6992):623–628, 2004.

V. Coulon, K. Bulthuis, P. L. Whitehouse, S. Sun, K. Haubner, L. Zipf, and F. Pattyn. Contrasting response of west and east antarctic ice sheets to glacial isostatic adjustment. *Journal of Geophysical Research: Earth Surface*, 126(7):e2020JF006003, 2021.

H. K. Coxall, P. A. Wilson, H. Pälike, C. H. Lear, and J. Backman. Rapid stepwise onset of antarctic glaciation and deeper calcite compensation in the pacific ocean. *Nature*, 433(7021):53–57, 2005.

L. L. . v. d. W. R. de Boer, B. Persistent 400,000-year variability of antarctic ice volume and the carbon cycle is revealed throughout the plio-pleistocene. *Nat Commun*, page 2999, 2014. doi: 10.1038/ncomms3999. URL https://doi.org/10.1038/ncomms3999.

C. de Lavergne, J. Palter, and E. e. a. Galbraith. Cessation of deep convection in the open southern ocean under anthropogenic climate change. *Nature Clim Change*, 4:278–282, 2014. doi: 10.1038/nclimate2132. URL https://doi.org/10.1038/nclimate2132.

G. DeBlonde and W. Peltier. A one-dimensional model of continental ice volume fluctuations through the pleistocene: implications for the origin of the mid-pleistocene climate transition. *Journal of Climate*, 4(3):318–344, 1991.

R. DeConto and D. Pollard. Rapid cenozoic glaciation of antarctica induced by declining atmospheric co2. *Nature*, 421:245–249, 2003a. doi: 10.1038/nature01290. URL https://doi.org/10.1038/nature01290.

R. DeConto and D. Pollard. Contribution of antarctica to past and future sea-level rise. *Nature*, 531:591–597, 2016. doi: 10.1038/nature17145. URL https://doi.org/10.1038/nature17145.

R. M. DeConto and D. Pollard. A coupled climate–ice sheet modeling approach to the early cenozoic history of the antarctic ice sheet. *Palaeogeography, Palaeoclimatology, Palaeoecology*, 198(1-2):39–52, 2003b.

M. A. Depoorter, J. L. Bamber, J. A. Griggs, J. T. Lenaerts, S. R. Ligtenberg, M. R. van den Broeke, and G. Moholdt. Calving fluxes and basal melt rates of antarctic ice shelves. *Nature*, 502(7469):89–92, 2013.

T. Dupont and R. Alley. Assessment of the importance of ice-shelf buttressing to ice-sheet flow. *Geophysical Research Letters*, 32(4), 2005.

G. Durand, O. Gagliardini, T. Zwinger, E. Le Meur, and R. C. Hindmarsh. Full stokes modeling of marine ice sheets: influence of the grid size. *Annals of Glaciology*, 50(52): 109–114, 2009.

M. Eby, K. Zickfeld, A. Montenegro, D. Archer, K. Meissner, and A. Weaver. Lifetime of anthropogenic climate change: Millennial time scales of potential co 2 and surface temperature perturbations. *Journal of climate*, 22(10):2501–2511, 2009.

T. Extier. *Climate and low latitude water cycle variations during the Quaternary : a model-data approach*. PhD thesis, Université Paris Saclay, 2019.

V. Eyring, S. Bony, G. A. Meehl, C. A. Senior, B. Stevens, R. J. Stouffer, and K. E. Taylor. Overview of the Coupled Model Intercomparison Project Phase 6 (CMIP6) experimental design and organization. *Geosci. Model Dev.*, 9:1937–1958, 2016. doi: 10.5194/gmd-9-1937-2016.

L. Favier, G. Durand, S. L. Cornford, G. H. Gudmundsson, O. Gagliardini, F. Gillet-Chaulet, T. Zwinger, A. Payne, and A. M. Le Brocq. Retreat of pine island glacier controlled by marine ice-sheet instability. *Nature Climate Change*, 4(2):117–121, 2014.

L. Favier, N. C. Jourdain, A. Jenkins, N. Merino, G. Durand, O. Gagliardini, F. Gillet-Chaulet, and P. Mathiot. Assessment of sub-shelf melting parameterisations using the ocean–ice-sheet coupled model nemo(v3.6)–elmer/ice(v8.3). *Geoscientific Model Development*, 12(6):2255–2283, 2019. doi: 10.5194/gmd-12-2255-2019. URL https://gmd.copernicus.org/articles/12/2255/2019/.

T. Fichefet and M. A. Morales Maqueda. Sensitivity of a global sea ice model to the treatment of ice thermodynamics and dynamics. *J. Geophys. Res.*, 102:12609–12646, 1997. doi: 10.1029/97JC00480.

C. J. Fogwill, S. J. Phipps, C. S. M. Turney, and N. R. Golledge. Sensitivity of the southern ocean to enhanced regional antarctic ice sheet meltwater input. *Earth's Future*, 3 (10):317–329, 2015. doi: https://doi.org/10.1002/2015EF000306. URL https://agupubs.onlinelibrary.wiley.com/doi/abs/10.1002/2015EF000306.

G. L. Foster, C. H. Lear, and J. W. Rae. The evolution of pco2, ice volume and climate during the middle miocene. *Earth and Planetary Science Letters*, 341:243–254, 2012.

G. L. Foster, D. L. Royer, and D. J. Lunt. Future climate forcing potentially without precedent in the last 420 million years. *Nature communications*, 8(1):1–8, 2017.

B. Fox-Kemper, H. Hewitt, C. Xiao, G. Aðalgeirsdóttir, S. Drijfhout, T. Edwards, N. Golledge, M. Hemer, R. Kopp, G. Krinner, A. Mix, D. Notz, S. Nowicki, I. Nurhati, L. Ruiz, J.-B. Sallée, A. Slangen, and Y. Yu. *Ocean, Cryosphere and Sea Level Change. In Climate Change 2021: The Physical Science Basis. Contribution of Working Group I to the Sixth Assessment Report of the Intergovernmental Panel on Climate Change*, page 1211–1362. Cambridge University Press, Cambridge, United Kingdom, UK and New York, NY, USA, 2021. doi: 10.1017/9781009157896.011.

P. Fretwell, H. D. Pritchard, D. G. Vaughan, J. L. Bamber, N. E. Barrand, R. Bell, C. Bianchi, R. G. Bingham, D. D. Blankenship, G. Casassa, G. Catania, D. Callens, H. Conway, A. J. Cook, H. F. J. Corr, D. Damaske, V. Damm, F. Ferraccioli, R. Forsberg, S. Fujita, Y. Gim, P. Gogineni, J. A. Griggs, R. C. A. Hindmarsh, P. Holmlund, J. W. Holt, R. W. Jacobel, A. Jenkins, W. Jokat, T. Jordan, E. C. King, J. Kohler, W. Krabill, M. Riger-Kusk, K. A. Langley, G. Leitchenkov, C. Leuschen, B. P. Luyendyk, K. Matsuoka, J. Mouginot, F. O. Nitsche, Y. Nogi, O. A. Nost, S. V. Popov, E. Rignot, D. M. Rippin, A. Rivera, J. Roberts, N. Ross, M. J. Siegert, A. M. Smith, D. Steinhage, M. Studinger, B. Sun, B. K. Tinto, B. C. Welch, D. Wilson, D. A. Young, C. Xiangbin, and A. Zirizzotti. Bedmap2: improved ice bed, surface and thickness datasets for Antarctica. *Cryosphere*, 7(1):375–393, 2013. doi: 10.5194/tc-7-375-2013.

P. Friedlingstein, M. W. Jones, M. O'Sullivan, R. M. Andrew, D. C. E. Bakker, J. Hauck, C. Le Quéré, G. P. Peters, W. Peters, J. Pongratz, S. Sitch, J. G. Canadell, P. Ciais, R. B. Jackson, S. R. Alin, P. Anthoni, N. R. Bates, M. Becker, N. Bellouin, L. Bopp,

T. T. T. Chau, F. Chevallier, L. P. Chini, M. Cronin, K. I. Currie, B. Decharme, L. M. Djeutchouang, X. Dou, W. Evans, R. A. Feely, L. Feng, T. Gasser, D. Gilfillan, T. Gkritzalis, G. Grassi, L. Gregor, N. Gruber, O. Gürses, I. Harris, R. A. Houghton, G. C. Hurtt, Y. Iida, T. Ilyina, I. T. Luijkx, A. Jain, S. D. Jones, E. Kato, D. Kennedy, K. Klein Goldewijk, J. Knauer, J. I. Korsbakken, A. Körtzinger, P. Landschützer, S. K. Lauvset, N. Lefèvre, S. Lienert, J. Liu, G. Marland, P. C. McGuire, J. R. Melton, D. R. Munro, J. E. M. S. Nabel, S.-I. Nakaoka, Y. Niwa, T. Ono, D. Pierrot, B. Poulter, G. Rehder, L. Resplandy, E. Robertson, C. Rödenbeck, T. M. Rosan, J. Schwinger, C. Schwingshackl, R. Séférian, A. J. Sutton, C. Sweeney, T. Tanhua, P. P. Tans, H. Tian, B. Tilbrook, F. Tubiello, G. R. van der Werf, N. Vuichard, C. Wada, R. Wanninkhof, A. J. Watson, D. Willis, A. J. Wiltshire, W. Yuan, C. Yue, X. Yue, S. Zaehle, and J. Zeng. Global carbon budget 2021. *Earth System Science Data*, 14(4):1917–2005, 2022. doi: 10.5194/essd-14-1917-2022. URL https://essd.copernicus.org/articles/14/1917/2022/.

J. J. Fürst, G. Durand, F. Gillet-Chaulet, L. Tavard, M. Rankl, M. Braun, and O. Gagliardini. The safety band of antarctic ice shelves. *Nature Climate Change*, 6(5):479–482, 2016.

J. Fyke, O. Sergienko, M. Löfverström, S. Price, and J. T. M. Lenaerts. An overview of interactions and feedbacks between ice sheets and the earth system. *Reviews of Geophysics*, 56(2):361–408, 2018. doi: https://doi.org/10.1029/2018RG000600. URL https://agupubs.onlinelibrary.wiley.com/doi/abs/10.1029/2018RG000600.

O. Gagliardini, G. Durand, T. Zwinger, R. Hindmarsh, and E. Le Meur. Coupling of ice-shelf melting and buttressing is a key process in ice-sheets dynamics. *Geophysical Research Letters*, 37(14), 2010.

J. Gaillardet, B. Dupré, P. Louvat, and C. Allegre. Global silicate weathering and co2 consumption rates deduced from the chemistry of large rivers. *Chemical geology*, 159 (1-4):3–30, 1999.

S. Galeotti, P. Bijl, H. Brinkuis, R. M. DeConto, C. Escutia, F. Florindo, E. G. Gasson, J. Francis, D. Hutchinson, A. Kennedy-Asser, et al. The eocene-oligocene boundary climate transition: an antarctic perspective. In *Antarctic Climate Evolution*, pages 297–361. Elsevier, 2022.

V. Galy, C. France-Lanord, O. Beyssac, P. Faure, H. Kudrass, and F. Palhol. Efficient organic carbon burial in the bengal fan sustained by the himalayan erosional system. *Nature*, 450:407–410, 2007. doi: 10.1038/nature06273. URL https://doi.org/10.1038/nature06273.

A. Ganopolski and V. Brovkin. Simulation of climate, ice sheets and co 2 evolution during the last four glacial cycles with an earth system model of intermediate complexity. *Climate of the Past*, 13(12):1695–1716, 2017.

A. Ganopolski and R. Calov. The role of orbital forcing, carbon dioxide and regolith in 100 kyr glacial cycles. *Climate of the Past*, 7(4):1415–1425, 2011.

A. Ganopolski, R. Winkelmann, and H. J. Schellnhuber. Critical insolation–co2 relation for diagnosing past and future glacial inception. *Nature*, 529(7585):200–203, 2016.

J. Garbe, T. Albrecht, A. Levermann, J. Donges, and R. Winkelmann. The hysteresis of the antarctic ice sheet. *Nature*, 585:538–544, 2020. doi: 10.1038/s41586-020-2727-5. URL https://doi.org/10.1038/s41586-020-2727-5.

E. Gasson, D. J. Lunt, R. DeConto, A. Goldner, M. Heinemann, M. Huber, A. LeGrande, D. Pollard, N. Sagoo, M. Siddall, et al. Uncertainties in the modelled co 2 threshold for antarctic glaciation. *Climate of the Past*, 10(2):451–466, 2014.

F. Gillet-Chaulet, G. Durand, O. Gagliardini, C. Mosbeux, J. Mouginot, F. Rémy, and C. Ritz. Assimilation of surface velocities acquired between 1996 and 2010 to constrain the form of the basal friction law under pine island glacier. *Geophysical Research Letters*, 43(19):10,311–10,321, 2016. doi: https://doi.org/10.1002/2016GL069937. URL https://agupubs.onlinelibrary.wiley.com/doi/abs/10.1002/2016GL069937.

H. Goelzer, P. Huybrechts, M.-F. Loutre, and T. Fichefet. Last interglacial climate and sea-level evolution from a coupled ice sheet–climate model. *Climate of the Past*, 12 (12):2195–2213, 2016.

D. N. Goldberg, C. M. Little, O. V. Sergienko, A. Gnanadesikan, R. Hallberg, and M. Oppenheimer. Investigation of land ice-ocean interaction with a fully coupled ice-ocean model: 1. model description and behavior. *Journal of Geophysical Research: Earth Surface*, 117(F2), 2012. doi: https://doi.org/10.1029/2011JF002246. URL https://agupubs.onlinelibrary.wiley.com/doi/abs/10.1029/2011JF002246.

N. R. Golledge, R. H. Levy, R. M. McKay, C. J. Fogwill, D. A. White, A. G. Graham, J. A. Smith, C.-D. Hillenbrand, K. J. Licht, G. H. Denton, et al. Glaciology and geological signature of the last glacial maximum antarctic ice sheet. *Quaternary Science Reviews*, 78:225–247, 2013.

N. R. Golledge, L. Menviel, L. Carter, C. J. Fogwill, M. H. England, G. Cortese, and R. H. Levy. Antarctic contribution to meltwater pulse 1a from reduced southern ocean overturning. *Nature communications*, 5(1):1–10, 2014.

N. R. Golledge, D. E. Kowalewski, T. R. Naish, R. H. Levy, C. J. Fogwill, and E. G. Gasson. The multi-millennial antarctic commitment to future sea-level rise. *Nature*, 526(7573):421–425, 2015.

N. Gomez, D. Pollard, and D. Holland. Sea-level feedback lowers projections of future antarctic ice-sheet mass loss. *Nature communications*, 6(1):1–8, 2015.

S. A. Good, M. J. Martin, and N. A. Rayner. En4: Quality controlled ocean temperature and salinity profiles and monthly objective analyses with uncertainty estimates. *Journal of Geophysical Research: Oceans*, 118(12):6704–6716, 2013. doi: https://doi.org/10.1002/2013JC009067. URL https://agupubs.onlinelibrary.wiley.com/doi/abs/10.1002/2013JC009067.

H. Goosse and T. Fichefet. Importance of ice-ocean interactions for the global ocean circulation: a model study. *J. Geophys. Res.*, 104:23337–23355, 1999. doi: 10.1029/1999JC900215.

H. Goosse, J.-M. Campin, T. Fichefet, and E. Deleersnijder. Sensitivity of a global ice-ocean model to the Bering Strait throughflow. *Clim. Dynam.*, 13:349–358, 1997. doi: 10.1007/s003820050170.

H. Goosse, V. Brovkin, T. Fichefet, R. Haarsma, P. Huybrechts, J. Jongma, A. Mouchet, F. Selten, P. Y. Barriat, J. M. Campin, E. Deleersnijder, E. Driesschaert, H. Goelzer, I. Janssens, M. F. Loutre, M. A. Morales Maqueda, T. Opsteegh, P. P. Mathieu, G. Munhoven, E. J. Pettersson, H. Renssen, D. M. Roche, M. Schaeffer, B. Tartinville, A. Timmermann, and S. L. Weber. Description of the Earth system model of intermediate complexity LOVECLIM version 1.2. *Geosci. Model Dev.*, 3(2):603–633, 2010. doi: 10.5194/gmd-3-603-2010.

C. A. Greene, A. S. Gardner, N.-J. Schlegel, and A. D. Fraser. Antarctic calving loss rivals ice-shelf thinning. *Nature*, 609(7929):948–953, 2022.

J. M. Gregory, S. E. George, and R. S. Smith. Large and irreversible future decline of the greenland ice sheet. *The Cryosphere*, 14(12):4299–4322, 2020.

S. P. Gulick, A. E. Shevenell, A. Montelli, R. Fernandez, C. Smith, S. Warny, S. M. Bohaty, C. Sjunneskog, A. Leventer, B. Frederick, et al. Initiation and long-term instability of the east antarctic ice sheet. *Nature*, 552(7684):225–229, 2017.

J. Hays, J. Imbrie, and N. J. Shackleton. Variations in the earth's orbit: Pacemaker of the ice ages. *Science*, 194:1121–1132, 01 1976. doi: 10.1126/science.194.4270.1121.

J. I. Hedges and R. G. Keil. Sedimentary organic matter preservation: an assessment and speculative synthesis. *Marine Chemistry*, 49(2):81–115, 1995. ISSN 0304-4203. doi: https://doi.org/10.1016/0304-4203(95)00008-F. URL https://www.sciencedirect.com/science/article/pii/030442039500008F.

M. Heinemann, A. Timmermann, O. Elison Timm, F. Saito, and A. Abe-Ouchi. Deglacial ice sheet meltdown: Orbital pacemaking and co 2 effects. *Climate of the Past*, 10(4): 1567–1579, 2014.

R. G. Hilton and A. J. West. Mountains, erosion and the carbon cycle. *Nature Reviews Earth Environment*, 1:284–299, 2020. ISSN 0012-821X. doi: 10.1038/s43017-020-0058-6. URL https://doi.org/10.1038/s43017-020-0058-6.

P. R. Holland, A. Jenkins, and D. M. Holland. The response of ice shelf basal melting to variations in ocean temperature. *Journal of Climate*, 21(11):2558 – 2572, 2008. doi: 10.1175/2007JCLI1909.1. URL https://journals.ametsoc.org/view/journals/clim/21/11/2007jcli1909.1.xml.

B. Hönisch, N. G. Hemming, D. Archer, M. Siddall, and J. F. McManus. Atmospheric carbon dioxide concentration across the mid-pleistocene transition. *Science*, 324(5934): 1551–1554, 2009.

P. O. Hopcroft, G. Ramstein, T. A. M. Pugh, S. J. Hunter, F. Murguia-Flores, A. Quiquet, Y. Sun, N. Tan, and P. J. Valdes. Polar amplification of pliocene climate by elevated trace gas radiative forcing. *Proceedings of the National Academy of Sciences*, 117(38): 23401–23407, 2020. doi: 10.1073/pnas.2002320117. URL https://www.pnas.org/doi/abs/10.1073/pnas.2002320117.

J. Imbrie and J. Z. Imbrie. Modeling the climatic response to orbital variations. *Science*, 207(4434):943–953, 1980. doi: 10.1126/science.207.4434.943. URL https://science.sciencemag.org/content/207/4434/943.

J. Z. Imbrie, A. Imbrie-Moore, and L. E. Lisiecki. A phase-space model for pleistocene ice volume. *Earth Planet. Sc. Lett.*, 307(1-2):94–102, 2011.

IPCC. *Summary for Policymakers*, page 332. Cambridge University Press, Cambridge, United Kingdom and New York, NY, USA, 2021. doi: 10.1017/9781009157896.001.

R. F. Ivanovic, L. J. Gregoire, M. Kageyama, D. M. Roche, P. J. Valdes, A. Burke, R. Drummond, W. R. Peltier, and L. Tarasov. Transient climate simulations of the deglaciation 21–9 thousand years before present (version 1) – pmip4 core experiment design and boundary conditions. *Geoscientific Model Development*, 9(7):2563–2587, 2016. doi: 10.5194/gmd-9-2563-2016. URL https://gmd.copernicus.org/articles/9/2563/2016/.

A. Jenkins. A one-dimensional model of ice shelf-ocean interaction. *Journal of Geophysical Research: Oceans*, 96(C11):20671–20677, 1991. doi: https://doi.org/10.1029/91JC01842. URL https://agupubs.onlinelibrary.wiley.com/doi/abs/10.1029/91JC01842.

F. Joos, R. Roth, J. S. Fuglestvedt, G. P. Peters, I. G. Enting, W. Von Bloh, V. Brovkin, E. J. Burke, M. Eby, N. R. Edwards, et al. Carbon dioxide and climate impulse response functions for the computation of greenhouse gas metrics: a multi-model analysis. *Atmospheric Chemistry and Physics*, 13(5):2793–2825, 2013.

I. Joughin, B. E. Smith, and B. Medley. Marine ice sheet collapse potentially under way for the thwaites glacier basin, west antarctica. *Science*, 344(6185):735–738, 2014.

N. C. Jourdain, X. Asay-Davis, T. Hattermann, F. Straneo, H. Seroussi, C. M. Little, and S. Nowicki. A protocol for calculating basal melt rates in the ismip6 antarctic ice sheet projections. *The Cryosphere*, 14(9):3111–3134, 2020. doi: 10.5194/tc-14-3111-2020. URL https://tc.copernicus.org/articles/14/3111/2020/.

J. Jouzel, V. Masson-Delmotte, O. Cattani, G. Dreyfus, S. Falourd, G. Hoffmann, B. Minster, J. Nouet, J. M. Barnola, J. Chappellaz, H. Fischer, J. C. Gallet, S. Johnsen, M. Leuenberger, L. Loulergue, D. Luethi, H. Oerter, F. Parrenin, G. Raisbeck, D. Raynaud, A. Schilt, J. Schwander, E. Selmo, R. Souchez, R. Spahni, B. Stauffer, J. P. Steffensen, B. Stenni, T. F. Stocker, J. L. Tison, M. Werner, and E. W. Wolff. Orbital and millennial antarctic climate variability over the past 800,000 years. *Science*, 317(5839):793–796, 2007. doi: 10.1126/science.1141038. URL https://www.science.org/doi/abs/10.1126/science.1141038.

M. Kageyama, S. Albani, P. Braconnot, S. P. Harrison, P. O. Hopcroft, R. F. Ivanovic, F. Lambert, O. Marti, W. R. Peltier, J.-Y. Peterschmitt, D. M. Roche, L. Tarasov, X. Zhang, E. C. Brady, A. M. Haywood, A. N. LeGrande, D. J. Lunt, N. M. Mahowald, U. Mikolajewicz, K. H. Nisancioglu, B. L. Otto-Bliesner, H. Renssen, R. A. Tomas, Q. Zhang, A. Abe-Ouchi, P. J. Bartlein, J. Cao, Q. Li, G. Lohmann, R. Ohgaito, X. Shi, E. Volodin, K. Yoshida, X. Zhang, and W. Zheng. The PMIP4 contribution to CMIP6 – Part 4: Scientific objectives and experimental design of the PMIP4-CMIP6 Last Glacial Maximum experiments and PMIP4 sensitivity experiments. *Geosci. Model Dev.*, 10:4035–4055, 2017. doi: 10.5194/gmd-10-4035-2017.

J. F. Kasting. The goldilocks planet? how silicate weathering maintains earth "just right". *Elements: An International Magazine of Mineralogy, Geochemistry, and Petrology*, 15 (4):235–240, 2019.

J. P. Kennett. Cenozoic evolution of antarctic glaciation, the circum-antarctic ocean, and their impact on global paleoceanography. *Journal of geophysical research*, 82(27): 3843–3860, 1977.

D. C. Kitover, R. van Balen, D. M. Roche, J. Vandenberghe, and H. Renssen. Advancement toward coupling of the VAMPER permafrost model within the Earth system model iLOVECLIM (version 1.0): description and validation. *Geosci. Model Dev.*, 8: 1445–1460, 2019. doi: 10.5194/gmd-8-1445-2015.

I. J. Kocken, M. J. Cramwinckel, R. E. Zeebe, J. J. Middelburg, and A. Sluijs. The 405 kyr and 2.4 myr eccentricity components in cenozoic carbon isotope records. *Climate of the Past*, 15(1):91–104, 2019. doi: 10.5194/cp-15-91-2019. URL https://cp.copernicus.org/articles/15/91/2019/.

M. J. Kohn. Carbon isotope compositions of terrestrial c3 plants as indicators of (paleo) ecology and (paleo) climate. *Proceedings of the National Academy of Sciences*, 107 (46):19691–19695, 2010.

H. Konrad, I. Sasgen, V. Klemann, M. Thoma, K. Grosfeld, and Z. Martinec. Sensitivity of grounding-line dynamics to viscoelastic deformation of the solid-earth in an idealized scenario. *Polarforschung*, 85(2):89–99, 2016.

J.-B. Ladant, Y. Donnadieu, V. Lefebvre, and C. Dumas. The respective role of atmospheric carbon dioxide and orbital parameters on ice sheet evolution at the eocene-oligocene transition. *Paleoceanography*, 29(8):810–823, 2014.

K. Lambeck, H. Rouby, A. Purcell, Y. Sun, and M. Sambridge. Sea level and global ice volumes from the last glacial maximum to the holocene. *Proceedings of the National Academy of Sciences*, 111(43):15296–15303, 2014. doi: 10.1073/pnas.1411762111. URL https://www.pnas.org/doi/abs/10.1073/pnas.1411762111.

E. Larour, H. Seroussi, M. Morlighem, and E. Rignot. Continental scale, high order, high spatial resolution, ice sheet modeling using the ice sheet system model (issm). *Journal of Geophysical Research: Earth Surface*, 117(F1), 2012. doi: https://doi.org/10.1029/2011JF002140. URL https://agupubs.onlinelibrary.wiley.com/doi/abs/10.1029/2011JF002140.

J. Laskar, P. Robutel, F. Joutel, M. Gastineau, A. C. M. Correia, and B. Levrard. A long-term numerical solution for the insolation quantities of the earth. *A&A*, 428 (1):261–285, 2004. doi: 10.1051/0004-6361:20041335. URL https://doi.org/10.1051/0004-6361:20041335.

J. Laskar, A. Fienga, M. Gastineau, and H. Manche. La2010: a new orbital solution for the long-term motion of the earth. *A&A*, 532:A89, 2011. doi: 10.1051/0004-6361/201116836. URL https://doi.org/10.1051/0004-6361/201116836.

V. Lauretano, K. Littler, M. Polling, J. C. Zachos, and L. J. Lourens. Frequency, magnitude and character of hyperthermal events at the onset of the early eocene climatic optimum. *Climate of the Past*, 11(10):1313–1324, 2015. doi: 10.5194/cp-11-1313-2015. URL https://cp.copernicus.org/articles/11/1313/2015/.

W. M. J. Lazeroms, A. Jenkins, G. H. Gudmundsson, and R. S. W. van de Wal. Modelling present-day basal melt rates for antarctic ice shelves using a parametrization of buoyant meltwater plumes. *The Cryosphere*, 12(1):49–70, 2018. doi: 10.5194/tc-12-49-2018. URL https://tc.copernicus.org/articles/12/49/2018/.

W. M. J. Lazeroms, A. Jenkins, S. W. Rienstra, and R. S. W. van de Wal. An analytical derivation of ice-shelf basal melt based on the dynamics of meltwater plumes. *Journal of Physical Oceanography*, 49(4):917 – 939, 2019. doi: 10.1175/JPO-D-18-0131.1. URL https://journals.ametsoc.org/view/journals/phoc/49/4/jpo-d-18-0131.1.xml.

E. Le Meur and P. Huybrechts. A comparison of different ways of dealing with isostasy: examples from modelling the antarctic ice sheet during the last glacial cycle. *Annals of Glaciology*, 23:309–317, 1996. doi: 10.3189/S0260305500013586.

J.-Y. Lee, J. Marotzke, G. Bala, L. Cao, S. Corti, J. Dunne, F. Engelbrecht, E. Fischer, J. Fyfe, C. Jones, A. Maycock, J. Mutemi, O. Ndiaye, S. Panickal, and T. Zhou. *Future Global Climate: Scenario-Based Projections and Near-Term Information*, page 553–672. Cambridge University Press, Cambridge, United Kingdom and New York, NY, USA, 2021. doi: 10.1017/9781009157896.006.

G. Leloup and D. Paillard. Influence of the choice of insolation forcing on the results of a conceptual glacial cycle model. *Climate of the Past*, 18(3):547–558, 2022. doi: 10.5194/cp-18-547-2022. URL https://cp.copernicus.org/articles/18/547/2022/.

T. M. Lenton and C. Britton. Enhanced carbonate and silicate weathering accelerates recovery from fossil fuel co2 perturbations. *Global Biogeochemical Cycles*, 20(3), 2006.

D. Liebrand, H. M. Beddow, L. J. Lourens, H. Pälike, I. Raffi, S. M. Bohaty, F. J. Hilgen, M. J. Saes, P. A. Wilson, A. E. van Dijk, D. A. Hodell, D. Kroon, C. E. Huck, and S. J. Batenburg. Cyclostratigraphy and eccentricity tuning of the early oligocene through early miocene (30.1–17.1 ma): Cibicides mundulus stable oxygen and carbon isotope records from walvis ridge site 1264. *Earth and Planetary Science Letters*, 450:392–405, 2016. ISSN 0012-821X. doi: https://doi.org/10.1016/j.epsl.2016.06.007. URL https://www.sciencedirect.com/science/article/pii/S0012821X16302941.

L. E. Lisiecki and M. E. Raymo. A pliocene-pleistocene stack of 57 globally distributed benthic δ18o records. *Paleoceanography*, 20(1), 2005.

A. J. Lloyd, D. A. Wiens, H. Zhu, J. Tromp, A. A. Nyblade, R. C. Aster, S. E. Hansen, I. W. Dalziel, T. J. Wilson, E. R. Ivins, et al. Seismic structure of the antarctic upper mantle imaged with adjoint tomography. *Journal of Geophysical Research: Solid Earth*, 125(3), 2020.

R. A. Locarnini, A. V. Mishonov, O. K. Baranova, T. P. Boyer, M. M. Zweng, H. E. Garcia, J. R. Reagan, D. Seidov, K. Weathers, C. R. Paver, and I. Smolyar. World ocean atlas 2018, volume 1: Temperature. *A. Mishonov Technical Ed.; NOAA Atlas NESDIS 81*, 2018. URL https://www.ncei.noaa.gov/access/world-ocean-atlas-2018/.

N. S. Lord, A. Ridgwell, M. C. Thorne, and D. J. Lunt. An impulse response function for the "long tail" of excess atmospheric co2 in an earth system model. *Global Biogeochemical Cycles*, 30(1):2–17, 2016. doi: https://doi.org/10.1002/

2014GB005074. URL https://agupubs.onlinelibrary.wiley.com/doi/abs/10.1002/2014GB005074.

N. S. Lord, M. Crucifix, D. J. Lunt, M. C. Thorne, N. Bounceur, H. Dowsett, C. L. O'Brien, and A. Ridgwell. Emulation of long-term changes in global climate: application to the late pliocene and future. *Climate of the Past*, 13(11):1539–1571, 2017. doi: 10.5194/cp-13-1539-2017. URL https://cp.copernicus.org/articles/13/1539/2017/.

N. S. Lord, D. Lunt, and M. Thorne. Modelling changes in climate over the next 1 million years, 2019.

L. Loulergue, A. Schilt, R. Spahni, V. Masson-Delmotte, T. Blunier, B. Lemieux, J.-M. Barnola, D. Raynaud, T. F. Stocker, and J. Chappellaz. Orbital and millennial-scale features of atmospheric ch4 over the past 800,000 years. *Nature*, 453(7193):383–386, 2008.

D. Lüthi, M. Le Floch, B. Bereiter, T. Blunier, J.-M. Barnola, U. Siegenthaler, D. Raynaud, J. Jouzel, H. Fischer, K. Kawamura, et al. High-resolution carbon dioxide concentration record 650,000–800,000 years before present. *nature*, 453(7193):379–382, 2008.

D. R. MacAyeal. A catastrophe model of the paleoglimate. *Journal of Glaciology*, 24(90): 245–257, 1979. doi: 10.3189/S0022143000014775.

M. Martinez and G. Dera. Orbital pacing of carbon fluxes by a ˜9-my eccentricity cycle during the mesozoic. *Proceedings of the National Academy of Sciences*, 112(41): 12604–12609, 2015. ISSN 0027-8424. doi: 10.1073/pnas.1419946112. URL https://www.pnas.org/content/112/41/12604.

M. McMillan, A. Shepherd, A. Muir, J. Gaudelli, A. E. Hogg, and R. Cullen. Assessment of cryosat-2 interferometric and non-interferometric sar altimetry over ice sheets. *Advances in Space Research*, 62(6):1281–1291, 2018.

M. Meinshausen, S. J. Smith, K. Calvin, J. S. Daniel, M. L. Kainuma, J.-F. Lamarque, K. Matsumoto, S. A. Montzka, S. C. Raper, K. Riahi, et al. The rcp greenhouse gas concentrations and their extensions from 1765 to 2300. *Climatic change*, 109(1): 213–241, 2011.

M. Meinshausen, Z. R. J. Nicholls, J. Lewis, M. J. Gidden, E. Vogel, M. Freund, U. Beyerle, C. Gessner, A. Nauels, N. Bauer, J. G. Canadell, J. S. Daniel, A. John, P. B. Krummel, G. Luderer, N. Meinshausen, S. A. Montzka, P. J. Rayner, S. Reimann, S. J. Smith, M. van den Berg, G. J. M. Velders, M. K. Vollmer, and R. H. J. Wang. The shared socio-economic pathway (ssp) greenhouse gas concentrations and their extensions to 2500. *Geoscientific Model Development*, 13(8):3571–3605, 2020. doi: 10.5194/gmd-13-3571-2020. URL https://gmd.copernicus.org/articles/13/3571/2020/.

J. H. Mercer. West antarctic ice sheet and co2 greenhouse effect: a threat of disaster. *Nature*, 271(5643):321–325, 1978.

M. Meredith, S. M. Sommerkorn, C. Cassotta, A. Derksen, A. Ekaykin, G. Hollowed, A. Kofinas, J. Mackintosh, M. Melbourne-Thomas, G. Muelbert, H. Ottersen, Pritchard, and E. Schuur. *Polar Regions.*, pages 203–320. Cambridge University Press, Cambridge, United Kingdom, UK and New York, NY, USA, 2019. doi: 10.1017/9781009157964.005.

M. Milankovitch. Kanon der erdbestrahlung und seine anwendung auf das eiszeitenproblem. *Royal Serbian Academy Special Publication*, 133:1–633, 1941.

K. G. Miller, J. V. Browning, W. J. Schmelz, R. E. Kopp, G. S. Mountain, and J. D. Wright. Cenozoic sea-level and cryospheric evolution from deep-sea geochemical and continental margin records. *Science advances*, 6(20):eaaz1346, 2020.

S. Moon, C. Chamberlain, and G. Hilley. New estimates of silicate weathering rates and their uncertainties in global rivers. *Geochimica et Cosmochimica Acta*, 134:257–274, 2014.

R. Mottram, N. Hansen, C. Kittel, J. M. van Wessem, C. Agosta, C. Amory, F. Boberg, W. J. van de Berg, X. Fettweis, A. Gossart, N. P. M. van Lipzig, E. van Meijgaard, A. Orr, T. Phillips, S. Webster, S. B. Simonsen, and N. Souverijns. What is the surface mass balance of antarctica? an intercomparison of regional climate model estimates. *The Cryosphere*, 15(8):3751–3784, 2021. doi: 10.5194/tc-15-3751-2021. URL https://tc.copernicus.org/articles/15/3751/2021/.

J. Mouginot, E. Rignot, B. Scheuchl, and R. Millan. Comprehensive annual ice sheet velocity mapping using landsat-8, sentinel-1, and radarsat-2 data. *Remote Sensing*, 9 (4), 2017. ISSN 2072-4292. doi: 10.3390/rs9040364. URL https://www.mdpi.com/2072-4292/9/4/364.

L. Muntjewerf, M. Petrini, M. Vizcaino, C. Ernani da Silva, R. Sellevold, M. D. Scherrenberg, K. Thayer-Calder, S. L. Bradley, J. T. Lenaerts, W. H. Lipscomb, et al. Greenland ice sheet contribution to 21st century sea level rise as simulated by the coupled cesm2. 1-cism2. 1. *Geophysical Research Letters*, 47(9):e2019GL086836, 2020.

R. D. Müller and A. Dutkiewicz. Oceanic crustal carbon cycle drives 26-million-year atmospheric carbon dioxide periodicities. *Science Advances*, 4(2):eaaq0500, 2018. doi: 10.1126/sciadv.aaq0500. URL https://www.science.org/doi/abs/10.1126/sciadv.aaq0500.

S. Nowicki, H. Goelzer, H. Seroussi, A. J. Payne, W. H. Lipscomb, A. Abe-Ouchi, C. Agosta, P. Alexander, X. S. Asay-Davis, A. Barthel, T. J. Bracegirdle, R. Cullather, D. Felikson, X. Fettweis, J. M. Gregory, T. Hattermann, N. C. Jourdain, P. Kuipers Munneke, E. Larour, C. M. Little, M. Morlighem, I. Nias, A. Shepherd, E. Simon, D. Slater, R. S. Smith, F. Straneo, L. D. Trusel, M. R. van den Broeke, and R. van de Wal. Experimental protocol for sea level projections from ismip6 standalone ice sheet models. *The Cryosphere*, 14(7):2331–2368, 2020. doi: 10.5194/tc-14-2331-2020. URL https://tc.copernicus.org/articles/14/2331/2020/.

S. M. J. Nowicki, A. Payne, E. Larour, H. Seroussi, H. Goelzer, W. Lipscomb, J. Gregory, A. Abe-Ouchi, and A. Shepherd. Ice sheet model intercomparison project (ismip6) contribution to cmip6. *Geoscientific Model Development*, 9(12):4521–4545, 2016. doi: 10.5194/gmd-9-4521-2016. URL https://gmd.copernicus.org/articles/9/4521/2016/.

J. Oerlemans. Model experiments on the 100,000-yr glacial cycle. *Nature*, 287(5781): 430–432, 1980.

H. H. Olbers, D. A box model of circulation and melting in ice shelf caverns.o. *Ocean Dynamics*, 60:141–153, 2010. doi: 10.1007/s10236-009-0252-. URL https://doi.org/10.1007/s10236-009-0252-z.

B. L. Otto-Bliesner, P. Braconnot, S. P. Harrison, D. J. Lunt, A. Abe-Ouchi, S. Albani, P. J. Bartlein, E. Capron, A. E. Carlson, A. Dutton, H. Fischer, H. Goelzer, A. Govin, A. Haywood, F. Joos, A. N. LeGrande, W. H. Lipscomb, G. Lohmann, N. Mahowald, C. Nehrbass-Ahles, F. S. R. Pausata, J.-Y. Peterschmitt, S. J. Phipps, H. Renssen, and Q. Zhang. The pmip4 contribution to cmip6 – part 2: Two interglacials, scientific objective and experimental design for holocene and
last interglacial simulations. *Geoscientific Model Development*, 10(11):3979–4003, 2017. doi: 10.5194/gmd-10-3979-2017. URL https://gmd.copernicus.org/articles/10/3979/2017/.

M. Pagani, M. Huber, Z. Liu, S. M. Bohaty, J. Henderiks, W. Sijp, S. Krishnan, and R. M. DeConto. The role of carbon dioxide during the onset of antarctic glaciation. *science*, 334(6060):1261–1264, 2011.

D. Paillard. The timing of pleistocene glaciations from a simple multiple-state climate model. *Nature*, 391(6665):378–381, 1998. doi: 10.1038/3489.

D. Paillard. Glacial cycles: toward a new paradigm. *Reviews of Geophysics*, 39(3):325–346, 2001.

D. Paillard. The plio-pleistocene climatic evolution as a consequence of orbital forcing on the carbon cycle. *Climate of the Past*, 13(9):1259–1267, 2017. doi: 10.5194/cp-13-1259-2017. URL https://cp.copernicus.org/articles/13/1259/2017/.

D. Paillard and F. Parrenin. The Antarctic ice sheet and the triggering of deglaciations. *Earth and Planetary Science Letters*, 227:263–271, 2004. doi: 10.1016/j.epsl.2004.08.023.

F. Parrenin and D. Paillard. Amplitude and phase of glacial cycles from a conceptual model. *Earth Planet. Sc. Lett.*, 214(1-2):243–250, 2003. doi: 10.1016/S0012-821X(03)00363-7.

F. Parrenin and D. Paillard. Terminations vi and viii ($\sim$ 530 and $\sim$ 720 kyr bp) tell us the importance of obliquity and precession in the triggering of deglaciations. *Clim. Past*, 8 (6):2031–2037, 2012. doi: 10.5194/cp-8-2031-2012. URL https://cp.copernicus.org/articles/8/2031/2012/.

F. Pattyn. Sea-level response to melting of antarctic ice shelves on multi-centennial timescales with the fast elementary thermomechanical ice sheet model (f.etish v1.0). *The Cryosphere*, 11(4):1851–1878, 2017. doi: 10.5194/tc-11-1851-2017. URL https://tc.copernicus.org/articles/11/1851/2017/.

F. Pattyn and M. Morlighem. The uncertain future of the antarctic ice sheet. *Science*, 367(6484):1331–1335, 2020.

G. J. Paxman, S. S. Jamieson, K. Hochmuth, K. Gohl, M. J. Bentley, G. Leitchenkov, and F. Ferraccioli. Reconstructions of antarctic topography since the eocene–oligocene boundary. *Palaeogeography, palaeoclimatology, palaeoecology*, 535:109346, 2019.

P. N. Pearson, G. L. Foster, and B. S. Wade. Atmospheric carbon dioxide through the eocene–oligocene climate transition. *Nature*, 461(7267):1110–1113, 2009.

T. Pelle, M. Morlighem, and J. H. Bondzio. Brief communication: Picop, a new ocean melt parameterization under ice shelves combining pico and a plume model. *The Cryosphere*, 13(3):1043–1049, 2019. doi: 10.5194/tc-13-1043-2019. URL https://tc.copernicus.org/articles/13/1043/2019/.

S. Petsch. Treatise of geochemistry, 2014.

S. Petsch, K. Edwards, and T. Eglinton. Microbial transformations of organic matter in black shales and implications for global biogeochemical cycles. *Palaeogeography, Palaeoclimatology, Palaeoecology*, 219(1):157–170, 2005. ISSN 0031-0182. doi: https://doi.org/10.1016/j.palaeo.2004.10.019. URL https://www.sciencedirect.com/science/article/pii/S0031018204005966. Geobiology: Objectives, Concept, Perspectives.

G. Philippon, G. Ramstein, S. Charbit, M. Kageyama, C. Ritz, and C. Dumas. Evolution of the antarctic ice sheet throughout the last deglaciation: A study with a new coupled climate—north and south hemisphere ice sheet model. *Earth and Planetary Science Letters*, 248(3):750–758, 2006. ISSN 0012-821X. doi: https://doi.org/10.1016/j.epsl.2006.06.017. URL https://www.sciencedirect.com/science/article/pii/S0012821X06004390.

D. Pollard. A simple parameterization for ice sheet ablation rate1. *Tellus*, 32(4):384–388, 1980. doi: https://doi.org/10.1111/j.2153-3490.1980.tb00965.x. URL https://onlinelibrary.wiley.com/doi/abs/10.1111/j.2153-3490.1980.tb00965.x.

D. Pollard. A simple ice sheet model yields realistic 100 kyr glacial cycles. *Nature*, 296 (5855):334–338, 1982.

D. Pollard. A coupled climate-ice sheet model applied to the quaternary ice ages. *Journal of Geophysical Research: Oceans*, 88(C12):7705–7718, 1983.

D. Pollard. A retrospective look at coupled ice sheet–climate modeling. *Climatic Change*, 100:173–194, 2010. doi: 10.1007/s10584-010-9830-9. URL https://doi.org/10.1007/s10584-010-9830-9.

D. Pollard and R. DeConto. Description of a hybrid ice sheet-shelf model, and application to antarctica. *Geoscientific Model Development*, 5(5):1273–1295, 2012.

D. Pollard and R. M. DeConto. Hysteresis in cenozoic antarctic ice-sheet variations. *Global and Planetary Change*, 45(1-3):9–21, 2005.

H. Pälike, R. D. Norris, J. O. Herrle, P. A. Wilson, H. K. Coxall, C. H. Lear, N. J. Shackleton, A. K. Tripati, and B. S. Wade. The heartbeat of the oligocene climate system. *Science*, 314(5807):1894–1898, 2006. doi: 10.1126/science.1133822. URL https://www.science.org/doi/abs/10.1126/science.1133822.

A. Quiquet and C. Dumas. The grisli-lsce contribution to the ice sheet model intercomparison project for phase 6 of the coupled model intercomparison project (ismip6) – part 2: Projections of the antarctic ice sheet evolution by the end of the 21st century. *The Cryosphere*, 15(2):1031–1052, 2021. doi: 10.5194/tc-15-1031-2021. URL https://tc.copernicus.org/articles/15/1031/2021/.

A. Quiquet, C. Dumas, C. Ritz, V. Peyaud, and D. M. Roche. The GRISLI ice sheet model (version 2.0): calibration and validation for multi-millennial changes of the antarctic ice sheet. *Geoscientific Model Development*, 11(12):5003–5025, 2018a. doi: 10.5194/gmd-11-5003-2018. URL https://gmd.copernicus.org/articles/11/5003/2018/.

A. Quiquet, D. M. Roche, C. Dumas, and D. Paillard. Online dynamical downscaling of temperature and precipitation within the iLOVECLIM model (version 1.1). *Geoscientific Model Development*, 11:453–466, 2018b. doi: 10.5194/gmd-11-453-2018. URL https://gmd.copernicus.org/articles/11/453/2018/.

A. Quiquet, D. M. Roche, C. Dumas, N. Bouttes, and F. Lhardy. Climate and ice sheet evolutions from the last glacial maximum to the pre-industrial period with an ice-sheet–climate coupled model. *Climate of the Past*, 17(5):2179–2199, 2021. doi: 10.5194/cp-17-2179-2021. URL https://cp.copernicus.org/articles/17/2179/2021/.

J. W. Rae, Y. G. Zhang, X. Liu, G. L. Foster, H. M. Stoll, and R. D. Whiteford. Atmospheric co2 over the past 66 million years from marine archives. *Annual Review of Earth and Planetary Sciences*, 49, 2021.

M. E. Raymo, R. Kozdon, D. Evans, L. Lisiecki, and H. L. Ford. The accuracy of mid-pliocene 18o-based ice volume and sea level reconstructions. *Earth-Science Reviews*, 177:291–302, 2018. ISSN 0012-8252. doi: https://doi.org/10.1016/j.earscirev.2017.11.022. URL https://www.sciencedirect.com/science/article/pii/S0012825217305937.

N. Reeh. Parameterization of melt rate and surface temperature in the greenland ice sheet. *Polarforschung*, 59(3):113–128, 1991.

R. Reese, T. Albrecht, M. Mengel, X. Asay-Davis, and R. Winkelmann. Antarctic subshelf melt rates via pico. *The Cryosphere*, 12(6):1969–1985, 2018. doi: 10.5194/tc-12-1969-2018. URL https://tc.copernicus.org/articles/12/1969/2018/.

G. J. Retallack. Greenhouse crises of the past 300 million years. *Geological Society of America Bulletin*, 121(9-10):1441–1455, 2009.

A. Ridgwell and J. Hargreaves. Regulation of atmospheric co2 by deep-sea sediments in an earth system model. *Global Biogeochemical Cycles*, 21(2), 2007.

E. Rignot, S. Jacobs, J. Mouginot, and B. Scheuchl. Ice-shelf melting around antarctica. *Science*, 341(6143):266–270, 2013.

C. Ritz, V. Rommelaere, and C. Dumas. Modeling the evolution of antarctic ice sheet over the last 420,000 years: Implications for altitude changes in the vostok region. *Journal of Geophysical Research: Atmospheres*, 106(D23):31943–31964, 2001. doi: https://doi.org/10.1029/2001JD900232. URL https://agupubs.onlinelibrary.wiley.com/doi/abs/10.1029/2001JD900232.

A. Robinson, R. Calov, and A. Ganopolski. An efficient regional energy-moisture balance model for simulation of the greenland ice sheet response to climate change. *The Cryosphere*, 4(2):129–144, 2010. doi: 10.5194/tc-4-129-2010. URL https://tc.copernicus.org/articles/4/129/2010/.

A. Robinson, R. Calov, and A. Ganopolski. Multistability and critical thresholds of the greenland ice sheet. *Nature Climate Change*, 2(6):429–432, 2012.

D. M. Roche. ^{18}o water isotope in the iloveclim model (version 1.0) – part 1: Implementation and verification. *Geoscientific Model Development*, 6(5):1481–1491, 2013. doi: 10.5194/gmd-6-1481-2013. URL https://gmd.copernicus.org/articles/6/1481/2013/.

D. M. Roche and T. Caley. ^{18}o water isotope in the iloveclim model (version 1.0) – part 2: Evaluation of model results against observed ^{18}o in water samples. *Geoscientific Model Development*, 6(5):1493–1504, 2013. doi: 10.5194/gmd-6-1493-2013. URL https://gmd.copernicus.org/articles/6/1493/2013/.

D. M. Roche, C. Dumas, M. Bügelmayer, S. Charbit, and C. Ritz. Adding a dynamical cryosphere to iLOVECLIM (version 1.0): coupling with the GRISLI ice-sheet model. *Geoscientific Model Development*, 7:1377–1394, 2014. doi: 10.5194/gmd-7-1377-2014.

T. Russon, D. Paillard, and M. Elliot. Potential origins of 400–500 kyr periodicities in the ocean carbon cycle: A box model approach. *Global Biogeochemical Cycles*, 24(2), 2010.

T. Scambos, H. A. Fricker, C.-C. Liu, J. Bohlander, J. Fastook, A. Sargent, R. Massom, and A.-M. Wu. Ice shelf disintegration by plate bending and hydro-fracture: Satellite observations and model results of the 2008 wilkins ice shelf break-ups. *Earth and Planetary Science Letters*, 280(1):51–60, 2009. ISSN 0012-821X. doi: https://doi.org/10.1016/j.epsl.2008.12.027. URL https://www.sciencedirect.com/science/article/pii/S0012821X08007887.

H. D. Scher, S. M. Bohaty, B. W. Smith, and G. H. Munn. Isotopic interrogation of a suspected late eocene glaciation. *Paleoceanography*, 29(6):628–644, 2014.

C. Schoof. Ice sheet grounding line dynamics: Steady states, stability, and hysteresis. *Journal of Geophysical Research: Earth Surface*, 112(F3), 2007.

H. Seddik, R. Greve, T. Zwinger, F. Gillet-Chaulet, and O. Gagliardini. Simulations of the greenland ice sheet 100 years into the future with the full stokes model elmer/ice. *Journal of Glaciology*, 58(209):427–440, 2012. doi: 10.3189/2012JoG11J177.

H. Seroussi, Y. Nakayama, E. Larour, D. Menemenlis, M. Morlighem, E. Rignot, and A. Khazendar. Continued retreat of thwaites glacier, west antarctica, controlled by bed topography and ocean circulation. *Geophysical Research Letters*, 44(12):6191–6199, 2017. doi: https://doi.org/10.1002/2017GL072910. URL https://agupubs.onlinelibrary.wiley.com/doi/abs/10.1002/2017GL072910.

H. Seroussi, S. Nowicki, A. J. Payne, H. Goelzer, W. H. Lipscomb, A. Abe-Ouchi, C. Agosta, T. Albrecht, X. Asay-Davis, A. Barthel, R. Calov, R. Cullather, C. Dumas,

B. K. Galton-Fenzi, R. Gladstone, N. R. Golledge, J. M. Gregory, R. Greve, T. Hattermann, M. J. Hoffman, A. Humbert, P. Huybrechts, N. C. Jourdain, T. Kleiner, E. Larour, G. R. Leguy, D. P. Lowry, C. M. Little, M. Morlighem, F. Pattyn, T. Pelle, S. F. Price, A. Quiquet, R. Reese, N.-J. Schlegel, A. Shepherd, E. Simon, R. S. Smith, F. Straneo, S. Sun, L. D. Trusel, J. Van Breedam, R. S. W. van de Wal, R. Winkelmann, C. Zhao, T. Zhang, and T. Zwinger. Ismip6 antarctica: a multi-model ensemble of the antarctic ice sheet evolution over the 21st century. *The Cryosphere*, 14(9):3033–3070, 2020. doi: 10.5194/tc-14-3033-2020. URL https://tc.copernicus.org/articles/14/3033/2020/.

A. R. Simms, L. Lisiecki, G. Gebbie, P. L. Whitehouse, and J. F. Clark. Balancing the last glacial maximum (lgm) sea-level budget. *Quaternary Science Reviews*, 205:143–153, 2019.

R. S. Smith, P. Mathiot, A. Siahaan, V. Lee, S. L. Cornford, J. M. Gregory, A. J. Payne, A. Jenkins, P. R. Holland, J. K. Ridley, et al. Coupling the uk earth system model to dynamic models of the greenland and antarctic ice sheets. *Journal of Advances in Modeling Earth Systems*, 13(10):e2021MS002520, 2021.

S. Solomon, G.-K. Plattner, R. Knutti, and P. Friedlingstein. Irreversible climate change due to carbon dioxide emissions. *Proceedings of the national academy of sciences*, 106 (6):1704–1709, 2009.

R. Spahni, J. Chappellaz, T. F. Stocker, L. Loulergue, G. Hausammann, K. Kawamura, J. Fluckiger, J. Schwander, D. Raynaud, V. Masson-Delmotte, et al. Atmospheric methane and nitrous oxide of the late pleistocene from antarctic ice cores. *Science*, 310(5752):1317–1321, 2005.

A. D. Sproson. Pacing of the latest ordovician and silurian carbon cycle by a 4.5 myr orbital cycle. *Palaeogeography, Palaeoclimatology, Palaeoecology*, 540:109543, 2020. ISSN 0031-0182. doi: https://doi.org/10.1016/j.palaeo.2019.109543. URL https://www.sciencedirect.com/science/article/pii/S0031018219308867.

M. Sprovieri, N. Sabatino, N. Pelosi, S. J. Batenburg, R. Coccioni, M. Iavarone, and S. Mazzola. Late cretaceous orbitally-paced carbon isotope stratigraphy from the bottaccione gorge (italy). *Palaeogeography, Palaeoclimatology, Palaeoecology*, 379-380:81–94, 2013. ISSN 0031-0182. doi: https://doi.org/10.1016/j.palaeo.2013.04.006. URL https://www.sciencedirect.com/science/article/pii/S0031018213001685.

L. B. Stap, R. S. W. van de Wal, B. de Boer, R. Bintanja, and L. J. Lourens. Interaction of ice sheets and climate during the past 800 000 years. *Climate of the Past*, 10(6): 2135–2152, 2014. doi: 10.5194/cp-10-2135-2014. URL https://cp.copernicus.org/articles/10/2135/2014/.

L. B. Stap, C. J. Berends, M. D. W. Scherrenberg, R. S. W. van de Wal, and E. G. W. Gasson. Net effect of ice-sheet–atmosphere interactions reduces simulated transient miocene antarctic ice-sheet variability. *The Cryosphere*, 16(4):1315–1332, 2022. doi: 10.5194/tc-16-1315-2022. URL https://tc.copernicus.org/articles/16/1315/2022/.

M. Steinthorsdottir, A. S. Porter, A. Holohan, L. Kunzmann, M. Collinson, and J. C. McElwain. Fossil plant stomata indicate decreasing atmospheric co 2 prior to the eocene–oligocene boundary. *Climate of the Past*, 12(2):439–454, 2016.

S. Sun, F. Pattyn, E. G. Simon, T. Albrecht, S. Cornford, R. Calov, C. Dumas, F. Gillet-Chaulet, H. Goelzer, N. R. Golledge, and et al. Antarctic ice sheet response to sudden and sustained ice-shelf collapse (abumip). *Journal of Glaciology*, 66(260):891–904, 2020. doi: 10.1017/jog.2020.67.

S. Talento and A. Ganopolski. Reduced-complexity model for the impact of anthropogenic co_2 emissions on future glacial cycles. *Earth Syst. Dynam. Discuss.*, 12:1275–1293, 2021. doi: 10.5194/esd-12-1275-2021.

L. Tarasov and W. R. Peltier. Terminating the 100 kyr ice age cycle. *Journal of Geophysical Research: Atmospheres*, 102(D18):21665–21693, 1997.

J. E. Tierney, C. J. Poulsen, I. P. Montañez, T. Bhattacharya, R. Feng, H. L. Ford, B. Hönisch, G. N. Inglis, S. V. Petersen, N. Sagoo, et al. Past climates inform our future. *Science*, 370(6517):eaay3701, 2020a.

J. E. Tierney, J. Zhu, J. King, S. B. Malevich, G. J. Hakim, and C. J. Poulsen. Glacial cooling and climate sensitivity revisited. *Nature*, 584:569–573, 2020b. doi: 10.1038/s41586-020-2617-x.

M. Torres, A. West, and G. Li. Sulphide oxidation and carbonate dissolution as a source of co2 over geological timescales. *Nature*, 507:346–349, 2014. doi: 10.1038/nature03814. URL https://doi.org/10.1038/nature13030.

M. A. Torres, A. J. West, K. E. Clark, G. Paris, J. Bouchez, C. Ponton, S. J. Feakins, V. Galy, and J. F. Adkins. The acid and alkalinity budgets of weathering in the andes–amazon system: Insights into the erosional control of global biogeochemical cycles. *Earth and Planetary Science Letters*, 450:381–391, 2016.

A. Treasure, F. Roquet, I. Ansorge, M. Bester, L. Boehme, H. Bornemann, J.-B. Charrassin, D. Chevallier, D. Costa, M. Fedak, C. Guinet, M. Hammill, R. Harcourt, M. Hindell, K. Kovacs, M.-A. Lea, P. Lovell, A. Lowther, C. Lydersen, T. McIntyre, C. McMahon, M. Muelbert, K. Nicholls, B. Picard, G. Reverdin, A. Trites, G. Williams, and P. de Bruyn. Marine mammals exploring the oceans pole to pole: A review of the meop consortium. *Oceanography*, June 2017. URL https://doi.org/10.5670/oceanog.2017.234.

V. C. Tsai, A. L. Stewart, and A. F. Thompson. Marine ice-sheet profiles and stability under coulomb basal conditions. *Journal of Glaciology*, 61(226):205–215, 2015. doi: 10.3189/2015JoG14J221.

T. Tyrrell, J. G. Shepherd, and S. Castle. The long-term legacy of fossil fuels. *Tellus B: Chemical and Physical Meteorology*, 59(4):664–672, 2007.

J. Van Breedam, H. Goelzer, and P. Huybrechts. Semi-equilibrated global sea-level change projections for the next 10 000 years. *Earth System Dynamics*, 11(4):953–976, 2020.

J. Van Breedam, P. Huybrechts, and M. Crucifix. A gaussian process emulator for simulating ice sheet–climate interactions on a multi-million-year timescale: Clisemv1.0. *Geoscientific Model Development*, 14(10):6373–6401, 2021. doi: 10.5194/gmd-14-6373-2021. URL https://gmd.copernicus.org/articles/14/6373/2021/.

J. Van Breedam, P. Huybrechts, and M. Crucifix. Modelling evidence for late eocene antarctic glaciations. *Earth and Planetary Science Letters*, 586:117532, 2022. ISSN 0012-821X. doi: https://doi.org/10.1016/j.epsl.2022.117532. URL https://www.sciencedirect.com/science/article/pii/S0012821X22001686.

J. van den Berg, R. van de Wal, and H. Oerlemans. A mass balance model for the eurasian ice sheet for the last 120,000 years. *Global and Planetary Change*, 61(3):194–208, 2008. ISSN 0921-8181. doi: https://doi.org/10.1016/j.gloplacha.2007.08.015. URL https://www.sciencedirect.com/science/article/pii/S0921818107001361.

W. van der Wal, P. L. Whitehouse, and E. J. Schrama. Effect of gia models with 3d composite mantle viscosity on grace mass balance estimates for antarctica. *Earth and Planetary Science Letters*, 414:134–143, 2015.

J. Van Wessem, C. Reijmer, M. Morlighem, J. Mouginot, E. Rignot, B. Medley, I. Joughin, B. Wouters, M. Depoorter, J. Bamber, and et al. Improved representation of east antarctic surface mass balance in a regional atmospheric climate model. *Journal of Glaciology*, 60(222):761–770, 2014. doi: 10.3189/2014JoG14J051.

J. C. G. Walker, P. B. Hays, and J. F. Kasting. A negative feedback mechanism for the long-term stabilization of earth's surface temperature. *Journal of Geophysical Research: Oceans*, 86(C10):9776–9782, 1981. doi: https://doi.org/10.1029/JC086iC10p09776. URL https://agupubs.onlinelibrary.wiley.com/doi/abs/10.1029/JC086iC10p09776.

P. Wang, J. Tian, and L. J. Lourens. Obscuring of long eccentricity cyclicity in pleistocene oceanic carbon isotope records. *Earth and Planetary Science Letters*, 290(3):319–330, 2010. ISSN 0012-821X. doi: https://doi.org/10.1016/j.epsl.2009.12.028. URL https://www.sciencedirect.com/science/article/pii/S0012821X09007511.

J. Weertman. On the sliding of glaciers. *Journal of Glaciology*, 3(21):33–38, 1957. doi: 10.3189/S0022143000024709.

J. Weertman. Stability of the junction of an ice sheet and an ice shelf. *Journal of Glaciology*, 13(67):3–11, 1974.

T. Westerhold. Cenozoic global reference benthic carbon and oxygen isotope dataset (CENOGRID), 2020. URL https://doi.org/10.1594/PANGAEA.917503.

T. Westerhold, U. Röhl, B. Donner, H. K. McCarren, and J. C. Zachos. A complete high-resolution paleocene benthic stable isotope record for the central pacific (odp site 1209). *Paleoceanography*, 26(2), 2011. doi: https://doi.org/10.1029/2010PA002092. URL https://agupubs.onlinelibrary.wiley.com/doi/abs/10.1029/2010PA002092.

T. Westerhold, N. Marwan, A. J. Drury, D. Liebrand, C. Agnini, E. Anagnostou, J. S. K. Barnet, S. M. Bohaty, D. D. Vleeschouwer, F. Florindo, T. Frederichs, D. A. Hodell, A. E. Holbourn, D. Kroon, V. Lauretano, K. Littler, L. J. Lourens, M. Lyle, H. Pälike, U. Röhl, J. Tian, R. H. Wilkens, P. A. Wilson, and J. C. Zachos. An astronomically dated record of earth’s climate and its predictability over the last 66 million years. *Science*, 369(6509):1383–1387, 2020. doi: 10.1126/science.aba6853. URL https://www.science.org/doi/abs/10.1126/science.aba6853.

P. L. Whitehouse, M. J. Bentley, G. A. Milne, M. A. King, and I. D. Thomas. A new glacial isostatic adjustment model for antarctica: calibrated and tested using observations of relative sea-level change and present-day uplift rates. *Geophysical Journal International*, 190(3):1464–1482, 2012.

M. Willeit, A. Ganopolski, R. Calov, and V. Brovkin. Mid-pleistocene transition in glacial cycles explained by declining co2 and regolith removal. *Science Advances*, 5 (4):eaav7337, 2019.

C. J. R. Williams, D. J. Lunt, A. T. Kennedy-Asser, and N. S. Lord. Uncertainties in modelled climate changes at forsmark over the next 1 million years, 2022.

D. Wilson, T. van de Flierdt, R. M. M. McKay, and T. Naish. *Pleistocene Antarctic climate variability: ice sheet - ocean-climate interactions*. Elsevier, 2021.

D. S. Wilson, S. S. Jamieson, P. J. Barrett, G. Leitchenkov, K. Gohl, and R. D. Larter. Antarctic topography at the eocene–oligocene boundary. *Palaeogeography, Palaeoclimatology, Palaeoecology*, 335:24–34, 2012.

D. S. Wilson, D. Pollard, R. M. DeConto, S. S. Jamieson, and B. P. Luyendyk. Initiation of the west antarctic ice sheet and estimates of total antarctic ice volume in the earliest oligocene. *Geophysical Research Letters*, 40(16):4305–4309, 2013.

R. Winkelmann, A. Levermann, A. Ridgwell, and K. Caldeira. Combustion of available fossil fuel resources sufficient to eliminate the antarctic ice sheet. *Science advances*, 1 (8):e1500589, 2015.

Y. G. Zhang, M. Pagani, Z. Liu, S. M. Bohaty, and R. DeConto. A 40-million-year history of atmospheric co2. *Philosophical Transactions of the Royal Society A: Mathematical, Physical and Engineering Sciences*, 371(2001):20130096, 2013.

C. Zweck and P. Huybrechts. Modeling of the northern hemisphere ice sheets during the last glacial cycle and glaciological sensitivity. *Journal of Geophysical Research: Atmospheres*, 110(D7), 2005. doi: https://doi.org/10.1029/2004JD005489. URL https://agupubs.onlinelibrary.wiley.com/doi/abs/10.1029/2004JD005489.

List of Figures

List of Tables

Acronyms

AIS Antarctic Ice Sheet.

AM Amplitude Modulation.

CMIP Coupled Model Intercomparison Project.

EAIS East Antarctic Ice Sheet.

EMIC Earth system Model of Intermediate Complexity.

GCM General Circulation Model.

IPCC Intergovernmental Panel on Climate Change.

LGM Last Glacial Maximum.

MISI Marine Ice Sheet Instability.

MPT Mid-Pleistocene Transition.

PDD Positive Degree Days.

RCP Representative Concentration Pathways.

SMB Surface Mass Balance.

SSP Shared Socio-economic Pathways.

WAIS West Antarctic Ice Sheet.